Thermoelectric Energy Conversion based on Sn-Chalcogenides: Electronic Structure Modulation and Low Thermal Conductivity

A thesis

Submitted for the Degree of

Doctor of Philosophy

by

ANANYA BANIK

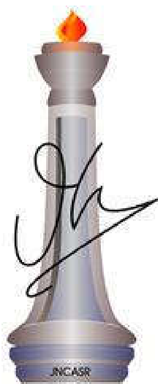

New Chemistry Unit
Jawaharlal Nehru Centre for Advanced Scientific Research
(A deemed University)
Bangalore-560064, India

October 2018

Dedicated to my late grandfather

DECLARATION

I hereby declare that this thesis entitled "**Thermoelectric Energy Conversion based on Sn-Chalcogenides: Electronic Structure Modulation and Low Thermal Conductivity**" is a result of studies carried out by me at the New Chemistry Unit, Jawaharlal Nehru Centre for Advanced Scientific Research, Bangalore, India, under the supervision of Prof. Kanishka Biswas. This work has not been submitted elsewhere for the award of any degree or diploma.

In keeping with the general practices of reporting scientific observations, due acknowledgements have been made wherever the work described is based on the findings of other investigators in a collaborative pursuit. Any omission which might have occurred by oversight or error in judgment is regretted.

Bangalore, India

Ananya Banik

CERTIFICATE

I hereby certify that the work described in this thesis titled "**Thermoelectric Energy Conversion based on Sn-Chalcogenides: Electronic Structure Modulation and Low Thermal Conductivity**" has been carried out by Ms. Ananya Banik at New Chemistry Unit, Jawaharlal Nehru Centre for Advanced Scientific Research, Bangalore, India under my supervision and that it has not been submitted elsewhere for the award of any degree or diploma.

Bangalore, India

Prof. Kanishka Biswas
(Research Supervisor)

ACKNOWLEDGEMENTS

Completion of my Ph.D thesis necessitated a lot of guidance and supports from many people. I take this opportunity to mention a few of them. However, my sincere thanks extend to everyone who has played a role in making this dream a reality.

Firstly, I would like to thank my research supervisor, Prof. Kanishka Biswas for suggesting me research problems and guiding me throughout. His valuable instructions and comments in scientific communications have helped me immensely. I express my hearty gratitude to him for giving me an opportunity to work under his guidance.

I would like to thank Bharat Ratna Prof. C. N. R. Rao, FRS, the chairman of New Chemistry Unit (NCU) for his generous support and encouragement throughout my stay in JNCASR. His presence has given me immense inspiration to indulge in active research. I also thank him for providing the infrastructure and facilities to carry out my research work.

I would like to thank Prof. Umesh V. Waghmare, Prof. Ranjan Datta, Prof. Goutam Sheet, Dr. Ajay Soni, Dr. Pralay K. Santra, Dr. Sandhya, Raagya, Juhi, Shashwat, Badri, Ananmul for the fruitful scientific collaborations and all the insightful discussions. I have learnt a lot whenever we had meeting with them or discussion with them.

I am thankful to all faculty members of New Chemistry Unit and Chemistry & Physics Material Science Unit of JNCASR for their courses.

I thank all my beloved labmates Dr. Guin, Dr. Chatterjee, Dr. Jana, Dr. Ghosh, Dr. Shidaling, Dr. P. Chithaiah, Dr. Pal, Dr. Perumal, Subhajit, Manisha, Ekashmi, Moinak, Arka, Sujoy, Sushmita, Paribesh, Krishnendu and Debattam for their cheerful company and help in various occasions.

I thank Dr. Somnath Ghara and Mr. Premakumar for their help during Hall measurement. I thank Mr. Rajasekhar (IISc.) for Hardness measurement. I would like to thank Dr. Jay Ghatak for various fruitful discussions.

I would like to thank JNCASR for providing me all the facilities.

Constant assistance and a friendly nature of the technical staff helped me doing my experiments smoothly. Here, I would like to acknowledge Mrs. Usha, Mr. Vasu, Mr. Anil, Ms. Selvi, Dr. Jay Ghatak, Mr. Mahesh, Mr. Jagadish, Mr. Shiva, Mr. Kanan, Mr. N. Kishore, Mr. M. Gowda, Mr. Dileep, Mr. Peer, Mr. Srinivas and others. I am thankful to all the academic, administrative, technical, security, complab and health center staffs for making our campus life smooth and easy.

I express my deep gratitude to all my high school and undergraduate teachers for training me to be disciplined, the basics of science and for growing my interest in research field.

I thank all of my 2012 Int. Ph. D. batchmates for having a wonderful time with them.

I have been benefited a lot from my JNC friends. Their help and advice made my academic and non-academic life a memorable and comfortable one here at JNC. I am thankful to all of them. A special thanks to Sohini, Soumyabrata, Syamantak, CD, Abhijit,

Saurav, Arka, Arpan, Somananda, Balaka, Moumita, Amrita, Asmita and Arjun for all the moments I spent with them and also for supporting me any time I required.

Lastly, I would like to acknowledge the most important people of my life, my parents and my family. Without their unconditional love and support all my efforts would have gone to vain. I am grateful to you all for whatever you gave me and I dedicate my thesis to you.

PREFACE

Thermoelectric effect enables direct conversion of thermal to electrical energy or vice versa and will play an important role in future energy management. Although PbTe is the most efficient material for mid-temperature power generation application, environmental concern about lead (Pb) prevents its use in thermoelectric module for large scale applications. Hence, the goal of thermoelectric community is to design Pb- free thermoelectric materials with high performance. Tin chalcogenide based materials are believed to substitute lead chalcogenides for thermoelectric power generation because of their promising structural, electrical, thermal and mechanical properties. The thesis entitled "**Thermoelectric Energy Conversion based on Sn-Chalcogenides: Electronic Structure Modulation and Low Thermal Conductivity**" demonstrate the journey of tin chalcogenides towards high thermoelectric performance. The thesis has been divided into seven chapters.

Chapter 1 of this thesis begins with a brief introduction of thermoelectrics and presents the different strategies for tuning of thermoelectric properties in inorganic solids. Then, I have addressed the key issues that make tin chalcogenide as potential alternative of lead chalcogenides and highlights why such a system was chosen for investigation, culminating into the thesis work. In the last part of this chapter, a general discussion on metal chalcogenide synthesis, detailed characterizations and thermoelectric measurement techniques are presented.

Chapter 2 discusses about the introduction of resonance dopant indium to improve the thermoelectric performance in *p*-type $SnTe_{1-x}Se_x$ System (x = 0-0.15). Resonance level formation in the valence band through indium (In) doping significantly improves the Seebeck coefficient, which results in a promising thermoelectric figure of merit, zT, of ~0.8 at 860 K in *p*-type 1.5 mol% In doped $SnTe_{0.85}Se_{0.15}$ sample.

Chapter 3 reports the enhancement of thermoelectric performance of SnTe by valence band convergence. **Chapter 3A** deals with the effect of Mg alloying on the electronic structure and the thermoelectric properties of SnTe. We have shown that Mg alloying in SnTe modulates its electronic structure by increasing the principal band gap of SnTe. Thus, solid solution alloying with Mg enhances the contribution of heavy hole valence band,

leading to significant improvement in the Seebeck coefficient in Mg alloyed SnTe, which in turn results in remarkable enhancement in thermoelectric figure of merit (*zT* ~1.2 at ~860 K for *p*-type $Sn_{0.94}Mg_{0.09}Te$). **Chapter 3B** presents impact of AgI alloying ($Sn_{1-x}Ag_xTe_{1-x}I_x$, x = 0-0.06) on the thermoelectric properties of SnTe. AgI alloying in SnTe simultaneously decreases energy difference between the light hole and heavy hole valence bands and optimizes the *p*-type carrier concentration. We have achieved significantly enhanced Seebeck coefficient and highest *zT* of ~1.05 in $Sn_{0.95}Ag_{0.05}Te_{0.95}I_{0.05}$.

Chapter 4 deals with synergistic effect of resonance level and valence band convergence to enhance thermoelectric properties of SnTe. **Chapter 4A** demonstrates the synergistic effect of In and Ag co-doping on the electronic structure and thermoelectric properties of SnTe-$AgInTe_2$ (i.e. $SnAg_xIn_xTe_{1+2x}$), where In doping creates resonance levels and valence band convergence is enabled by Ag doping in *p*-type SnTe. We have achieved a synergistic enhancement of Seebeck coefficient and record high power factor (σS^2) in $SnAg_xIn_xTe_{1+2x}$ over a broad temperature range (300−860 K) compared to that of controlled In doped SnTe and Ag doped SnTe. **Chapter 4B** concentrates on further improvement of thermoelectric transport properties of Ag & In co-doped SnTe by addition of SnS which reduces the κ_{lat} through nanostructuring. We have shown that by integrating synergistic approaches: (a) carrier engineering, (b) resonance level formation, (c) valence band convergence and (d) nanostructuring, we can achieve a maximum *zT* of ~1.3 at 871 K in $Sn_{1.03}Te_{1-x}S_x$-$AgInTe_2$, which is significantly higher than that of pristine SnTe.

Chapter 5 reports reduction of lattice thermal conductivity near to the theoretical minimum limit, κ_{min}, in SnTe. A detailed microscopic understanding of the origin of the low κ_{lat} in $Sn_{1-x}Sb_xTe$ has been discussed. High-resolution transmission electron microscopic imaging of $Sn_{1-x}Sb_xTe$ samples reveals the formation of super-structured intergrowth nanodomains of $Sn_mSb_{2n}Te_{3n+m}$, which are the key features responsible for the significant reduction of lattice thermal conductivity in SnTe.

Chapter 6 is focused on the study of design, synthesis and thermoelectric properties of layered tin chalcogenides. **Chapter 6A** describes the solution based synthesis and charecterizations of ultrathin 2D nanosheets of layered intergrowth heterostructures from $Sn_mBi_{2n}Te_{3n+m}$ homologous family by a simple low temperature solution based method.

Nanosheets of homologous $Sn_mBi_{2n}Te_{3n+m}$ compounds exhibit ultra low lattice thermal conductivity, κ_{lat} (~0.3-0.5 W/mK) due to significant phonon scattering by heterostructure surfaces/interfaces with long unit cell and stacking faults. **Chapter 6B** presents a simple solution-based synthesis and thermoelectric transport properties of ultrathin few layers nanosheets of *n*-type $SnSe_2$.

Chapter 7 reports a new strategy to significantly reduce the κ_{lat} without degrading carrier mobility of SnTe by engineering the ferroelectricity instability. We have utilized the substitution of Ge (0–30 mol%) in SnTe to strengthen its ferroelectric instability near room temperatures and reduce the κ_{lat} (κ_{lat} ~ 0.67 W/mK at 300 K in $Sn_{0.7}Ge_{0.3}Te$, for SnTe, κ_{lat} ~3 W/mK). Further, $Sn_{1-x}Ge_xTe$ samples exhibit high carrier mobility which can be ascribed to effective dielectric screening of charge carriers from the impurities/defects. With the synergy among ultra-low κ_{lat}, high carrier mobility and enhanced Seebeck coefficient, we achieve highest thermoelectric figure of merit, *zT*, of ~ 1.6 at 721 K in carrier optimized Sb-doped $Sn_{0.7}Ge_{0.3}Te$. This chapter opens up a new avenue to inhibit thermal conduction while retaining high carrier mobility in crystalline solids by employing local distortion associated with ferroelectric instability.

TABLE OF CONTENTS

DECLARATION .... **III**
CERTIFICATE .... **V**
ACKNOWLEDGEMENTS .... **VII**
PREFACE .... **IX**

Chapter 1: A Brief Introduction to Thermoelectrics: Tin Chalcogenides, an Alternative to PbTe **1**
Summary... 3
1.1 Introduction 5
1.2 Origin of thermoelectric effect 6
1.3 Thermoelectric efficiency 7
1.4 Recent advances in TE materials research 10
1.4.1 Increment of the power factor 11
1.4.1.1 Carrier concentration optimization 11
1.4.1.2 Resonance Level 12
1.4.1.3 Convergence of electronic band valleys 13
1.4.2 Reduction of thermal conductivity 14
1.4.2.1 Phonon-phonon scattering 15
1.4.2.2 Point defect phonon scattering 15
1.4.2.3 Nanostructuring 16
1.4.2.4 Mesoscale grain boundary 17
1.4.2.5 All-scale hierarchical architectures 17
1.4.2.6 Intrinsic phonon scattering 18
1.5 Tin chalcogenides as potential thermoelectric material 19
1.6 Lattice dynamics of tin chalcogenides 20
1.7 Electronic structures of tin chalcogenides 24
1.8 Tin telluride (SnTe) 26
1.9 Sn-based layered chalcogenides 29
1.10 Synthesis and characterizations 31
1.10.1 Synthesis 32
1.10.2 Characterizations 34
1.10.2.1 Powder X-ray diffraction (PXRD) 34
1.10.2.2 Transmission electron microscope (TEM) 35
1.10.2.3 Field emission scanning electron microscope (FESEM) 36
1.10.2.4 High-angle annular dark-field scanning transmission electron microscopy (HAADF-STEM) 36
1.10.2.5 Energy dispersive X-ray analysis (EDAX) 37
1.10.2.6 X-ray photoelectron spectroscopy (XPS) 37

1.10.2.7 Inductively coupled plasma-atomic emission spectroscopy (ICP-AES) ...38
1.10.2.8 Optical band gap ...38
1.10.2.9 Differential scanning calorimetry (DSC) ...39
1.10.2.10 Raman spectroscopy...39
1.11 Thermoelectric measurements ...40
1.11.1 Seebeck coefficient...40
1.11.2 Electrical conductivity...40
1.11.3 Thermal conductivity...41
1.11.4 Hall effect ...43
1.12 Scope of the thesis ...44
1.13 References...46

Chapter 2: Introduction of Resonance Dopant Indium Improves the Thermoelectric Performance in *p*-type $SnTe_{1-x}Se_x$ System ...53
Summary ...55
2.1 Introduction...57
2.2 Methods...59
2.2.1 Synthesis ...59
2.2.2 Characterizations...59
2.2.3 Transport properties ...59
2.3 Results & Discussion ...60
2.3.1 Solid solution alloying in $SnTe_{1-x}Se_x$...60
2.3.2 Indium doping in $SnTe_{1-x}Se_x$...64
2.4 Conclusions...67
2.5 References...68

Chapter 3: Enhancement of Thermoelectric Performance of SnTe by Valence Band Convergence ...69

Chapter 3A: Mg Alloying in SnTe Facilitates Valence Band Convergence and Optimizes Thermoelectric Properties...71
Summary ...71
3A.1 Introduction...73
3A.2 Methods ...74
3A.2.1 Synthesis ...74
3A.2.2 Characterizations ...75
3A.2.3 Transport properties...75
3A.2.4 Computational details ...75
3A.3 Results & Discussion...76
3A.4 Conclusions...84
3A.5 References...85

Chapter 3B: AgI Alloying in SnTe Boosts the Thermoelectric Performance via Simultaneous Valence Band Convergence and Carrier Concentration Optimization ...87
Summary... ...87
3B.1 Introduction...89

3B.2 Methods ... 90
3B.2.1 Synthesis ... 90
3B.2.2 Characterizations ... 90
3B.2.3 Transport properties ... 90
3B.3 Results & Discussion ... 91
3B.4 Conclusions ... 99
3B.5 References ... 100

Chapter 4: Synergistic Effect of Resonance Level and Valence Band Convergence in Enhancing Thermoelectric Properties of SnTe ... 101

Chapter 4A: High Power Factor and Enhanced Thermoelectric Performance of SnTe-$AgInTe_2$: Synergistic Effect of Resonance Level and Valence Band Convergence ... 103
Summary... ... 103
4A.1 Introduction ... 105
4A.2 Methods ... 106
4A.2.1 Synthesis ... 106
4A.2.2 Characterizations ... 106
4A.2.3 Transport properties ... 106
4A.2.4 Computational details ... 107
4A.3 Results & Discussion ... 108
4A.4 Conclusions ... 116
4A.5 References ... 118

Chapter 4B: Synergistic Effect of Nanostructuring, Valence Band Convergence and Resonance Level Formation Boost The Thermoelectric Performance of SnTe-SnS ... 121
Summary.. ... 121
4B.1 Introduction ... 123
4B.2 Methods ... 124
4B.2.1 Synthesis ... 124
4B.2.2 Charaterizations ... 124
4B.2.3 Transport properties ... 125
4B.3 Results & Discussion ... 125
4B.4 Conclusions ... 134
4B.5 References ... 135

Chapter 5: The Origin of Low Thermal Conductivity in $Sn_{1-x}Sb_xTe$: Phonon Scattering via Layered Intergrowth Nanostructures ... 137
Summary ... 139
5.1 Introduction ... 141
5.2 Methods ... 142
5.2.1 Synthesis ... 142
5.2.2 Characterizations ... 143
5.2.3 Transport properties ... 143
5.2.4 Mechanical properties ... 143

5.3 Results & Discussion 144
5.4 Conclusions 153
5.5 References 155

Chapter 6: Synthesis and Thermoelectric Transport Properties of Nanosheets of Layered 2D Sn-Chalcogenides 157

Chapter 6A: Synthetic Nanosheets of Natural van der Waals Heterostructures 159
Summary... 159
6A.1 Introduction 161
6A.2 Methods 162
6A.2.1 Synthesis 162
6A.2.2 Characterizations 165
6A.2.3 Transport properties 165
6A.3 Results & Discussion 166
6A.4 Conclusions 177
6A.5 References 179

Chapter 6B: Ultrathin Few Layer Nanosheets of *n*-type $SnSe_2$ 181
Summary... 181
6B.1 Introduction 183
6B.2 Methods 185
6B.2.1 Synthesis 185
6B.2.2 Characterizations 186
6B.2.3 Transport properties 187
6B.3 Results & Discussion 187
6B.4 Conclusions 194
6B.5 References 196

Chapter 7: Engineering Ferroelectric Instability to Achieve Ultralow Thermal Conductivity and High Thermoelectric Performance in $Sn_{1-x}Ge_xTe$ 199
Summary 201
7.1 Introduction 203
7.2 Methods 205
7.2.1 Synthesis 205
7.2.2 Characterizations 205
7.2.3 Transport properties 206
7.2.4 Computational details 207
7.3 Results & Discussion 208
7.4 Conclusions 218
7.5 References 220

List of Publications 223
Biography 225

CHAPTER 1

A Brief Introduction to Thermoelectrics: Tin Chalcogenides, an Alternative to PbTe

Chapter 1

A Brief Introduction to Thermoelectrics: Tin Chalcogenides, an Alternative to PbTe[†]

Summary

Thermoelectric materials can convert waste heat into useful electricity, and constitute a viable means of efficient energy management. Lead chalcogenides and their alloys belong to the heart of thermoelectrics due to their large thermoelectric figure of merit (zT). However, recent research shows the limitation in the applicability of lead (Pb)-based materials due to their toxicity and inspired to avail non-toxic analogue of lead chalcogenides. Tin chalcogenides have been predicted to be promising for this purpose for their unique electronic structure and phonon dispersion. In this chapter, I have addressed the key issues that make tin chalcogenide as a potential alternative of lead chalcogenides and highlights why such a system was chosen for investigation with the main emphasis towards the bonding, crystal structures, electronic band structures, phonon dispersion and thermoelectric properties. Thermal transport properties of tin chalcogenides have been explained based on lattice dynamics, where resonant bonding and local structural distortion play an important role to create lattice anharmonicity, thereby low lattice thermal conductivity. Last part of this chapter is focused on a general discussion of metal chalcogenide synthesis, characterizations and thermoelectric measurements.

[†]*A part of this chapter has been published in the form of perspective article in* ***Chem. Commun.*** 2018, *54,* 6573.

1.1 Introduction

The rising global energy demand is causing a dramatic acceleration of social unrest. Impact of climate change on the environment due to the combustion of nonrenewable energy sources is becoming increasingly alarming. To mitigate the dramatic surge of the global energy crisis and furnishing sustainable, renewable and environment-friendly energy source hold precedence not only to the scientific community but also to the global population as a whole. Heat can be considered as a renewable energy source owing to its pervasive and ineluctable nature. Thermal processes produce >90% of the energy we use, whereas ~60% of energy is inevitably lost through heat dissipation.[1-3] Thus, designing of efficient thermoelectric (TE) materials will cater to its purpose due to their ability to convert waste heat to electricity reversibly.[1,3,4] Exhaust from domestic heating, automobiles and industrial produce a large amount of unused waste heat that could be converted to electricity by using thermoelectric devices.[1,2] Thermoelectric (TE) module consists of both *p*-type and *n*-type semiconductors connected through metallic conducting pad.[5] A TE module or device comprises an array of *p*- and *n*-type TE couples, which are arranged electrically in series and thermally in parallel. Both power generation and refrigeration can be accomplished as shown in figure 1.1. As thermoelectric generators are all solid-state devices without any mobile parts, they are suitable for small-scale power generation and distribution. For the past 40 years, thermoelectric generators are consistently providing power in remote terrestrial and extraterrestrial locations (radioisotope thermoelectric generators, RTGs in Voyager 1, Voyager 2, Galileo, Ulysses, Cassini, and New Horizons spacecraft),[6,7] Solid-state Peltier coolers offer precise thermal management for optoelectronics and automobiles.[8-10] Efforts are already underway to replace the alternator in cars with a thermoelectric generator mounted on the exhaust stream, thereby improving the fuel efficiency.[9] The reliability and stability of thermoelectrics makes them suitable for wider applications such as sub-ambient cooling of infrared detectors and thermal management systems in microprocessors etc.[2] More recently, research on the topic of solar-thermoelectrics is gaining attention where the IR-part of the solar spectrum is utilized for thermoelectric-solar power generation.[11,12]

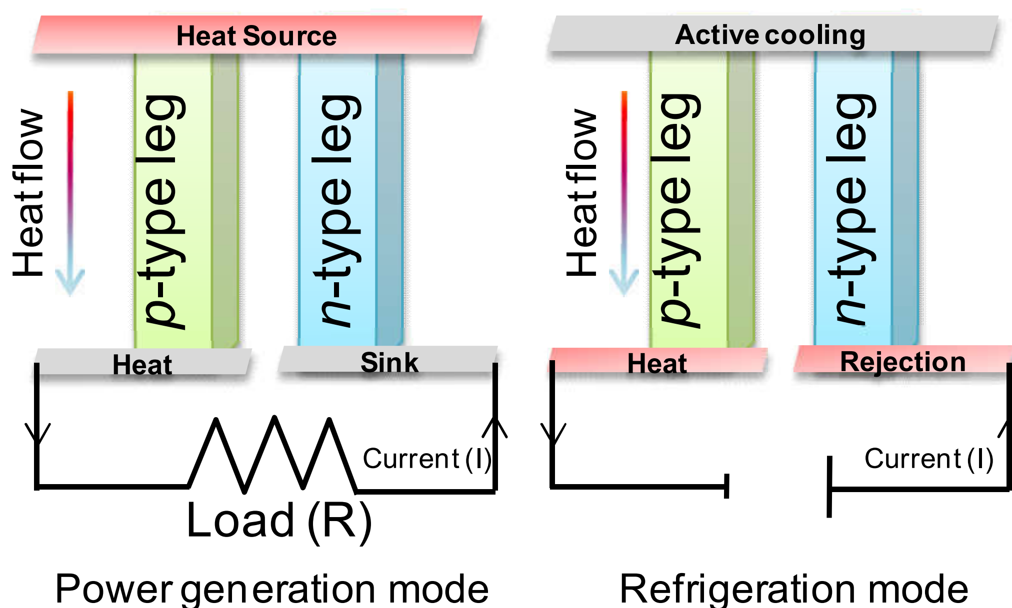

Figure 1.1 Generic diagram of thermoelectric modules made of *p*-type and *n*-type thermoelectric materials for power generation and refrigeration application. Reproduced with permission from ref. 64 © The Royal Society of Chemistry.

1.2 Origin of thermoelectric effect

Thermoelectric phenomena were first discovered at the beginning of the 19th century by the German scientist, Thomas J. Seebeck, who observed the deviation of a compass needle when keeping the two junctions of dissimilar metals at different temperatures.[5,13] However, Seebeck believed it to be a magnetic phenomenon and tried to correlate the Earth's magnetism with the temperature difference between the equator and the Poles. Later, it was realized that a "Thermoelectric Force" induced an electrical current, which deflected the magnet following Ampere's law. More specifically, the temperature difference (ΔT) produces an electric potential (ΔV) which drives an electric current in a closed circuit. The proportionality constant is known as the Seebeck coefficient (S), and frequently referred to "thermopower" even though it is more related to potential than power. Shortly thereafter, in 1834, a complementary effect was discovered by French scientist Jean C. A. Peltier who observed the temperature change in the vicinity of the junction between dissimilar conductors when a current passed.[13] However, he was unable

to realize the fundamental nature of his observations or relate the effect to the findings of Seebeck. The true nature of the Peltier effect was explained by the Russian scientist, Lenz in 1838. He stated that heat can be absorbed or generated at a junction between two conductors, depending upon the direction of the current flow. The Peltier coefficient, Π can be described as the ratio of heat flow (Q) to applied current (I), ($\Pi = \frac{Q}{I}$). In 1851 W. Thomson (Lord Kelvin) established the relationship between the Seebeck and Peltier coefficients and predicted the existence of a third thermoelectric effect, the Thomson effect, which describes the heating or cooling in a single homogeneous conductor when a current passes along it in the presence of a temperature gradient.

1.3 Thermoelectric efficiency

The possible use of thermoelectric phenomena in electricity generation was first considered in the year of 1885 by Rayleigh who first calculated, although incorrectly, the efficiency of a thermoelectric generator.[13] In 1909, Altenkirch analyzed the efficiency of a thermoelectric generator and derived an expression for the load resistance that yields the highest efficiency in a TE generator. Altenkirch's paper described the role of thermal conductivity, κ_{total}, and electrical conductivity, σ on its power conversion efficiency. In 1947, Telkes presented an extensive historical review of TE generators, including consideration of desirable properties, but with no discussion of a single figure of merit. Later, Ioffe introduced the figure of merit, zT as a part of TE efficiency.[14] The thermoelectric conversion efficiency for a material requires both high zT values and a large temperature difference across the thermoelectric materials, as given by the following relation:

$$\eta_{TE} = \eta_c \frac{\left(\sqrt{1+zT} - 1\right)}{\left(\sqrt{1+zT} + \frac{T_C}{T_H}\right)} \tag{1.1}$$

where η_c, T_H and T_C are Carnot Efficiency, the temperatures of the hot and cold ends and zT, the dimensionless figure of merit is expressed as

$$zT = \frac{\sigma S^2}{\kappa_{\text{total}}} T \qquad (1.2)$$

Where σ, S, κ_{total} and T are the electrical conductivity, Seebeck coefficient, thermal conductivity and absolute temperature, respectively.[1,2,15]

To maximize the thermoelectric figure of merit (zT) of a material, high electrical conductivity, a large Seebeck coefficient and a low thermal conductivity are needed.[15]

The quantity σS^2 is defined as power factor and is the key to achieve high thermoelectric performance. A large power factor means the generation of large voltage and a high current. For high σS^2, a material is needed to have high electrical conductivity (σ) and large Seebeck coefficient (S). For metals or degenerate semiconductors (parabolic band, energy-independent scattering approximation[2]), the Seebeck coefficient is proportional to the effective mass (m^*) and temperature, and inversely proportional to the charge carrier concentration (n_{H}), as seen in equation 1.3.[2]

$$S = \frac{8\pi^2 k_B^2}{3eh^2} m^* T \left(\frac{\pi}{3n_H}\right)^{2/3} \qquad (1.3)$$

where k_B is the Boltzmann constant, h is the Planck constant, and e is the electron charge. Thus, a large Seebeck coefficient indicates a large effective mass which is equivalent to a large density-of-states (DOS) or flat bands at the Fermi level.[2,3] High electrical conductivity requires a large mobility (μ) and a large carrier (electrons or holes) concentration (n_{H}), as seen in equation 1.4.

$$\sigma = ne\mu \qquad (1.4)$$

Where mobility, μ can be defined by the following expression:

$$\mu = \frac{e\tau}{m^*} \qquad (1.5)$$

Here τ is the relaxation time and m^* is the carrier effective mass.[1]

On the other hand, thermal conductivity (κ_{total}) has two parts: the lattice or phonon contribution (κ_{lat}) and the electronic contribution (κ_{el}) (Equation 1.6).

$$\kappa_{total} = \kappa_{el} + \kappa_{lat} \qquad (1.6)$$

κ_{el} is proportional to the electrical conductivity through the Wiedemann–Franz law.[16]

$$\kappa_{el} = L\sigma T \tag{1.7}$$

where L is the Lorenz Number. For free electrons, it is 2.45×10^{-8} $W\Omega K^{-2}$. The Lorenz number varies with the material's carrier concentration and can be reduced by as much as 20% from the free-electron value for the materials with low-carrier-concentration. From equation 1.7, it is clear that increasing electrical conductivity is detrimental to realize high zT because of simultaneous enhancement in electrical and thermal conductivity.

Since κ_{el} is proportional to σ via Wideman-Franz law (Equation 1.7), the only way to achieve low thermal conductivity (κ_{total}) is to manipulate the lattice thermal conductivity (κ_{lat}). According to the kinetic theory of phonon 'gas', the lattice thermal conductivity of a solid material can be described as[17]

$$\kappa_{lat} = \frac{1}{3} c_V \vartheta l \tag{1.8}$$

where c_V is the specific heat capacity at constant volume, l is phonon mean free path (MFP, defined as the average distance traveled by phonons between successive scatterings), and ϑ is the average velocity of sound.

Unlike c_V and l, the velocity of sound (ϑ) is material-dependent and varies very little with changes in temperature, morphology, or doping. At high temperatures ($T \gg \Theta_D$, Debye temperature), since the energy carried by each atom in bulk materials approaches to $3k_BT$, specific heat reaches the Dulong–Petit limit ($3k_B$ per atom), resulting in the difficulty for manipulating the specific heat of thermoelectric materials. Thus, above Debye temperature (Θ_D), κ_{lat} primarily depends on phonon mean free path, l. Phonon mean free path is determined by rate of a) phonon-phonon scattering and (b) scattering with grain-boundaries or static impurities. In case of semiconductors when carrier concentration is lesser than 10^{19}-10^{20} cm^{-3}, κ_{lat} usually dominates the κ_{total}. Moreover, acoustic phonons usually dominate κ_{lat} over optical phonons because of their higher group velocities, $\vartheta_i = \frac{\partial \omega}{\partial k}$ (here i refers to polarization of acoustic phonons i.e., longitudinal (LA) or transverse (TA1, TA2)). Since phonon mean free path of any material is limited by inter atomic distance, minimum the lattice thermal conductivity, κ_{min} cannot be reduced lower than that of the amorphous limit, as defined by Cahill.[18]

$$\kappa_{min} = \frac{1}{2}(\frac{\pi}{6})^{\frac{1}{3}} k_B V^{-(\frac{2}{3})}(2\vartheta_t + \vartheta_l) \quad (1.9)$$

where, V is average volume per atom, k_B is the Boltzman constant, ϑ_t and ϑ_l are the transverse and longitudinal sound velocities.

1.4 Recent advances in TE materials research

Thermoelectric have always been a materials design problem relating complicated tuning of structure-property relationships in inorganic solids through principles of solid state chemistry. Several years ago Slack and thereafter Mahan has portrayed the chemical characteristics of materials those might be proven to be good candidates for a TE application. According to them, narrow-band gap semiconductors (e.g., $E_g \approx 10\ k_BT$ or $\approx$ 0.25 eV at 300 K) with high-mobility carriers are the ideal candidate for TE application.[13] In semiconductors, the Seebeck coefficient and the electrical conductivity (both in the numerator of zT) depend on the doping level and chemical composition. In addition to this, material's κ_{lat} should be low. Therefore, to design a high performance TE material, these quantities must be optimized. The major obstacle lies in the optimization of all of these parameters together in a single material due to their strong interdependence.[1,2,4] However, in the last few years, numerous efforts have been devoted to decoupling and synergizing individual TE parameters. Approaches to improve the power factor includes enhancement of the Seebeck coefficient through the formation of resonance level in the electronic bands[19-21] and convergence of degenerate electronic band valleys through alloying and carrier engineering.[22-24] Significantly low lattice thermal conductivity has been achieved via phonon scattering by solid solution point defects,[1,16] second phase nanoprecipitates,[25-28] meso-scale grain boundaries[1,29] and intrinsic bond anharmonicity.[30] In the following section, I will summarize the most recent approaches of designing high-performance TE materials.

1.4.1 Increment of the power factor

Power factor (σS^2) is a purely electronic property, governed by materials' electronic structure and scattering mechanism.[20] Strategies to enhance power factor include: a) engineering of carrier-concentration (n_H) through chemical doping,[31] b) enhancement of the effective carrier mass (m^*) and Seebeck coefficient (S) via the convergence of multiple valence/conduction band extrema,[22] or distortion of the density of states near Fermi level by resonance impurity levels,[19] and c) enhancement of carrier mobility (μ) by modulation-doping[32].

1.4.1.1 Carrier concentration optimization

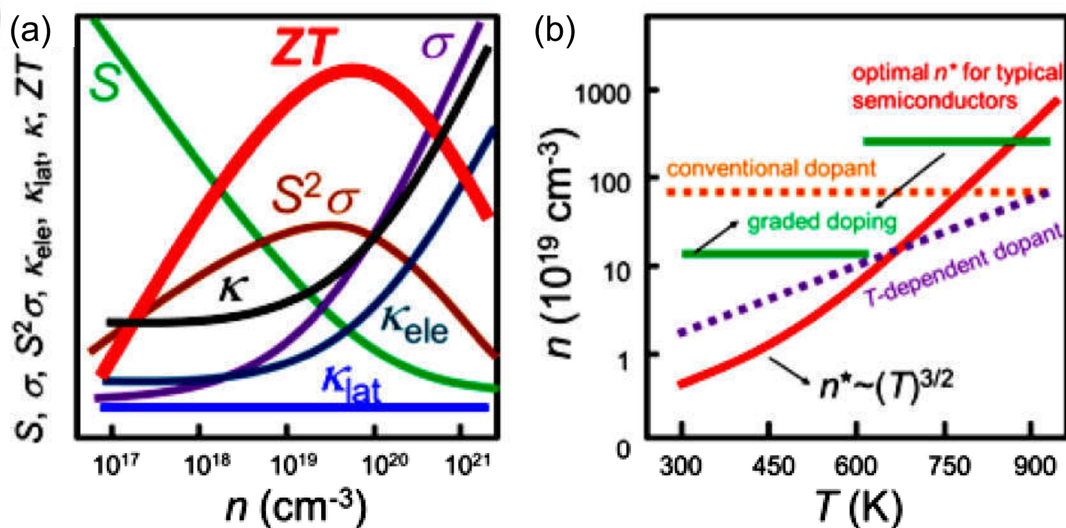

Figure 1.2 (a) Schematic diagram showing the dependence of ZT ($\sim zT$) and its parameters (electrical conductivity σ, Seebeck coefficient S, power factor $S^2\sigma$, electronic thermal conductivity κ_{ele}, lattice thermal conductivity κ_{lat} and total thermal conductivity, κ) on carrier concentration n ($\sim n_H$). (b) Strategies for stabilizing the optimal carrier concentration. Reproduced with permission from ref. 1 © 2016 American Chemical Society.

The fundamental challenge of designing high-zT thermoelectric materials is strong interdependence of σ, S and κ_{total} through carrier concentration, n (Figure 1.2) which can be optimized by controlling the doping level. The maximum zT value arises in the carrier concentration range of 10^{19}-10^{21} cm^{-3}, which falls in between metals and semiconductors - that is concentration typically found in heavily doped semiconductors (i.e. degenerate semiconductor).[2] However, carrier concentration (n_H) increases rapidly with rising temperature, following the power law of $T^{3/2}$. Although conventional doping is effective

to tune room temperature carrier optimization, it is difficult to achieve optimum carrier concentration at high temperature. Thus the maximum theoretical zT cannot be fully realized at every working temperature. An effective solution to this issue is the use of functionally graded doping, by integrating two or multiple segments with dissimilar n_H.[1] The modifications to the conventional doping method to include temperature-dependent doping behavior are helpful to acquire larger average zT values which are especially important for technological applications.

1.4.1.2 Resonance level

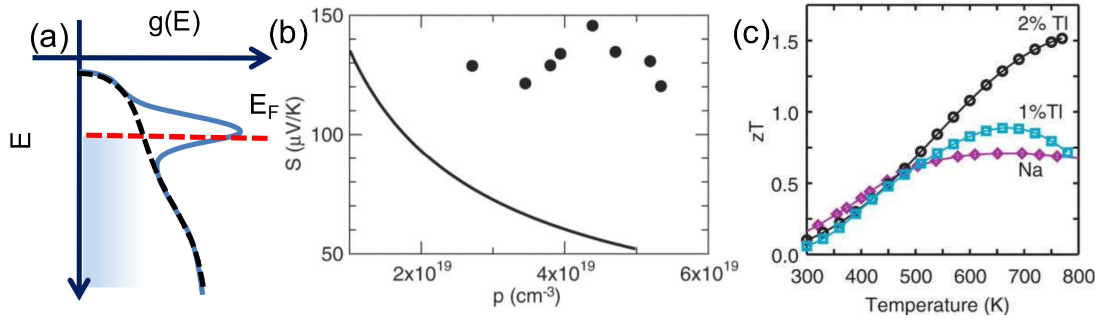

Figure 1.3 (a) Schematic diagram of resonance level in the valence band. Schematic diagram of density of state (DOS) of the valence band of pristine sample (dotted black line). Tl-doped PbTe shows asymmetric distortion of DOS (blue line) near Fermi level. (b) Pisarenko relation of Seebeck coefficient *vs* hole concentration, p for PbTe (solid line) at 300 K compared to the results on Tl-PbTe sample. Significantly large S value in Tl-doped PbTe confirmed the presence of resonance level. (c) The temperature dependent zT values for $Tl_{0.02}Pb_{0.98}Te$ (black circles) and $Tl_{0.01}Pb_{0.99}Te$ (blue squares) compared to that of a reference sample of Na-PbTe (purple diamonds). Figure (b) and (c) are reproduced with permission from ref. 19 © 2008 AAAS.

The concept of resonance level was first proposed in 1950.[33] Resonance level originates from the coupling between electrons of a dilute impurity with those of the valence or conduction band of the host solid near its Fermi level.[20] Thus, resonance dopant creates an excess density of states near the valence or the conduction band edge of the host compound (Figure 1.3a) and results in higher effective mass, m^* and thereby enhances Seebeck coefficient, according to Mott expression (Equation 1.10).[1]

$$\begin{aligned} S &= \frac{\pi^2}{3}\frac{k_B}{q}\,k_B T\left\{\frac{d[ln(\sigma(E))]}{dE}\right\}_{E=E_F} \\ &= \frac{\pi^2}{3}\frac{k_B}{q}\,k_B T\left\{\frac{1}{n_H}\frac{dn_H(E)}{dE}+\frac{1}{\mu}\frac{d\mu(E)}{dE}\right\}_{E=E_F} \end{aligned} \tag{1.10}$$

Here, $\sigma(E)$ is the electrical conductivity determined as a function of the band filling or Fermi energy, E_F ($\sigma(e) = n_H(E)q\mu(E)$) and $n_H(E)$ ($n_H(E) = g(E)f(E)$), the carrier density at the energy level, E (here q is the carrier charge, and $\mu(E)$ is the mobility as a function of energy, $f(E)$ is the Fermi function, $g(E)$ is density of state).

When electronic scattering is independent of energy, $\sigma(E)$ is just proportional to the density of states (DOS) at E. Based on the above expression it is clear that the system with rapid change in DOS near E_F is expected to have large Seebeck. Pisarenko plot represents the dependence of Seebeck on carrier concentration. A significantly higher S value than what a Pisarenko plot gives the indication of resonance level formation (Figure 1.3b).[19]

Group-III (mainly Al, In and Tl) dopants form resonance level in PbTe.[34] Heremans, *et al*. demonstrated experimentally that Tl doping improves S of PbTe by resonance level formation and thereby achieved the double value of zT, as seen in figure 1.3.[19]

1.4.1.3 Convergence of electronic band valleys

Multiple pockets in valence or conduction band extreme give rise to high Seebeck coefficient because these valleys (separate pockets of Fermi surface with the same energy) have the effect of producing large effective mass (m^*) without explicitly reducing μ, as seen in equation 1.11.[22]

$$m^* = N_V^{2/3} m_b^* \tag{1.11}$$

Where N_V represents orbital degeneracy and m_b^* represents single valley density of state effective mass of degenerate valleys.

Thus, effective doping to energetically align the electronic bands for a higher degree of band degeneracy lies at the core of the band-convergence scheme.[1,22] The aim is to enhance the Seebeck coefficient without substantially degrading the σ. When the system is heavily doped, overall effective mass can be enhanced through carrier redistribution to multiple valleys, thus results in high Seebeck coefficient. Since carrier mobility will be unaffected in this process, valence band convergence gives rise to significantly high σS^2 and zT in carrier optimized system.

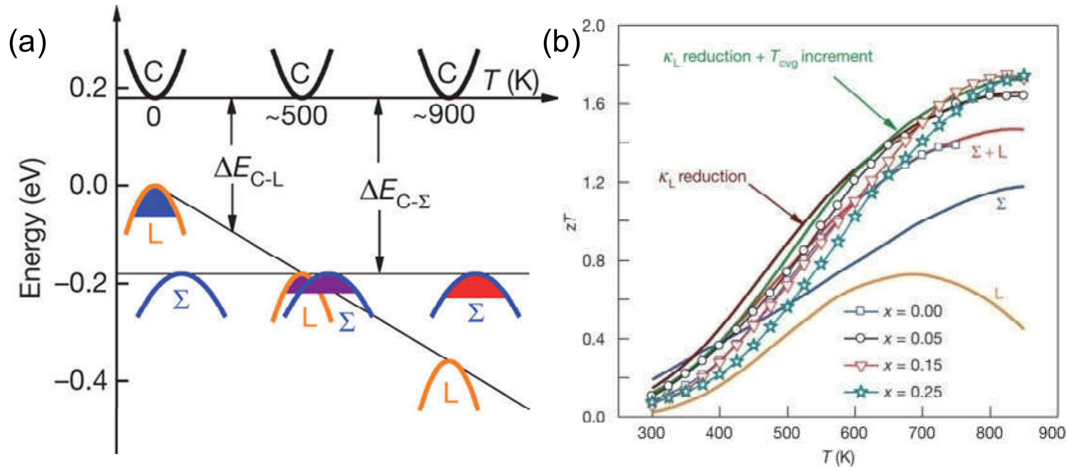

Figure 1.4 (a) Relative energy of the valence bands in $PbTe_{0.85}Se_{0.15}$. At, 500 K the two valence bands converge, resulting in contributions from both the L and Σ bands in the transport properties. (b) Temperature dependent zT of p-$PbTe_{1-x}Se_x$ materials doped with 2 atom % Na. Adopted with permission from ref. 22 © 2011 Nature Publishing Group.

Pei *et al.* have demonstrated the band convergence of at least 12 valleys in doped $PbTe_{1-x}Se_x$ alloys, leading to an extraordinarily high zT value of 1.8 at about 850 K, as seen in figure 1.4.[22] Alloying Se reduces the energy difference between the L and Σ bands of the PbTe making the two bands effectively converged. Hence enhancement in N_V from 4 (for L band) to 12 (for Σ band) results in an increase in m^* and Seebeck. A similar result was observed in PbTe, after it was alloyed with wide band gap chalcogenides (MgTe, CaTe, BaTe).

1.4.2 Reduction of thermal conductivity

Above Debye temperature, since κ_{lat} is mainly dominated by phonon mean free path, effective phonon scattering will lead to lower κ_{lat} in any material.[2] The effective mean free path, l_{eff}, can be expressed based on Matthiessen's rule.

$$\frac{1}{l_{eff}} = \frac{1}{l_p} + \frac{1}{l_n} + \frac{1}{l_b} + \frac{1}{l_{ph-ph}} \quad (1.12)$$

where l_p, l_n, l_b and l_{ph-ph} are the mean free path due to the phonon scattered at atomic scale defect, nanostructured second phase, mesoscale boundary and phonon–phonon scattering processes, respectively.

1.4.2.1 Phonon-phonon scattering

There are two types of phonon–phonon scattering process - normal process (N-process), and Umklapp process (U-process). While N-processes don't directly contribute to thermal resistance, U-processes hinder thermal transport. The effectiveness of U-processes in inhibiting heat transfer depends on 1) the scattering cross-section or frequency of collisions and 2) the amount of momentum loss during each collision. Since the U-process depends on the phonons density, it becomes more dominant as the temperature is increased, and the phonon mean free path corresponding to U-process is inversely proportional to temperature, $\sim 1/T$ ($T >> \Theta_D$). For ideal crystal, U-scattering is the dominant process for thermal resistivity at high temperatures.

1.4.2.2 Point defect phonon scattering

Introduction of lattice imperfections (point defects) in the host lattice (doping or alloying) is a well-known strategy of decreasing the κ_{lat} via scattering of short-wavelength phonons.[35,36] According to the thermal conductivity model developed by Callaway[37] and Klemens[38], reduction of κ_{lat} can be attributed to the combined effect of mass contrast and strain field fluctuations. The degree of κ_{lat} reduction can be evaluated by the following expression of scattering parameter (Γ):

$$\Gamma = x(1-x)\left[\left(\frac{\Delta M}{M}\right)^2 + \varepsilon\left(\frac{\Delta a}{xa}\right)^2\right] \tag{1.13}$$

where ε is a phenomenological parameter related to the material's Grüneisen parameter γ, M and a are the molar mass and lattice constant of the alloy, ΔM and Δa are the differences in mass and lattice constant between the two constituents. From equation 1.13, one can conclude that to maximize Γ and achieve the lowest κ_{lat}, it is necessary to have (1) a high doping fraction x, (2) a large mass difference between the dopant and the host element (ΔM) creating disorder in the lattice, and (3) a significant lattice mismatch (Δa) between the disordered phase and the host phase. Thus, solid solutions of $PbTe_{1-x}Se_x$ has lower κ_{lat} as compared to that of pure PbTe (Figure 1.5).[39] Recently The $(PbTe)_{1-2x}(PbSe)_x(PbS)_x$ system has shown ultra low thermal conductivity of ~0.5 W/m.K and highest zT of ~2 owing to strong point defect scattering.[35]

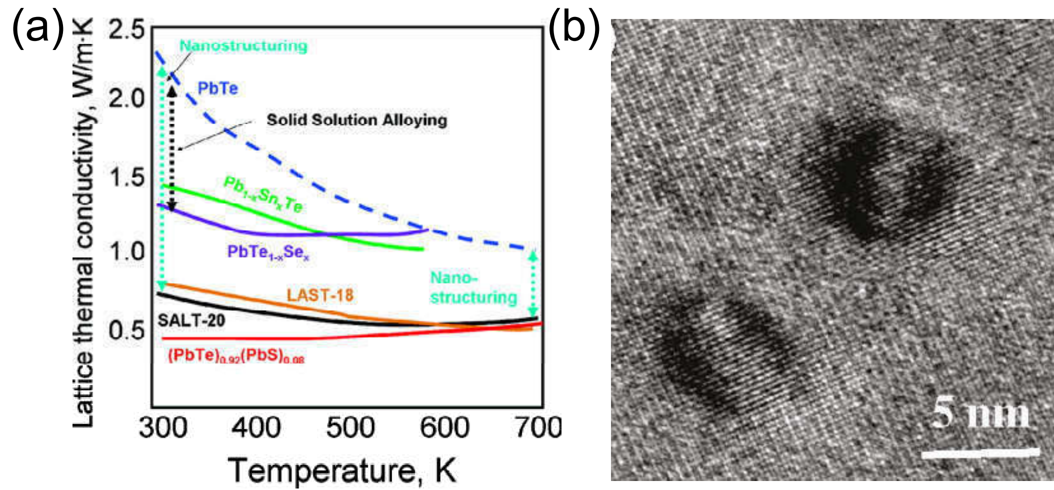

Figure 1.5 (a) Lattice thermal conductivity (κ_{lat}) as a function of temperature for various PbTe-based alloys and nanostructured samples. (b) High resolution transmission electron microscopy of a LAST-18 sample. Adopted with permission from ref. 39 © 2010 American Chemical Society.

1.4.2.3 Nanostructuring

Nanoscale inclusions (2-100 nm size) in bulk materials can effectively scatter the medium mean free path heat-carrying phonons and suppress the lattice thermal conductivity (Figure 1.5).[40] Such scattering happens at the interfaces between the precipitates and the matrix and from the mass contrast between the two phases. Approaches to achieving nanoscale precipitate, include ex-situ additions of guest phase by mechanical or chemical mixing[41] and in-situ second-phase precipitation through thermodynamically/kinetically driven processes.[25,28,40] While both have been accounted for nanostructures in thermoelectric materials, the latter is more favorable for charge transport because it can afford better dispersion and yield coherent interfaces between precipitate and matrix.[27] Spinodal decomposition,[26] and nucleation and growth,[42] matrix encapsulation[43] are the most common approaches for producing in-situ nanostructures in bulk matrix.

Nanostructuring phenomena was first observed in a high performance thermoelectric system, LAST-m ($AgPb_mSbTe_{m+2}$).[25] The room temperature κ_{lat} has been reduced from 2.0–2.5 W/m.K for PbTe to 0.5–0.8 W/m.K for LAST-m. The very low κ_{lat} of the LAST system was attributed to the spontaneous formation of nanostructured second phases in the PbTe matrix.

1.4.2.4 Mesoscale grain boundary

So far I have discussed about κ_{lat} reduction by scattering of low- and medium-mean free path phonons, which carry ~75 % of the transported heat. To further reduce κ_{lat} it is necessary to scatter phonons with long mean free path (~0.1-1 μm) (Figure 1.6). Necessary approaches involve the formation of crystal defects at submicrometer length scale (mesoscale, grain size ~0.1-3 μm), which can be engineered into materials through careful powder processing.

Rowe *et al*. investigated the thermal conductivities of SiGe alloys with different grain sizes and compared them with that of their single crystals.[29] They showed that grains with relatively small sizes (<5 μm) could scatter phonons strongly (∼20% reduction of thermal conductivity with respect to the single crystal). This work highlights the importance of mesoscale grains in impeding the phonon transport of bulk materials and points to further research to better understand mesoscale effects.

1.4.2.5 All-scale hierarchical architectures

When point defects, nanostructuring, and meso-structuring are all combined into a single thermoelectric material, it is termed as all-scale hierarchical architectures (Figure 1.6). Thermal conductivity in crystalline materials can be significantly decreased by defects present at different length scales with a broad range of wavelengths and mean free paths. Theoretical calculations suggest that, in PbTe, over 50% of the κ_{lat} value comes from the contribution by phonons with MFP less than 1 nm, which can be scattered significantly by atomic-scale point defects.[44] The remaining contribution to κ_{lat} is almost equally divided between phonon modes with MFP of 1−10 nm and phonon modes with MFP 10−1000 nm, (Figure 1.6), which can be notably impeded by nanoscale precipitates and mesoscale grains, respectively. Biswas and coworkers have demonstrated the substantial suppression of lattice thermal conductivity at high temperature in the PbTe-SrTe system that led to a record high zT of ~2.2 at 915 K in spark plasma sintered samples.[27] This is the result of introducing phonon scattering at all-length scales in a hierarchical fashion from atomic scale doping and endotaxial nanostructuring to mesoscale grain boundary engineering.

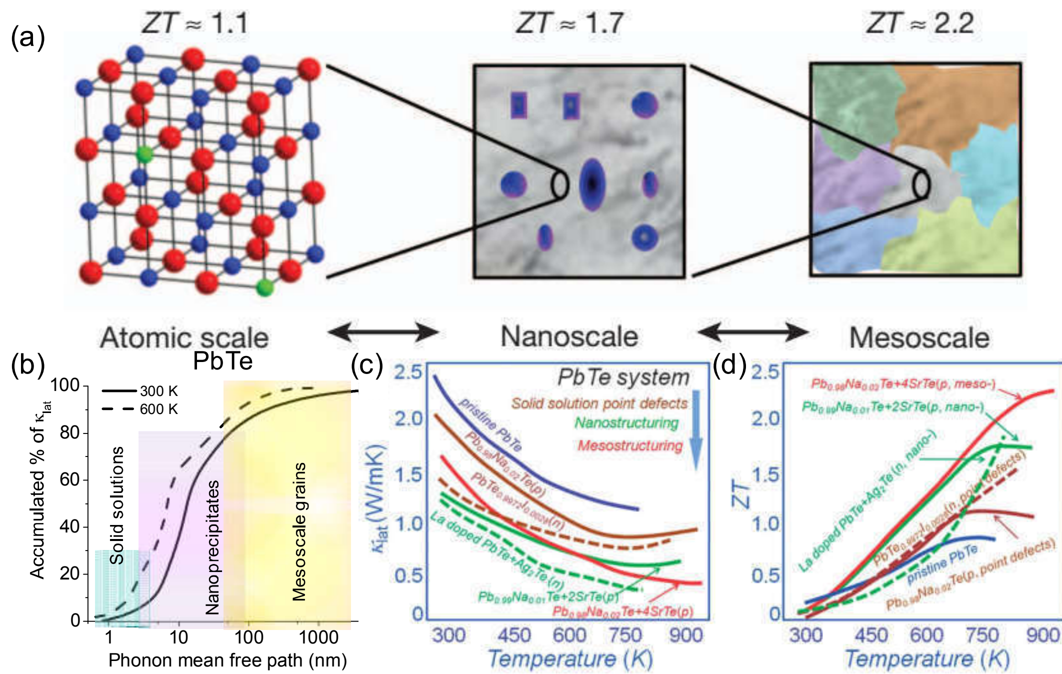

Figure 1.6 (a) Maximum achievable ZT ($\sim zT$) values for the respective length scales: the atomic scale (alloy scattering: red, Te; blue, Pb; green, dopant) the nanoscale (PbTe matrix, grey; SrTe nanocrystals, blue) to the mesoscale (grain-boundary scattering). (b) Contributions of phonons with different mean free paths to the cumulative κ_{lat} value for PbTe. Temperature dependent (c) lattice thermal conductivity (κ_{lat}) and (d) thermoelectric figure-of-merit ZT ($\sim zT$) for the all-scale hierarchical architecture PbTe system. Reproced with permission from ref. 4 and ref. 28 © 2014 The Royal Society of Chemistry and © 2012 Nature Publishing Group.

1.4.2.6 Intrinsic phonon scattering

In addition to the above mentioned strategies, materials having soft optical phonon modes exhibit low lattice thermal conductivity. In spite of having low phonon group velocity, soft optical phonons can interact with heat carrying acoustic phonons and cause additional scattering of acoustic phonons, indirectly affecting the lattice thermal conductivity. Theoretical and experimental studies demonstrate that the strong anharmonicity in PbTe is closely associated with ferroelectric instability, resulting in a strong acoustic–optical coupling and a significantly reduced phonon relaxation time.[45]

The above strategies for reducing the lattice thermal conductivity give emphasis to the reduction of the phonon relaxation time (τ) through the enhancement of phonon scattering. Besides these conventional approaches, solids with intrinsically low κ_{lat}, arising from complex crystal structures,[46] part-crystalline part-liquid state[47] rattling modes,[48-51] superionic substructures with liquid-like cation disordering,[46,52,53] resonant

bonding,[54,55] lattice anharmonicity due to lone pair[30,56] and anisotropic layered crystal structure,[54,57] has drawn huge attention of the thermoelectric community. Ultralow thermal conductivity in these materials arises either from low sound velocity or from low specific heat. Furthermore, discovery of topologically non-trivial materials sheds light on this pursuit because of heavy elements constituent and small band gaps.[3,58] Heavy elements have low frequencies of vibration that result in a low κ_{lat} necessary for a high thermoelectric figure of merit.[3]

1.5 Tin chalcogenides as potential thermoelectric material

In recent years, plenty of new TE materials have been identified with satisfactory TE properties. TE materials which are used for mid-temperature (500–1000 K) power conversion, are particularly interesting since the major share of the waste heat in industry and automobile exhaust is within this range.[59] Lead chalcogenides, in particular, has an influential history since 1950.[28,60-63] The thermoelectric figure of merit (zT) of PbTe and other lead chalcogenides has been raised to the peak *via* synergistic effect of band engineering (resonance levels formation,[19] band convergence and bands alignment[27]) and nano/microstructure manipulation in all scaled hierarchical architectures.[24,27,28,63] However, environmental concern about Pb, has slowed down the progress of its mass-market application. Hence, the solid state chemist and thermoelectric community demand discovery of Pb- free high performance thermoelectric materials.

The family of tin chalcogenides comprises a variety of potential thermoelectric materials due to resonant bonding, non-trivial topology and favorable crystal structure, which represents it as an environment-friendly thermoelectric alternative of PbTe. However, tin chalcocogenide was neglected to thermoelectric community till 2013 due to their poor thermoelectric performance.[64] In 2014, an exceptionally high zT value of 2.6 at 923K was achieved in the tin chalcogenide family (p-type SnSe single crystal), which has re-initiated the research on tin chalcogenides like $SnSe_2$, SnS.[54,59] Tin telluride has recently attracted increasing attention because it has the same crystal structure and a similar electronic structure to that of PbTe.[59,65,66] Moreover, Tananka *et al*. have

discovered the presence of mirror symmetry protected surface state in SnTe, which has stimulated the search for other topologically non-trivial tin chalcogenides.[67-70]

1.6 Lattice dynamics of tin chalcogenides

Understanding the lattice dynamics of tin chalcogenides is crucial to improving its thermoelectric performance. In this section, I will be discussing the crystal structure and chemical bonding, which is important to understand the κ_{lat} of tin chalcogenides discussed in the later section of this thesis.

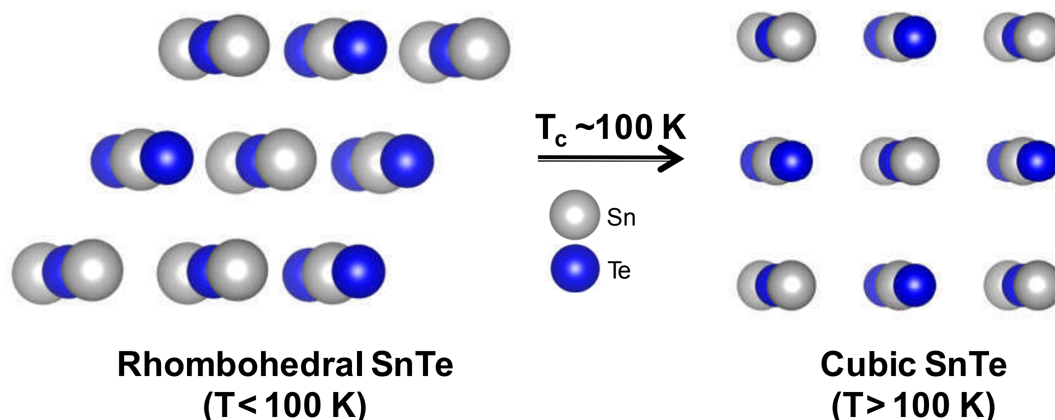

Figure 1.7 Temperature dependent ferroelectric phase transition in SnTe, when the structures transform from high temperature rocksalt to low temperature rhombohedral phase. Reproduced with permission from ref. 64 © 2018 The Royal Society of Chemistry.

Tin chalcogenides like SnTe, SnSe, $SnBi_2Te_4$, $SnBi_4Te_7$ etc are known to crystallize in rocksalt cubic or in distorted rocksalt structure (rhombohedral or orthorhombic) with soft chemical bonds (resonant bonding) originating from delocalization of electron density.[55,70,71] Thus, these materials are known to have large electronic polarizability and near-ferroelectric behavior. Typically, the rhombohedral phase of SnTe is stable only below 100 K (Figure 1.7).[72,73] Near room temperature, SnTe crystallizes in rocksalt structure (space group *Fm-3m*, lattice parameter, a= 6.32 Å), where both Sn and Te occupy the octahedral coordination sites.[55] Both Sn and Te atom have three valence electrons on average; however, the required number of valence electrons per atom is six for forming six bonds (Figure 1.7). Due to the presence of insufficient electrons, resonance between different electronic configurations leads to the formation of soft Sn-Te

bonding, which further couples with $5s^2$ lone pair of Sn resulting in distortion of the crystal structure locally and large polarizability.[74,75] Thus, local ferroelectric ordering has been experimentally observed in the rocksalt phase of SnTe by piezoresponse force microscopy (PFM) (Figure 1.8).[76]

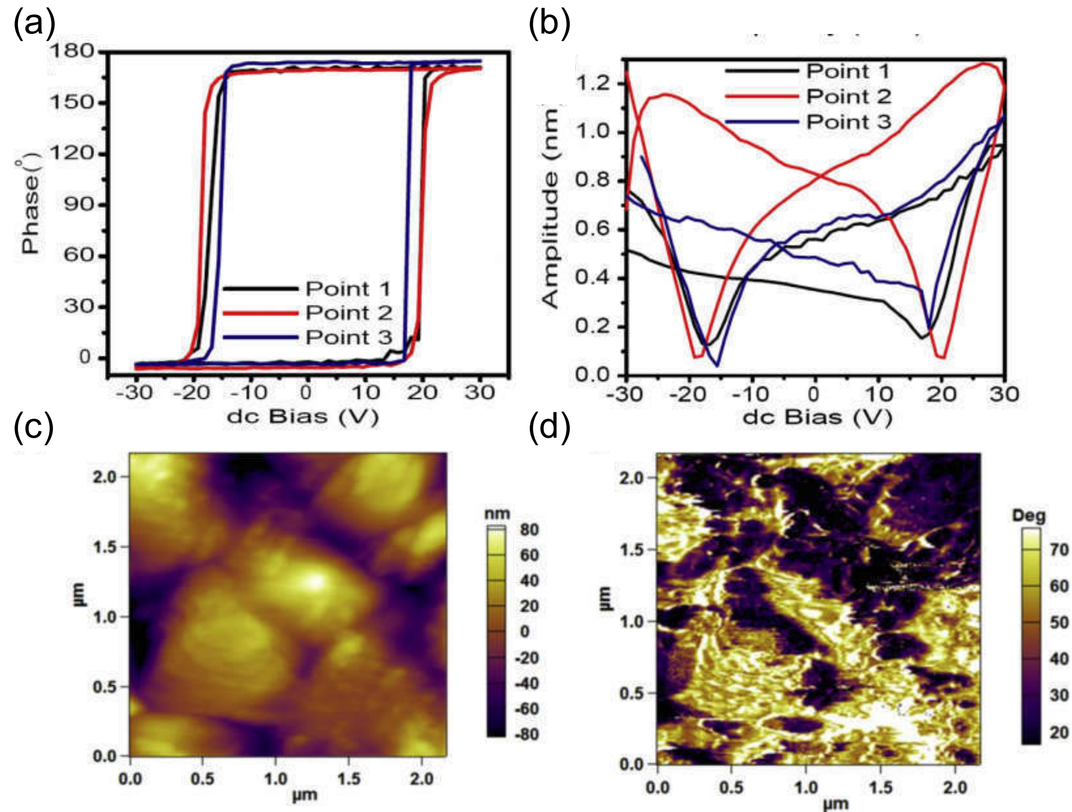

Figure 1.8 Piezoelectric response and evidence of ferroelectric domains at room temperature phase of SnTe using PFM. (a) Hysteresis loops between phase and DC bias. (b) "Butterfly- like loops" between response signal and DC bias. (c) Topographic image and (d) phase image of SnTe samples showing room temperature ferroelectric domains. Reproduced with permission from ref. 76 © 2016 The Chinese Ceramic Society. Production and hosting by Elsevier B.V.

All ferroelectric materials are believed to be piezoelectric in nature. In case of piezoelectric materials, the materials experience a mechanical deformation under the exposure of electric field. It is well-known that the hysteretic nature of the piezoelectricity reflects in the amplitude response of the cantilever with the DC bias in a curve commonly known as "butterfly loop". Butterfly loop has been observed in SnTe, when local strain has been measured as a function of applied electric field, owing to ferroelectric polarization switching (Figure 1.8). Presence of local ferroelectricity in SnTe has been

confirmed from the ferroelectric domains imaging using DART (Dual AC Resonance tracing) PFM imaging mode, as depicted in Figure 1.8c and Figure 1.8d. Furthermore, optical phonons exhibit triply degenerate instability with the frequency of 23i cm^{-1} at the *Γ* point, as seen in the phonon band structure of cubic SnTe (Figure 1.9). Thus, cubic SnTe showed polar instabilities which arose from the long-range resonant *p*-bonding network, coupled with stereochemically active Sn 5s orbital. The energetics of this *Γ* distortion has been quantified from the magnitude of local displacement of Sn along the <111> direction, which corresponds to the local rhombohedral strain (a=4.55Å, α=59.78^o) in the cubic unit cell. Recent studies based on temperature dependent pair distribution function analysis (PDF) as well as extended X-ray absorption fine structure (EXAFS) have confirmed realization of such local distortion in the global rock-salt SnTe crystal structure on warming.[75,77] Inelastic neutron scattering and first principle calculations have confirmed the evidence of ferroelectric instability mode.[78]

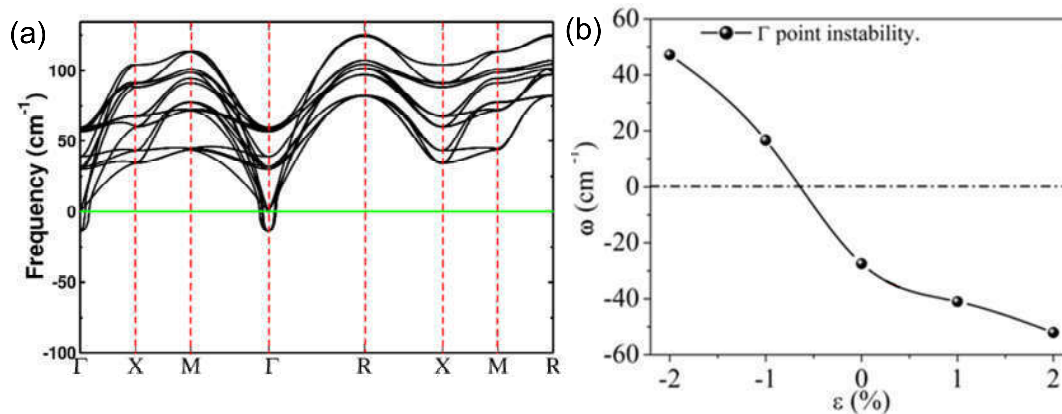

Figure 1.9 Phonon dispersion of (a) SnTe in the centrosymmetric cubic rocksalt structure (b) Dependence of unstable phonon frequencies at q = 2π/a (0 0 0) on hydrostatic strain ($\epsilon = (a - a_0)/a_0$), where a_0 = 6.419 Å. Reproduced with permission from ref. 76 © 2016 The Chinese Ceramic Society. Production and hosting by Elsevier B.V.

SnTe is much more resistant to heat conduction compared to another polycrystalline thermoelectric alloy with a strong mass disorder like InSb (InSb, κ_{lat}=16 W/m.K; SnTe, κ_{lat} ~3 W/ m.K).[55,79] This can be attributed to the development of local rhombohedral distortion (Sn-off centering) in the globally cubic structure of SnTe, which results in the generation of soft ferroelectric transverse optical mode (Figure 1.9a).[74,76-78] The strong anharmonic interaction between soft ferroelectric transverse optic mode and longitudinal acoustic modes causes low sound velocity and consequently lower lattice thermal

conductivity (Figure 1.9b).[76] However, due to relatively high charge carrier density in pristine SnTe originating from intrinsic Sn vacancies, it is commonly believed that such local distortion of crystal structure may not take the system into a locally ferroelectric state, where the electric polarization can be controlled by an external electric field.[59] Recently, Chang *et al*. have discovered stable in-plane ferroelectricity in atomic-thin films of SnTe.[80] These uncover SnTe as an important member of the new class of multi-functional materials, namely ferroelectric–thermoelectrics.

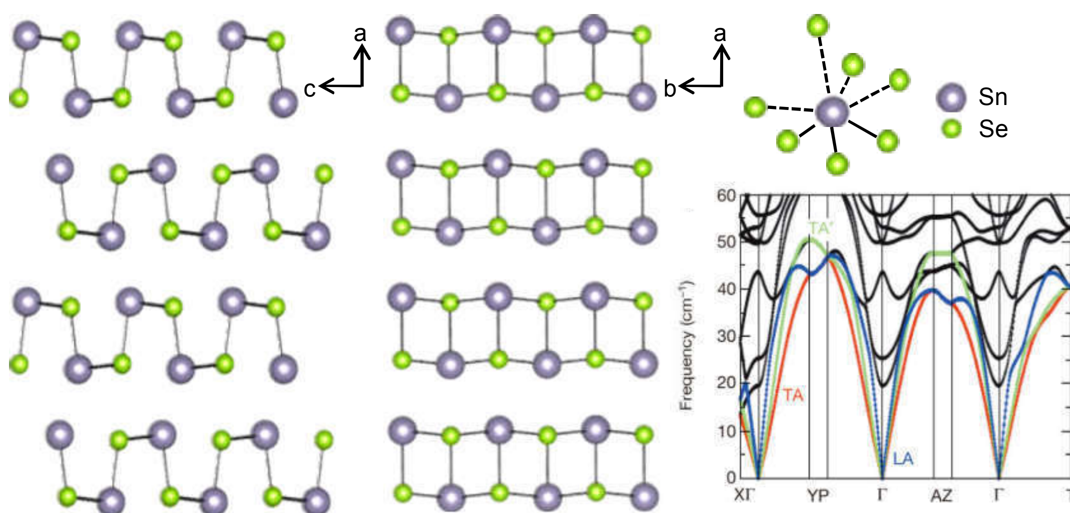

Figure 1.10 Crystal structure and phonon dispersion of SnSe (Pnma). Reproduced with permission from ref. 54. © 2014, Nature Publishing Group.

Apart from SnTe, other tin chalcogenides such as SnSe, $SnSe_2$, SnS, $SnBi_2Te_4$ and $SnBi_4Te_7$ have layered two dimensional (2D) structures at room temperature.[54,81-84] These layered tin chalcogenides exhibit variation in their transport properties for different crystallographic directions owing to the anisotropic crystal structure and chemical bonding.[85] SnSe and SnS both crystallizes in layered orthorhombic crystal structure (space group *Pnma*, SnSe, lattice parameters, a = 11.502 Å, b = 4.15 Å, c = 4.45 Å; SnS, lattice parameters, a = 11.19 Å b = 3.96 Å, c = 4.33 Å) at room temperature with sterically accommodated lone pair.[86,87] When temperature increases (~800 K for SnSe and ~878 K for SnS), both SnSe and SnS undergoes a second-order displacive phase transition to a higher symmetric five-fold coordinated *Cmcm* phase.[59] Since both SnSe & SnS exhibit similar chemical structure, I am going to describe the phase behavior of only SnSe in this article. In figure 1.10, I presented room temperature crystal structure of SnSe.

The distorted $SnSe_7$ coordination polyhedral contains two types of Sn-Se bonds: three short Sn-Se bond and four long bonds. Stereochemically active lone pair of Sn^{2+} atom resides between four weaker Sn-Se bonds.[54] Phonon dispersion spectra of SnSe shows much softer acoustic mode along the Γ-X Brillouin zone (BZ) direction (*a*-axis) as compared to Γ-Y (*b*-axis) or Γ-Z BZ directions (*c*-axis), suggesting weak inter-atomic bonding and strong anharmonicity owing to highly distorted $SnSe_7$ polyhedra and the zig-zag accordion-like slabs within the *b*-*c* plane. When mechanical stress is applied along the *b* and *c* directions, the zig-zag geometry deforms itself to a retractable spring. Furthermore, along the *a*-direction, the weaker bonding between SnSe slabs makes it an excellent stress buffer, hence dissipating phonon transport laterally. This anisotropic crystal structure of SnSe is responsible for directional thermal and electronic transport properties. Recently, strong lattice anharmonicity of SnSe has been experimentally confirmed through inelastic neutron scattering.[88] The giant phonon scattering emerges from an unstable electronic structure and orbital interactions leading to ferroelectric-like lattice instability. This portrays a microscopic image connecting electronic structure and phonon anharmonicity in SnSe, and offers new insights on how electron–phonon and phonon–phonon interactions may lead to the realization of ultralow κ_{lat}.

1.7 Electronic structures of tin chalcogenides

The energy gap between valence and conduction band in semiconductors plays a pivotal role in optimizing the thermoelectric performance. Since electrical transport properties (σ and S) of semiconductors depend on the nature of electronic states near the Fermi level, it is crucial to understand electronic structure to explain, predict, and optimize the electrical transport properties. Electronic structure of rock salt tin telluride, SnTe (space group Fm-3m) was proposed initially from measurements of the temperature dependent Seebeck coefficient, S and *p*-type carrier concentrations.[65] In most of the semiconductors (with rocksalt structure), high electronegative anion forms the valence band and *p*-orbital of cation contributes to the bottom of the conduction bands; and form band gap near Γ point in BZ.[17] Whereas, $5s^2$ lone pair in SnTe reforms the nature of both the bands and shift the gap from Γ to L point and exhibit a band gap of ~ 0.18 eV.[17,66] The band structure of

SnTe resembles with that of PbTe throughout the Brillouin zone except at and near the *L* point.[89] The symmetries of the valence band (top) and the conduction band (bottom) are inverted in SnTe compared to those of PbTe.[66] The calculated electronic structure for SnTe indicates the presence of two sets of valence-band maxima, one at *L* and the other in the *Σ* point of BZ of the cubic supercell.

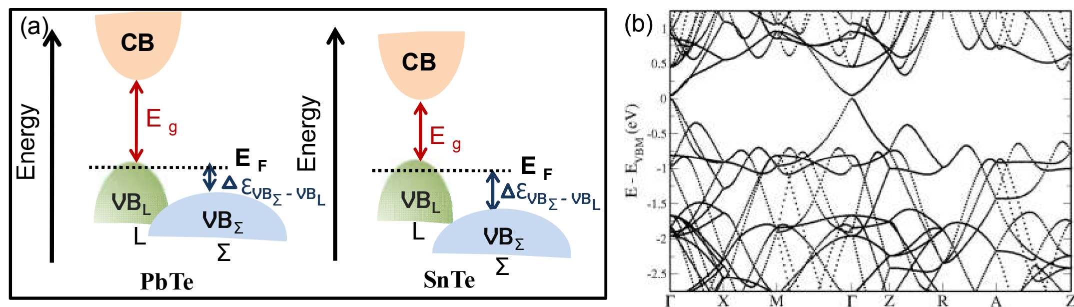

Figure 1.11 (a) Schematic energy diagram of electronic structure of PbTe and SnTe. (b) Electronic structure of SnTe. Figure 1.11(b) has been adopted with permission from ref. 91 © 2010 American Chemical Society.

Interestingly, IV–VI chalcogenides involve heavy mass valence bands in electronic transport at high temperature as energy separation between the light-hole valence band (*L*) and heavy-hole valence band (*Σ*) valence band decreases.[90] The energy gap between two valence bands in SnTe is ~ 0.35 eV which is much higher than that of PbTe (~ 0.17 eV), resulting from the higher energy *s*-state of Sn in SnTe compared to that of Pb in PbTe (Figure 1.11a).[66] Therefore, the participation of the second valence band for electronic transport is easier in PbTe than SnTe. Hence, tailoring of the energy gap between two valence bands is very important to optimize the thermoelectric properties of SnTe. Figure 1.11b shows the calculated electronic structure of SnTe, where valence band (VB) maximum and conduction band (CB) minimum occurring at the *L* point in the BZ of cubic SnTe folds on to the *Γ* point and the heavy hole VB appearing along *Σ* folds on to $Z+\delta$ in the BZ of the 32 atoms ($\sqrt{2}$ x $\sqrt{2}$ x 2) tetragonal supercell.[91]

SnTe, is unique among isostructural IV-VI semiconductors, is a topological non-trivial material, also a good thermoelectric material. The uniqueness of SnTe mainly comes from its electronic structure. The symmetry ordering of the conduction and valence bands in SnTe is reversed compared to PbTe at *L* points.[66]

Unlike cubic SnTe, other tin monochalcogenides such as SnSe and SnS are indirect band gap semiconductors with band gap 0.90 eV and 1.07 eV, respectively.[92] Typically,

SnSe is having multiple valence band maxima within a small energy difference, which can be accessed via carrier engineering.[86] Favorably, materials with multiple valence bands provide an additional impact on thermoelectrics due to enhanced Seebeck coefficient originating from the complex electronic structure.

Although there are several reports on tin based binary chalcogenides, information on ternary phases is limited in the literature because of their structural complexity. Ternary compounds with general formula $Sn_mB_{2n}X_{m+3n}$ (B = Sb/Bi; X = Te/Se/S; m and n represent stoichiometry of SnX and B_2X_3 respectively), consisting several tetradymite-like layered intergrowth compounds.[57,83,93] Recently, Vergniory *et al*. have reported bulk and surface electronic structures of these ternary chalcogenides,[94] which demonstrate the bulk band gap of these compounds is ~0.1 eV. The valence band is mainly contributed by the Sn and Bi/Sb atoms, whereas chalcogen contributes to the conduction band. Density Functional Theory (DFT) calculation predicted that Sn-based ternary compounds such as SnB_2Te_4, SnB_4Te_7, and $SnBi_6Te_{10}$ are 3D topological insulators.[70,94]

1.8 Tin telluride (SnTe)

SnTe, a homolog of PbTe, has the potential to be a good thermoelectric material due to its valence band (light hole and heavy hole valence bands) characteristic similar to PbTe.[65,66] However, it was neglected to thermoelectric community till 2013 due to its poor thermoelectric performance.[65] The following sections will focus on the challenges those are responsible for poor thermoelectric properties of SnTe.

SnTe is a *p*-type degenerate semiconductor with large carrier concentration (~10^{21} cm^{-3}) resulting from intrinsic Sn vacancy.[96,97] This results in high σ (~8000 S/cm, at room temperature), high κ_{el} (~6 W/mK, at room temperature) and low S (~20 μV/K, at room temperature) (Figure 1.12 and Figure 1.13).[65] Since, electrical conductivity, Seebeck coefficient and electronic thermal conductivity depending on the carrier concentration of SnTe, significant enhancement in zT can only be realized via optimization of *p*-type carrier concentration (Figure 1.12c).[95,98] However, the presence of non-stoichiometric defects in SnTe made it unpredictable to understand dopant's nature in SnTe.[99] I have

tried to reduce the carrier concentration (n_H) of SnTe by both cation and anion site doping (Chapter 3 and 5).[57,100]

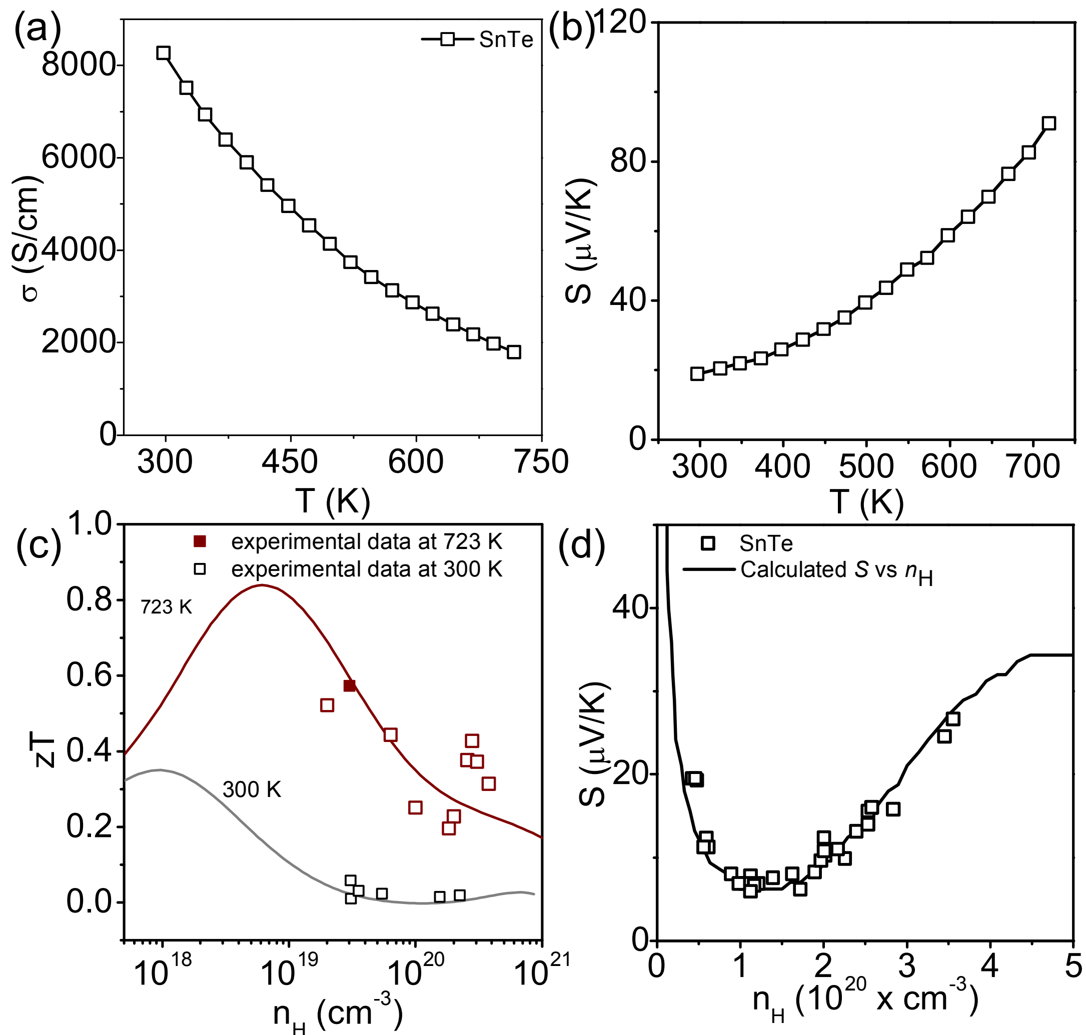

Figure 1.12 Temperature dependent (a) electrical conductivity (σ), (b) Seebeck coefficient (S) of SnTe. (c) zT and (d) Seebeck coefficient (room temperature) as a function of Hall carrier concentration, n_H of SnTe. Solid line represents theoretical zT vs n_H plot and Pisarenko plot (S vs n_H), calculated using two valence band model.[95]

In SnTe, the primary valence band (light hole) and secondary valence band (heavy hole) energy separation is ~0.35 eV, which is much higher than that of PbTe (~ 0.17 eV), at room temperature.[66] Moreover, the light valence band is having valley degeneracy of 4, whereas the heavy hole band degeneracy is 12.[66] A two-band model (a Valence band model considering contribution of both the light hole band and a parabolic heavy hole valence band) has been used to fit the experimental Seebeck coefficient of SnTe (Figure

1.12d).[95] Strikingly in contrast to the normal Pisarenko relationship based on the single parabolic band (SPB) model, acceptor-doping, which increases the Hall carrier concentration, also increases the Seebeck coefficient, due to the dominant contribution from the heavy valence band. However, the n_H (>10^{20} cm^{-3}) is massively higher than needed for optimized zT (zT of ~0.6 at 900 K). Earlier investigation based on temperature dependent Hall coefficient measurement of SnTe suggests that the convergence of these bands occurs at around 700 K.[25] Therefore, it is important to engineer the electronic structure of SnTe to increase the heavy hole band's contribution in the electronic transport which can enhance the Seebeck coefficient via enhancing the valley degeneracy, as seen from equation 1.3 and 1.11. Seebeck coefficient of PbTe based materials has been significantly enhanced via resonance level formation and band convergence, which is known to distort the electronic structure of PbTe near Fermi level. To achieve this in SnTe, the concept of resonance level formation and valence band convergence have been adopted (Chapter 2-4).

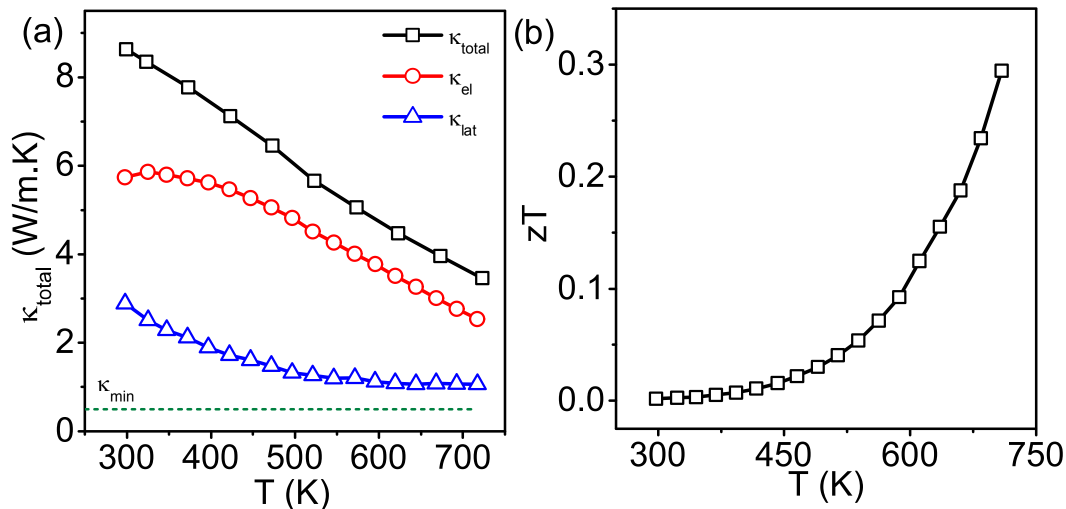

Figure 1.13 Temperature dependent (a) total thermal conductivity (κ_{total}), electronic thermal conductivity (κ_{el}), lattice thermal conductivity (κ_{lat}) and (b) zT of SnTe.

Pristine SnTe shows room temperature κ_{lat} values of ~2.9 W/mK, which is much higher compared to the theoretical limit for minimum lattice thermal conductivity (κ_{min}) of SnTe (~0.5 W/m.K) (Figure 1.13).[57] This hints about the occurrence of enormous opportunity to improve the zT through κ_{lat} reduction in SnTe. Various efforts focus on the reduction of κ_{lat} to enhance zT of SnTe through phonon scattering at hierarchical length

scale.[57,101-113] κ_{lat} of SnTe has been reduced through solid solution alloying in SnTe-SnSe alloy, where minimal κ_{lat} of 1.25 $Wm^{-1}K^{-1}$ has been achieved via creation of mass and size contrasts between the host and guest atoms (Chapter 2).[38,101] Surprisingly, an even lower κ_{lat} can be achieved in SnTe by alloying it with In_2Te_3, Cu_2Te and Ag, which suggest dominant impact of interstitials point defect for effective phonon scattering.[106,107,114]

When the concentration of a solute is beyond its solubility limit at equilibrium, it precipitates out to form fine nanostructures under proper synthesis conditions. Such a fine nanostructure may provide high-density boundary interfaces for the scattering of the phonon with long wavelengths.[4] Hence, nanostructuring is widely exploited strategy to reduce κ_{lat} of SnTe. Successful examples include SnTe-$AgBiTe_2$ alloy,[112] SnTe-HgTe,[111] SnTe-CdTe-CdS,[103] SnTe-InTe-CdTe-CdS,[104] SnTe-SrTe,[115] SnTe-MnTe[110] and SnTe-AgGdTe[113] systems, where the fine nanostructures are obtained by ball milling, adding insoluble solutes, or by thermodynamic precipitation. However, the room temperature thermal conductivity values are still higher compared to that of κ_{min} of SnTe. I have realized ultralow κ_{lat} in $Sn_{1-x}Sb_xTe$ resulting from layered 2D nanostructure formation in the SnTe matrix, which has been discussed in chapter 5. In chapter 7, I have presented a new strategy to significantly reduce the κ_{lat} without degrading carrier mobility by engineering the ferroelectricity instability in a crystalline solid.

1.9 Sn-based layered chalcogenides

Layered metal chalcogenides have appeared as a hot spot of extensive research due to their unique electronic structure arising from the crystal structure, weak interlayer van der Waals interaction, variable compositions and rich phase stability.[116-121] The ultralow thermal conductivity of layered chalcogenides originating from bonding asymmetry and anharmonicity has specifically drawn the attention of thermoelectric community toward layered tin chalcogenides.

Layered tin selenide (SnSe), a narrow band gap semiconductor, is one of the active members of this tin chalcogenide family (Figure 1.10). Recently, SnSe has become the heart of thermoelectric community due to its ultra high zT of ~ 2.6.[54] The observed record high value arises from favourable combination of high carrier mobility, large Seebeck

coefficient and extremely low lattice thermal conductivity originating from existence of multiple valence bands near Fermi level and strong bonding anharmonicity.[122,123] However, it was very difficult to find out suitable dopant for SnSe due to its locally distorted bonding arrangement around the Sn and Se atoms. Zhao *et al*. have successfully prepared hole doped SnSe single crystals using Na as an effective acceptor dopant.[122] Duong *et al*. could able to prepare single crystalline *n*-type SnSe with a remarkable *zT* value of 2.2 by Bi doping.[124] Nevertheless, the use of layered single crystalline materials in thermoelectric devices is prevented by their inferior mechanical properties in comparison to polycrystalline materials. Therefore, it became crucial to investigate the thermoelectric potential of polycrystalline SnSe.[125,126] After extensive research, a *zT* of 2.1 has been achieved in polycrystalline $Sn_{1-x}Se$ system.[127,128]

Tin diselenide ($SnSe_2$), an additional layered compound belonging to Sn-Se phase diagram, has recently emerged as a potential *n*-type thermoelectric material.[84,129,130] $SnSe_2$ possesses CdI_2 type structure (with *P-3m1* space group, lattice parameters, a = 3.81 Å, c = 6.14 Å).[131,132] The layered structure of $SnSe_2$ along *c*-axis predicts anisotropic transport properties in bulk $SnSe_2$. However, experimental studies on the thermoelectric transport properties were almost unexplored till 2016. As a part of my thesis work, I have studied thermoelectric properties of ultrathin few layer *n*-type $SnSe_2$ nanosheets, synthesized via a simple solution-based low-temperature route, which has been discussed in chapter 6B.

Tin sulfide (SnS) attracted the attention of thermoelectric community as an inexpensive, nontoxic tin chalcogenide with its complex band structure.[82] Like SnSe, SnS shows anisotropic thermoelectric properties and exceptionally low lattice thermal conductivity due to the layered structure, as discussed in the earlier section. However, unlike SnSe, SnS is having very low electrical conductivity arising from low carrier concentration (~10^{16} cm^{-3}).[133,134] A maximum *zT* value of just 0.16 was reported at 823 K for undoped SnS.[87] Bera *et al*. studied effect of various *p*-type dopants that could potentially enhance the carrier concentration in SnS.[135] Tan *et al*. have synthesized Ag-doped SnS by mechanical alloying followed by spark plasma sintering.[87] The carrier concentration increases to ~ 3.6 x 10^{18} cm^{-3} at room temperature, which is in good agreement with the theoretical prediction. Han *et al*. have studied the thermoelectric

properties of the SnSe–SnS solid solution.[136] A maximum *zT* of 0.82 was reported for *n*-type $SnSe_{0.8}S_{0.2}$ in the direction parallel to the pressing direction.

The rich chemical and physical properties of tin chalcogenides have motivated researcher to study the design, synthesis and properties of new layered ternary tin chalcogenides. Phase homology, a collective representation of different structures constructed on the same structural rule with certain unit expanding in different dimensions in standard increments, is a powerful approach to design new compounds with predictable composition and crystal structure.[137,138] Thus, an attractive path to progress the field of material chemistry with structural diversity is to identify phase homology which allows arrangement of phases under a widespread parasol. Several of tetradymite-like (Bi_2Te_2S) layered intergrowth ternary compounds exist in the homologous family, $Sn_mB_{2n}X_{m+3n}$ (B = Sb/Bi; X = Se/Te), where m and n represent stoichiometry of SnTe and B_2Te_3 respectively.[83,93,139] Most of the layered compounds in this homologous series resemble natural van der Waals heterostructure and are predicted to be 3D-topological insulators.[70,94,140] However, incongruent nature of these materials averts synthesis of pure bulk phases by the conventional high temperature solid state melting reaction. Formation of these compounds in nanosheets form can offer excess metallic surfaces with scattering resistant transport and high carrier mobility. Potential applications of these intergrowth nanosheets in the field of topological materials and thermoelectrics have grown interest to study the layered complex compounds in the pseudo-binary homologous series $Sn_m{}^{IV}Bi_{2n}{}^{V}Te_{m+3n}$.[140] I have synthesized few-layer 2D nanosheets of layered ternary tin chalcogenides from $Sn_m{}^{IV}Bi_{2n}{}^{V}Te_{m+3n}$ homologous family via a generalized generalised simple low temperature solution chemistry method, where dimensionality plays an important role to stabilize the kinetically controlled phases (Chapter 6A).[83]

1.10 Synthesis and characterizations

Till now, I have discussed the key factors those make tin chalcogenide as a potential alternative of lead chalcogenides and highlights why such a system was chosen for investigation, culminating into the thesis work. In the last part of this chapter, I will be

discussing synthesis strategies, detailed characterizations and thermoelectric measurement techniques those I have adopted to study the thermoelectric transport properties of tin chalcogenide system.

1.10.1 Synthesis

The successful utilization of TE devices depends critically on the synthesis techniques. A great majority of chalcogenides known to date have been synthesized by sealed-tube reactions in vacuum (10^{-3}-10^{-5} Torr) either by employing high-temperature melt cooling or alkali metal polychalcogenide fluxes A_2Q_n (Q = S/Se/Te) at low temperatures. In high temperature vacuum sealed tube melting reaction, appropriate quantities of starting materials (mostly in their elemental form) are heated above the melting point of the desired product in absence of air, followed by cooling of the subsequent reaction mixture at a specific cooling speed depending upon material's nature (congruent/incongruent). Products of the reactions are generally thermodynamically stable polycrystalline or single-crystalline ingots. Low-temperature polychalcogenide flux synthesis has resulted in many kinetically stable new ternary and quaternary metal chalcogenides.

The Spark plasma sintering (SPS) is newly developed technique for the syntheses and processing of thermoelectric materials employing ON-OFF pulse DC voltage / current (Figure 1.14).[141-143] This is considered as an energy-saving sintering technology due to its short processing time and a small number of processing steps. The SPS process is based on the electrical spark discharge phenomenon. Application of a high energy, low voltage spark pulse (spark discharge) momentarily produces a local high temperature state (several to ten thousand degree) in the gap between the particles of a material via joule heating (Figure 1.14c, 1.14d and 1.14e). This results in vaporization and melting of the powder particles' surfaces and formation of constricted shapes or "necks" around the contact area between the particles. These constricted shapes gradually develop and plastic transformation progresses during sintering, resulting in a sintered material with density of ≥99%. By application of voltage and current repeatedly with this ON-OFF, the discharge point and the Joule heating point (locally high-temperature generation field) move throughout the sample, resulting in less power consumption and efficient sintering. Since only the surface temperature of the particles rises rapidly by self-heating, particle growth

of the starting powder materials is controlled. Therefore, a precision sintered compact is manufactured in a shorter time. At the same time, bulk fabrication of particles with an amorphous structure and crystalline nanostructure formation are now possible without changing their characteristics. Vaporization, melting and sintering are completed in short periods of approximately 5-20 minutes, including temperature rise and holding times. SPS sintering temperatures range from low to over 2000 ℃ which are 200-500 ℃ lower than with conventional sintering.

In order to prepare high performance thermoelectric materials, we have done spark plasma sintering (SPS) of the melt grown ingots in SPS-211Lx, Fuji Electronic Industrial Co., Ltd. The SPS process and geometrical configuration of the punches, mould and powder are illustrated in figure 1.14. Powders to be consolidated, are placed in a die and heated by applying the electric current. The melt grown ingots were first ground into fine powders using a mortar and pestle to reduce the grains size in an inert glove box. This powder was then pressed into cylindrical shape by SPS method (SPS-211Lx, Fuji Electronic Industrial Co., Ltd.) at specific temperature and pressure under vacuum (Figure 1.14). Highly dense (~ ≥98% of theoretical density) disk-shaped pellets with ~10 mm diameter and ~10 mm thickness were obtained.

Novel nanostructured metal chalcogenide (MC) synthesized on a large scale with controlled morphology, size, composition, and structure lie at the heart of their practical applications. To achieve this, conventional solid-state strategies are often unsatisfactory. On the other hand, soft-chemical solution phase synthesis has been witnessed to be very powerful for obtaining desired nanostructured MC. In this process, the employed solutions and/or surfactants can be rationally selected based on the target MCs, and the nucleation and growth process of the products can be easily controlled by adjusting the thermodynamic and kinetic parameters of the reaction. Additionally, liquid-based synthetic routes do not involve the use of drastic conditions (e.g., high temperatures, high pressures) and yield products in large amounts. At present, many solution-based methods have been established to synthesize high-quality MCs.

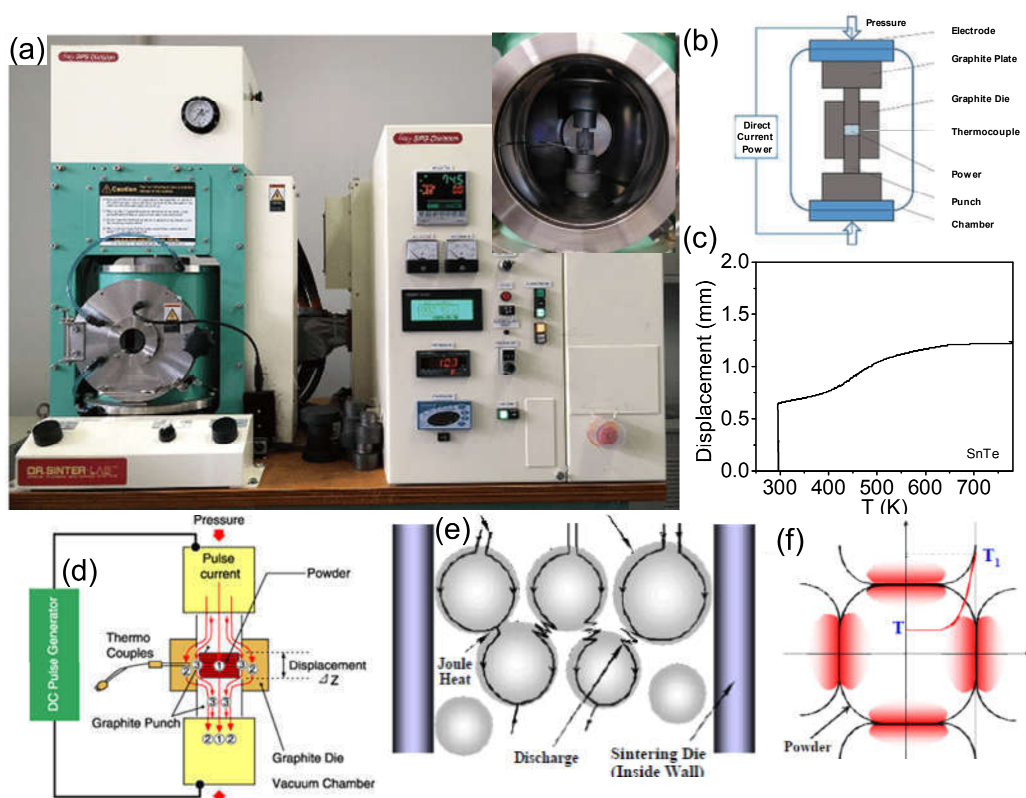

Figure 1.14 (a) Photograph of SPS-211Lx instrument. The inset image shows sitering chamber. (b) Schematic illustration of a spark plasma sintering equipment. (c) Typical graphite punch displacement rate versus temperature plot for SnTe during SPS processing. (d) Schematic of ON-OFF pulsed current path. (e) Possible electric current path through powder particles inside the die. (f) The temperature image on powder particles surface. Contact surface temperature (T_1) differs significantly from average temperature (T).[142,143]

For my Ph.D. work, I have used both the vacuum sealed melting routes and soft-chemical solution phase synthesis. I have synthesized nanosheets of several layered tin chalcogenides using solution phase route at inert atmosphere in Schlenk line, which was not possible through melting reaction.

1.10.2 Characterizations

I have used the following characterization techniques for my thesis works.

1.10.2.1 Powder X-ray diffraction (PXRD)

PXRD is the most commonly used technique in solid state inorganic chemistry and has several uses from analysis and assessing phase purity to determining the crystal structure. The Bragg equation, $n\lambda = 2d\sin\theta$ is one of the basis in understanding X-ray diffraction,

where n is an positive integer, λ is the characteristic wavelength of the X-rays impinging on the crystallize sample, d is the interplanar spacing and θ is the angle of the X-ray beam with respect to these planes. When the above equation is satisfied, X-rays scattered by the atoms in the plane of a periodic structure are in phase and diffraction occurs in the direction defined by the angle θ. In the simplest instance, an X-ray diffraction experiment consists of a set of diffracted intensities and the angles at which they are observed. This diffraction pattern can be considered as a chemical fingerprint, and basic chemical identification can be performed by comparing this diffraction pattern to a database of known patterns.

For my thesis work, room temperature PXRD are carried out in Bruker D8 Advance diffractometer using Cu-Kα radiation having wavelength, λ of 1.54 Å. Powdered sample was placed on a glass plate sample holder for the measurement. Each powder particle acts as a tiny crystal oriented in random directions so that the Bragg's reflection condition is satisfied for all lattice planes.

1.10.2.2 Transmission electron microscope (TEM)

TEM is a very powerful tool for characterization of the microscopic structure of crystalline materials. A high energy beam of electrons is shone through a very thin sample, and the interactions between the electrons and the atoms is utilized to characterize the microscopic features such as the crystal structure, dislocations, grain boundaries, nanoscale precipitate. I have done TEM imaging both for bulk and nanodimensional samples. Bulk TEM samples were prepared by conventional mechanical thinning followed by Ar ion milling in the precision ion polishing system (PIPS) with the ion energy of 4.5 eV and beam angle of 7 deg, in order to generate large electron transparent thin area. The bright field imaging, HRTEM imaging, Diffraction pattern imaging was performed using an aberration corrected FEI TITAN cubed 80-300 kV transmission electron microscope operating at 300 kV. For nanomaterials, very dilute solution of nanosheets dispersed in ethanol solution was taken in a holey carbon coated Cu grid for TEM imaging. The grid was dried under IR-lamp to evaporate the solvent before imaging. TEM experiments were performed using JEM3010 TEM (fitted with a

Gatan CCD camera operating at a 300 kV accelerating voltage), FEI TECNAI G^2 20 STWIN TEM (operating at 200 kV) and also FEI TITAN cubed 80-300 kV.

1.10.2.3 Field emission scanning electron microscope (FESEM)

A FESEM is used to visualize topographic details of the sample surface. Similar to TEM, FESEM microscope also uses electrons as a light source. Electrons are ejected from a field emission source and accelerated in a high electrical field gradient. These electrons (termed as primary electrons) produce a narrow scan beam within the high vacuum column, which bombards the sample material. The incident electrons cause emission of electrons from the sample due to elastic and inelastic scattering. The angle and velocity of these secondary electrons produced by inelastic collision of accelerated electrons with sample atoms relate to the surface structure of the object. High-energy electrons those are produced by an elastic collision of a primary electrons with atom's nucleus of the sample are termed as backscattered electrons (BSE). Larger atoms (with a high atomic number, Z) have a higher chances of producing elastic collisions because of their greater cross-sectional area. Thus, a "brighter" BSE intensity correlates with higher average Z in the sample, and "dark" areas have lower average Z. BSE images are very helpful for obtaining high-resolution compositional maps of a sample.

In my Ph.D work, I have performed both normal and BSE mode FESEM experiments using NOVA NANO SEM 600 (FEI, Germany) operated at 15 kV to study surface morphology and phase homogeneity. Solid sample was used for bulk materials, whereas nanomaterials required dilute well-dispersed sample drop-casted on alumina or silicon wafer. For BSE imaging, I have used a finely polished sample in the back-scattering mode to produce a BSE image of the surface.

1.10.2.4 High-angle annular dark-field scanning transmission electron microscopy (HAADF-STEM)

Scanning transmission electron microscope (STEM) is a special kind of transmission electron microscope, where the electron beam is focused to a fine spot (with the typical spot size of ~0.05-0.2 nm) and then scanned over the sample in such way that at each point, sample illuminated with the beam is parallel to the optical axis. HAADF-STEM is a STEM technique which receives inelastically scattered electrons at high angles using an

annular dark-field (ADF) detector (from ～50 mrad to sufficiently high angle, e.g. ～200 mrad). The HAADF image intensity is reported to be proportional to the square of the *Z*-contrast (atomic number). For HAADF-STEM, I have prepared the sample by adopting similar sample preparation technique to that of TEM.

1.10.2.5 Energy dispersive X-ray analysis (EDAX)

EDAX is an analytical technique used for elemental composition analysis of the sample. EDAX makes use of the X-ray spectrum emitted by a solid sample bombarded with a focused beam of electrons. For EDAX analysis, an X-ray detector is generally integrated with FESEM or TEM instrument. Its characterization capabilities are due in large part to the fundamental principle that each element has a unique atomic structure allowing a unique set of peaks on its electromagnetic emission spectrum. I have performed EDAX using EDAX Genesis instrument attached to FESEM column. The STEM-EDAX has also been used for elemental mapping.

1.10.2.6 X-ray photoelectron spectroscopy (XPS)

XPS is a surface analysis technique, which measures surface composition, chemical and electronic state of the present elements in a material. This technique is based on Einstein's photoelectric effect. When an X-Ray beam directs to the sample surface, the energy of the X-Ray photon is absorbed completely by core electrons of the atoms presents at the surface. XPS spectra are obtained by irradiating a material with a beam of X-rays while simultaneously measuring the kinetic energy ($E_{kinetic}$) and the number of core electrons of atoms that escape from the top 0-10 nm of the material being analyzed. A typical XPS spectrum is a plot of the number of electrons detected *vs* the binding energy of the detected electrons ($E_{binding}$), as obtained from Einstein relationship ($E_{photon} = E_{binding} + E_{kinetic} + \varphi$, where φ is threshold frequency). Each element produces a characteristic set of XPS peaks at characteristic $E_{binding}$ values that directly identify each element presents in or on the surface of the material being analyzed. Since core electrons are close to nucleus and have binding energies characteristic of the certain chemical environment, XPS allows determining the atomic compositions of a sample or chemical state of certain elements. From the binding energy and intensity of a photoelectron peak, the elemental identity, chemical state, and quantity of a detected

element can be determined. For my research work, XPS measurement has been performed on a powdered sample using Mg−Kα (1253.6 eV) X-ray source with a relative composition detection better than 0.1% on an Omicron Nano-technology spectrometer.

1.10.2.7 Inductively coupled plasma-atomic emission spectroscopy (ICP-AES)

ICP-AES is an analytical technique used to determine the accurate elemental composition of the sample. Through the use of the Inductively Coupled Plasma, an ICP-AES produces excited ions and atoms (by ionization in an intense electromagnetic field) that emit detectable amounts of light at characteristic wavelengths, with intensities proportional to the concentration of the ion. As indicated by the name, the spectra is measured and analyzed by atomic emission spectrometer (AES) using concentration-intensity correlations which are similar to the Beer-Lambert Law.

ICP-AES measurements were done in Perkin-Elmer Optima 7000DV instrument. Samples were prepared by dissolved powdered samples in aqua regia (HNO_3:HCl = 1:3) followed by dilution with Millipore water.

1.10.2.8 Optical band gap

In my thesis work, the diffuse reflectance method has been used for the determination of band gap of the solid powdered materials. Diffuse reflectance is an excellent sampling tool for powdered crystalline materials. When light shines onto a powder sample, two types of reflections can occur. Some of the light undergoes specular reflection at the powder surface. Diffuse reflection happens when radiation penetrates into the sample and then emerges at all the angles after suffering multiple reflections and refractions by sample particles. A diffuse reflection accessory is designed to minimize the specular component. To estimate optical energy difference between the valence band and conduction band, optical diffuse reflectance measurements have been done with finely ground powder at room temperature using FT-IR Bruker IFS 66V/S spectrometer and Perkin-Elmer Lambda 900, UV/Vis/NIR spectrometer. Absorption (α/Λ) data were estimated from reflectance data using Kubelka−Munk equations: $\alpha/\Lambda=(1-R)^2/(2R)$, where R is the reflectance, α and Λ are the absorption and scattering coefficients, respectively. The energy band gaps were derived from α/Λ vs E (eV) plots.

1.10.2.9 Differential scanning calorimetry (DSC)

DSC is a thermoanalytical technique in which the difference in the amount of heat required to increase the temperature of a sample and reference is measured as a function of temperature. Both the sample and reference are maintained at nearly the same temperature throughout the experiment. The basic principle underlying this technique is that when the sample undergoes any physical transformation such as phase transition, melting etc, amount of heat flow required to maintain both of them at the same temperature will be different. When the amount of heat required for the sample is lesser than the reference, the process is termed as exothermic. Endothermic process requires a higher amount of heat flow to maintain the temperature. By observing the difference in heat flow between the sample and reference, differential scanning calorimeters are able to measure the amount of heat absorbed or released during such transitions.

DSC data were collected using METTLER-TOLEDO Differential Scanning Calorimeter (DSC 822 e) in N_2 atmosphere. The temperature range has been given in the relevant chapter.

1.10.2.10 Raman spectroscopy

Raman spectroscopy is one of the vibrational spectroscopic techniques used to provide information on molecular vibrations and crystal structures. This technique is based on inelastic scattering of monochromatic light. A change in the molecular polarizability with respect to the vibronic coordinate is required for a molecule to exhibit Raman effect. Normally, a laser source Nd-YAG with a fixed wavelength of 532 nm, an Argon ion laser source at 514 nm or He-Ne laser at 633 nm is used as light source. The laser light interacts with molecular vibrations, phonons or other excitations in the system, resulting in the energy of the laser photons being shifted up or down. The shift in energy gives information about the vibrational modes in the system.

Room temperature Raman spectroscopic measurements were carried out on pellet shaped samples using Horiba HR-Evolution spectrometer with 532 nm excitation laser and HORIBA LABRAM HR800 spectrometer with the excitation wavelength of the laser 514 nm.

1.11 Thermoelectric measurements

Electrical conductivity (σ) and Seebeck coefficient (S) are measured simultaneously under He atmosphere by a ULVAC-RIKO ZEM-3 instrument. The typical sample for electrical transport measurement requires parallelepiped shape with the dimensions of ~2 × 2 × 8 mm^3. The longer direction coincides with the direction in which the thermal conductivity is measured. The thermal conductivity, κ_{total} is estimated from temperature dependent thermal diffusivity, D measured by using NETZSCH LFA-457 instrument. Coins with ~8 mm (or ~ 10 mm) diameter and ~2 mm thickness are used in thermal diffusivity measurements. Owing to the instrumental factors, the percent error in the measured data is 5% each for electrical conductivity, Seebeck coefficient, and thermal diffusivity.

1.11.1 Seebeck coefficient

Seebeck coefficient (S) is the ratio of a resulting voltage gradient (ΔV) to an applied temperature gradient (ΔT). For the Seebeck measurement, the temperature is varied around a constant base temperature, and the slope of ΔV *vs*. ΔT plot gives the Seebeck coefficient at a given base temperature (the slope method). Bar-shaped sample (~2 mm ×2 mm ×8 mm) is held vertically between the top and bottom Ni electrodes. Two R-type thermocouples are pressed against the sample for probing and simultaneously. The base temperature of the sample-chamber is maintained by an infrared-furnace while $\Delta \boldsymbol{T}$ values of 5, 10 and 15 K at each of the base temperatures is achieved by a joule-heater attached to the bottom electrode (Figure 1.15).

1.11.2 Electrical conductivity

For measuring electrical resistivity, a constant current (I) is passed along the length of the bar-shaped sample kept in between the Ni electrodes. From the voltage drop across the sample (V), resistance ($R = V/I$) can be obtained, and one can calculate the resistivity (x) using $R = x.l/A$. where A is the sample's cross-sectional area and l is the separation between the two voltage probes (R-type thermocouples). Electrical conductivity is calculated as $\sigma = 1/x$. A schematic showing the sample-chamber and four-probe

configuration for measuring the Seebeck coefficient and electrical conductivity in a commercial ULVAC-RIKO ZEM3 apparatus is shown in figure 1.15.

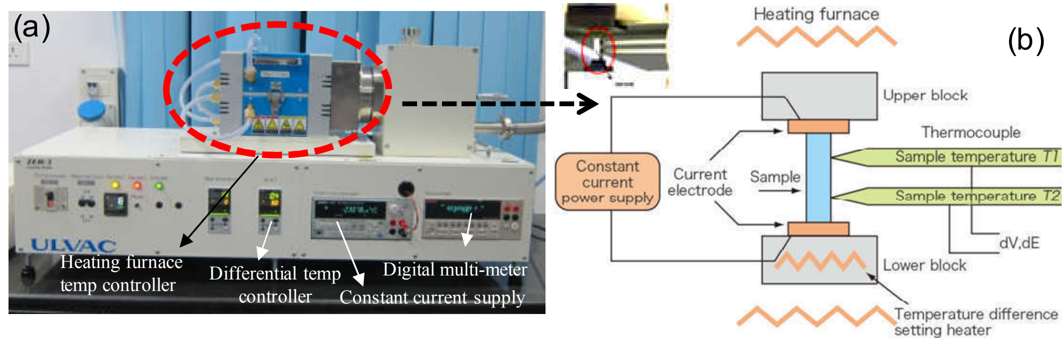

Figure 1.15 (a) Photograph of sample-chamber in ULVAC-ZEM3 apparatus. (b) Schematic of UlVAC-ZEM 3 four-probe measurement system.[144]

1.11.3 Thermal conductivity

The thermal diffusivity, D, was measured on a sample with 8 mm (or ~10 mm) diameter and 2 mm thickness in the N_2 atmosphere using the laser flash diffusivity technique in Netzsch LFA-457 instrument. In this technique, a short pulse of energy is applied to one side of a thin sample by a laser flash, while the temperature of the other side is monitored continuously by an infrared (IR) detector. The temperature will rise to a maximum, after which it will decay. The time taken for the temperature to rise to half-maximum ($t_{1/2}$) is used to calculate the thermal diffusivity (Equation 1.14).

$$D = 0.1388 \frac{l^2}{t_{0.5}} \quad (1.14)$$

where l is the sample-thickness,[146] assuming an axial flow of heat in the sample whose thickness is smaller than the diameter.

Samples are loaded in SiC holders. An Nd-Glass pulsed laser (wavelength ~1054 nm) is used as the source of energy pulse and liquid N_2 cooled InSb is used as the IR detector. Both faces of the sample were coated with a thin layer of graphite to ensure good absorption of the laser pulse and maximum signal-to-noise ratio at the detector. A correction proposed by Cowan was employed to account for the heat-losses on the sample-faces.[147] A schematic of the laser flash apparatus is shown in figure 1.16. Total thermal conductivity (κ_{total}) was estimated using the equation 1.15.

$$\kappa_{total} = DC_p\rho \quad (1.15)$$

where ρ is the sample's density and C_p is the specific heat capacity obtained indirectly with respect to a standard pyroceram reference.

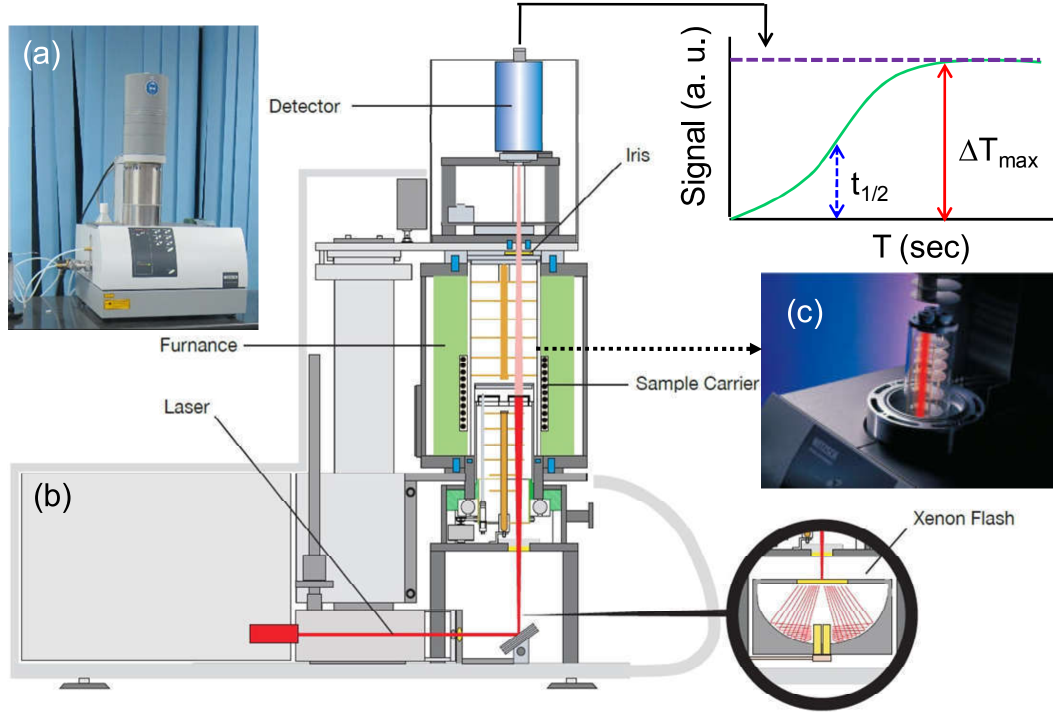

Figure 1.16 (a) Photograph of NETZSCH LFA-457 instrument. (b) and (c) Schematic of LFA- 457 diffusivity measurement apparatus.[145]

Lattice thermal conductivity (κ_{lat}) is extracted by subtracting the electronic thermal conductivity (κ_{el}) from total thermal conductivity. κ_{el} is estimated using the Wiedemann Franz law (Equation1.7). Lorenz number, L is estimated from the reduced chemical potential and temperature dependent Seebeck coefficient assuming single parabolic band conduction and dominant acoustic phonon scattering of carriers using the following expressions.[148]

$$S = \pm\frac{k_B}{e}\left(\frac{2F_1(\eta)}{F_0(\eta)} - \eta\right) \quad (1.16)$$

$$F_n(\eta) = \int_0^\infty \frac{x^n}{1 + e^{x-\eta}}dx \quad (1.17)$$

$$L = \left(\frac{k_B}{e}\right)^2 \frac{3F_0(\eta)F_2(\eta) - 4F_1(\eta)^2}{F_0(\eta)^2} \tag{1.18}$$

where η is the reduced Fermi energy ($\frac{E_F}{k_B T}$); $F_n(\eta)$ is the nth order Fermi integral $F_n(\eta)$; κ_B, the Boltzmann constant; e, the absolute electron charge; h, the Planck constant and x, the reduced carrier energy. Experimental S vs. T data is fitted with equation 1.16 to obtain η. L is estimated as a function of temperature using the calculated values of $F_n(\eta)$ (Equations 1.17 and 1.18).

1.11.4 Hall effect

The Hall effect describes the behavior of the free carriers in a semiconductor when applying an electric as well as a magnetic field along the perpendicular direction.[149] Thus, measurement of the Hall voltage is used to determine the type of charge carrier present in the system, the free carrier density and the carrier mobility. When a current-carrying semiconductor is kept in a magnetic field, the charge carriers of the semiconductor experience a force in a direction perpendicular to both the magnetic field and the current (Figure 1.17b). At equilibrium, a voltage appears at the semiconductor edges. The ratio of the induced voltage to the product of the current density (*I*/*t*, where *I* is applied current and *t* is sample thickness) and the applied magnetic field (*B*) is defined as Hall coefficient (R_H) (Equation 1.19 and 1.20).

$$R_H = \frac{Vt}{IB} \tag{1.19}$$

$$n_H = \frac{1}{R_H e} \tag{1.20}$$

where, e is the charge of an electron (1.602 x 10^{-19} C).

To measure carrier concentration of the samples, I have done Hall measurement both in the PPMS system and in a Hall equipment developed by Excel instrument (Figure 1.17a). We have used a four-contact Hall-bar geometry and a varying magnetic field up for the measurements (as shown in Figure 1.17c).

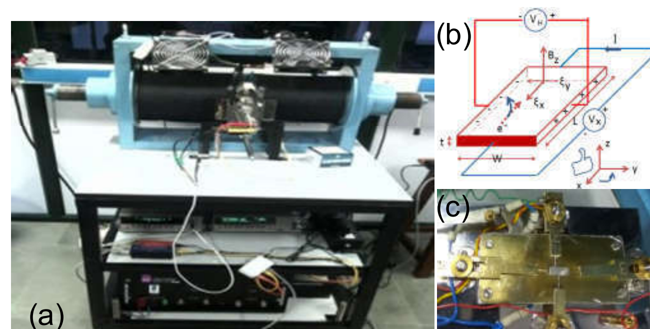

Figure 1.17 (a) Photograph of Hall measurement equipment developed by Excel instrument. (b) Schematic illustration of Hall measurement setup. (c) Sample with typical Hall-bar geometry is mounted on its board for Hall-coefficient measurement.[149]

1.12 Scope of the thesis

In the 21st century, a broader application of thermoelectrics requires the discovery and development of environment-friendly high performance earth-abundant materials. Thus, tin chalcogenides, an environment friendly alternative to lead chalcogenide will have potential impact in thermoelectrics. To reach the goal of developing tin chalcogenide based high performance thermoelectric materials, several issues need to be addressed. In spite of being a homologue of PbTe, researcher in thermoelctrics could not able to achieve similar high *zT* in SnTe, which hints about the enormous amount of research opportunities waiting to be performed in future. Since, PbTe has risen to the peak of thermoelectrics via utilization of the concepts of electronic structure engineering (i.e. formation of resonance levels[19] and valence band valley convergence[22]) and nano/microstructure manipulation in all scale,[28] it is necessary to adopt all these successful strategies to SnTe with the goal of improvement in *zT* relative to that of PbTe. Along with that, new concepts need to be developed to reduce the thermal transport yet maintaining/increasing electrical transport properties in SnTe. To reach the goal of developing tin chalcogenide based high performance thermoelectric module, I have studied various strategies to effectively utilize their promising structural, electrical, thermal and mechanical properties. In the following chapters of my thesis, I have discussed the journey of tin chalcogenides towards high performance thermoelectric material in terms of its bonding, local/global structure, electronic structure, phonon

dispersion. Apart from the present introductory part, my thesis work is divided into six chapters.

A major part of my thesis is focused on the optimization of the thermoelectric performance of SnTe. Since one of the major drawbacks of SnTe was its low Seebeck coefficient, I have tried to improve its Seebeck coefficient and power factor of SnTe via carrier concentration optimization and modulation of electronic structure (Chapter 2-4). On the other hand, I have strived to achieve minimum κ_{lat} from tin chalcogenide family. Chapter 5 reports the reduction of lattice thermal conductivity near to the theoretical minimum limit, κ_{min}, in SnTe. In chapter 6, I have focused on the study of design, synthesis and thermoelectric properties of layered tin chalcogenides. I have synthesized nanosheets of various binary and ternary layered Sn-chalcogenides.

Structural phase transitions are known to influence the transport properties of thermoelectric materials. Near the close proximity to a ferroelectric phase transition, the phase itself plays a key role in suppressing κ_{lat}. Since most of the binary tin chalcogenides undergo a displacive ferroelectric phase transition, I have studied thermoelectric transport properties of materials near the verge of phase transition (Chapter 7). This results in a new strategy to significantly reduce the κ_{lat} without degrading carrier mobility by engineering the ferroelectricity instability near the phase transition. Impact of local rhombohedral distortion associated with ferroelectric instability on the electronic structure and thermal conductivity of globally cubic tin chalcogenides was studied through phonon dispersion calculation, Raman spectroscopy and PXRD.

In summary, tin chalcogenide based materials are believed to substitute lead chalcogenides for thermoelectric application because of their promising structural, electrical, thermal and mechanical properties. In my thesis, I have discussed the journey of tin chalcogenides in terms of its bonding, local/global structure, electronic structure, phonon dispersion and thermoelectric properties, which will have significant impact on the future development of Sn-chalcogenide based thermoelectric module.

1.13 References

1. G. Tan, L.-D. Zhao and M. G. Kanatzidis, *Chem. Rev.*, 2016, **116**, 12123.
2. G. J. Snyder and E. S. Toberer, *Nat. Mater.*, 2008, **7**, 105.
3. J. R. Sootsman, D. Y. Chung and M. G. Kanatzidis, *Angew. Chem., Int. Ed.*, 2009, **48**, 8616.
4. L.-D. Zhao, V. P. Dravid and M. G. Kanatzidis, *Energy Environ. Sci.*, 2014, **7**, 251.
5. T. M. Tritt and M. A. Subramanian, *MRS Bull.*, 2006, **31**, 188.
6. J. Yang and T. Caillat, *MRS Bull.*, 2006, **31**, 224.
7. T. C. Holgate, R. Bennett, T. Hammel, T. Caillat, S. Keyser and B. Sievers, *J. Electron. Mater.*, 2015, **44**, 1814.
8. J. Yang and F. R. Stabler, *J. Electron. Mater.*, 2009, **38**, 1245.
9. B. Orr, A. Akbarzadeh, M. Mochizuki and R. Singh, *Appl. Therm. Eng.*, 2016, **101**, 490.
10. L. Yang, Z.-G. Chen, M. S. Dargusch and J. Zou, *Adv. Energy Mater.*, 2018, **8**, 1701797.
11. D. Kraemer, B. Poudel, H.-P. Feng, J. C. Caylor, B. Yu, X. Yan, Y. Ma, X. Wang, D. Wang, A. Muto, K. McEnaney, M. Chiesa, Z. Ren and G. Chen, *Nat. Mater.*, 2011, **10**, 532.
12. K. W. Mauser, S. Kim, S. Mitrovic, D. Fleischman, R. Pala, K. C. Schwab and H. A. Atwater, *Nat. Nanotechnol.*, 2017, **12**, 770.
13. D. M. Rowe, *CRC handbook of thermoelectrics*, CRC press, 1995.
14. D. Nemir and J. Beck, *J. Electron. Mater.*, 2010, **39**, 1897.
15. J. He and T. M. Tritt, *Science*, 2017, **357**, eaak9997.
16. P. F. P. Poudeu, J. D'Angelo, H. Kong, A. Downey, J. L. Short, R. Pcionek, T. P. Hogan, C. Uher and M. G. Kanatzidis, *J. Am. Chem. Soc.*, 2006, ***128***, 14347.
17. W. G. Zeier, A. Zevalkink, Z. M. Gibbs, G. Hautier, M. G. Kanatzidis and G. J. Snyder, *Angew. Chem., Int. Ed.*, 2016, **55**, 6826.
18. D. G. Cahill, S. K. Watson and R. O. Pohl, *Phys. Rev. B*, 1992, **46**, 6131.
19. J. P. Heremans, V. Jovovic, E. S. Toberer, A. Saramat, K. Kurosaki, A. Charoenphakdee, S. Yamanaka and G. J. Snyder, *Science*, 2008, **321**, 554.
20. J. P. Heremans, B. Wiendlocha and A. M. Chamoire, *Energy Environ. Sci.*, 2012, **5**, 5510.
21. S. Ahmad, K. Hoang and S. D. Mahanti, *Phys. Rev. Lett.*, 2006, **96**, 056403.
22. Y. Pei, X. Shi, A. LaLonde, H. Wang, L. Chen and G. J. Snyder, *Nature*, 2011, **473**, 66.
23. W. Liu, X. Tan, K. Yin, H. Liu, X. Tang, J. Shi, Q. Zhang and C. Uher, *Phys. Rev. Lett.*, 2012, **108**, 166601.
24. L. Zhao, H. Wu, S. Hao, C.-I. Wu, X. Zhou, K. Biswas, J. He, T. P. Hogan, C. Uher and C. Wolverton, *Energy Environ. Sci.*, 2013, ***6***, 3346.
25. K. F. Hsu, S. Loo, F. Guo, W. Chen, J. S. Dyck, C. Uher, T. Hogan, E. K. Polychroniadis and M. G. Kanatzidis, *Science*, 2004, **303**, 818.
26. J. Androulakis, C.-H. Lin, H.-J. Kong, C. Uher, C.-I. Wu, T. Hogan, B. A. Cook, T. Caillat, K. M. Paraskevopoulos and M. G. Kanatzidis, *J. Am. Chem. Soc.*, 2007, **129**, 9780.

27. K. Biswas, J. He, Q. Zhang, G. Wang, C. Uher, V. P. Dravid and M. G. Kanatzidis, *Nat. Chem.*, 2011, **3**, 160.
28. K. Biswas, J. He, I. D. Blum, C.-I. Wu, T. P. Hogan, D. N. Seidman, V. P. Dravid and M. G. Kanatzidis, *Nature*, 2012, **489**, 414.
29. D. M. Rowe, V. S. Shukla and N. Savvides, *Nature*, 1981, **290**, 765.
30. D. T. Morelli, V. Jovovic and J. P. Heremans, *Phys. Rev. Lett.*, 2008, **101**, 035901.
31. Y. Pei, A. D. LaLonde, N. A. Heinz, X. Shi, S. Iwanaga, H. Wang, L. Chen and G. J. Snyder, *Adv. Mater.*, 2011, **23**, 5674.
32. Y.-L. Pei, H. Wu, D. Wu, F. Zheng and J. He, *J. Am. Chem. Soc.*, 2014, **136**, 13902.
33. J. Korringa and A. N. Gerritsen, *Physica*, 1953, **19**, 457.
34. Y. I. Ravich and S. A. Nemov, *Semiconductors*, 2002, **36**, 1.
35. R. J. Korkosz, T. C. Chasapis, S.-h. Lo, J. W. Doak, Y. J. Kim, C.-I. Wu, E. Hatzikraniotis, T. P. Hogan, D. N. Seidman, C. Wolverton, V. P. Dravid and M. G. Kanatzidis, *J. Am. Chem. Soc.*, 2014, **136**, 3225.
36. M. Samanta and K. Biswas, *J. Am. Chem. Soc.*, 2017, **139**, 9382.
37. J. Callaway and H. C. von Baeyer, *Phys. Rev.*, 1960, **120**, 1149.
38. P. G. Klemens, *Phys. Rev.*, 1960, **119**, 507.
39. M. G. Kanatzidis, *Chem. Mater.*, 2010, **22**, 648.
40. C. J. Vineis, A. Shakouri, A. Majumdar and M. G. Kanatzidis, *Adv. Mater.*, 2010, **22**, 3970.
41. Y. Min, J. W. Roh, H. Yang, M. Park, S. I. Kim, S. Hwang, S. M. Lee, K. H. Lee and U. Jeong, *Adv. Mater.*, 2013, **25**, 1425.
42. J. He, M. G. Kanatzidis and V. P. Dravid, *Mater. Today*, 2013, **16**, 166.
43. J. R. Sootsman, R. J. Pcionek, H. Kong, C. Uher and M. G. Kanatzidis, *Chem. Mater.*, 2006, **18**, 4993.
44. B. Qiu, H. Bao, G. Zhang, Y. Wu and X. Ruan, *Comput. Mater. Sci.*, 2012, **53**, 278.
45. O. Delaire, J. Ma, K. Marty, A. F. May, M. A. McGuire, M. H. Du, D. J. Singh, A. Podlesnyak, G. Ehlers, M. D. Lumsden and B. C. Sales, *Nat. Mater*, 2011, **10**, 614.
46. S. Roychowdhury, M. K. Jana, J. Pan, S. N. Guin, D. Sanyal, U. V. Waghmare and K. Biswas, *Angew. Chem., Int. Ed.*, 2018, **57**, 4043.
47. W. Qiu, L. Xi, P. Wei, X. Ke, J. Yang and W. Zhang, *Proc. Natl. Acad. Sci. USA*, 2014, **111**, 15031.
48. H. Euchner, S. Pailhès, L. T. K. Nguyen, W. Assmus, F. Ritter, A. Haghighirad, Y. Grin, S. Paschen and M. de Boissieu, *Phys. Rev. B*, 2012, **86**, 224303.
49. D. J. Voneshen, K. Refson, E. Borissenko, M. Krisch, A. Bosak, A. Piovano, E. Cemal, M. Enderle, M. J. Gutmann, M. Hoesch, M. Roger, L. Gannon, A. T. Boothroyd, S. Uthayakumar, D. G. Porter and J. P. Goff, *Nat. Mater.*, 2013, **12**, 1028.
50. M. K. Jana, K. Pal, U. V. Waghmare and K. Biswas, *Angew. Chem., Int. Ed.*, 2016, **55**, 7792.
51. M. K. Jana, K. Pal, A. Warankar, P. Mandal, U. V. Waghmare and K. Biswas, *J. Am. Chem. Soc.*, 2017, **139**, 4350.
52. H. Liu, X. Shi, F. Xu, L. Zhang, W. Zhang, L. Chen, Q. Li, C. Uher, T. Day and G. J. Snyder, *Nat. Mater.*, 2012, **11**, 422.
53. S. N. Guin, J. Pan, A. Bhowmik, D. Sanyal, U. V. Waghmare and K. Biswas, *J. Am. Chem. Soc.* , 2014, **136**, 12712.

54. L.-D. Zhao, S.-H. Lo, Y. Zhang, H. Sun, G. Tan, C. Uher, C. Wolverton, V. P. Dravid and M. G. Kanatzidis, *Nature*, 2014, **508**, 373.
55. S. Lee, K. Esfarjani, T. Luo, J. Zhou, Z. Tian and G. Chen, *Nat. Commun.*, 2014, **5**, 3525.
56. S. N. Guin, A. Chatterjee, D. S. Negi, R. Datta and K. Biswas, *Energy Environ. Sci.*, 2013, **6**, 2603.
57. A. Banik, B. Vishal, S. Perumal, R. Datta and K. Biswas, *Energy Environ. Sci.*, 2016, **9**, 2011.
58. L. Müchler, F. Casper, B. Yan, S. Chadov and C. Felser, *Phys. Status Solidi RRL*, 2013, **7**, 91.
59. M. Zhou, G. J. Snyder, L. Li and L.-D. Zhao, *Inorg. Chem. Front.*, 2016, **3**, 1449.
60. I. Cadoff and E. Miller, *Corp., New York*, 1960.
61. L.-D. Zhao, J. He, C.-I. Wu, T. P. Hogan, X. Zhou, C. Uher, V. P. Dravid and M. G. Kanatzidis, *J. Am. Chem. Soc.*, 2012, **134**, 7902.
62. Y. Xiao, H. Wu, W. Li, M. Yin, Y. Pei, Y. Zhang, L. Fu, Y. Chen, S. J. Pennycook, L. Huang, J. He and L.-D. Zhao, *J. Am. Chem. Soc.*, 2017, **139**, 18732.
63. G. Tan, F. Shi, S. Hao, L.-D. Zhao, H. Chi, X. Zhang, C. Uher, C. Wolverton, V. P. Dravid and M. G. Kanatzidis, *Nat. Commun.*, 2016, **7**, 12167.
64. A. Banik, S. Roychowdhury and K. Biswas, *Chem. Commun.*, 2018, **54**, 6573.
65. R. Brebrick and A. Strauss, *Phys. Rev.*, 1963, **131**, 104.
66. L. M. Rogers, *J. Phys. D: Appl. Phys.*, 1968, **1**, 845.
67. Y. Tanaka, Z. Ren, T. Sato, K. Nakayama, S. Souma, T. Takahashi, K. Segawa and Y. Ando, *Nat. Phys.*, 2012, **8**, 800.
68. Y. Sun, Z. Zhong, T. Shirakawa, C. Franchini, D. Li, Y. Li, S. Yunoki and X.-Q. Chen, *Phys. Rev. B*, 2013, **88**, 235122.
69. W. Jin, S. Vishwanath, J. Liu, L. Kong, R. Lou, Z. Dai, J. T. Sadowski, X. Liu, H.-H. Lien, A. Chaney, Y. Han, M. Cao, J. Ma, T. Qian, S. Wang, M. Dobrowolska, J. Furdyna, D. A. Muller, K. Pohl, H. Ding, J. I. Dadap, H. G. Xing and R. M. Osgood, *Phys. Rev. X*, 2017, **7**, 041020.
70. K. Yang, W. Setyawan, S. Wang, M. B. Nardelli and S. Curtarolo, *Nat. Mater.*, 2012, **11**, 614.
71. K. Shportko, S. Kremers, M. Woda, D. Lencer, J. Robertson and M. Wuttig, *Nat. Mater.*, 2008, **7**, 653.
72. M. Iizumi, Y. Hamaguchi, K. F. Komatsubara and Y. Kato, *J. Phys. Soc. Jpn.*, 1975, **38**, 443.
73. K. L. I. Kobayashi, Y. Kato, Y. Katayama and K. F. Komatsubara, *Phys. Rev. Lett.*, 1976, **37**, 772.
74. U. V. Waghmare, N. A. Spaldin, H. C. Kandpal and R. Seshadri, *Phys. Rev. B*, 2003, **67**, 125111.
75. K. V. Mitrofanov, A. V. Kolobov, P. Fons, M. Krbal, T. Shintani, J. Tominaga and T. Uruga, *Phys. Rev. B*, 2014, **90**, 134101.
76. L. Aggarwal, A. Banik, S. Anand, U. V. Waghmare, K. Biswas and G. Sheet, *J. Materiomics*, 2016, **2**, 196.
77. K. R. Knox, E. S. Bozin, C. D. Malliakas, M. G. Kanatzidis and S. J. L. Billinge, *Phys. Rev. B*, 2014, **89**, 014102.
78. C. W. Li, O. Hellman, J. Ma, A. F. May, H. B. Cao, X. Chen, A. D. Christianson, G. Ehlers, D. J. Singh, B. C. Sales and O. Delaire, *Phys. Rev. Lett.*, 2014, **112**, 175501.

79. D. H. Damon, *J. Appl. Phys.*, 1966, **37**, 3181.
80. K. Chang, J. Liu, H. Lin, N. Wang, K. Zhao, A. Zhang, F. Jin, Y. Zhong, X. Hu, W. Duan, Q. Zhang, L. Fu, Q.-K. Xue, X. Chen and S.-H. Ji, *Science*, 2016, **353**, 274.
81. F. A. S. Al-Alamy, A. A. Balchin and M. White, *J. Mater. Sci.*, 1977, **12**, 2037.
82. D. Parker and D. J. Singh, *J. Appl. Phys.*, 2010, **108**, 083712.
83. A. Banik and K. Biswas, *Angew. Chem., Int. Ed.*, 2017, **56**, 14561.
84. S. Saha, A. Banik and K. Biswas, *Chem. - Eur. J.*, 2016, **22**, 15634.
85. S. N. Guin, A. Banik and K. Biswas, in *2d Inorganic Materials Beyond Graphene*, World Scientific (WS), 2017, ch. 6, p. 239.
86. L.-D. Zhao, C. Chang, G. Tan and M. G. Kanatzidis, *Energy Environ. Sci.*, 2016, **9**, 3044.
87. Q. Tan, L.-D. Zhao, J.-F. Li, C.-F. Wu, T.-R. Wei, Z.-B. Xing and M. G. Kanatzidis, *J. Mater. Chem. A*, 2014, **2**, 17302.
88. C. W. Li, J. Hong, A. F. May, D. Bansal, S. Chi, T. Hong, G. Ehlers and O. Delaire, *Nat. Phys.*, 2015, **11**, 1063.
89. J. O. Dimmock, I. Melngailis and A. J. Strauss, *Phys. Rev. Lett.*, 1966, **16**, 1193.
90. A. Andreev, *Soviet Phys. Solid State*, 1967, **9**, 1232.
91. A. Banik, U. S. Shenoy, S. Anand, U. V. Waghmare and K. Biswas, *Chem. Mater.*, 2015, **27**, 581.
92. M. Parenteau and C. Carlone, *Phys. Rev. B*, 1990, **41**, 5227.
93. L. E. Shelimova, O. G. Karpinskii, P. P. Konstantinov, E. S. Avilov, M. A. Kretova and V. S. Zemskov, *Inorg. Mater.*, 2004, **40**, 451.
94. M. G. Vergniory, T. V. Menshchikova, I. V. Silkin, Y. M. Koroteev, S. V. Eremeev and E. V. Chulkov, *Phys. Rev. B*, 2015, **92**, 045134.
95. M. Zhou, Z. M. Gibbs, H. Wang, Y. Han, C. Xin, L. Li and G. J. Snyder, *Phys. Chem. Chem. Phys.*, 2014, **16**, 20741.
96. J. A. Kafalas, R. F. Brebrick and A. J. Strauss, *Appl. Phys. Lett.*, 1964, **4**, 93.
97. U. Jun-ichi, J. Manu and O. Toshihiro, *Jpn. J. Appl. Phys.*, 1962, **1**, 277.
98. W. Li, Y. Wu, S. Lin, Z. Chen, J. Li, X. Zhang, L. Zheng and Y. Pei, *ACS Energy Lett.*, 2017, **2**, 2349.
99. E. I. Rogacheva, *J. Phys. Chem. Solids*, 2008, **69**, 259.
100. A. Banik and K. Biswas, *J. Solid State Chem.*, 2016, **242**, 43.
101. A. Banik and K. Biswas, *J. Mater. Chem. A*, 2014, **2**, 9620.
102. R. Al Rahal Al Orabi, N. A. Mecholsky, J. Hwang, W. Kim, J.-S. Rhyee, D. Wee and M. Fornari, *Chem. Mater.*, 2016, **28**, 376.
103. G. Tan, L.-D. Zhao, F. Shi, J. W. Doak, S.-H. Lo, H. Sun, C. Wolverton, V. P. Dravid, C. Uher and M. G. Kanatzidis, *J. Am. Chem. Soc.*, 2014, **136**, 7006.
104. G. Tan, F. Shi, S. Hao, H. Chi, L.-D. Zhao, C. Uher, C. Wolverton, V. P. Dravid and M. G. Kanatzidis, *J. Am. Chem. Soc.*, 2015, **137**, 5100.
105. A. Banik, U. S. Shenoy, S. Saha, U. V. Waghmare and K. Biswas, *J. Am. Chem. Soc.*, 2016, **138**, 13068.
106. G. Tan, W. G. Zeier, F. Shi, P. Wang, G. J. Snyder, V. P. Dravid and M. G. Kanatzidis, *Chem. Mater.*, 2015, **27**, 7801.
107. Y. Pei, L. Zheng, W. Li, S. Lin, Z. Chen, Y. Wang, X. Xu, H. Yu, Y. Chen and B. Ge, *Adv. Electron. Mater.*, 2016, **2**, 1600019.
108. Q. Zhang, B. Liao, Y. Lan, K. Lukas, W. Liu, K. Esfarjani, C. Opeil, D. Broido, G. Chen and Z. Ren, *Proc. Natl. Acad. Sci. USA* 2013, **110**, 13261.

109. H. Wu, C. Chang, D. Feng, Y. Xiao, X. Zhang, Y. Pei, L. Zheng, D. Wu, S. Gong, Y. Chen, J. He, M. G. Kanatzidis and L.-D. Zhao, *Energy Environ. Sci.*, 2015, **8**, 3298.
110. G. Tan, F. Shi, S. Hao, H. Chi, T. P. Bailey, L.-D. Zhao, C. Uher, C. Wolverton, V. P. Dravid and M. G. Kanatzidis, *J. Am. Chem. Soc.*, 2015, **137**, 11507.
111. G. Tan, F. Shi, J. W. Doak, H. Sun, L.-D. Zhao, P. Wang, C. Uher, C. Wolverton, V. P. Dravid and M. G. Kanatzidis, *Energy Environ. Sci.*, 2015, **8**, 267.
112. G. Tan, F. Shi, H. Sun, L.-D. Zhao, C. Uher, V. P. Dravid and M. G. Kanatzidis, *J. Mater. Chem. A*, 2014, ***2***, 20849.
113. L. Zhang, J. Wang, Z. Cheng, Q. Sun, Z. Li and S. Dou, *J. Mater. Chem. A*, 2016, **4**, 7936.
114. M. H. Lee, D.-G. Byeon, J.-S. Rhyee and B. Ryu, *J. Mater. Chem. A*, 2017, **5**, 2235.
115. L.-D. Zhao, X. Zhang, H. Wu, G. Tan, Y. Pei, Y. Xiao, C. Chang, D. Wu, H. Chi, L. Zheng, S. Gong, C. Uher, J. He and M. G. Kanatzidis, *J. Am. Chem. Soc.*, 2016, **138**, 2366.
116. V. Nicolosi, M. Chhowalla, M. G. Kanatzidis, M. S. Strano and J. N. Coleman, *Science*, 2013, **340**, 1226419.
117. J. N. Coleman, M. Lotya, A. O'Neill, S. D. Bergin, P. J. King, U. Khan, K. Young, A. Gaucher, S. De, R. J. Smith, I. V. Shvets, S. K. Arora, G. Stanton, H.-Y. Kim, K. Lee, G. T. Kim, G. S. Duesberg, T. Hallam, J. J. Boland, J. J. Wang, J. F. Donegan, J. C. Grunlan, G. Moriarty, A. Shmeliov, R. J. Nicholls, J. M. Perkins, E. M. Grieveson, K. Theuwissen, D. W. McComb, P. D. Nellist and V. Nicolosi, *Science*, 2011, **331**, 568.
118. M. Chhowalla, H. S. Shin, G. Eda, L.-J. Li, K. P. Loh and H. Zhang, *Nat. Chem.*, 2013, **5**, 263.
119. X. Cao, C. Tan, X. Zhang, W. Zhao and H. Zhang, *Adv. Mater.*, 2016, **28**, 6167.
120. K. Xu, P. Chen, X. Li, C. Wu, Y. Guo, J. Zhao, X. Wu and Y. Xie, *Angew. Chem., Int. Ed.*, 2013, **52**, 10477.
121. V. Nicolosi, M. Chhowalla, M. G. Kanatzidis, M. S. Strano and J. N. Coleman, *Science*, 2013, **340**.
122. L.-D. Zhao, G. Tan, S. Hao, J. He, Y. Pei, H. Chi, H. Wang, S. Gong, H. Xu, V. P. Dravid, C. Uher, G. J. Snyder, C. Wolverton and M. G. Kanatzidis, *Science*, 2016, **351**, 141.
123. F. Q. Wang, S. Zhang, J. Yu and Q. Wang, *Nanoscale*, 2015, **7**, 15962.
124. A. T. Duong, V. Q. Nguyen, G. Duvjir, V. T. Duong, S. Kwon, J. Y. Song, J. K. Lee, J. E. Lee, S. Park, T. Min, J. Lee, J. Kim and S. Cho, *Nat. Commun.*, 2016, **7**, 13713.
125. Q. Zhang, E. K. Chere, J. Sun, F. Cao, K. Dahal, S. Chen, G. Chen and Z. Ren, *Adv. Energy Mater.*, 2015, **5**, 1500360.
126. G. Tang, W. Wei, J. Zhang, Y. Li, X. Wang, G. Xu, C. Chang, Z. Wang, Y. Du and L.-D. Zhao, *J. Am. Chem. Soc.*, 2016, **138**, 13647.
127. W. Wei, C. Chang, T. Yang, J. Liu, H. Tang, J. Zhang, Y. Li, F. Xu, Z. Zhang, J.-F. Li and G. Tang, *J. Am. Chem. Soc.*, 2018, **140**, 499.
128. S. Li, X. Li, Z. Ren and Q. Zhang, *J. Mater. Chem. A*, 2018, **6**, 2432.
129. Y. Luo, Y. Zheng, Z. Luo, S. Hao, C. Du, Q. Liang, Z. Li, K. A. Khor, K. Hippalgaonkar, J. Xu, Q. Yan, C. Wolverton and M. G. Kanatzidis, *Adv. Energy Mater.*, 2017, **8**, 1702167.
130. Y. Ding, B. Xiao, G. Tang and J. Hong, *J. Phys. Chem. C*, 2016, **121**, 225.
131. J. Y. Harbec, B. M. Powell and S. Jandl, *Phys. Rev. B*, 1983, **28**, 7009.

132. B.-Z. Sun, Z. Ma, C. He and K. Wu, *Phys. Chem. Chem. Phys.*, 2015, **17**, 29844.
133. M. M. Nassary, *J. Alloys Compd.*, 2005, **398**, 21.
134. W. Albers, C. Haas, H. J. Vink and J. D. Wasscher, *J. Appl. Phys.*, 1961, **32**, 2220.
135. C. Bera, S. Jacob, I. Opahle, N. S. H. Gunda, R. Chmielowski, G. Dennler and G. K. H. Madsen, *Phys. Chem. Chem. Phys.*, 2014, **16**, 19894.
136. Y.-M. Han, J. Zhao, M. Zhou, X.-X. Jiang, H.-Q. Leng and L.-F. Li, *J. Mater. Chem. A*, 2015, **3**, 4555.
137. M. G. Kanatzidis, *Acc. Chem. Res.*, 2005, **38**, 361.
138. M. G. Kanatzidis, *Inorg. Chem.*, 2017, **56**, 3158.
139. M. B. Babanly, E. V. Chulkov, Z. S. Aliev, A. V. Shevelkov and I. R. Amiraslanov, *Russ. J. Inorg. Chem.*, 2017, **62**, 1703.
140. K. Nakayama, K. Eto, Y. Tanaka, T. Sato, S. Souma, T. Takahashi, K. Segawa and Y. Ando, *Phys. Rev. Lett.*, 2012, **109**, 236804.
141. Z. A. Munir, U. Anselmi-Tamburini and M. Ohyanagi, *J. Mater. Sci.*, 2006, **41**, 763.
142. http://fuji-sps.sakura.ne.jp/principles/principles.html.
143. G. Xie, *J. Powder. Metall. Min.*, 2013, **2**, e109.
144. U. Z. RIKO, *Seebeck-Coefficient & Electric-Resistivity Measuring System Manual*, 2012.
145. K. A. Borup, J. de Boor, H. Wang, F. Drymiotis, F. Gascoin, X. Shi, L. Chen, M. I. Fedorov, E. Müller, B. B. Iversen and G. J. Snyder, *Energy Environ. Sci.*, 2015, **8**, 423.
146. W. J. Parker, R. J. Jenkins, C. P. Butler and G. L. Abbott, *J. Appl. Phys.*, 1961, **32**, 1679.
147. R. D. Cowan, *J. Appl. Phys.*, 1963, **34**, 926.
148. K. Biswas, J. He, G. Wang, S.-H. Lo, C. Uher, V. P. Dravid and M. G. Kanatzidis, *Energy Environ. Sci.*, 2011, **4**, 4675.
149. E. H. Hall, *Am. J. Math.*, 1879, **2**, 287.

CHAPTER 2

Introduction of Resonance Dopant Indium Improves the Thermoelectric Performance in *p*-type $SnTe_{1-x}Se_x$ System

Chapter 2

Introduction of Resonance Dopant Indium Improves the Thermoelectric Performance in *p*-type $SnTe_{1-x}Se_x$ System[†]

Summary

Lead chalcogenides are the best performers for thermoelectric power generation at mid/high temperatures (500-900 K); however, environmental concern about Pb prevents its use in large-scale thermoelectric applications. SnTe, a Pb-free IV-VI narrow band gap semiconductor, has potential to be a good thermoelectric material due to having similar crystal structure and valence band characteristics as PbTe. This chapter presents the promising thermoelectric performance in high quality crystalline ingots of In-doped $SnTe_{1-x}Se_x$ *(x = 0-0.15) synthesized by simple vacuum sealed tube melting reaction. First, we have optimized the lattice thermal conductivity of SnTe by solid solution alloying with SnSe. Resonance level formation in the valence band through In doping along with the increased contribution of heavy hole valence band through solid solution alloying significantly improved the Seebeck coefficient, resulting in a promising zT of ~0.8 at 860 K in Pb-free p-type 1.5 mol% In doped* $SnTe_{0.85}Se_{0.15}$ *sample.*

[†] *Paper based on this study has been published in* ***J. Mater. Chem. A*** 2014, *2,* 9602.

2.1 Introduction

Tin telluride (SnTe), a Pb free IV-VI narrow band gap semi-conductor, has the potential to be a good thermoelectric material due to the presence of similar valence band characteristics (light hole and heavy hole valence bands)[1-3] as PbTe. However, SnTe has received limited attention to the thermoelectric and solid state chemistry community because of the inability to control its very high carrier concentration (10^{20}-10^{21} cm^{-3}) which results in low S and high κ_{el}.[1,4] Intrinsic Sn vacancies is responsible for high *p*-type carrier concentration in SnTe.[4] In SnTe, energy difference between light hole valence band (L band) and heavy hole valence band (Σ band) is ~0.35 eV,[1-3] which is much higher than that of PbTe ($\Delta E_{L-\Sigma}$ ~0.05-0.1 eV[3]). Another drawback of SnTe is its high lattice thermal conductivity (~ 2.9 W/mK), which restricted SnTe to be considered as high performance thermoelectric (TE) material. In this chapter we focused on systemtic improvement of the thermoelectric performance of SnTe by enhancing Seebeck coefficient through the electronic structure modulation and reducing the lattice thermal conductivity by solid solution alloying.

According to Boltzmann transport theory, Seebeck coefficient of material is proportional to the energy derivative of electronic density of states (DOS) near Fermi level *via* Mott relation.[5]

$$\begin{aligned} S &= \frac{\pi^2}{3}\frac{k_B}{q}k_BT\left\{\frac{d[ln(\sigma(E))]}{dE}\right\}_{E=E_F} \\ &= \frac{\pi^2}{3}\frac{k_B}{q}k_BT\left\{\frac{1}{n}\frac{dn(E)}{dE}+\frac{1}{\mu}\frac{d\mu(E)}{dE}\right\}_{E=E_F} \end{aligned} \quad (2.1)$$

Here, $\sigma(E)$ is the electronic conductivity determined as a function of the band filling or Fermi energy, E_F ($\sigma(E) = n(E)q\mu(E)$) and $n(E)$ ($n(E) = g(E)f(E)$), the carrier density at the energy level, E (here q is the carrier charge, and $\mu(E)$ is the mobility as a function of energy, $f(E)$ is the Fermi function, $g(E)$ is density of state). When electronic scattering is independent of energy, $\sigma(E)$ is just proportional to the density of states (DOS) at E. Thus, S of thermoelectric material can be significantly enhanced by manipulating the DOS so that the number of electronic states sharply increases over a narrow energy range near the Fermi level.[6-8] This could be accomplished through the introduction of resonance

impurity states, which involves a coupling between electrons of a dopant and those in the valence or the conduction band of the host.[8] This creates an excess density of states near the valence or the conduction band edge of the host compound and results in higher effective mass, m* and thereby enhances Seebeck coefficient.[9]

Group III (mainly Al, In and Tl) dopants impart specific properties to IV–VI semiconductors and primarily associated with the formation of resonance states.[10,11] The relative energy level of the dopants and the host determines the formation of resonace state either in the valance or in the conduction band. For example, indium (In) in PbTe and other lead chalcogenides gives rise to resonance states in the conduction band, whereas thallium (Tl) in lead chalcogenides forms resonance states inside the valence band.[10] The resulting significant enhancement in Seebeck coefficient of PbTe due to the resonance level formation motivated us to explore similar strategy for SnTe to improve its Seebeck coefficient.[12] However, unlike in PbTe, indium (In) is the only effective dopant that introduces resonance state in SnTe.[10,13] The valance and conduction band character is inverted in SnTe compared to PbTe in the way that in SnTe light hole and heavy hole valance bands are formed by Sn 5*p* and Te 5*p* orbitals, respectively.[3,14] Thus, interaction of energetically similar In-s orbital and Te-p orbital gives rise to the formation of resonant state in In-doped SnTe.[10,15]

Significant improvement of the power factor (σS^2) coupled with low lattice thermal conductivity (κ_{lat}) is necessary to improve the performance of present thermoelectric materials. Pristine SnTe shows room temperature κ_{lat} values of ~2.9 W/mK, which is much higher compared to the theoretical minimum lattice thermal conductivity (κ_{min}) of SnTe (~0.5 W/mK, according to Cahill's model.[16]).[17] Phonon scattering by point defects is one of the major strategies for minimizing the lattice thermal conductivity (κ_{lat}) in thermoelectric materials.[18] In this regard, it is of considerable interest to study the behavior of an isostructural, isovalent solid solution (e.g., Substitution of Sn and Te with Pb/Ge and Se, S, respectively). Use of SnTe-SnSe alloying can be the most effective approach, where the introduction of Se in place of Te create mass and strain fluctuations resulting in the scattering of short wavelength phonons and reduced κ_{lat}. Furthermore, substitution of Te (electronegativity ~2.1 according to Pauling scale) with higher electronegative Se (electronegativity ~2.55 according to Pauling scale) is expected to

increase the principle band gap and decrease the energy difference between the two valence bands of SnTe, and facilitate the band convergence.[19-21]

This chapter presents the promising thermoelectric performance in Pb-free In-doped $SnTe_{1-x}Se_x$ (x = 0-0.15) synthesized by simple sealed tube melting reaction. We first optimize the κ_{lat} of SnTe through solid solution alloying with SnSe. Minimal κ_{lat} of 1.25 W/mK is achieved in $SnTe_{0.85}Te_{0.15}$ sample at ~500 K. The optimized sample is used for further improvement in Seebeck coefficient by In doping. Resonance level formation in the valence bands through In doping along with convergence of valence bands through solid solution alloying significantly improved the Seebeck coefficient, resulting in a promising zT of ~0.8 at 860 K in 1.5 mol% In doped $SnTe_{0.85}Se_{0.15}$.

2.2 Methods

2.2.1 Synthesis

Tin (Alfa Aesar 99.99+ %), tellurium (Alfa Aesar 99.999+ %), selenium (Alfa Aesar 99.999+ %) and indium (Alfa Aesar 99.99+ %) were used for synthesis without further purification.

Polycrystalline ingots (~7 g) of $SnTe_{1-x}Se_x$ (x = 0-0.15) were synthesized by mixing stoichiometric ratios of high-purity starting materials of Sn, Se and Te in a quartz tube. The tubes were sealed under vacuum (10^{-5} Torr) and slowly heated to 450 ^{o}C over 12 hrs, then heated up to 900 ^{o}C in 5 hrs, soaked for 10 hrs, and cooled slowly to room temperature. Indium doped $SnTe_{1-x}Se_x$ samples were synthesized via the similar procedure using stoichiometric ratios of Sn, In, Te and Se.

2.2.2 Characterizations

Powder X-ray diffraction (PXRD) for all of the samples were recorded using a Cu K_α (λ = 1.5406 Å) radiation on a Bruker D8 diffractometer.

2.2.3 Transport properties

Electrical conductivity (σ) and Seebeck coefficients (S) were measured simultaneously under He atmosphere from room temperature to 873 K in a ULVAC-RIKO ZEM-3 instrument system (measurement details are given in chapter 1). Carrier concentrations (n_H) were determined using Hall coefficient measurements at room temperature with a

PPMS system(measurement details are given in chapter 1). Thermal diffusivity, D, was directly measured in the range 300−873 K by using laser flash diffusivity method in a Netzsch LFA-457. The total thermal conductivity, κ_{total}, was calculated using the formula, $\kappa_{total} = DC_p\rho$ (measurement details are given in chapter 1).

2.3 Results & Discussion

The designing strategy for improving the thermoelectric performance of SnTe is described below as two rational steps. First, the lattice thermal conductivity of SnTe was optimized by solid solution alloying with SnSe. Moreover, solid solution alloying facilitates valence band convergence in $SnTe_{1-x}Se_x$. Finally, the sample having lowest κ_{lat} have been chosen for further improvement in Seebeck coefficient through In doping.

2.3.1 Solid solution alloying in $SnTe_{1-x}Se_x$

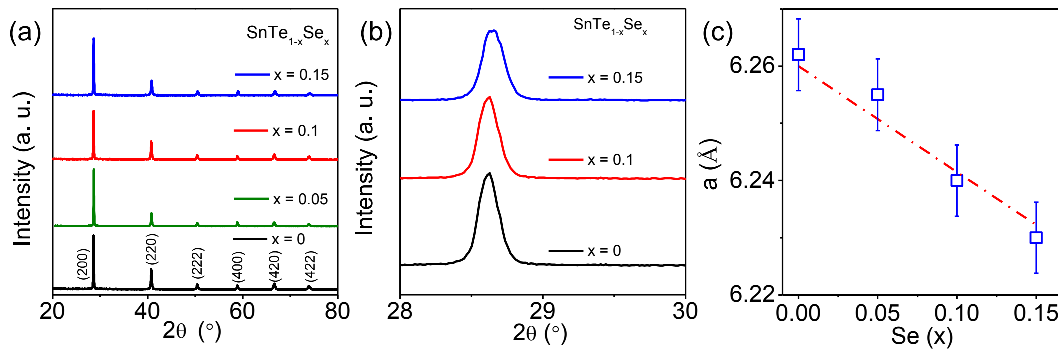

Figure 2.1 (a) PXRD pattern of $SnTe_{1-x}Se_x$ [x =0-0.15]. (b) Magnified PXRD pattern (28°-30°) shows systematic higher angle shift of (200) peak in $SnTe_{1-x}Se_x$. (c) Variation of lattice parameter (a) with Se concentration (x) in $SnTe_{1-x}Se_x$ (x = 0-0.15) with error bar of 0.1%. Dashed line indicates the Vegard's law for solid solution.

In an effort to reap the lowest lattice thermal conductivity (κ_{lat}), we have thoroughly studied the SnTe-SnSe solid solution. Up to 15 mol% of Se incorporation, solid solution nature was retained in $SnTe_{1-x}Se_x$. PXRD of the $SnTe_{1-x}Se_x$ (x = 0-0.15) samples could be indexed on the cubic SnTe structure (*Fm*-3*m* space group) with no other second phase within the detection limits of PXRD (Figure 2.1a). Systematic higher angle shift of PXRD peak (Figure 2.1b) with increasing Se concentrations and the observed linear contraction in the lattice parameter in $SnTe_{1-x}Se_x$ (x = 0-0.15) (Figure 2.1c) indicate the solid solution

behavior. Ionic radius of Se (184 pm) is smaller than that of Te (207 pm). As smaller Se is introduced in the place of bigger Te, the unit cell undergoes a systematic contraction, leading to decrease in the lattice parameter. This gradual decrease of lattice parameter indicates an isomorphic substitution of bigger Te position by smaller Se.

With a specific end goal to comprehend the change in electronic structure, we have attempted to measure optical absorption spectra. Unfortunately, we could not resolve the band gap (E_g) of the $SnTe_{1-x}Se_x$ (x = 0-0.15) samples by diffuse IR reflectance spectroscopy as the present samples are highly self-doped (n_H ~10^{20} cm^{-3}) due to large intrinsic Sn vacancy. However, systematic increase in the E_g was observed earlier in thin film samples of $SnTe_{1-x}Se_x$ with n_H.[22] If the energy of light hole valence band reduced as the principle band gap increases, which reduces the band offset between L and Σ point valence bands in SnTe, the heavy hole Σ band will play a significant role to increase in Seebeck in properly doped $SnTe_{1-x}Se_x$ samples. A similar decrease in the energy difference between L and Σ valence bands in lead chalcogenides have been achieved when alloyed with high band gap alkaline earth (Mg/Sr) chalcogenides.[23,24]

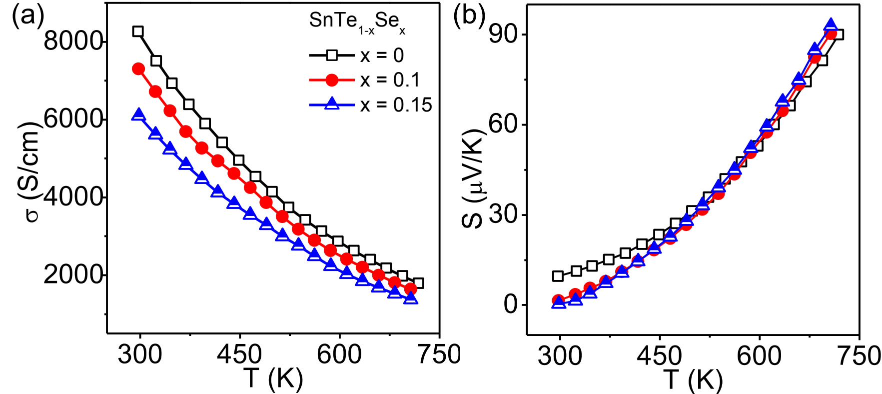

Figure 2.2 Temperature dependent (a) electrical conductivity (σ) and (b) Seebeck coefficient (S) of $SnTe_{1-x}Se_x$ [x =0-0.15].

Figure 2.2 presents temperature dependent electrical conductivity (σ) and Seebeck coefficient (S) of $SnTe_{1-x}Se_x$ (x = 0-0.15). For all the $SnTe_{1-x}Se_x$ (x = 0-0.15) samples, σ decreases with increasing temperature, confirming degenerate semiconduction. Introduction of Se in Te position reduces the electrical conductivity of SnTe originating from reduced n_H. At room temperature, SnTe is having σ of ~8269 S/cm, which decreases to ~6094 S/cm for $SnTe_{0.85}Se_{0.15}$. To understand the effect of Se in the electrical transport properties of SnTe, we measured the room temperature Hall coefficient for SnTe and

$SnTe_{0.85}Se_{0.15}$. Like pristine SnTe, $SnTe_{1-x}Se_x$ with x = 0.15 exhibits positive Hall coefficient confirming the effective contribution of *p*-type charge carrier. Substitution of Te with Se increases the vacancy formation energy of SnTe, and thus shows decreased n_H.[22] This resulted in an effective reduction of carrier-carrier scattering and an enhanced the carrier mobility (defined as $\mu = \sigma/n_H e$) from ~160 cm^2/Vs to ~270 cm^2/Vs in $SnTe_{0.85}Se_{0.15}$ sample.

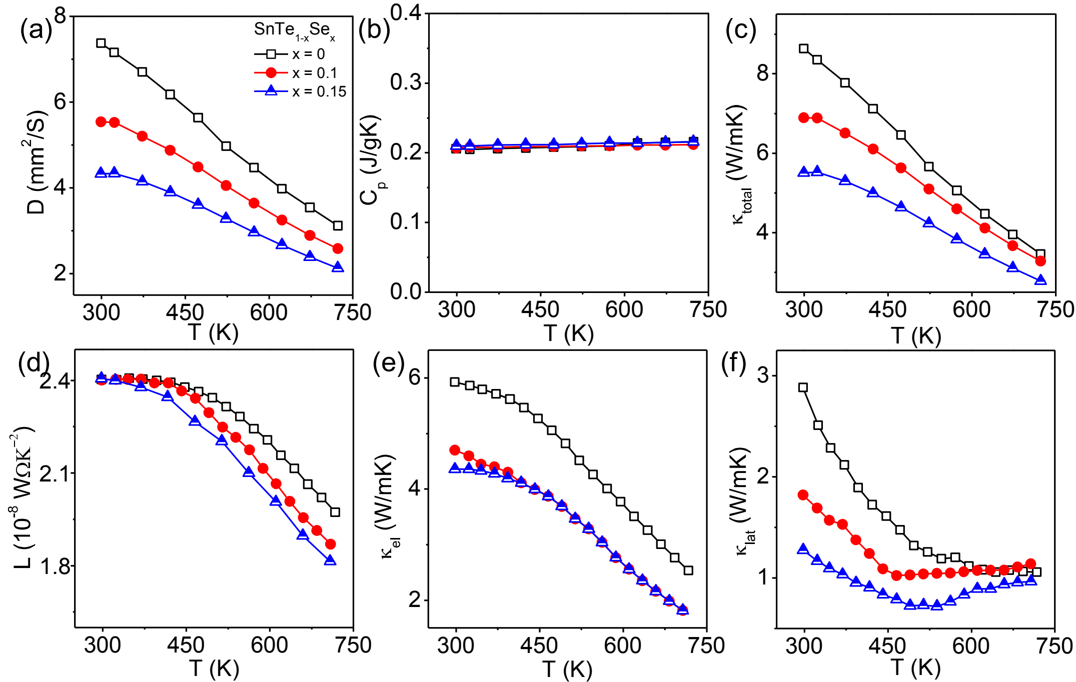

Figure 2.3 Temperature dependent (a) thermal diffusivity (D), (b) heat capacity (C_p) (c) total thermal conductivity (κ_{total}), (d) Lorenz number (L), (e) electronic thermal conductivity (κ_{el}) and (f) lattice thermal conductivity (κ_{lat}) of $SnTe_{1-x}Se_x$ [x =0-0.15].

The positive Seebeck coefficient of $SnTe_{1-x}Se_x$ samples (x = 0-0.15) is in well agreement with Hall measurement data (Figure 2.2b). Pristine SnTe possesses Seebeck coefficient of ~20 μV/K at room temperature because of its high hole concentration as mentioned in chapter 1. Interestingly, the room temperature Seebeck coefficient decreases gradually with increasing Se concentration despite the reduced n_H, which is opposite from the usual behaviour of a *p*-type semiconductor. This anomalous reduction of S can be explained considering the presence of two nondegenerate valence bands near Fermi level (at the L and Σ points of the Brillouin zone) of SnTe.[1,3] Because of the very high hole concentration (~10^{20} cm^{-3}) in pristine SnTe, the Fermi level resides closer to the heavy-hole valence band. Thus heavy hole valence band also participates in the electronic

transport and Seebeck coefficient. With increasing Se concentration, the Fermi level rises and gradually shifts away from the heavy-hole band due to reduced n_H. Reduced contribution of second valence band gives rise to lowering of room temperature S in $SnTe_{1-x}Se_x$ as compared to that of pristine SnTe. In addition to this, $SnTe_{1-x}Se_x$ samples with lower Seebeck coefficients (low n_H) at lower temperature have slightly higher Seebeck coefficients when temperature is above 573 K, which is attributed to the increasing contribution of the heavy hole Σ band at rising temperatures, similar to high temperature band structure of PbTe.[21] Thus, higher S of $SnTe_{1-x}Se_x$ samples as compared of to SnTe is combined result of carrier optimization (n_H) and reduced two valence band energy separation.

In figure 2.3, we present the temperature dependent thermal transport properties of $SnTe_{1-x}Se_x$ (x = 0-0.15). Thermal diffusivity (D) decreases with increasing Se concentration, as seen in figure 2.3a. Pristine SnTe shows room temperature C_p of 0.208 $Jg^{-1}K^{-1}$ (Figure 2.3b), which is in close agreement with the Dulong-Petit C_p value of SnTe (0.2025 $Jg^{-1}K^{-1}$). We have estimated κ_{total} based on experimentally measured thermal diffusivity (D) and C_p. Incorporation of Se in Te position reduces the room temperature κ_{total} from 8.63 W/mK to 5.51 W/mK (Figure 2.3c). To understand the electronic and phonon contribution in heat transport, we calculated electronic thermal conductivity, κ_{el} and lattice thermal conductivity, κ_{lat} of $SnTe_{1-x}Se_x$ (x = 0-0.15) systems. The electronic thermal conductivities, $\kappa_{el} = L \cdot \sigma \cdot T$, are extracted based on fitting of the respective S values that estimate the reduced chemical potential from which we got the Lorenz number, L (Figure 2.3d) (Detailed discussion is in chapter 1). The κ_{lat} is obtained after subtracting the electronic part, κ_{el} (Figure 2.3e), from the κ_{total} (Figure 2.3f). A significant decrease of κ_{lat} have been achieved in $SnTe_{1-x}Se_x$ (x = 0-0.15) samples compared to that of pristine SnTe (Figure 2.3f), which is due to the excess phonon scattering by the solid solution point defects formation and mass fluctuation.[25] Typically, $SnTe_{0.85}Se_{0.15}$ sample has κ_{lat} of ~1.27 W/mK at 300 K, then it passes through minima (~0.7 W/mK) at 535 K and reaches ~0.94 W/mK at 710 K (Figure 2.3f). Since the 15 mol% Se incorporated SnTe has lowest κ_{lat}, this sample has been used for In doping.

2.3.2 Indium doping in $SnTe_{1-x}Se_x$

$SnTe_{1-x}Se_x$ with x = 0.15, the sample having lowest κ_{lat} has been chosen for further improvement in Seebeck coefficient through In doping.

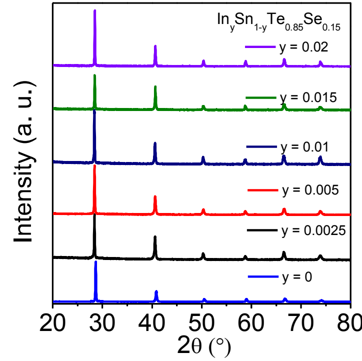

Figure 2.4 PXRD pattern of $In_ySn_{1-y}Te_{0.85}Se_{0.15}$ (y = 0-0.025).

We have synthesized several In (0-2.5 mol%) doped $SnTe_{0.85}Se_{0.15}$ by similar sealed tube melting reaction. PXRD patterns of the In-doped $SnTe_{0.85}Se_{0.15}$ could be indexed on the cubic SnTe structure (F*m*-3*m* space group) with no other impurity phase within the detection limits of PXRD (Figure 2.4).

The electrical conductivity (σ) decreases with increasing In concentration up to 2.5 mol%, especially at room temperature from 6110 S/cm to 1240 S/cm (Figure 2.5a). Typically, the room temperature σ of 1.5 mol% In doped $SnTe_{0.85}Se_{0.15}$ is to be ~1670 S/cm, which decreases to ~640 S/cm at 855 K, showing a typical degenerate semiconductor behavior. The room temperature Hall coefficients, R_H, of all In doped $SnTe_{0.85}Se_{0.15}$ samples are positive, which indicates the *p*-type conduction in this system. Carrier concentration (n_H) at 300 K increases with increasing the In doping concentration up to 1 mol% and then decreases with further increasing the In doping up to 2 mol% (Figure 2.5b). Indium in IV-VI semiconductors is known to exhibit amphoteric donor-acceptor behaviour (Indium can be present in both monovalent, In^+ and the trivalent states, In^{3+}).[26] In the present case, first, In substitutes the Sn in $SnTe_{0.85}Se_{0.15}$ and acts as acceptor (In^+), thus *p*-type carrier concentration increases. When the In concentration reaches beyond 1 mol%, extra In atom acts as donors (In^{3+}), which decreases the hole carrier concentration in $SnTe_{0.85}Se_{0.15}$. Similar mixed *p* and *n*-type doping beaviour of In in SnTe have been observed in recently reported In doped SnTe samples.[13] Room temperature hole mobility, for various In doped $SnTe_{0.85}Se_{0.15}$ samples is plotted in figure 2.5c. Decrease in room temperature σ value with the increase in In doping

concentration is due to the significant decrease in μ. Carrier mobility decreases in In (< 1 mol%) doped SnTe0.85Se0.15 due to impurity scattering.[13]

Figure 2.6 presents the temperature dependent Seebeck coefficient (*S*) data of In (0-2.5 mol%) doped $SnTe_{0.85}Se_{0.15}$ samples. Positive value of *S* indicates the *p*-type carriers which supports the Hall measurement. Significant improvement in the *S* have been achieved by In doping in $SnTe_{0.85}Se_{0.15}$, especially at room temperature from ~0.5 μV/K to ~70 μV/K with a In doping concentration of 2 mol%. Typically, the room temperature *S* value measured for 1.5 mol% In doped $SnTe_{0.85}Se_{0.15}$ was ~67 μV/K which linearly increases to ~175 μV/K at 865 K.

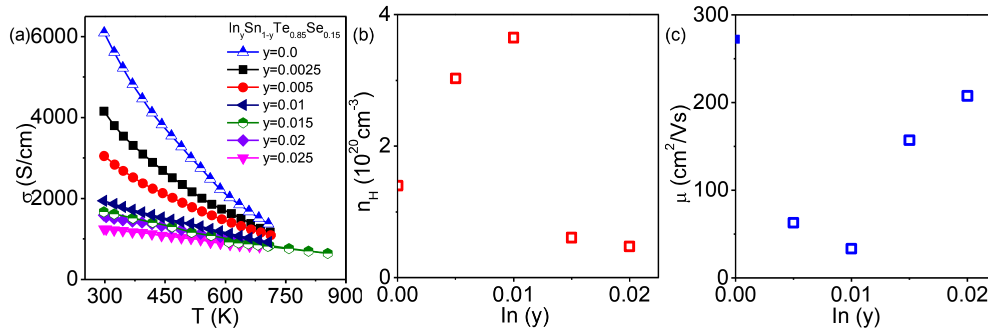

Figure 2.5 (a) Temperature dependent electrical conductivity (σ), room temperature (b) carrier concentration (n_H) and (c) carrier mobility (μ) with respect to doping content y in $In_ySn_{1-y}Te_{0.85}Se_{0.15}$ (y = 0-0.025).

In figure 2.6b, we compare the present room temperature *S* vs. n_H data with previously reported experimental data on In doped SnTe (ball mill + SPS samples)[13] and with the theoretical *S* vs. n_H curve.[3,13] Theoretical Pisarenko (*S* vs. n_H) curves at room temperature have been calculated earlier by considering the contribution of both the light hole valence band (*L* point) and heavy hole valence band (*Σ* point) of SnTe.[13] This model uses a light hole band effective mass of ~0.168 m_e, a heavy hole band effective mass of ~1.92 m_e, and an energy gap between two valence bands of 0.35 eV, respectively. Seebeck coefficient of SnTe and $SnTe_{0.85}Se_{0.15}$ falls in the theoretical *S* vs n_H. Significant enhancement in the present *S* values in In (0-2.5 mol%) doped $SnTe_{0.85}Se_{0.15}$ compared to the theoretical Pisarenko plots have been noticed, thus it indicates the creation of resonance level in the valence band of $SnTe_{0.85}Se_{0.15}$ by In doping.

Figure 2.6c presents the temperature dependent power factor (σS^2) data of In (0-2.5 mol%) doped $SnTe_{0.85}Se_{0.15}$ samples. Significant improvement in σS^2 has been achieved mainly due to the enhancement of the thermopower in the present sample. Typically, at room temperature, σS^2 value for 1.5 mol% In doped $SnTe_{0.85}Se_{0.15}$ is ~7.3 μW/cmK^2

which rises almost linearly to ~19.2 μW/cmK^2 at ~860 K. Enhancement of σS^2 have achieved due to the resonance level effect and also due to contribution of heavy hole valence band especially at high temperature in In doped $SnTe_{1-x}Se_x$.

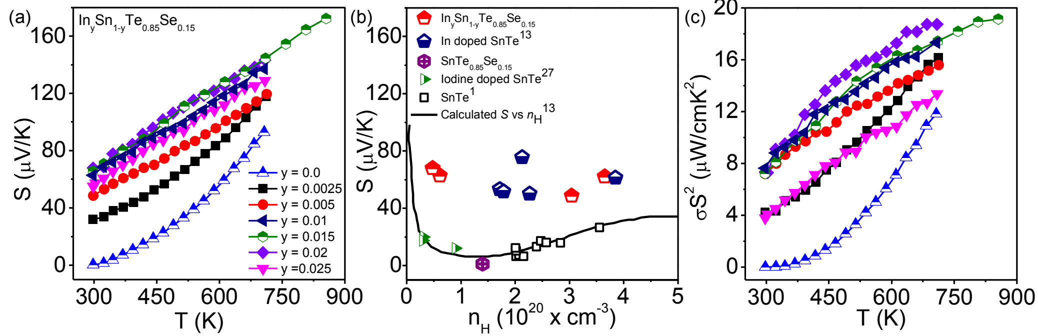

Figure 2.6 (a) Temperature dependent Seebeck coefficient (S) of $In_ySn_{1-y}Te_{0.85}Se_{0.15}$ (y = 0-0.025) (b) Room temperature S vs. n_H plot of $In_ySn_{1-y}Te_{0.85}Se_{0.15}$ showing sharp rise over theretical Pisarenko curve (solid line)[13]. For comparison previously reported S vs n_H plot of In doped SnTe and iodine doped SnTe,[27] and also pristine SnTe samples are given[22]. (c) Temperature dependent power factor (σS^2) of $In_ySn_{1-y}Te_{0.85}Se_{0.15}$ (y = 0-0.025).

Indium doping in $SnTe_{0.85}Se_{0.15}$ further optimizes the temperature dependent κ_{total} (Figure 2.7a) by controlling the κ_{el}. Typically, the room temperature κ_{total} value measured for 1.5 mol% In doped $SnTe_{0.85}Se_{0.15}$ is ~2.3 W/mK which decreases to ~2.15 W/mK at 873 K. With In doping temperature dependent κ_{el} decreases significantly due to the decrease in the temperature dependent σ (Figure 2.7b). The lattice thermal conductivity, κ_{lat}, was estimated after subtracting the electronic part, κ_{el}, from the κ_{total} (Figure 2.7c).

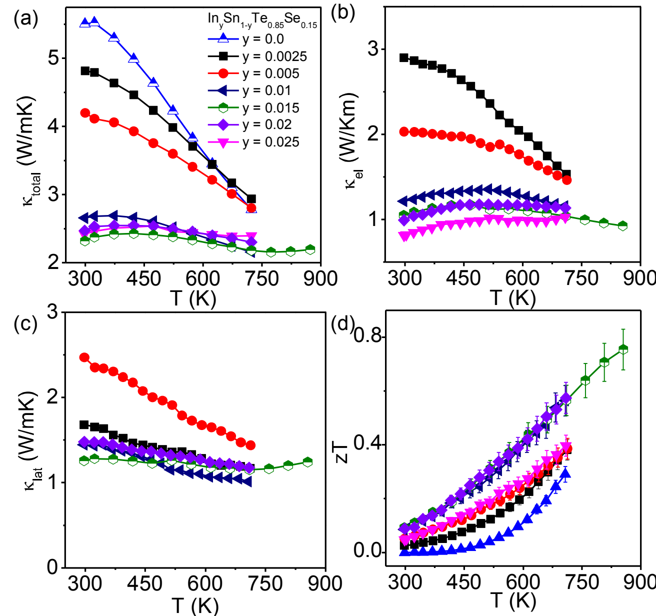

Figure 2.7 Temperature dependent (a) total thermal conductivity (κ_{total}), (b) electronic thermal conductivity (κ_{el}), (c) lattice thermal conductivity (κ_{lat}) and (d) thermoelectric figure of merit (zT) (with 10% error bar) of $In_ySn_{1-y}Te_{0.85}Se_{0.15}$ [y =0-0.025].

In figure 2.7d we present temperature dependent *zT* of all In doped $SnTe_{0.85}Se_{0.15}$. The highest *zT* value of ~0.8 at 860 K was achieved for 1.5 mol% In doped $SnTe_{0.85}Se_{0.15}$, which is significantly higher compared to undoped SnTe (*zT* ~0.29) and $SnTe_{0.85}Se_{0.15}$ (*zT* ~0.31) samples.

2.4 Conclusions

High quality crystalline ingots of In-doped $SnTe_{1-x}Se_x$ (x = 0-0.15) have been synthesized by simple vacuum sealed tube melting reaction. First, κ_{lat} of SnTe has been minimized by solid solution alloying with SnSe. Resonance level formation in the valence band through In doping along with convergence of valence band through solid solution alloying significantly improved the Seebeck coefficient in In doped $SnTe_{1-x}Se_x$, resulting in a enhanced power factor of 19.2 μW/cmK^2 at 860 K. Improved power factor with relatively low thermal conductivity have resulted a *zT* of ~0.8 in Pb-free $SnTe_{1-x}Se_x$ system.

2.5 References

1. R. Brebrick and A. Strauss, *Phys. Rev.*, 1963, **131**, 104.
2. B. Efimova, V. Kaidanov, B. Y. Moizhes and I. Chernik, *Sov. Phys. Solid State*, 1966, *7*, 2032.
3. L. M. Rogers, *J. Phys. D: Appl. Phys.*, 1968, **1**, 845.
4. R. Brebrick, *J. Phys. Chem. Solids*, 1963, **24**, 27.
5. N. F. Mott and H. Jones, *The theory of the properties of metals and alloys*, Dover Publications, New York, 1958.
6. J. R. Sootsman, D. Y. Chung and M. G. Kanatzidis, *Angew. Chem., Int. Ed.*, 2009, **48**, 8616.
7. G. Mahan and J. Sofo, *Proc. Natl. Acad. Sci. U. S. A.*, 1996, **93**, 7436.
8. J. P. Heremans, B. Wiendlocha and A. M. Chamoire, *Energy Environ. Sci.*, 2012, **5**, 5510.
9. G. Tan, L.-D. Zhao and M. G. Kanatzidis, *Chem. Rev.*, 2016, **116**, 12123.
10. V. I. Kaĭdanov and Y. I. Ravich, *Sov. Phys. Usp.*, 1985, **28**, 31.
11. Y. I. Ravich and S. A. Nemov, *Semiconductors*, 2002, **36**, 1.
12. J. P. Heremans, V. Jovovic, E. S. Toberer, A. Saramat, K. Kurosaki, A. Charoenphakdee, S. Yamanaka and G. J. Snyder, *Science*, 2008, **321**, 554.
13. Q. Zhang, B. Liao, Y. Lan, K. Lukas, W. Liu, K. Esfarjani, C. Opeil, D. Broido, G. Chen and Z. Ren, *Proc. Natl. Acad. Sci. USA,* 2013, **110**, 13261.
14. J. O. Dimmock, I. Melngailis and A. J. Strauss, *Phys. Rev. Lett.*, 1966, **16**, 1193.
15. X. Tan, G. Liu, J. Xu, H. Shao, J. Jiang and H. Jiang, *Phys. Chem. Chem. Phys.*, 2016, **18**, 20635.
16. D. G. Cahill, S. K. Watson and R. O. Pohl, *Phys. Rev. B*, 1992, **46**, 6131.
17. A. Banik, B. Vishal, S. Perumal, R. Datta and K. Biswas, *Energy Environ. Sci.*, 2016, **9**, 2011.
18. L.-D. Zhao, V. P. Dravid and M. G. Kanatzidis, *Energy Environ. Sci.*, 2014, **7**, 251.
19. Y. Pei, X. Shi, A. LaLonde, H. Wang, L. Chen and G. J. Snyder, *Nature*, 2011, **473**, 66.
20. Q. Zhang, F. Cao, W. Liu, K. Lukas, B. Yu, S. Chen, C. Opeil, D. Broido, G. Chen and Z. Ren, *J. Am. Chem. Soc.*, 2012, **134**, 10031.
21. W. G. Zeier, A. Zevalkink, Z. M. Gibbs, G. Hautier, M. G. Kanatzidis and G. J. Snyder, *Angew. Chem., Int. Ed.*, 2016, **55**, 6826.
22. L. I. Soliman, B. S. Farag, H. A. Zayed and F. M. Shehata, *Indian J. Pure Appl. Phys.*, 2003, **41**, 131.
23. L. Zhao, H. Wu, S. Hao, C.-I. Wu, X. Zhou, K. Biswas, J. He, T. P. Hogan, C. Uher and C. Wolverton, *Energy Environ. Sci.*, 2013, ***6***, 3346.
24. H. Wang, Z. M. Gibbs, Y. Takagiwa and G. J. Snyder, *Energy Environ. Sci.*, 2014, **7**, 804.
25. P. G. Klemens, *Phys. Rev.*, 1960, **119**, 507.
26. S. Ahmad, K. Hoang and S. D. Mahanti, *Phys. Rev. Lett.*, 2006, **96**, 056403.
27. M. Zhou, Z. M. Gibbs, H. Wang, Y. Han, C. Xin, L. Li and G. J. Snyder, *Phys. Chem. Chem. Phys.*, 2014, **16**, 20741.

CHAPTER 3

Enhancement of Thermoelectric Performance of SnTe by Valence Band Convergence

Chapter 3A

Mg Alloying in SnTe Facilitates Valence Band Convergence and Optimizes Thermoelectric Properties†

Summary

SnTe, having valence band structure similar to PbTe, recently has attracted attention for thermoelectric heat to electricity generation. However, pristine SnTe is a poor thermoelectric material because of very high hole concentration resulting from intrinsic Sn vacancies, which give rise to low Seebeck coefficient and high electrical thermal conductivity. In this chapter, we show that SnTe can be optimized to be a high performance thermoelectric material for power generation by controlling the hole concentration and significantly improving the Seebeck coefficient. Mg (2-10 mol%) alloying in SnTe modulates its electronic structure by increasing the principal band gap of SnTe, and results in decrease in the energy separation between its light and heavy hole valence bands. Thus, solid solution alloying with Mg enhances the contribution of heavy hole valence band, leading to significant improvement in the Seebeck coefficient in Mg alloyed SnTe, which in turn results in remarkable enhancement in power factor. Maximum thermoelectric figure of merit, zT, of ~1.2 is achieved at 860K in high quality crystalline ingot of p-type $Sn_{0.94}Mg_{0.09}Te$.

†*Paper based on this study has been published in* **Chem. Mater**. 2015, *27*, 581.

3A.1 Introduction

Tin telluride (SnTe), the homolog of PbTe, has the potential to be a good thermoelectric material due to its valence band (light hole and heavy hole valence bands) characteristic.[1-3] However, SnTe has rarely been considered to be efficient thermoelectric material because of the inability to control its very high carrier concentration (10^{20}-10^{21} cm^{-3}) which results in low S and high κ_{el}.[3] Intrinsic Sn vacancy is responsible for high *p*-type carrier concentration in SnTe.[4] In chapter 2, I have discussed the effective role of resonance dopant indium to improve Seebeck coefficient of SnTe.[5] Although the resonance level formation is crucial to room temperature Seebeck enhancement, this does not have significant effect on high temperature transport properties.[6] Thus, in order to enhance the Seebeck coefficient of SnTe, one of the effective approaches is band convergence which means partial/well alignment of two valence bands.

In SnTe, valence band and conduction band edges are located at the *L*-point of Brillouin zone and the energy gap is ~0.15 eV at room temperature.[3] Interestingly, a heavy hole valence band (Σ -point of Brillouin zone) lies ~0.35 eV below the light hole valence band (*L* band).[1,3,4] The light valence band is having valley degeneracy of 4, whereas the heavy hole band degeneracy is 12.[3] A valley degeneracy, N_v has the effect of increasing effective mass, m_b^* by a factor of $N_v^{2/3}$, where N_v includes orbital degeneracy, and m_b^* is, the average (single valley) density-of-states effective mass of the degenerate valleys. Therefore, it is important to engineer the electronic structure of SnTe to increase contribution of the heavy hole band's in the electronic transport which can enhance the Seebeck coefficient drastically. However, the large energy separation of two valence bands restricts contribution of the heavy hole valence band in the transport properties. According to previous temperature dependent Hall coefficient (R_H) measurement, the band energy offset of pristine SnTe shows effective reduction only above 700 K.[7] Although a n_H of $>10^{20}$ cm^{-3} could involve contribution from the low-lying heavy hole band of SnTe to the transport properties, these n_H are massively higher than needed for optimized zT, leading to the very low zT of ~0.35 at 900 K.[8] Alloying of SnTe (E_g~0.18 eV) with wide band gap semiconductor, opens up the principle band gap of SnTe, which can decrease the energy difference between two valence bands of SnTe, thereby can facilitate the convergence of the valence band valleys.[9] Such valence band convergence is believed to enhance the Seebeck coefficient due to contribution from both the valence

bands, which gives rise to asymmetric increase in the density of states near the Fermi energy. Furthermore, the reduction in energy between light and heavy hole valence bands leads to more conducting channels for charge carriers, resulting in scattering less transport which enables much higher electrical conductivity at a given reduced Fermi energy (i.e., a given S).[10] Enhancement in the Seebeck coefficient has been achieved by Cd or Hg alloying in SnTe, which decreases the energy separation between light and heavy hole valence band.[11,12] Alloying of SnTe (E_g~0.15 eV) with MgTe, which is a wide band gap (E_g ~3.5 eV) semiconductor, may open up the band gap of SnTe, which can decrease the energy difference of the two valence bands of SnTe, thus it will facilitate the convergence of the valence band valleys.

This chapter presents effects of Mg alloying on the electronic structure and the thermoelectric properties of SnTe which is synthesized by simple sealed tube melting reactions. We first suppress the excess hole concentration of SnTe by Sn-self compensation ($Sn_{1.03}Te$).[11] Mg alloying in $Sn_{1.03}Te$ samples increases the band gap, with direct evidence from the infrared diffuse reflectance spectroscopy and electronic structure calculations. Moreover, Mg alloying significantly tunes the electronic structure of SnTe, which essentially decreases energy difference between the light hole and heavy hole valence bands, leading to an enhanced Seebeck coefficient. As a result, *p*-type $Sn_{0.94}Mg_{0.09}Te$ sample exhibits a maximum zT of ~1.2 at ~860 K. These findings make SnTe-based materials an important contender for thermoelectric power generation, and should stimulate further investigation and optimization.

3A.2 Methods

3A.2.1 Synthesis

Tin (Alfa Aesar 99.99+ %), tellurium (Alfa Aesar 99.999+ %), and magnesium powder (Alfa Aesar 99.999+ %) were used for synthesis without further purification.

High quality crystalline ingots (~7 g) of $Sn_{1.03-x}Mg_xTe$ (x = 0-0.12) were synthesized by mixing appropriate ratios of high-purity starting materials of Sn, Mg and Te in a carbon coated quartz tube following same heating profile of chapter 2.

3A.2.2 Characterizations

Powder X-ray diffraction (PXRD) patterns for all of the samples were recorded using a Cu K_α (λ = 1.5406 Å) radiation on a Bruker D8 diffractometer. To estimate optical energy difference between valence band and conduction band optical diffuse reflectance measurement has been done with finely ground powder at room temperature using FT-IR Bruker IFS 66V/S spectrometer in a frequency range 4000-400 cm^{-1} with 2 cm^{-1} resolution and 50 scans. Absorption (α/Λ) data were calculated from reflectance data using Kubelka−Munk equations: $\alpha/\Lambda=(1-R)^2/(2R)$, where R is the reflectance, α and Λ are the absorption and scattering coefficients, respectively. The energy band gaps were derived from α/Λ vs E (eV) plots.

3A.2.3 Transport properties

Electrical conductivity and Seebeck coefficients were measured simultaneously under He atmosphere from room temperature to 873 K on a ULVAC-RIKO ZEM-3 instrument system (Details are given in chapter 1). Carrier concentrations were determined using Hall coefficient measurements at room temperature with a PPMS system. Thermal diffusivity, D, was directly measured in the range 300−873 K by using laser flash diffusivity method in a Netzsch LFA-457 (Details are given in chapter 1). The total thermal conductivity, κ_{total}, was calculated using the formula, $\kappa_{total} = DC_p\rho$.

3A.2.4 Computational details

To investigate the impact of Mg on the electronic structure of SnTe, we have collaborated with Prof. Umesh Waghmare's group at JNCASR, Bangalore, India. Density functional theoretical (DFT) electronic structure calculations of pristine SnTe and Mg alloyed SnTe were carried out using Quantum Expresso package.[13] Scalar relativistic norm conserving pseudo potentials and a Generalized Gradient Approximation (GGA) to exchange-correlation energy with functional of Perdew, Burke, and Erzenhoff (PBE) were used to perform the DFT calculations.[14] The valence electrons of Sn, Te and Mg ($5s^25p^2$, $5s^25p^4$ and $3s^2$ respectively) are included in calculations through the use of pseudo potentials. SnTe is known to crystallize in rocksalt structure, while MgTe occurs in the zinc blende structure.[15] Mg-substituted in the zinc blend site of SnTe was simulated with a tetragonal supercell ($\sqrt{2}$ x $\sqrt{2}$ x 2) containing 32 atoms. Plane wave basis for

representing wavefunctions are terminated with energy cut off of 40 Ry, and 14X14X10 mesh of k points was used in sampling Brillouin zone integrations. Electronic structure of $Sn_{16}Te_{16}$, $Sn_{15}MgTe_{16}$ and $Sn_{14}Mg_2Te_{16}$ with Mg atoms substituted for Sn atoms in SnTe is determined along high symmetry lines in the Brillouin zone, using theoretical equilibrium lattice constant of 6.417Å.

3A.3 Results & Discussion

Previously, SnTe was not considered to be a good thermoelectric material due to its very high carrier concentration (~10^{21}) resulting from intrinsic Sn vacancy.[1] Presence of non-stoichiometric defects in SnTe made it unpredictable to understand dopant's nature in SnTe.[16] Till 2014, very few strategies have been explored to reduce the n_H of SnTe. Electron donor dopant such as iodine doping in SnTe has optimized the thermoelectric properties by decreasing the carrier concentration.[17] However, presence of iodine decreases high temperature (> 700 K) Seebeck coefficient of SnTe due to electron-hole bipolar effect. Kanatzidis and co-workers have shown that self-compensation of Sn is an effective path for optimizing the thermoelectric performance of SnTe (For $Sn_{1.03}Te$, ~1.2 x 10^{20} cm^{-3}; for SnTe, ~4.5 x 10^{20} cm^{-3}).[11,12] Thus, we have studied the thermoelectric properties of Mg-alloyed self compensated SnTe ($Sn_{1.03}Te$) sample to realize high Seebeck coefficient through valence band convergence.

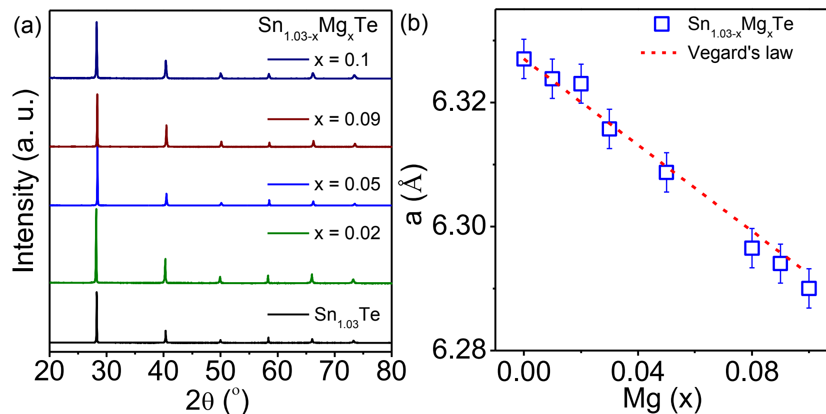

Figure 3A.1 (a) Powder XRD patterns of $Sn_{1.03-x}Mg_xTe$ (x = 0 -0.1) samples. (b) Lattice parameter (*a*) vs. Mg concentration (*x*) in $Sn_{1.03-x}Mg_xTe$ and red line indicates the Vegard's law for solid solution.

$Sn_{1.03-x}Mg_xTe$ (x=0- 0.1) samples were synthesized by vacuum sealed tube melting reaction and characterized by PXRD. Figure 3A.1a confirms the formation of single

phase nature within detection limit of PXRD and the patterns could be indexed on SnTe structure (*F*m-3m space group). As shown in figure 3A.1b, the lattice parameter decreases with increasing the Mg concentration, consistent with the smaller radius of Mg^{2+} (86 pm) compared to that of Sn^{2+} (93 pm). The linear decrease in the lattice parameter follows solid solution Vegard's law.

We could able to resolve the band gap of $Sn_{1.03-x}Mg_xTe$ (x=0-0.12) by diffuse reflectance IR spectroscopy (Figure 3A.2). With increasing Mg concentration up to 12 mol% the electronic absorption spectra of SnTe show a shift of absorption edge towards high energy. Generally, if MgTe (E_g ~3.5 eV) was dissolving in SnTe an increase in the band gap would be expected. The band gap derived from the plot show an increase from ~0.11 eV to ~0.26 eV in going from 0 mol % to 12 mole % Mg in $Sn_{1.03}Te$. This result is similar to that of MgTe alloyed with PbTe.[18] Substitution of Mg in Sn position enhances the ionic character of SnTe resulting in an enhanced band gap. Increase in the band gap with Mg incorporation in SnTe is indicating the reduction of the energy separation of light hole and heavy hole valence bands which will be discussed further in the later part of this chapter.

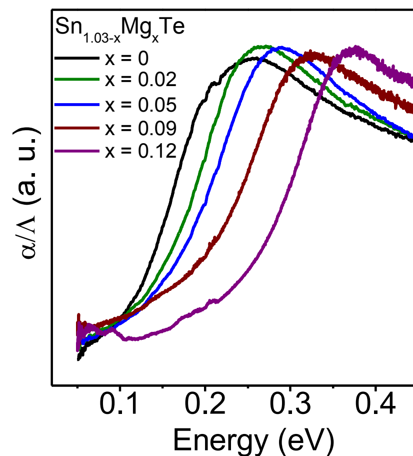

Figure 3A.2 Optical absorption spectra of $Sn_{1.03-x}Mg_xTe$.

Figure 3A.3 shows electrical transport properties of $Sn_{1.03-x}Mg_xTe$(x=0-0.1). For all samples, electrical conductivity (σ) decreases with increase in temperature which is typical of degenerate semiconductor (Figure 3A.3a). The electrical conductivity decreases with increasing Mg concentration up to 9 mol %, especially at room temperature from 9650 S/cm to 3114 S/cm (Figure 3A.3a). Typically, the room temperature σ of

$Sn_{0.94}Te_{0.09}Te$ is to be ~3114 S/cm, which decreases to 1015 S/cm at 856 K. The room temperature Hall coefficients, R_H, of all $Sn_{1.03-x}Mg_xTe$ (x=0-0.1) samples are positive, which indicates the *p*-type conduction in this system. Interestingly, carrier concentration (n_H) at 300 K increases with increasing the Mg concentration (Figure 3A.3b). Anomalous change in the carrier concentration with the increase of Mg is difficult to explain, but similar behavior has been observed recently in In doped SnTe[8] and $SnTe_{1-x}Se_x$[5] and Cd alloyed SnTe.[11] Recent report also shows the anomalous change in the carrier concentration of Hg doped SnTe.[12] Although Mg, Cd and Hg is supposed to be isovalent with Sn; Cd appears to act as electron donor, whereas Mg and Hg acts as electron acceptor. Effect of different doping on the carrier concentration of SnTe is not very clear yet. Room temperature carrier mobility (μ) decreases with Mg concentration in $Sn_{1.03-x}Mg_xTe$ (Figure 3A.3c), which is probably due to the impurity scattering and the increased effective mass of holes caused by electronic band structure modification.[5,8] Decrease in room temperature σ value with the increase in Mg doping concentration is due to the decrease in μ.

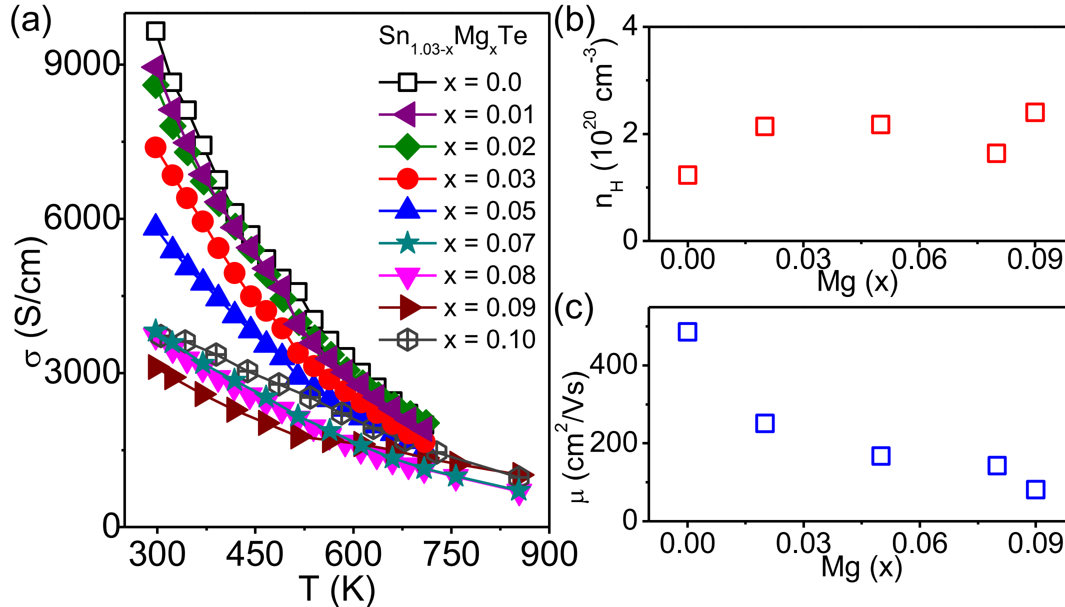

Figure 3A.3 (a) Temperature dependent electrical conductivity (σ) of $Sn_{1.03-x}Mg_xTe$ (x = 0-0.1) samples. (b) Carrier concentration (n_H) and (c) carrier mobility (μ) at room temperature with respect to Mg doping concentration (x) in $Sn_{1.03-x}Mg_xTe$.

Figure 3A.4a represents the temperature dependence of Seebeck coefficient (*S*) of $Sn_{1.03-x}Mg_xTe$ samples. The positive value of *S* indicates *p*-type conduction which supports the Hall coefficient measurement. Significant enhancement in *S* has been

achieved by Mg alloying in $Sn_{1.03}Te$, both at room temperature and high temperatures. Typically, the room temperature *S* value measured for $Sn_{0.95}Mg_{0.08}Te$ was ~38 μV/K which linearly increases to ~200 μV/K at 856 K. High temperature (~856 K) *S* values for $Sn_{0.96}Mg_{0.07}Te$, $Sn_{0.95}Mg_{0.08}Te$, $Sn_{0.94}Mg_{0.09}Te$ and $Sn_{0.93}Mg_{0.1}Te$ are 192, 200, 175 and 165 μV/K respectively. We have estimated the density of state effective mass (m^*) of $Sn_{1.03-x}Mg_xTe$ samples from the measured *S* and room temperature Hall carrier concentration (n_H).[19,20] Although the accurate calculation of m^* requires consideration of non-parabolic band and multiple band model, present calculation of m^* considers following expressions for single parabolic band for simplicity.[19,20]

$$m^* = \frac{h^2}{2k_BT}\left[\frac{n}{4\pi F_{\frac{1}{2}}(\eta)}\right]^{2/3} \tag{3A.1}$$

$$S = \frac{k_B}{e}\left[\frac{2F_1(\eta)}{F_0(\eta)} - \eta\right]^{2/3} \tag{3A.2}$$

$$F_n(\eta) = \int_0^{\infty} \frac{x^n}{1+e^{x-\eta}} \tag{3A.3}$$

Where η is the reduced Fermi energy, $F_n(\eta)$ is the nth order Fermi integral, k_B is the Boltzmann constant, *e* is the electron charge, *h* is the Plank constant. The reduced Fermi energy was extracted based on fitting the respective Seebeck data. With increasing the Mg concentration (from 0 to 9 mol%), m* increases from ~0.16 m_e to ~0.69 m_e (Table 3A.1), which further indicates the increasing contribution of the heavy hole valence band in the transport properties of $Sn_{1.03}Te$.

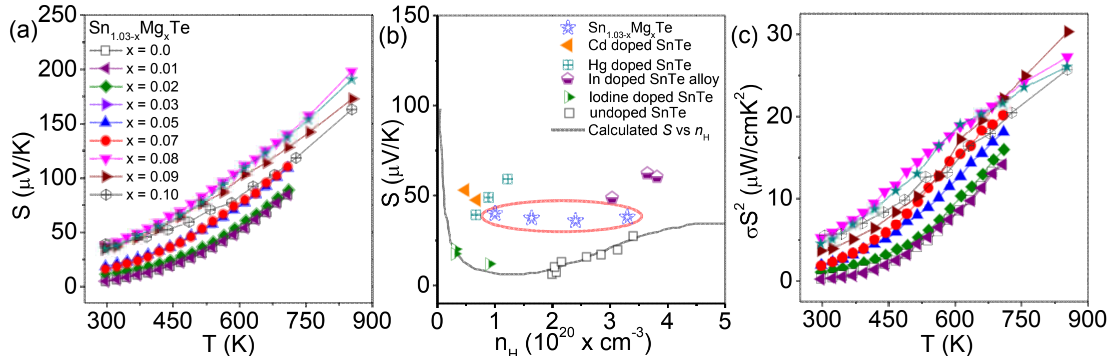

Figure 3A.4 (a) Temperature dependent Seebeck coefficient (*S*) of $Sn_{1.03-x}Mg_xTe$ samples. (b) Room temperature *S* vs. n_H plot of the present $Sn_{1.03-x}Mg_xTe$ samples. For comparison, previously reported *S* vs. n_H experimental data of undoped SnTe,[1] Cd doped SnTe,[11] In doped SnTe alloy,[5,8] Hg doped SnTe[12] and theoretical Pisarenko curve [8] are given in (b). (c) Temperature dependence of power factor (σS^2) of $Sn_{1.03-x}Mg_xTe$ [x = 0-0.1].

In figure 3A.4b, we compare the present room temperature S vs. n_H data of $Sn_{1.03-x}Mg_xTe$ samples with previously reported experimental data on In doped SnTe,[8] In doped $SnTe_{1-x}Se_x$,[5] Cd alloyed SnTe,[11] Hg alloyed SnTe,[12] iodine doped SnTe[17] and also with the earlier reported theoretical Pisarenko curves by Zhang *et al*.[8] Detailed discussion on theoretical Pisarenko plot of is given in chapter 2. Indium and Cd/Hg alloyed SnTe samples show much higher Seebeck coefficient than that of theoretical Pisarenko curve due to the effect of resonance level formation[5,8] and valence band convergence,[11] respectively. We observe that $Sn_{1.03-x}Mg_xTe$ samples also show significantly large Seebeck coefficients than that of Pisarenko curve (Figure 3A.4b) confirming modulation of electronic structure, which will be verified from electronic structure calculation, as discussed in the later part of this chapter.

Table 3A.1 Room temperature carrier concentration (n_H) and effective mass (m^*) of $Sn_{1.03-x}Mg_xTe$ samples where m_e is mass of electron.

Composition	n_H (10^{20} cm^{-3})	m^* (m_e)
$Sn_{1.03}Te$	1.2	0.16
$Sn_{1.01}Mg_{0.02}Te$	2.1	0.24
$Sn_{0.98}Mg_{0.05}Te$	2.2	0.33
$Sn_{0.96}Mg_{0.07}Te$	3.3	0.91
$Sn_{0.95}Mg_{0.08}Te$	1.6	0.55
$Sn_{0.94}Mg_{0.09}Te$	2.4	0.69
$Sn_{0.93}Mg_{0.1}Te$	1.0	0.43

In order to understand the origin of large Seebeck coefficient of Mg-alloyed $Sn_{1.03}Te$, electronic structures of SnTe and Mg-alloyed SnTe (Figure 3A.5a) have been calculated based on DFT. For $Sn_{16}Te_{16}$, $Sn_{15}MgTe_{16}$ (6 mol% Mg alloyed SnTe) and $Sn_{14}Mg_2Te_{16}$ (12 mol% Mg alloyed) systems, the principal valence band (light hole) maximum (VBM) and conduction band minima (CBM) occur at Γ point; and the heavy hole band is at $Z+\delta$ along $Z \rightarrow R$ direction. The VBM and CBM occurring at the L point in the Brillouin zone of the cubic cell of SnTe fold on to the Γ point and the heavy hole valence band appearing along Σ folds on to $Z+\delta$ in the Brillouin zone of the 32 atoms ($\sqrt{2}$ x $\sqrt{2}$ x 2) tetragonal supercell. Band gap of SnTe increases with increasing Mg alloying, consistent with the

experimental band gap measured by diffuse reflectance spectroscopy. Band gap of ~0.049 eV was obtained in the case of SnTe, which is in good agreement with previous calculation without considering spin-orbit coupling.[11] Band gap of 0.049 eV of $Sn_{16}Te_{16}$ at Γ point increases to 0.069 eV and 0.084 eV with substitution of 6 mol% and 12 mol% Mg for Sn atoms, respectively (Figure 3A.5b). This is due to the larger decrease in the energy of valence band in comparison with the conduction band at Γ point leading to the opening of the band gap (Figure 3A.5c).

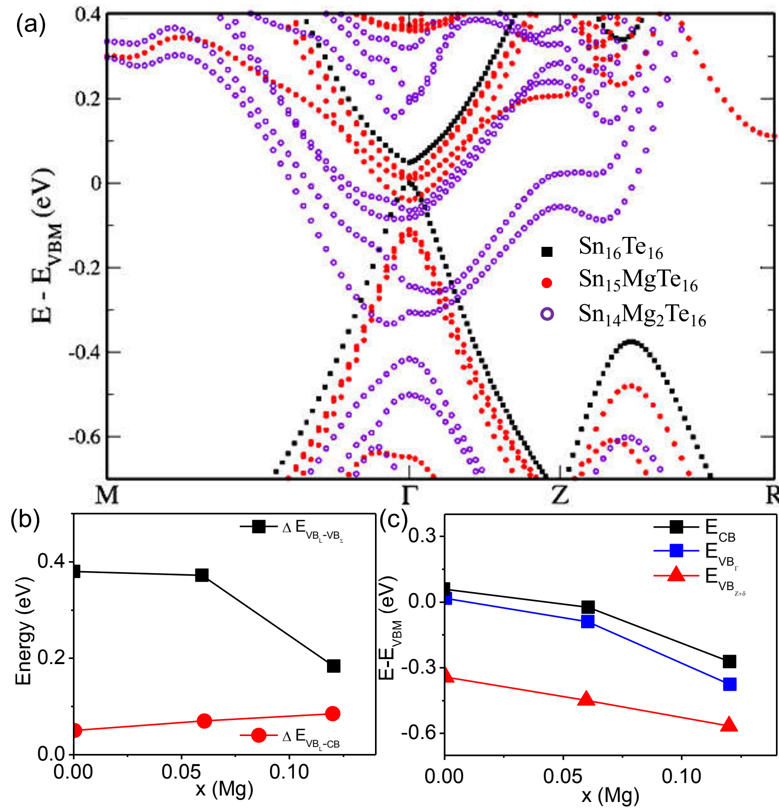

Figure 3A.5 (a) Band structures of $Sn_{16}Te_{16}$, $Sn_{15}MgTe_{16}$, $Sn_{14}Mg_2Te_{16}$ supercell as a function of wavevector in supercell brillouin zone. The energies shown are relative to the valence band maxima of $Sn_{16}Te_{16}$. The band gap appears at *Γ*-point and heavy hole band at *Z+δ* due to folding of the brillouin zone in the present supercell calculation. (b) Principal band gap and valence bands (*Γ* and *Z+δ*) energy difference as a function of concentration of Mg. (c) The energies of light hole valence band (*Γ*), heavy hole valence band (*Z + δ*) and conduction band (*Γ*) as a function of concentration of Mg in SnTe.

A significant decrease in the energy separation between the light and heavy valence band of SnTe is achieved with Mg alloying. The energy separation between the light hole and the heavy hole valence band decreases from 0.375 eV for pristine SnTe to 0.18 eV for 12 mol% Mg alloyed SnTe sample (Figure 3A.5b and Figure 3A.5c). Thus, incorporation of Mg in the SnTe leads to an increase in the valence band degeneracy. Such valence

band convergence is expected to result in enhancement of the Seebeck coefficient due to contribution from both the bands, as there is an asymmetric increase in the density of states near the Fermi energy. Similar band modification have been found in Cd/Hg alloyed SnTe[11,12] and Cd and Mg alloyed PbTe.[18,21]

Figure 3A.4c represents temperature dependent power factor (σS^2) data of $Sn_{1.03-x}Mg_xTe$(x=0-0.1) samples. Benefiting from the significant enhancement in Seebeck coefficient both in low and high temperatures, Mg alloyed $Sn_{1.03}Te$ samples have much higher power factors than the undoped $Sn_{1.03}Te$ sample, with maximum values exceeding ~30.3 μW/cmK^2 (Figure 3A.4c). Maximum power factor value obtained in the present $Sn_{1.03-x}Mg_xTe$ ingot samples are indeed higher than previously reported spark plasma sintered In and Cd/Hg alloyed SnTe samples.[8,11,12] Typically, at room temperature, σS^2 value for $Sn_{0.94}Mg_{0.09}Te$ is to be ~3.5 μW/cmK^2 which rises to ~30.3μW/ cmK^2 at ~856 K.

Figure 3A.6 present the temperature dependent thermal transport properties of $Sn_{1.03-x}Mg_xTe$ (x=0-0.1) samples. Thermal diffusivity, D, is plotted in figure 3A.6a. Room temperature C_P is in close agreement with Dulong-Petit C_p value (Figure 3A.6b). Thermal conductivity decreases with increasing Mg concentration (Figure 3A.6c). The electronic thermal conductivities, $\kappa_{el}= L\cdot\sigma\cdot T$, were extracted based on fitting of the respective Seebeck values that estimate the reduced chemical potential from which the Lorenz number, L, can be obtained as explained in detail previously (Figure 3A.6d).[18,19] Mg alloying in $Sn_{1.03}Te$ optimizes the temperature dependent κ_{total} by controlling the κ_{el} (Figure 3A.6e).

With increasing the Mg concentration κ_{total} decreases due to the systematic decrease in κ_{el}. Typically, the room temperature κ_{total} value measured for $Sn_{0.94}Mg_{0.09}Te$ is ~4.9 W/mK which decreases to ~2.2 W/m.K at 873 K. Interestingly we have not observed any systematic trend for κ_{lat} with Mg concentration in $Sn_{1.03}Te$ (Figure 3A.6f). Typically, the room temperature κ_{lat} value measured for $Sn_{0.94}Mg_{0.09}Te$ is ~2.7 W/m.K which decreases to ~0.78 W/m.K at 856 K, which is slightly higher compared to Cd/Hg alloyed SnTe samples.[29] For all the samples, heating and cooling cycles give repeatable thermoelectric properties (Figure 3A.7).

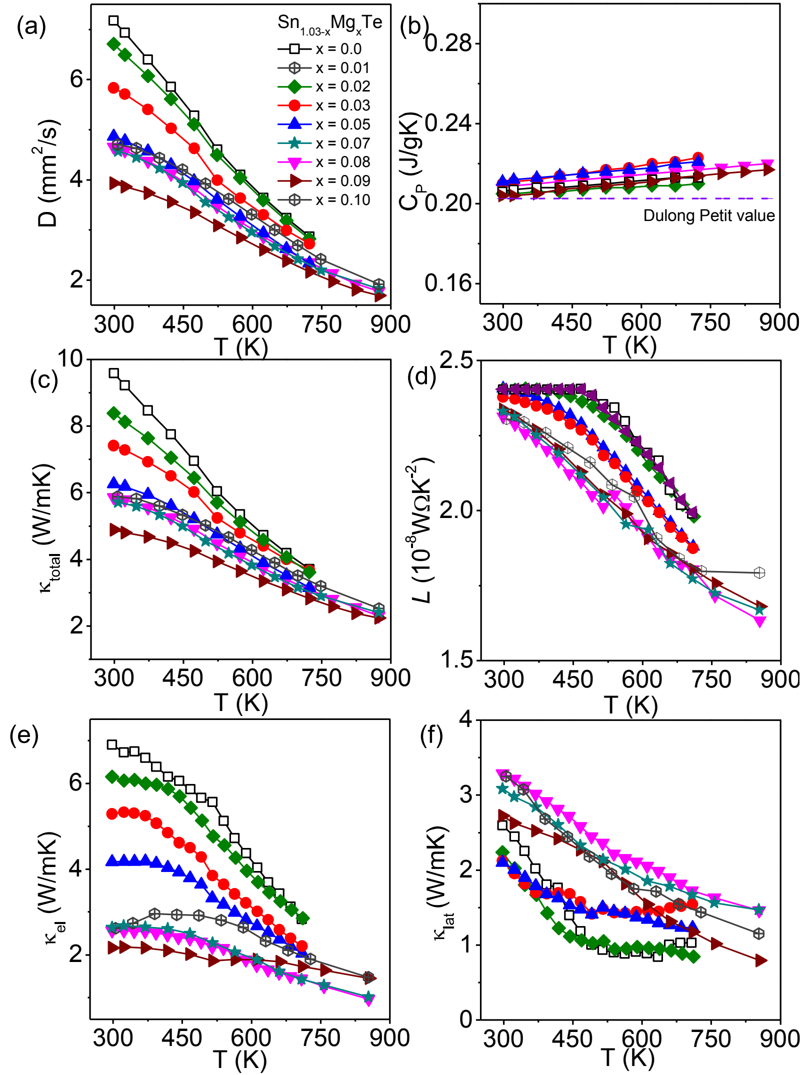

Figure 3A.6 Temperature dependent (a) thermal diffusivity (D), (b) heat capacity (C_p), (c) total thermal conductivity (κ_{total}) (d) Lorenz number (L), (e) electrical thermal conductivity (κ_{el}) and (f) lattice thermal conductivity (κ_{lat}) of $Sn_{1.03-x}Mg_xTe$ (x = 0-0.1).

In Figure 3A.7, we present temperature dependent zT of $Sn_{1.03-x}Mg_xTe$ (x=0-0.10) samples. The highest zT value of ~1.2 at 856 K was achieved for $Sn_{0.94}Mg_{0.09}Te$, which is significantly higher compared to undoped $Sn_{1.03}Te$ sample. Highest zT obtained in the present crystalline ingot sample synthesized by simple melting reaction is indeed comparable to previously reported maximum zT of spark plasma sintered Cd alloyed (zT ~ 1.3 at 873 K),[11] Hg alloyed (zT ~1.35 at 910 K)[12] and In doped (zT~1.1 at 873 K) SnTe[8] samples. Average zT, zT_{avg} of $Sn_{0.94}Mg_{0.09}Te$ is ~0.6 by considering the hot and cold end to be 860 and 300 K, respectively; which is indeed comparable to the In doped SnTe (zT_{ave} ~0.6) and Cd-doped SnTe (zT_{ave} ~0.65).

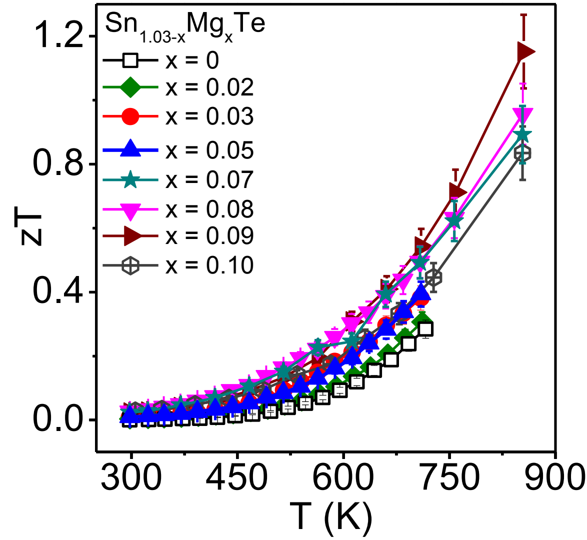

Figure 3A.7 Temperature dependent zT of $Sn_{1.03-x}Mg_xTe$.

3A.4 Conclusions

p-type SnTe can be optimized to be a good thermoelectric material for power generation by controlling the hole concentration and improving the Seebeck coefficient. Mg alloying increases the band gap of $Sn_{1.03-x}Mg_xTe$ (x=0-0.9) samples, which resulted in decrease in the energy separation between two valence bands (light and heavy hole) of SnTe. Thus, the effective convergence of the valence bands giving rise to a significant enhancement in the Seebeck coefficient resulted in a remarkable increase in the power factor of $Sn_{1.03-x}Mg_xTe$(x=0-0.1). This type of band engineering is a crucial finding of this work and is important in achieving a high figure of merit of ~1.2 at 856 K for *p*-type $Sn_{0.94}Mg_{0.09}Te$ sample. The present research suggests that SnTe-based materials are important candidates for thermoelectric power generation and provides the promise to act as an alternative of lead chalcogenides in near future.

3A.5 References

1. R. Brebrick and A. Strauss, *Phys. Rev.*, 1963, **131**, 104.
2. B. Efimova, V. Kaidanov, B. Y. Moizhes and I. Chernik, *Sov. Phys. Solid State*, 1966, **7**, 2032.
3. L. M. Rogers, *J. Phys. D: Appl. Phys.*, 1968, **1**, 845.
4. R. Brebrick, *J. Phys. Chem. Solids*, 1963, **24**, 27.
5. A. Banik and K. Biswas, *J. Mater. Chem. A*, 2014, **2**, 9620.
6. G. Tan, F. Shi, S. Hao, H. Chi, L.-D. Zhao, C. Uher, C. Wolverton, V. P. Dravid and M. G. Kanatzidis, *J. Am. Chem. Soc.*, 2015, **137**, 5100.
7. A. Andreev, *Soviet Phys. Solid State*, 1967, **9**, 1232.
8. Q. Zhang, B. Liao, Y. Lan, K. Lukas, W. Liu, K. Esfarjani, C. Opeil, D. Broido, G. Chen and Z. Ren, *Proc. Natl. Acad. Sci. USA,* 2013, **110**, 13261.
9. A. Banik, U. S. Shenoy, S. Anand, U. V. Waghmare and K. Biswas, *Chem. Mater.*, 2015, **27**, 581.
10. K. Biswas, J. He, G. Wang, S.-H. Lo, C. Uher, V. P. Dravid and M. G. Kanatzidis, *Energy Environ. Sci.*, 2011, **4**, 4675.
11. G. Tan, L.-D. Zhao, F. Shi, J. W. Doak, S.-H. Lo, H. Sun, C. Wolverton, V. P. Dravid, C. Uher and M. G. Kanatzidis, *J. Am. Chem. Soc.*, 2014, **136**, 7006.
12. G. Tan, F. Shi, J. W. Doak, H. Sun, L.-D. Zhao, P. Wang, C. Uher, C. Wolverton, V. P. Dravid and M. G. Kanatzidis, *Energy Environ. Sci.*, 2015, **8**, 267.
13. G. Paolo, B. Stefano, B. Nicola, C. Matteo, C. Roberto, C. Carlo, C. Davide, L. C. Guido, C. Matteo, D. Ismaila, C. Andrea Dal, G. Stefano de, F. Stefano, F. Guido, G. Ralph, G. Uwe, G. Christos, K. Anton, L. Michele, M.-S. Layla, M. Nicola, M. Francesco, M. Riccardo, P. Stefano, P. Alfredo, P. Lorenzo, S. Carlo, S. Sandro, S. Gabriele, P. S. Ari, S. Alexander, U. Paolo and M. W. Renata, *J. Phys.: Condens. Matter*, 2009, **21**, 395502.
14. J. P. Perdew, K. Burke and M. Ernzerhof, *Phys. Rev. Lett.*, 1996, **77**, 3865.
15. O. Michihiro, B. Kanishka, L. Shih-Han, H. Jiaqing, C. D. Young, D. V. P. and K. M. G., *Adv. Energy Mater.*, 2012, **2**, 1117.
16. E. I. Rogacheva, *J. Phys. Chem. Solids*, 2008, **69**, 259.
17. M. Zhou, Z. M. Gibbs, H. Wang, Y. Han, C. Xin, L. Li and G. J. Snyder, *Phys. Chem. Chem. Phys.*, 2014, **16**, 20741.
18. L. Zhao, H. Wu, S. Hao, C.-I. Wu, X. Zhou, K. Biswas, J. He, T. P. Hogan, C. Uher and C. Wolverton, *Energy Environ. Sci.*, 2013, ***6***, 3346.
19. S. N. Guin, A. Chatterjee, D. S. Negi, R. Datta and K. Biswas, *Energy Environ. Sci.*, 2013, **6**, 2603.
20. S. N. Guin, D. S. Negi, R. Datta and K. Biswas, *J. Mater. Chem. A*, 2014, **2**, 4324.
21. Y. Pei, A. D. LaLonde, N. A. Heinz, X. Shi, S. Iwanaga, H. Wang, L. Chen and G. J. Snyder, *Adv. Mater.*, 2011, **23**, 5674.

Chapter 3B

AgI alloying in SnTe Boosts the Thermoelectric Performance via Simultaneous Valence Band Convergence and Carrier Concentration Optimization †

Summary

SnTe was earlier assumed to be a poor thermoelectric material due to excess p-type carrier concentration and large energy separation between light and heavy hole valence bands. Here, we present the enhancement of the thermoelectric performance of p-type SnTe by Ag and I co-doping. AgI (1-6 mol%) alloying in SnTe modulates its electronic structure by increasing the band gap of SnTe, which results in decrease in the energy separation between its light and heavy hole valence bands, thereby giving rise to valence band convergence. Additionally, iodine doping in the Te sublattice of SnTe decreases the excess p-type carrier concentration. Due to significant decrease in hole concentration and reduction of the energy separation between light and heavy hole valence bands, significant enhancement in Seebeck coefficient was achieved at the temperature range of 600-900 K for $Sn_{1-x}Ag_xTe_{1-x}I_x$ *samples. A maximum thermoelectric figure of merit, zT, of ~1.05 was achieved at 860 K in high quality crystalline ingot of p-type* $Sn_{0.95}Ag_{0.05}Te_{0.95}I_{0.05}$.

† *Paper based on this study has been published in* ***J. Solid State Chem***. 2016, *242,* 43.

3B.1 Introduction

The electrical conductivity, Seebeck coefficient and electronic part of thermal conductivity are interdependent via carrier concentration (n_H).[1] Hence, significant enhancement in zT can be achieved via simultaneous optimization of n_H and modulation of electronic structure. Dopant plays an important role to tune the n_H of solid material. Although pristine SnTe was neglected by thermoelectric community over a long period of time due to its very high p-type carrier concentration ($10^{20}-10^{21}$ cm^{-3}) and a large valence band energy separation (ΔE_v ~0.35 eV),[2,3] recent studies explicitly show that SnTe has the strong potential of being a promising thermoelectric material.[4-11] SnTe has been alloyed with other metal tellurides such as $AgSbTe_2$ and $AgBiTe_2$ in order to improve its thermoelectric performance via carrier concentration optimization and reduction of thermal conductivity.[12,13] Significant enhancement in the Seebeck coefficient of SnTe has been achieved due to the formation of the resonance level in the valence band through In doping, which resulted in a zT of ~1.1 at 873 K.[4] Resonance level formation through In doping along with the increase in the contribution of heavy hole valence band through solid solution alloying significantly improved the Seebeck coefficient, which resulted in a promising zT in p-type 1.5 mol% In doped $SnTe_{0.85}Se_{0.15}$ sample.[5] The introduction of Cd, Mg, Hg or Mn in the Sn-site of SnTe is effective in achieving valence band convergence, giving rise to a notable enhancement of the Seebeck coefficient and thus the zT.[6-8,10]

After the successful utilization of Mg as a valence band convergent in SnTe (Chapter 3A), our aim was to find out the dopants which can effectively enhance the Seebeck coefficient and thermoelectric performance of SnTe via simultaneous optimization of carrier concentration and modulation of electronic structure. To tune the carrier concentration and electrical conductivity, bismuth or iodine was mostly applied as donor atoms in SnTe.[14,15] Iodine doping effectively tunes carrier concentration in the light hole valence band of SnTe.[14] However, due to presence of electron-hole bipolar effect above 600 K, only iodine doping is not sufficient to provide the expected performance in SnTe.[14] Alloying SnTe with AgI, which has larger band gap (E_g ~2.26 eV[16]) compared to that of SnTe (E_g ~0.18 eV), has the potential to optimize thermoelectric properties both via electronic structure modulation and carrier concentration optimization.

This chapter presents investigation of the effect of AgI alloying ($Sn_{1-x}Ag_xTe_{1-x}I_x$, x = 0-0.06) on the thermoelectric properties of SnTe. Substitution of I^- for Te^{2-} in SnTe

reduces carrier concentration to a value of ~5.7 x 10^{19} cm^{-3}. In addition, AgI alloying in SnTe increases the principle band gap, which was directly evidenced from the infrared diffuse reflectance spectroscopy. Thus, AgI alloying significantly tunes the electronic structure of SnTe and decreases energy difference between the light hole and heavy hole valence bands, leading to an enhanced Seebeck coefficient in the temperature range of 500-900 K. As a result, *p*-type $Sn_{0.95}Ag_{0.05}Te_{0.95}I_{0.05}$ sample exhibits a maximum *zT* of ~1.05 at ~860 K.

3B.2 Methods

3B.2.1 Synthesis

Tin (Alfa Aesar 99.99+ %), tellurium (Alfa Aesar 99.999+ %), silver iodide powder (Alfa Aesar 99.999+ %), elemental silver ((Ag, 99.999%, metal basis) and tellurium iodide (TeI_4, 99.999%, metal basis) were used for the synthesis without further purification.

High quality crystalline ingots (~7 g) of $Sn_{1-x}Ag_xTe_{1-x}I_x$ (x = 0-0.06) were synthesized by mixing appropriate ratios of high-purity starting materials of Sn, AgI and Te in a quartz tube at 900 °C following the previously mentioned SnTe heating profile (Chapter 2). $Sn_{1-x}Ag_xTe$ (x = 0.05) was synthesized via the similar procedure using stoichiometric ratios of Sn, Ag and Te. For $SnTe_{1-x}I_x$ (x = 0.05) preparation, stoichiometric ratios of Sn, Te and TeI_4 (Iodine source) were used.

3B.2.2 Characterizations

Powder X-ray diffraction (PXRD) for all of the samples were recorded using a Cu K_α (λ = 1.5406 Å) radiation on a Bruker D8 diffractometer. To estimate optical band gap, IR diffuse reflectance measurements was performed with finely ground powder at room temperature using FT-IR Bruker IFS 66 V/S spectrometer in a frequency range of 4000-400 cm^{-1} with 2 cm^{-1} resolution and 50 scans.

3B.2.3 Transport properties

Electrical conductivity (σ) and Seebeck coefficients (S) were measured simultaneously under He atmosphere from room temperature to 873 K on a ULVAC-RIKO ZEM-3

instrument system (measurement details are given in chapter 1). Carrier concentrations were determined using Hall coefficient measurements at room temperature with a PPMS system (measurement details are given in chapter 1). Thermal diffusivity, *D*, was directly measured in the range 300−873 K by using laser flash diffusivity method in a Netzsch LFA-457. The total thermal conductivity, κ_{total}, was calculated using the formula, $\kappa_{total} = DC_p\rho$.

3B.3 Results & Discussion

Crystalline ingots of $Sn_{1-x}Ag_xTe_{1-x}I_x$ (x = 0-0.06) have been prepared by simple vacuum sealed tube reaction at 900 °C and characterized by PXRD. PXRD patterns in Figure 3B.1a confirm formation of single phase within detection limit which could be indexed based on SnTe structure (*F*m-3m). The lattice parameter (shown in Figure 3B.1b) increases with increasing AgI content up to x = 0.06, (following Vegard's law type behavior, denoted by the dashed line in Figure 3B.1b) consistent with the larger radius of Ag^+ (129 pm) compared to that of Sn^+ (93 pm). The observed linear increase in the lattice parameter in $Sn_{1-x}Ag_xTe_{1-x}I_x$ (x = 0-0.06) confirms the solid solution behaviour.

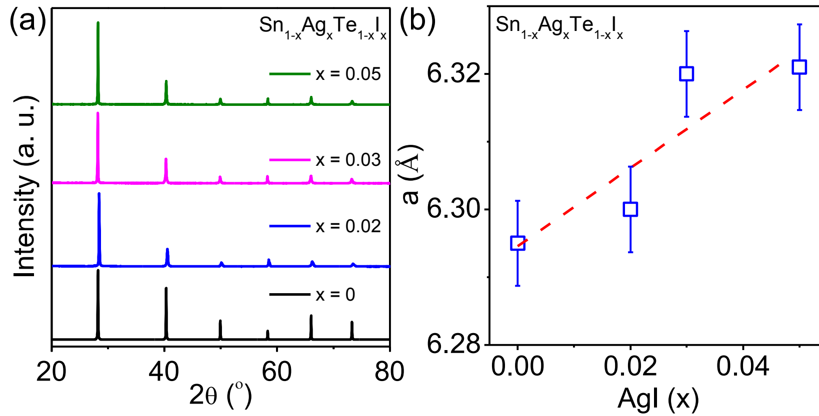

Figure 3B.1 (a) Powder XRD patterns of $Sn_{1-x}Ag_xTe_{1-x}I_x$ [x = 0-0.06]. (b) Variation of lattice parameter, *a*, with AgI concentration (*x*) in $Sn_{1-x}Ag_xTe_{1-x}I_x$ [x = 0-0.06] with 0.1% error bar. Dashed line indicates the Vegard's law for solid solution.

We have measured the band gap of $Sn_{1-x}Ag_xTe_{1-x}I_x$ by diffuse reflectance IR spectroscopy (Figure 3B.2a). With increasing AgI concentration, band gap shows a shift toward higher energy. AgI has larger band gap (E_g ~ 2.26 eV) compared to that of SnTe (E_g ~ 0.18 eV). Hence, if AgI is dissolving in SnTe matrix, an increase in the principle

band gap would be expected. The band gap derived from the plot shows an increase from ~0.09 eV to ~0.15 eV on going from 2 mol% to 5 mol% of AgI in SnTe. Although the band gap of pristine SnTe cannot be derived from the diffuse reflectance IR spectroscopy because of the strong interference from a large amount of free carriers (excess holes), the gradual shift of the absorption edges towards higher energy region upon AgI alloying indicates a systematic increase of band gap in $Sn_{1-x}Ag_xTe_{1-x}I_x$. For further understanding, we have measured absorption spectra of controlled $SnTe_{0.95}I_{0.05}$ and $Sn_{0.95}Ag_{0.05}Te$ (Figure 3B.2b). Iodine doping reduces carrier concentration[14], thus the band gap of the samples could be resolved. Measured band gap of $SnTe_{0.95}I_{0.05}$ is comparable to previously reported band gap of $Sn_{1.03}Te$[8], which confirms that the iodine doping does not affect the band gap of SnTe but reduces the *p*-type carrier concentration. Solely iodine doping does not change the band gap of SnTe, whereas solely Ag doping increases the band gap to ~0.31 eV (Figure 3B.2b). This result indicates that the increase in band gap in $Sn_{1-x}Ag_xTe_{1-x}I_x$ is mainly due to Ag substitution in Sn sublattice of SnTe. This ascending nature of band gap with incorporation of AgI in SnTe indicates the reduction of energy separation between light hole and heavy hole valence band which will be discussed in the following part of the chapter.

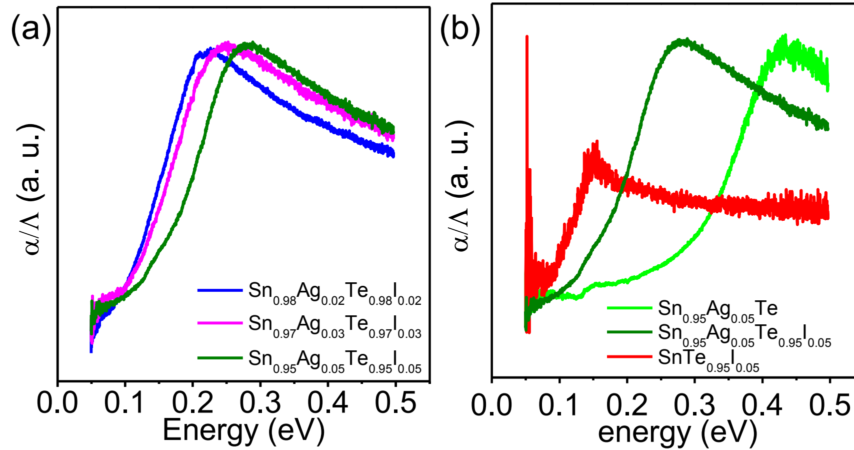

Figure 3B.2 (a) Optical absorption spectra of $Sn_{1-x}Ag_xTe_{1-x}I_x$ [x = 0-0.05] samples. (b) Optical absorption spectra of $SnTe_{0.95}I_{0.05}$, $Sn_{0.95}Ag_{0.05}Te$ and $Sn_{0.95}Ag_{0.05}Te_{0.95}I_{0.05}$.

The room temperature Hall coefficients, R_H of all $Sn_{1-x}Ag_xTe_{1-x}I_x$ (x=0-0.06) samples are positive, which indicates the *p*-type conduction in this system. Carrier concentration (n_H) and mobility (μ) of $Sn_{1-x}Ag_xTe_{1-x}I_x$ (x = 0.03, 0.05), $Sn_{1-x}Ag_xTe$ and $SnTe_{1-x}I_x$ samples are given in Table 3B.1. Ag acts as *p*-type dopant in SnTe. Hence, with Ag

incorporation in SnTe, a slight enhancement in carrier concentration has been observed compared to that of pristine SnTe. The carrier concentration of controlled $Sn_{0.95}Ag_{0.05}Te$ is 3.64 x 10^{20} cm^{-3}. Iodine acts as an *n*-type dopant in SnTe. Hence, substitution of Te sublattice with I decreases carrier concentration of SnTe from the value of 3.31 x 10^{20} cm^{-3} to 0.301 x 10^{20} cm^{-3}. Therefore, with AgI alloying, we expect a significant decrease in carrier concentration. Typically, for $Sn_{0.95}Ag_{0.05}Te_{0.95}I_{0.05}$, estimated carrier concentration is 0.57 x 10^{20} cm^{-3}, which is one order magnitude lower than that of SnTe. Interestingly, above results indicate that iodine doping decreases the *p*-type carrier concentration in SnTe [14], while Ag doping increases the band gap of SnTe, thus overall AgI alloying in SnTe should improve the thermoelectric properties of SnTe.

Table 3B.1 Room temperature carrier concentration (n_H) and carrier mobility (μ) of $Sn_{1-x}Ag_xTe_{1-x}I_x$ samples.

Composition	n_H (x 10^{20} cm^{-3})	μ (cm^2/Vs)
SnTe	3.31	157
$Sn_{0.95}Ag_{0.05}Te$	3.64	112.7
$SnTe_{0.95}I_{0.05}$	0.301	954.8
$Sn_{0.97}Ag_{0.03}Te_{0.97}I_{0.03}$	0.54	484.3
$Sn_{0.95}Ag_{0.05}Te_{0.95}I_{0.05}$	0.57	423.6

Figure 3B.3a shows the temperature dependence of electronic conductivity (σ) of $Sn_{1-x}Ag_xTe_{1-x}I_x$ samples. Electrical conductivity decreases with increasing temperature which confirms degenerate semiconducting nature of $Sn_{1-x}Ag_xTe_{1-x}I_x$. At room temperature, electrical conductivity decreases with increasing AgI concentration up to 6 mol %, from the value of ~ 8265 S/cm to ~ 3043 S/cm. Decrease in σ with the increase in AgI concentration in SnTe is attributed to decrease in hole concentration. Typically, the room temperature σ for $Sn_{0.95}Ag_{0.05}Te_{0.95}I_{0.05}$ is ~ 3906 S/cm, which decreases to 756 S/cm at 856 K.

Figure 3B.3b presents the Seebeck coefficient as a function of temperature of $Sn_{1-x}Ag_xTe_{1-x}I_x$ samples. Positive values of *S* indicates *p*-type conduction, which supports the Hall coefficient measurement. Although, room temperature Seebeck coefficient of $Sn_{1-x}Ag_xTe_{1-x}I_x$ is slightly higher compared to the Seebeck coefficient of pristine SnTe, significant enhancement has been achieved at higher temperatures (550-860 K) by AgI

alloying in SnTe. Typically, the room temperature S value measured for $Sn_{0.95}Ag_{0.05}Te_{0.95}I_{0.05}$ is ~30 μV/K which increases to ~185 μV/K at 856 K. High temperature (~856 K) S values for $Sn_{0.95}Ag_{0.05}Te_{0.95}I_{0.05}$ and $Sn_{0.97}Ag_{0.03}Te_{0.97}I_{0.03}$ are 185 μV/K and 192 μV/K, respectively. The reason behind enhancement of S can be attributed to both the decrease in carrier concentration and alloying of larger band gap AgI in SnTe.

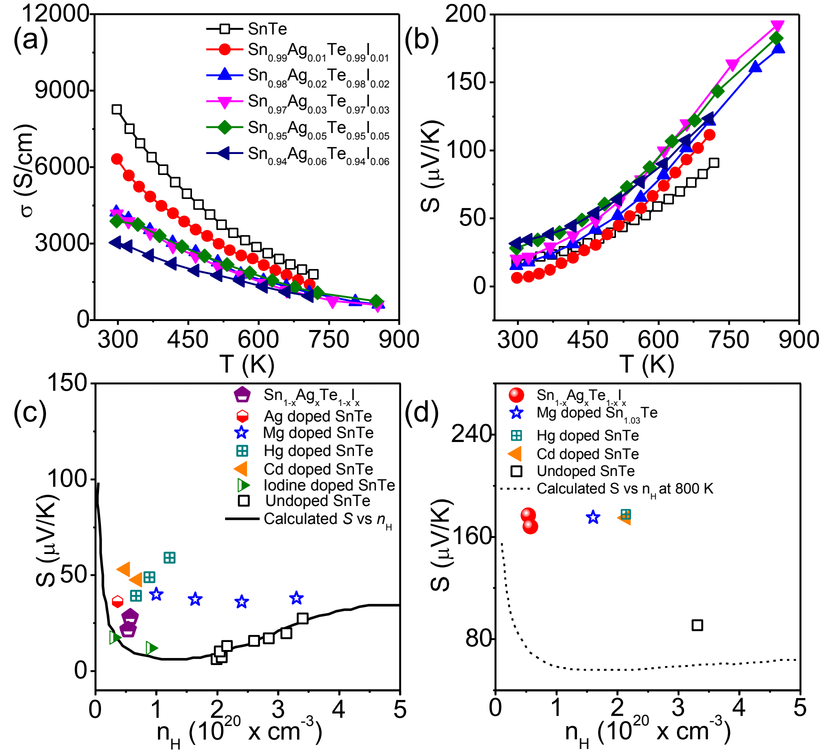

Figure 3B.3 Temperature dependent (a) electrical conductivity (σ), (b) Seebeck coefficient (S) of $Sn_{1-x}Ag_xTe_{1-x}I_x$ [x = 0-0.06] samples. (c) Room temperature S vs. n_H plot of the present $Sn_{1-x}Ag_xTe_{1-x}I_x$, Ag-doped SnTe and iodine doped SnTe samples. For comparison, previously reported S vs. n_H experimental data of un-doped SnTe,[2] Mg doped SnTe,[8] Hg doped SnTe,[7] Cd doped SnTe,[6] and theoretical Pisarenko curve based on VBM model[4] are given in (c). (d) S vs n_H plot of $Sn_{1-x}Ag_xTe_{1-x}I_x$ at 800 K. For comparison, previously reported S vs. n_H experimental data of Cd doped SnTe,[6] Hg doped SnTe, Mg doped SnTe[8] and theoretical Pisarenko curve based on VBM model[4] are given in (d).

In Figure 3B.3c, we compare the present room temperature S vs. n_H data of $Sn_{1-x}Ag_xTe_{1-x}I_x$ samples with previously reported experimental data on In doped SnTe[4], Cd alloyed SnTe[6], Hg alloyed SnTe,[7] Mg alloyed SnTe,[8] iodine doped SnTe,[14] undoped SnTe and also with the earlier reported theoretical S vs. n_H Pisarenko curve by Zhang *et al.*[4] Theoretical Pisarenko plot has been calculated previously by considering the contribution of both the light hole valence band (L point) and heavy hole valence band (Σ point) of SnTe. While the Seebeck coefficient values of undoped and iodine doped SnTe samples are following the theoretical S vs n_H curve, the previously reported Cd/Hg/Mg alloyed

SnTe samples show much higher Seebeck coefficient than that of theoretical Pisarenko curve due to valence band convergence[7]. At room temperature, the experimental thermopower (S) values for present $Sn_{1-x}Ag_xTe_{1-x}I_x$ are slightly higher than that of the Pisarenko line. However, as the temperature increases to 800 K, the S values of several $Sn_{1-x}Ag_xTe_{1-x}I_x$ compositions lies far above the corresponding high temperature Pisarenko line (Figure 3B.3d). The present high temperature S vs. n_H data of $Sn_{1-x}Ag_xTe_{1-x}I_x$ samples is comparable with previously reported experimental data of valence band converged Mg/Hg/Cd doped SnTe samples.[6-8] Higher Seebeck coefficient of AgI-containing SnTe samples than the theoretical Pisarenko curve indeed indicates modification of electronic structure of SnTe by AgI alloying. This result is indeed similar to the case of Cd/Hg/Mg/Mn doped SnTe.[6-8,10] Significantly high value of Seebeck coefficient compared to Pisarenko plot and enhancement in principle band gap in $Sn_{1-x}Ag_xTe_{1-x}I_x$ confirm that the decrease in energy separation between light hole (L point of the Brillouin zone) and heavy hole (Σ point) valence band in SnTe by AgI alloying.

Temperature dependent power factor (σS^2) data of $Sn_{1-x}Ag_xTe_{1-x}I_x$ samples are presented in Figure 3B.4. Typically, at room temperature, σS^2 value for $Sn_{0.95}Ag_{0.05}Te_{0.95}I_{0.05}$ is ~ 3.05 μW/cmK^2 which rises to ~25 μW/cmK^2 at ~ 856 K. Benefiting from the significant enhancement in Seebeck coefficient, AgI alloyed SnTe samples posses much higher power factors than that of the pristine SnTe sample.

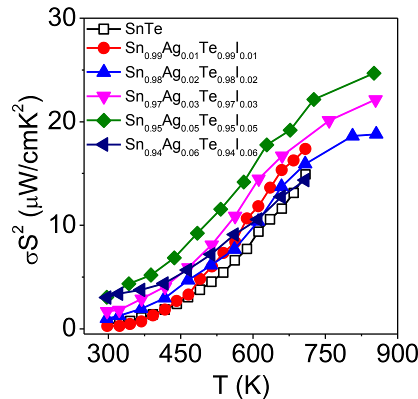

Figure 3B.4 Temperature dependent power factor (σS^2) of $Sn_{1-x}Ag_xTe_{1-x}I_x$ [x = 0-0.06] samples.

In Figure 3B.5, we present temperature dependent thermal transport properties of $Sn_{1-x}Ag_xTe_{1-x}I_x$ samples. With increasing the AgI concentration, κ_{total} (Figure 3B.5c) decreases. Typically for SnTe, room temperature κ_{total} is ~ 8.63 W/mK, which decreases to 5.2 W/mK for $Sn_{0.95}Ag_{0.05}Te_{0.95}I_{0.05}$. This decrease mostly corresponds to decrease of

electronic part of thermal conductivity. The electronic thermal conductivities, $\kappa_{el} = L \cdot \sigma \cdot T$, were extracted based on fitting of the respective Seebeck values that estimate the reduced chemical potential from which the Lorenz number, L (Figure 3B.5d) can be obtained as explained in detail in chapter 1.[17] Both κ_{total} and κ_{el} decreases with increasing temperature for the all samples. Typically, for $Sn_{0.95}Ag_{0.05}Te_{0.95}I_{0.05}$, κ_{total} decreases from 5.2 W/mK to 2 W/mK at 873 K temperature. The κ_{lat} has been obtained after subtracting the electronic part, κ_{el}, from the κ_{total} (Figure 3B.5f). We have not observed any systematic trend for κ_{lat} with increasing AgI concentration in SnTe. This behavior is well known with other doping in SnTe lattices[18]. The room temperature κ_{lat} value measured for $Sn_{0.99}Ag_{0.01}Te_{0.99}I_{0.01}$ is ~ 3 W/mK which decreases to ~0.85 W/mK at 700 K.

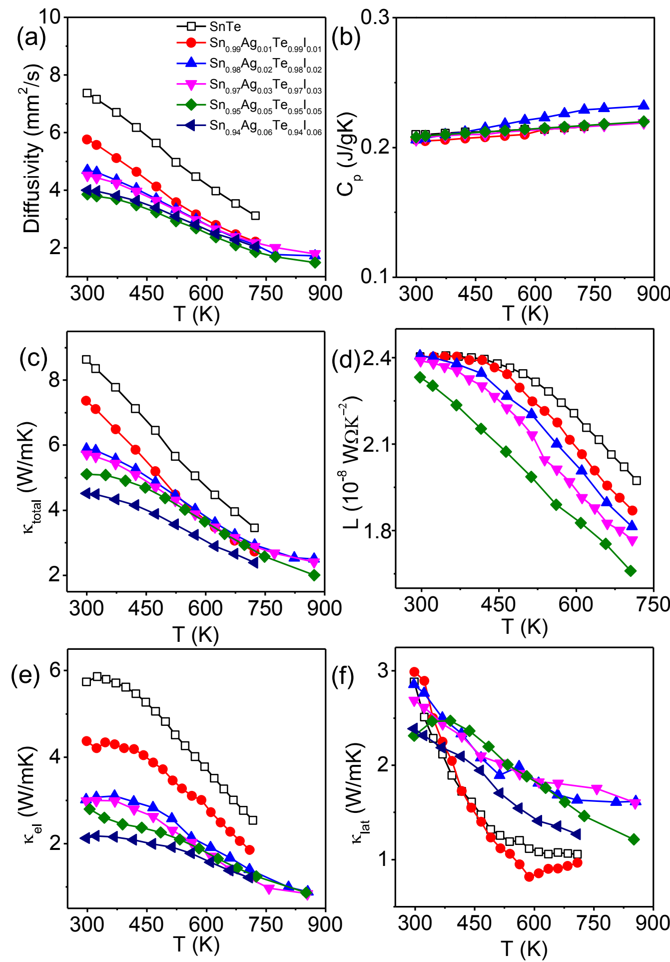

Figure 3B.5 Temperature dependent (a) thermal diffusivity (D), (b) heat capacity (C_p) (c) total thermal conductivity (κ_{total}), (d) Lorenz number (L), (e) electronic thermal conductivity (κ_{el}) and (f) lattice thermal conductivity (κ_{lat}) of $Sn_{1-x}Ag_xTe_{1-x}I_x$ [x =0-0.06].

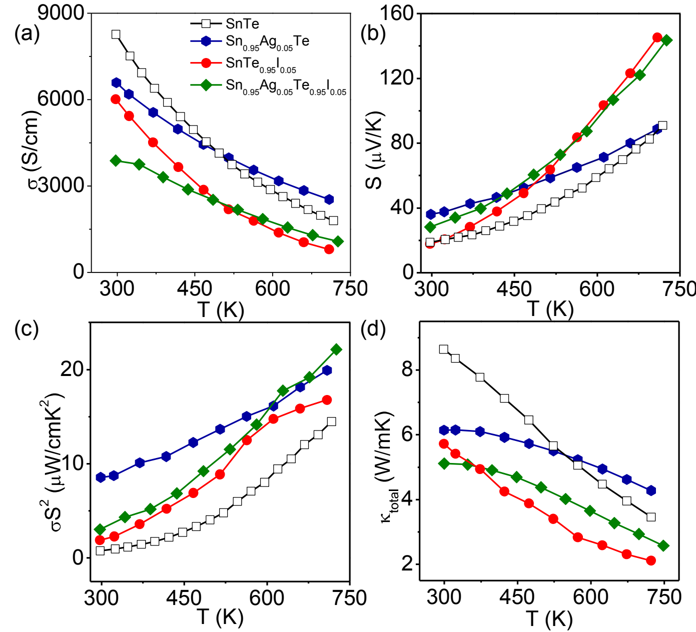

Figure 3B.6 Temperature dependent (a) electrical conductivity (σ), (b) Seebeck coefficient (S), (c) power factor (σS^2) and (d) total thermal conductivity (κ_{total}) data of SnTe, $Sn_{0.95}Ag_{0.05}Te$, $SnTe_{0.95}I_{0.05}$ and $Sn_{0.95}Ag_{0.05}Te_{0.95}I_{0.05}$.

In order to further understand individual effect of Ag and iodine on the transport properties of SnTe, we have measured transport properties of controlled samples, SnTe, $Sn_{0.95}Ag_{0.05}Te$ and $SnTe_{0.95}I_{0.05}$ and have compared with the $Sn_{0.95}Ag_{0.05}Te_{0.95}I_{0.05}$ (Figure 3B.6). Due to presence of large number of *p*-type carrier (n_H ~ 3.64 x 10^{20} cm^{-3}) in $Sn_{0.95}Ag_{0.05}Te$, we have observed significantly high value of electrical conductivity which decreases for $SnTe_{0.95}I_{0.05}$ and $Sn_{0.95}Ag_{0.05}Te_{0.95}I_{0.05}$ (Figure 3B.6a). This result indicates iodine doping solely plays important role in optimizing carrier concentration in $Sn_{0.95}Ag_{0.05}Te_{0.95}I_{0.05}$. The $Sn_{0.95}Ag_{0.05}Te$ sample possesses a Seebeck coefficient of ~36 μV/K at room temperature. Interestingly, the room temperature Seebeck coefficient decreases gradually from $Sn_{0.95}Ag_{0.05}Te$ to $Sn_{0.95}Ag_{0.05}Te_{0.95}I_{0.05}$ to $SnTe_{0.95}I_{0.05}$ despite of the reduced hole concentration in AgI and $SnTe_{1-x}I_x$, which is opposite from the usual behavior expected for a *p*-type semiconductor (Figure 3B.6b). Similarly, the band gap value also decreases systematically from $Sn_{0.95}Ag_{0.05}Te$ to $Sn_{0.95}Ag_{0.05}Te_{0.95}I_{0.05}$ to $SnTe_{0.95}I_{0.05}$ (Figure 3B.2b). Thus, Ag doping increases the band gap of SnTe, which gives rise to valence band convergence and high Seebeck coefficient in $Sn_{0.95}Ag_{0.05}Te$ and $Sn_{0.95}Ag_{0.05}Te_{0.95}I_{0.05}$. Although, $Sn_{0.95}Ag_{0.05}Te_{0.95}I_{0.05}$ sample shows slightly lower Seebeck coefficient value compared to that of $Sn_{0.95}Ag_{0.05}Te$ sample at room temperature, the Sebeeck value of $Sn_{0.95}Ag_{0.05}Te_{0.95}I_{0.05}$ rises at faster rate compared to that of

$Sn_{0.95}Ag_{0.05}Te$ when temperature rises above 475 K. The faster rise of the Seebeck coefficient in $Sn_{0.95}Ag_{0.05}Te_{0.95}I_{0.05}$ above 475 K is attributed to the increasing contribution of the heavy hole Σ band at high temperatures. Crossover point at ~475 K in *S* vs. *T* data denotes the crossover of light (*L*) to heavy (*Σ*) hole valence band and above 475 K electrical transport in SnTe is mainly contributed by heavy hole valence band.[6] At high temperature above 475 K, only heavy hole band (*Σ*) contributes to the electronic transport for $Sn_{0.95}Ag_{0.05}Te_{0.95}I_{0.05}$ (due to low n ~ 0.57 x 10^{20} cm^{-3}), whereas both light (*L*) and heavy hole (*Σ*) bands contribute in $Sn_{0.95}Ag_{0.05}Te$ due lowering of Fermi energy (high n ~ 3.64 x 10^{20} cm^{-3}). Similar crossover in *S* vs. *T* data was earlier observed in Na doped $Pb_{0.6}Sn_{0.4}Te$.[19]

Figure 3B.7 shows temperature dependent *zT* of $Sn_{1-x}Ag_xTe_{1-x}I_x$ samples. AgI alloying in SnTe shows significant improvement in the *zT* due to increase in power factor and decrease in electronic thermal conductivity. The highest *zT* value of ~1.05 was obtained for $Sn_{0.95}Ag_{0.05}Te_{0.95}I_{0.05}$ sample at 856 K. Highest *zT* obtained in the present crystalline ingot sample is higher than previously reported maximum *zT* of hot pressed $SnTe_{0.985}I_{0.015}$ (*zT* ~ 0.6 at 700 K) [14] and $(Ag_{0.366}Sb_{0.558}Te)_{1-x}(SnTe)_x$ alloys (*zT* ~0.8 at 610 K, for x = 50-60%)[12]. Mention must be made that *zT* vs *T* curve of only iodine doped SnTe sample passes through a maxima at 700 K[14], whereas *zT* vs *T* curve of AgI doped SnTe rises further up to 856 K, which supports increase of band gap in AgI doped SnTe.

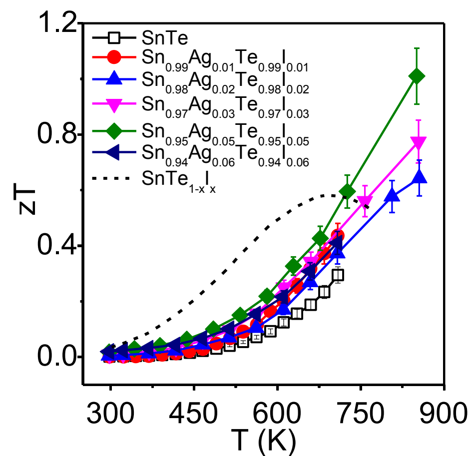

Figure 3B.7 Temperature dependent figure of merit (*zT*) of $Sn_{1-x}Ag_xTe_{1-x}I_x$ samples[x =0-0.06].

3B.4 Conclusions

AgI alloying in SnTe improves the thermoelectric performance by simultaneous optimization of *p*-type carrier concentration and valence band convergence. Substitution of iodine in the Te sublattice of SnTe reduces excess hole concentration, which is indeed a key requirement for optimization of the thermoelectric properties of SnTe. Co-doping strategy successfully leads to significant Ag alloying in SnTe. Moreover, band gap of SnTe increases due to alloying of larger band gap AgI, which resulted decrease in the energy separation between two valence bands (light and heavy hole) of SnTe. Thus, effective convergence of the valence bands and carrier concentration optimization giving rise to significant enhancement in the Seebeck coefficient, resulted in significant increase in power factor of $Sn_{1-x}Ag_xTe_{1-x}I_x$ (x=0-0.06). These multiple beneficial effects of AgI alloying in SnTe yield a high thermoelectric figure of merit of ~1.05 at 856 K for *p*-type $Sn_{0.95}Ag_{0.05}Te_{0.95}I_{0.05}$ sample. Present research suggests that SnTe-based materials are important candidates for thermoelectric power generation and provides the promise to act as an alternative of lead chalcogenides in near future.

3B.5 References

1. G. J. Snyder and E. S. Toberer, *Nat. Mater.*, 2008, **7**, 105.
2. R. Brebrick and A. Strauss, *Phys. Rev.*, 1963, **131**, 104.
3. R. Brebrick, *J. Phys. Chem. Solids*, 1963, **24**, 27.
4. Q. Zhang, B. Liao, Y. Lan, K. Lukas, W. Liu, K. Esfarjani, C. Opeil, D. Broido, G. Chen and Z. Ren, *Proc. Natl. Acad. Sci. USA,* 2013, **110**, 13261.
5. A. Banik and K. Biswas, *J. Mater. Chem. A*, 2014, **2**, 9620.
6. G. Tan, L.-D. Zhao, F. Shi, J. W. Doak, S.-H. Lo, H. Sun, C. Wolverton, V. P. Dravid, C. Uher and M. G. Kanatzidis, *J. Am. Chem. Soc.*, 2014, **136**, 7006.
7. G. Tan, F. Shi, J. W. Doak, H. Sun, L.-D. Zhao, P. Wang, C. Uher, C. Wolverton, V. P. Dravid and M. G. Kanatzidis, *Energy Environ. Sci.*, 2015, **8**, 267.
8. A. Banik, U. S. Shenoy, S. Anand, U. V. Waghmare and K. Biswas, *Chem. Mater.*, 2015, **27**, 581.
9. G. Tan, F. Shi, S. Hao, H. Chi, L.-D. Zhao, C. Uher, C. Wolverton, V. P. Dravid and M. G. Kanatzidis, *J. Am. Chem. Soc.*, 2015, **137**, 5100.
10. G. Tan, F. Shi, S. Hao, H. Chi, T. P. Bailey, L.-D. Zhao, C. Uher, C. Wolverton, V. P. Dravid and M. G. Kanatzidis, *J. Am. Chem. Soc.*, 2015, **137**, 11507.
11. J. He, X. Tan, J. Xu, G. Liu, H. Shao, Y. Fu, X. Wang, Z. Liu, J. Xu, H. Jiang and J. Jiang, *J. Mater. Chem. A*, 2015, **3**, 19974.
12. Y. Chen, M. D. Nielsen, Y.-B. Gao, T.-J. Zhu, X. Zhao and J. P. Heremans, *Adv. Energy Mater.*, 2012, **2**, 58.
13. G. Tan, F. Shi, H. Sun, L.-D. Zhao, C. Uher, V. P. Dravid and M. G. Kanatzidis, *J. Mater. Chem. A*, 2014, **2**, 20849.
14. M. Zhou, Z. M. Gibbs, H. Wang, Y. Han, C. Xin, L. Li and G. J. Snyder, *Phys. Chem. Chem. Phys.*, 2014, **16**, 20741.
15. V. P. Vedeneev, S. P. Krivoruchko and E. P. Sabo, *Semiconductors*, 1998, **32**, 241.
16. S. Ves, D. Glötzel, M. Cardona and H. Overhof, *Phys. Rev. B*, 1981, **24**, 3073.
17. L.-D. Zhao, S.-H. Lo, J. He, H. Li, K. Biswas, J. Androulakis, C.-I. Wu, T. P. Hogan, D.-Y. Chung, V. P. Dravid and M. G. Kanatzidis, *J. Am. Chem. Soc.*, 2011, **133**, 20476.
18. E. I. Rogacheva, *J. Phys. Chem. Solids*, 2008, **69**, 259.
19. S. Roychowdhury, U. S. Shenoy, U. V. Waghmare and K. Biswas, *Angew. Chem., Int. Ed.*, 2015, **54**, 15241.

CHAPTER 4

Synergistic Effect of Resonance Level and Valence Band Convergence in Enhancing Thermoelectric Properties of SnTe

Chapter 4A

High Power Factor and Enhanced Thermoelectric Performance of SnTe-$AgInTe_2$: Synergistic Effect of Resonance Level and Valence Band Convergence†

Summary

Understanding the basis of electronic transport and development of ideas to improve thermoelectric power factor is essential for production of efficient thermoelectric materials. Here, we present a significantly large thermoelectric power factor of ~31.4 μW/cmK^2 *at 856 K in Ag & In co-doped SnTe (i.e.* $SnAg_xIn_xTe_{1+2x}$*). This is the highest power factor so far reported for SnTe based materials, which arises from the synergistic effect of Ag and In on the electronic structure and improved electrical transport properties of SnTe. In and Ag play different but complementary roles in modifying the valence band structure of SnTe. In-doping introduces resonance levels inside the valence bands, leading to a significant improvement in Seebeck coefficient at room temperature. On the other hand, Ag-doping reduces the energy separation of light and heavy hole valence bands by widening of the principal band gap, which results in improved Seebeck coefficient. Additionally, Ag doping in SnTe enhances the p-type carrier mobility. Co-doping of the In and Ag in SnTe yields synergistically enhanced Seebeck coefficient and power factor over a wide range of temperature because of synergy of the introduction of resonance state and convergence of valence bands, which have been confirmed by first-principles density functional theory based electronic structure calculations. In consequence, we have achieved an improved thermoelectric figure of merit, zT, of ~1 in* $SnAg_{0.025}In_{0.025}Te_{1.05}$ *at 856 K.*

---

†*Paper based on this study has been published in* ***J. Am. Chem. Soc***. 2016*, 2,* 9602.

4A.1 Introduction

Modulation of electronic structure modulation is essential to achieve large power factor (σS^2), which evaluates the ability of a material to extract electrical power from a given temperature differences. Approaches to improve the power factor comprise enhancement of the Seebeck coefficient (*S*) through convergence of degenerate valleys of electronic bands,[1,2] formation of resonance level near Fermi level[3,4] and carrier engineering.[5,6] Pristine SnTe exhibit σS^2 0.46 μW/cmK^2 at room temperature, which increases to a value of 15 μW/cmK^2 at 710 K. Doping of Cd, Mg, Hg, Mn and Ca in SnTe provides efficient valence band convergence, which results in a significant enhancement of the Seebeck coefficient of SnTe.[7-11] Introduction of indium (In) in SnTe creates resonance levels in the valence band, as described in chapter 2.[4,12-14] Although the formation of resonance level in the valence band of SnTe enhances the Seebeck coefficients significantly at room temperature, the increase in its Seebeck at high temperature is not extraordinary.[15] In chapter 3B, we have shown that Ag doping in SnTe widens the principal band gap of SnTe, which provides significant valence band convergence and minimization of the number of the minority carriers at elevated temperature (less bipolar conduction). Hence, In and Ag have distinct but complementary roles, and co-doping of Ag and In in SnTe may results in synergistic enhancement in Seebeck coefficient and power factor. Coexistences of the resonance level induced by In doping and valence band convergence enabled by the Cd doping have been proved to be a powerful technique to improve thermoelectric efficiency of SnTe.[15] Understanding developed in these works has motivated us to study the thermoelectric properties of SnTe-$AgInTe_2$.

This chapter demonstrates the synergistic effect of In and Ag on the electronic structure and thermoelectric properties of SnTe-$AgInTe_2$ (i.e. $SnAg_xIn_xTe_{1+2x}$) ingots, where In doping creates resonance levels and valence band convergence is enabled by Ag doping in *p*-type SnTe. Electronic structure determined with first-principles density functional theoretical shows the simultaneous formation of resonance level and valence band convergence in $SnAg_xIn_xTe_{1+2x}$, which indeed support the experimental thermoelectric data. We have achieved a synergistic enhancement of Seebeck coefficient in $SnAg_xIn_xTe_{1+2x}$ over a broad temperature range (300−860 K) compared to that of controlled In doped SnTe and Ag doped SnTe. Moreover, co-doping of In and Ag

significantly tunes the electronic transport properties of SnTe leading to power factor (σS^2) of ~31.4 μW/cmK^2, which is the highest among those obtained for SnTe based materials till 2016. As a consequence, we have achieved maximum zT of ~1 at 856 K for In and Ag co-doped SnTe, which is significantly higher than that of the controlled ingots of In doped SnTe and Ag doped SnTe.

4A.2 Methods

4A.2.1 Synthesis

Sn shots (99.99+ %, Alfa Aesar), Te chunks (99.999+ %, Alfa Aesar), Ag shots (99.999%, metal basis, Alfa Aesar) and In shots (99.99+ %, In, Alfa Aesar) were used for the synthesis of $SnAg_xIn_xTe_{1+2x}$, controlled Ag-doped SnTe and controlled In-doped SnTe.

In order to synthesize crystalline ingots (~7 g) of $SnAg_xIn_xTe_{1+2x}$ (x = 0-0.04), we have taken Sn, Te, In and Ag in a quartz tube according to the desired nominal. The tubes were sealed under vacuum (10^{-5} Torr) and slowly heated to 900 ^{o}C in 10 hrs and kept at the same temperature for 10 hrs. Then it was slowly cooled to room temperature over 12 hrs.

4A.2.2 Characterizations

Powder X-ray diffraction (PXRD) for all of the samples were recorded using a Cu K_α (λ = 1.5406 Å) radiation on a Bruker D8 diffractometer.

4A.2.3 Transport properties

Electrical conductivity and Seebeck coefficients were measured simultaneously under He atmosphere from room temperature to 873 K on a ULVAC-RIKO ZEM-3 instrument system (Details are given in chapter 1). Carrier concentrations were determined using Hall coefficient measurements at room temperature with equipment made by Excel instrument. Four-contact Hall-bar geometry was used for the measurement and a varying magnetic field up to 0.57 Tesla was applied during the measurements. At 300 K, we have estimated the carrier concentration, n_H, from the formula: $n_H=1/eR_H$, where e is the electronic charge, R_H is Hall coefficient. Thermal diffusivity, D, was directly measured in

the range of 300−873 K by using laser flash diffusivity method in a Netzsch LFA-457. The total thermal conductivity, κ_{total}, was calculated using the formula, $\kappa_{total} = DC_p\rho$ (Details are given in chapter 1).

4A.2.4 Computational details

To investigate the impact of Ag & In codoping on the electronic structure of SnTe, we have collaborated with Prof. Umesh Waghmare's group at JNCASR, Bangalore, India. Electronic structure of Ag & In co-doped SnTe, controlled Ag doped SnTe, controlled In doped SnTe and undoped SnTe were determined by density functional theory (DFT) based first-principles calculations using Quantum Espresso package.[16] Since the atoms in these compounds have fairly high atomic numbers and masses, the relativistic effects cannot be neglected, and we have included the effects of spin-orbit coupling to elucidate realistic electronic structure. Fully relativistic ultra-soft pseudopotentials and a Generalized Gradient Approximated (GGA) exchange-correlation energy with parametrized functional of Perdew, Burke, and Erzenhoff (PBE) were used.[17] Valence and semicore electronic states of Sn, Te, Ag and In (in $4d^{10}$ $5s^2$ $5p^2$, $4d^{10}$ $5s^2$ $5p^4$, $4d^{10}$ $5s^1$ and $4d^{10}$ $5s^2$ $5p^1$ configurations respectively) were treated in valence through use of these pseudopotentials. SnTe is known to crystallize in the rocksalt structure with two atoms per unit cell and Fm-3m space group. Ag & In co-doped SnTe, controlled Ag doped SnTe, controlled In doped SnTe and undoped SnTe were simulated with a tetragonal ($\sqrt{2}$ x $\sqrt{2}$ x 2) supercell containing 32 atoms. Ag was substituted for Sn in the zincblende site of SnTe and indium was substituted for Sn in the rocksalt site of SnTe in the supercell. We have considered the defect pairs in fourth nearest neighbor positions in the Sn sublattice for the In and Ag co-doped SnTe. Kohn-Sham wave functions and charge density were represented with a plane wave basis truncated with energy cutoffs of 50 and 400 Ry respectively. 14x14x10 mesh of k points was used in sampling Brillouin zone integrations (such fine mesh is necessary because of many states near gap or E_F have nontrivial dispersion). The discontinuity in occupation numbers of electronic states was smeared using Gaussian function with a width (k_BT) of 0.003 Ry. Electronic spectra were determined at Bloch vectors along high symmetry lines (Γ - X - M - Γ - Z - R - A - Z) in the Brillouin zone.

4A.3 Results & Discussion

The crystalline ingots of SnTe and $SnAg_xIn_xTe_{1+2x}$ (x = 0-0.04) have been synthesized *via* solid state melting reaction at 900 °C followed by slow cooling. Figure 4A.1a shows PXRD pattern of $SnAg_xIn_xTe_{1+2x}$ (x= 0 -0.03) where all Bragg's diffraction peaks can be indexed based on the cubic SnTe, with Fm-3m space group. Lattice parameter of $SnAg_xIn_xTe_{1+2x}$ samples decreases with increasing $AgInTe_2$ content, which is consistent with the difference in lattice parameters of SnTe (6.325 Å) and $AgInTe_2$ (6.02 Å) (Figure 4A.1b). Linear decrease in the lattice parameter with increased concentration of $AgInTe_2$ and higher angle shift of PXRD peak confirms solid solution nature of $SnAg_xIn_xTe_{1+2x}$ samples.

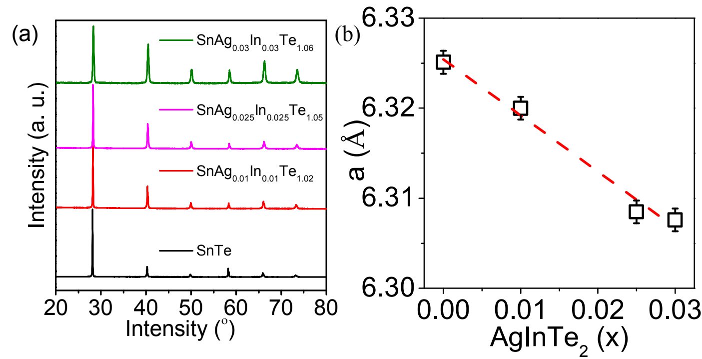

Figure 4A.1 (a) Powder XRD patterns of $SnAg_xIn_xTe_{1+2x}$ (x = 0-0.03) samples. (b) Variation of lattice parameter (a) with $AgInTe_2$ concentration (x) in $SnAg_xIn_xTe_{1+2x}$ [x = 0-0.03] with 0.1% error bar. Dashed line indicates the Vegard's law for solid solution.

In Figure 4A.2a, we present electrical conductivity (σ) of $SnAg_xIn_xTe_{1+2x}$ (x= 0.0-0.04) in 300-860K range. σ steadily decreases with increasing temperature confirming degenerate semiconducting behavior of all the $SnAg_xIn_xTe_{1+2x}$ samples. The room-temperature σ decreases with increasing $AgInTe_2$ concentration, which can be attributed to reduced carrier mobility of samples. Typically, the room temperature σ for $SnAg_{0.01}In_{0.01}Te_{1.02}$ is ~1668 S/cm, which decreases to 957 S/cm at 707 K. To estimate the carrier type and concentration, room temperature Hall measurements were carried out for all $SnAg_xIn_xTe_{1+2x}$ samples, controlled Ag doped SnTe and controlled In doped SnTe. Hole conduction (p-type) in all the samples was confirmed by the positive values of R_H. The resultant carrier concentration n_H and mobility μ are plotted in Figure 4A.2b and 4A.2c respectively. Hole concentration shows an interesting trend with increased $AgInTe_2$ concentration; it drops below the intrinsic value in the beginning, and starts to increase

when x > 0.01. For small concentration of $AgInTe_2$, Ag and In mainly occupy Sn vacancies.[4,15,18] SnTe is a typical nonstoichiometric compound with inherent Sn vacancies.[19] Thus the co-doping of In and Ag in SnTe reduce the Sn vacancies when the concentration of co-dopant is small. As the doping level is increased, however once all the Sn vacancies are filled, remaining In/Ag acts as acceptor, and the *p*-type carrier density increases. Similar types of behavior have been observed in SnTe based system where In or Ag atoms first act as donor dopant followed by its *p*-type nature.[4,18] Controlled 2.5 mol% In doped SnTe sample does not change the *p*-type carrier concentration in SnTe, but higher concentration of In doping in SnTe is known to increase the *p*-type carrier concentration.[4] Controlled 2.5 mol% Ag doped SnTe sample exhibits lower *p*-type carrier concentration compared to SnTe due to reduction of Sn vacancies by Ag doping, but higher concentration of Ag doping increases the *p*-type carrier concentration.

Carrier mobility, defined as $\mu = \sigma/n_H e$, at room temperature is plotted as function of dopant concentration in Figure 4A.2c. Pristine SnTe has a hole mobility of ~160 cm^2/Vs at 300 K, which together with its high hole density produces a large electrical conductivity of ~8269 S/cm at room temperature. Upon co-doping of In and Ag, carrier mobility, μ decreases significantly due to solid solution point defect scattering and possibly due to impurity scattering caused by In doping,[4,14] which together lead to the declined electrical conductivity described above. However, controlled Ag doping increases the carrier mobility in SnTe (Figure 4A.2c). Thus, the contrasting but beneficial effect of In and Ag is indeed important in overall enhancement of the thermoelectric performance of SnTe.

The weaker temperature dependence of electrical conductivity of $SnAg_xIn_xTe_{1+2x}$ can be attributed to reduced carrier-phonon scattering which results in higher σ at T>750 K compared to that of the pristine SnTe (Figure 4A.2a).[13] In order to understand the effects of Ag and In, electrical transport properties of controlled Ag doped SnTe and controlled In doped SnTe have been analyzed separately (Figure 4A.2d). In 2.5 mol% Ag-doped SnTe, we have observed significantly high value of electrical conductivity which decreases for 2.5 mol% indium-doped SnTe and $SnAg_xIn_xTe_{1+2x}$. In and Ag co-doped

samples have intermediate value of conductivity, which can be attributed to intermediate carrier concentration and mobility of $SnAg_xIn_xTe_{1+2x}$ samples.

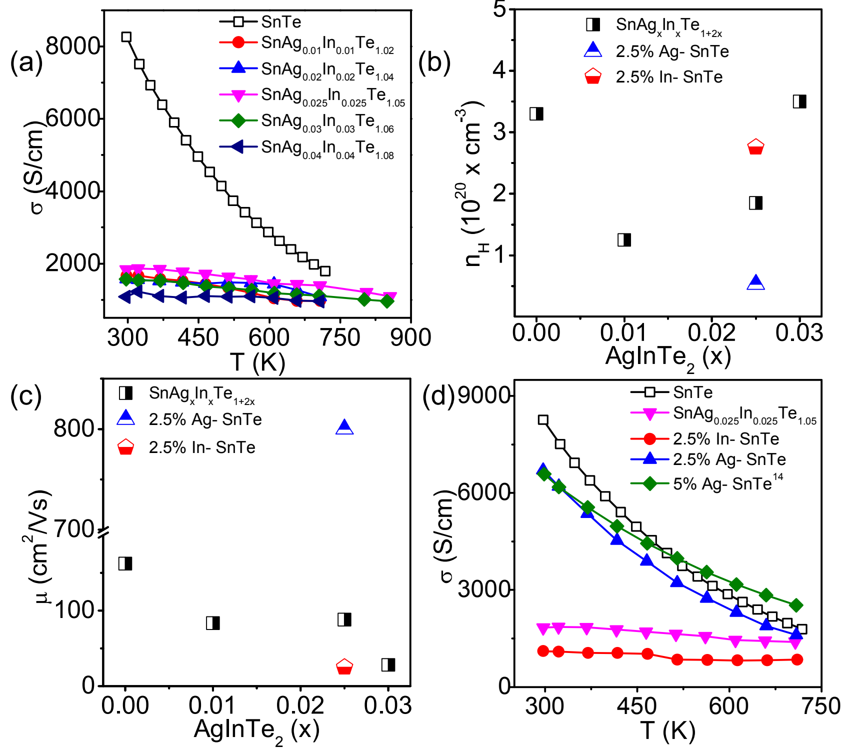

Figure 4A.2 (a) Temperature dependent electrical conductivity (σ) of $SnAg_xIn_xTe_{1+2x}$ (x = 0-0.04) samples. (b) Room temperature carrier concentration (n_H) and (c) carrier mobility (μ) with respect to $AgInTe_2$ alloying concentration (x) in $SnAg_xIn_xTe_{1+2x}$. (d) Comparison of electrical conductivity (σ) between pristine SnTe and doped SnTe with optimized compositions.

Temperature dependence of Seebeck coefficients for $SnAg_xIn_xTe_{1+2x}$, controlled 2.5 mol% In doped SnTe, and controlled 2.5 mol% Ag doped SnTe are shown in Figure 4A.3. All the samples exhibit positive Seebeck coefficients, which is in well agreement with the positive value of Hall coefficient. For all the samples, Seebeck coefficient increases with increasing temperature. Interestingly, for $SnAg_xIn_xTe_{1+2x}$, the Seebeck coefficients dramatically increased relative to the controlled In or Ag doped SnTe over the whole temperature range (Figure 4A.3b). Typically, for $SnAg_{0.025}In_{0.025}Te_{1.05}$, the room temperature Seebeck coefficient is ~97 μV/K, which linearly increases to ~167 μV/K at 854 K. This confirms synergistic effect of Ag and In on the thermoelectric properties of SnTe, leading to significant enhancement of Seebeck coefficient of SnTe over a broad temperature range.

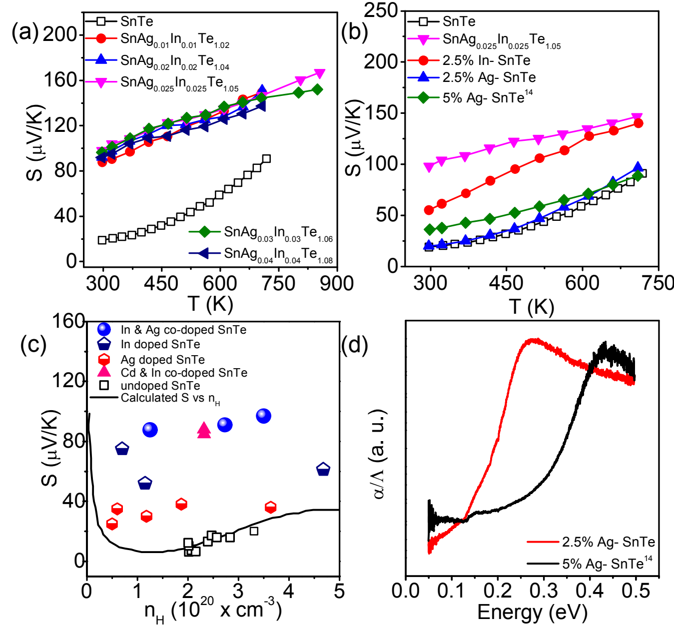

Figure 4A.3 (a) Temperature dependent Seebeck coefficient (*S*) of $SnAg_xIn_xTe_{1+2x}$ samples (x = 0-0.04). (b) Comparison of Seebeck coefficient between pristine SnTe and doped SnTe with optimized compositions. (c) Room temperature *S* vs. n_H plot of the present 2.5 mol% Ag doped SnTe, 2.5 mol% In doped SnTe and $SnAg_xIn_xTe_{1+2x}$ samples. The solid line is Pisarenko plot calculated for SnTe based on VBM model [4]. For comparison, previously reported *S* vs. n_H experimental data of un-doped SnTe,[20] Ag doped SnTe,[14] In doped SnTe[4] and In & Cd codoped SnTe[15] are given in (c). (d) Optical absorption spectra of Ag doped SnTe.

To understand the origin of enhanced Seebeck coefficient, we have compared the room temperature *S* as a function of n_H with the well-established Pisarenko line of SnTe, which has been calculated based on a two-valence-band model by Ren and co-workers (Figure 4A.3c).[4] This model considers the energy difference between light hole valence band (effective mass ~$0.168m_e$) and heavy hole valence band (effective mass of ~$1.92m_e$) to be 0.35 eV for SnTe.[4] Seebeck coefficient of pristine SnTe falls exactly on the Pisarenko line, demonstrating the strength of the adopted physical model.[20] Controlled In doped SnTe samples show relatively higher *S* value as compared to Pisarenko plot, which is attributed to resonance level formation in the valence band of SnTe introduced by the In dopant.[4,12] This resulted in lower value of hole mobility *via* sharp enhancement in effective mass and carrier scattering (Figure 4A.2c). Although the reduced hole concentrationis expected to decrease the contribution of heavy hole valence band to the Seebeck coefficient in controlled Ag doped SnTe, Ag doped samples also show relatively higher Seebeck coefficient as compared to theoretical Pisarenko curve (Figure 4A.3b). The Seebeck coefficient values of Ag doped samples are comparable to previously

reported S values of Cd/Mg doped SnTe, where enhancement of S was caused due to the valence band convergence.[7,8] Furthermore, Ag doping increases band gap of SnTe (Figure 4A.3d) suggesting that effective valence band convergence is achieved, which is also indicated in chapter 3B.[14] Higher value of Seebeck coefficient and large band gap motivated us to investigate electronic structure of Ag doped SnTe sample (see discussion below). $SnAg_xIn_xTe_{1+2x}$ samples exhibit much higher Seebeck coefficient compared to that of the controlled Ag doped SnTe and In doped SnTe samples with similar carrier concentrations (Figure 4A.3c). This indicates that resonance levels introduced by the In and band convergence caused by the Ag synergistically enhance the Seebeck coefficient further in $SnAg_xIn_xTe_{1+2x}$. We have compared the room temperature Seebeck coefficient of $SnAg_xIn_xTe_{1+2x}$ samples with previously reported In-Cd co-doped SnTe.[15] Similar S vs n_H behaviour compared to that of In & Cd co-doped SnTe and a remarkably higher value of Seebeck coefficient compared to that of controlled Ag doped SnTe and In doped SnTe motivated us to investigate the effect of In and Ag on the electronic structure of SnTe system.

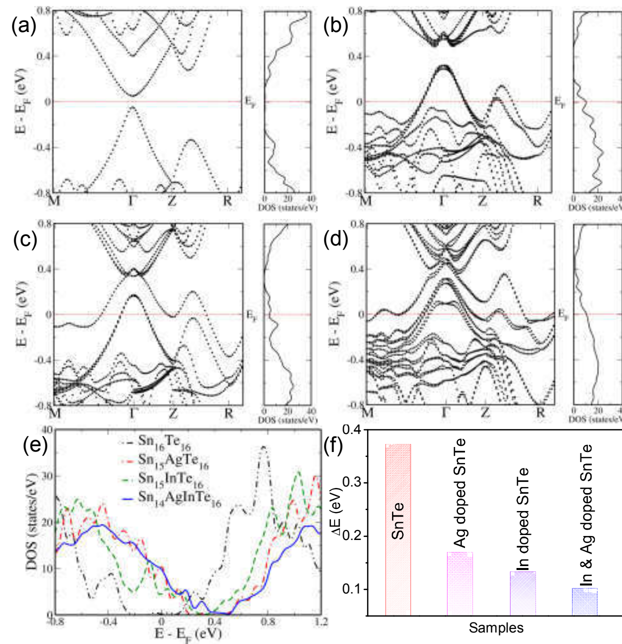

Figure 4A.4 Electronic structure and density of states of (a) $Sn_{16}Te_{16}$, (b) $Sn_{15}AgTe_{16}$, (c) $Sn_{15}InTe_{16}$, (d) $Sn_{14}AgInTe_{16}$ supercell as a function of wave vector in the supercell brillouin zone. The energies are shifted with respect to the fermi energy which is set to zero. The band gap appears at the Γ point and heavy hole band at $Z + \delta$ in the ($\sqrt{2} \times \sqrt{2} \times 2$) tetragonal supercell. The VBM and CBM occurring at L point in the rocksalt cell of SnTe fold on to the Γ point, and the heavy hole valence band appearing along Σ folds on to $Z + \delta$ in the case of present 32 atom ($\sqrt{2} \times \sqrt{2} \times 2$) tetragonal supercell. (e) DOS near the top valence band and (f) energy separations, ΔE between the upper valence band at Lpoint and the lower valence band at Σ point for pristine SnTe, In- and Ag-doped SnTe, and In and Ag alloyed SnTe.

To understand the origin of enhancement in Seebeck coefficient of SnTe upon co-doping with Ag and In, we used DFT calculations to determine electronic structure Ag & In co-doped SnTe, controlled Ag-doped SnTe, controlled In-doped SnTe and undoped SnTe (Figure 4A.4). Bloch wave functions of a supercell are related to those of a single unit cell according to a Brillouin zone folding based on the periodicity of reciprocal space. For (√2 x √2 x 2) supercell used in these simulations, the principal valence band (light hole) maximum (VBM) and conduction band minimum (CBM) occur at the Γ point, and the heavy hole valence band occurs at $Z + \delta$ along the $Z \rightarrow R$ direction. The VBM and CBM occur at the L point in the Brillouin zone of single cell of cubic SnTe. In the Brillouin zone of the supercell considered here, they fold back to Γ (zone center). Similarly, the heavy hole valence band along Σ-line corresponds to the states at $Z + \delta$ in the Brillouin zone of the 32 atoms ($\sqrt{2} \times \sqrt{2} \times 2$) tetragonal supercell. We find that the band gap of SnTe increases with Ag doping, consistent with the trend in the experimental band gaps measured with diffuse reflectance spectroscopy (Figure 4A.3d). Our estimated band gap of SnTe is ~0.097 eV, when the spin-orbit coupling was included (in comparison to the estimate of ~0.049 eV obtained from calculations without spin- orbit coupling). The band gap of $Sn_{16}Te_{16}$ at the Γ point increases to ~0.230 eV with doping of 6.25 mol % Ag for Sn atoms. Significant decrease in the separation between the energies of the light and heavy hole valence bands of SnTe is achieved with Ag doping; it decreases from ~0.382 eV in pristine SnTe to ~0.178 eV in the 6.25 mol % Ag doped SnTe (Figure 4A.4f). Thus, incorporation of Ag in SnTe leads to increase in the valence band degeneracy, and such valence band convergence is expected to result in enhancement of the Seebeck coefficient as the two bands contribute to the asymmetry reflected in slope of the density of states at or near Fermi energy.[8] Similar modifications have been found in the bands of Mg, Cd, Cd/Hg and Cd-In doped SnTe.[7-9,15] For 6.25 mol % In doped SnTe, calculated density of states reveals well-defined peaks within the valence band near the Fermi level indicating a resonance level (Figure 4A.4e). In this case too, we see that there is some degree of convergence of light and heavy hole valence bands. The energy separation between the two valence bands decreases to ~0.137 eV (Figure 4A.4f), in agreement with the reported value of 0.2 eV for ~4% In doped SnTe.[15] Electronic structure of Ag and In co-doped SnTe reveals both the formation of resonance

state and the convergence of the valence band (Figure 4A.4e). The energy difference between the light hole and heavy hole valence bands further reduces to ~0.105 eV (Figure 4A.4f) showing the synergistic effect of Ag and In (Figure 4A.4). Therefore, coexisting resonance level and the valence band convergence in Ag and In co-doped SnTe are responsible for the observed remarkable enhancement in the Seebeck coefficient.The temperature-dependent power factor (σS^2) of $SnAg_xIn_xTe_{1+2x}$ samples are presented in Figure 4A.5. Ag and In co-doped SnTe samples show significantly high value of the σS^2 over abroad range of temperature because of the enhanced Seebeck coefficient and an optimal electrical conductivity. Figure 4A.5b compares the power factors for pristine, In- and Ag-doped, and In & Ag co-doped SnTe. Clearly, In and Ag co-doped SnTe combines the advantages of both In and Ag doping. This indicates an additive and possibly synergistic effect of co-doping over individual dopant in SnTe. Typically, the room temperature σS^2 value for $SnAg_{0.025}In_{0.025}Te_{1.05}$ is ~18 μW/cmK^2 which increases to ~31.4 μW/cmK^2 at 856 K. We have compared the power factor of $SnAg_{0.025}In_{0.025}Te_{1.05}$ with the previously reported In & Cd co-doped SnTe,[15] SnTe-MnTe,[21] SnTe-CaTe[11] and SnTe-SrTe[22] (Figure 4A.5c). Maximum power factor value obtained in the $SnAg_xIn_xTe_{1+2x}$ ingot samples are higher compared to that of the previously reported SnTe based system. While the In & Ag co-doped SnTe exhibits similar Seebeck coefficient compared to that of In & Cd co-doped SnTe (Figure 4A.3c), the carrier mobility is relatively higher in In & Ag co-doped SnTe compared to that of In & Cd co-doped SnTe with similar carrier concentrations.[19] Thus, we observe higher power factor in In & Ag co-doped SnTe compared to that of In & Cd co-doped SnTe.

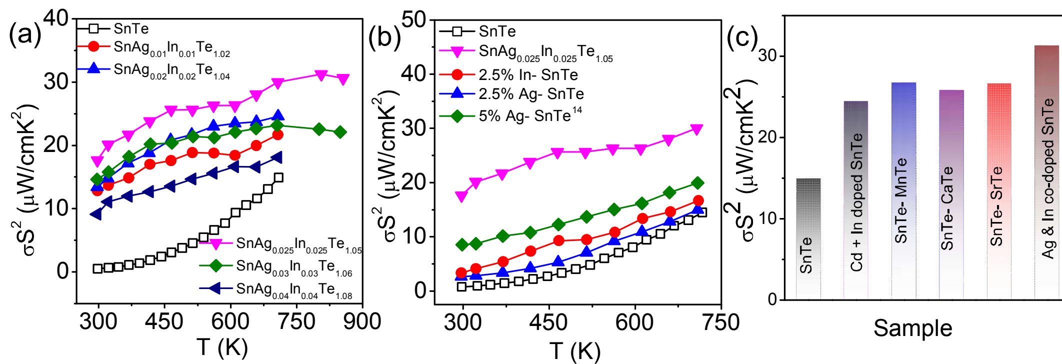

Figure 4A.5 (a) Temperature dependence of power factor (σS^2) of $SnAg_xIn_xTe_{1+2x}$ samples (x = 0-0.04). (b) Comparison of σS^2 among pristine SnTe, individual In and Ag doped SnTe and In & Ag co-doped SnTe. (c) Comparison of the room temperature σS^2 of the present $SnAg_xIn_xTe_{1+2x}$ sample with the previously reported high performance In & Cd codoped SnTe, [15] Mn alloyed SnTe,[10] SnTe-CaTe[11] and SnTe-SrTe[22].

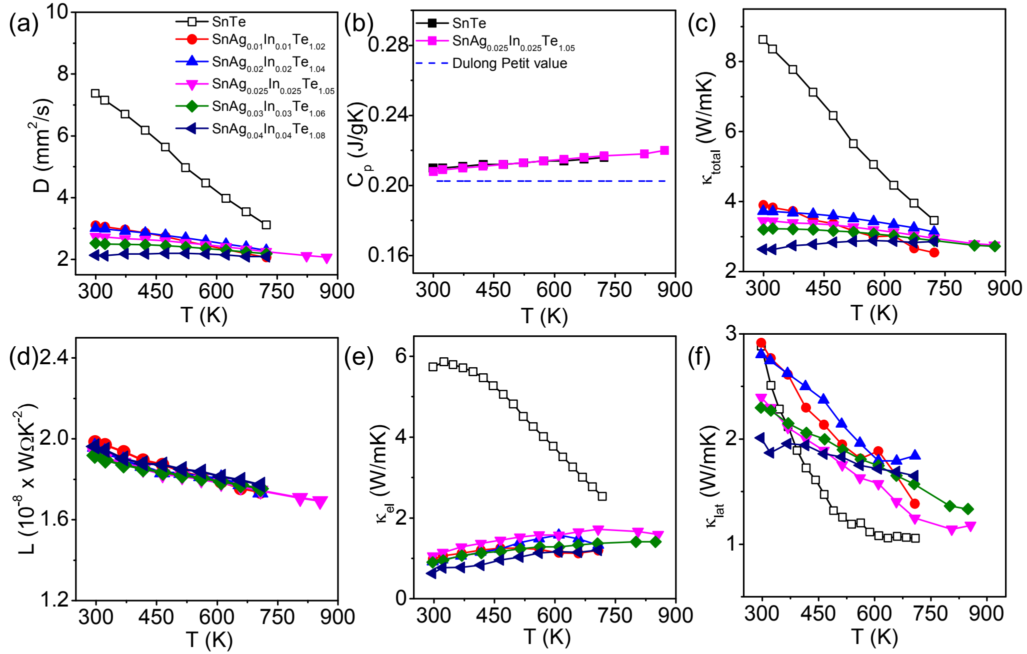

Figure 4A.6 Temperature-dependent (a) thermal diffusivity (*D*), (b) heat capacity (C_p), (c) total thermal conductivity (κ_{total}), (d) Lorenz number (*L*) (e) electronic thermal conductivity (κ_{el}) and (f) lattice thermal conductivity (κ_{lat}) of $SnAg_xIn_xTe_{1+2x}$ samples (x = 0-0.04).

In Figure 4A.6, we present the temperature dependent thermal transport properties of $SnAg_xIn_xTe_{1+2x}$ (x=0-0.04) samples. Ag and In co-doping in SnTe optimizes the temperature dependent κ_{total} by controlling the κ_{el}. With increasing the doping concentration, κ_{total} decreases due to the systematic decrease in κ_{el} (Figure 4A.6c). Typically, the room temperature κ_{total} measured for $SnAg_{0.025}In_{0.025}Te_{1.05}$ is ~3.45 W/mK, which decreases to ~2.72 W/mK at 873 K. The $\kappa_{el} = L{\cdot}\sigma{\cdot}T$ were estimated from calculated Lorenz number, *L*, measured electrical conductivity and temperature. *L* values were calculated from reduced Fermi energy, which is obtained fitting of the respective temperature dependent Seebeck data as indicated in chapter 1 (Figure 4A.6d).[23,24] The κ_{lat} was obtained after subtraction of the electronic part, κ_{el}, from the κ_{total}. Typically, the room temperature value of κ_{lat} measured for $SnAg_{0.025}In_{0.025}Te_{1.05}$ is ~2.39 W/mK which decreases to ~1.17 W/mK at 876 K (Figure 4A.6f). Although, we have not observed any systematic trend for κ_{lat} with varying the doping concentration in SnTe, κ_{lat} values of In and Ag co-doped SnTe samples are slightly higher than that of the pristine SnTe. In principle, increased point defects in SnTe sample are expected to lower κ_{lat} value. The above result is indicating that the used Lorenz number (*L*) value cannot properly account

for the electronic contribution to thermal conductivity. It has been shown earlier that in degenerate semiconductors with multiple bands coexistent at the Fermi level, a complex inter-valley scattering can occur in which the carriers move from one valley to the other, transferring larger amounts of heat than what is predicted by the degenerate *L* value.[25] Such an inter-valley carrier scattering has been observed in Na and K co-doped PbTe samples whose calculated κ_{lat}values were relatively larger than that of pristine PbTe due to an underestimation of κ_{el}.[26] In and Ag co-doping in SnTe increases the valence band convergence and the hole concentration, which possibly facilitate the inter-valley carrier scattering.

In Figure 4A.7, we present temperature dependent *zT* of $SnAg_xIn_xTe_{1+2x}$ (x = 0-0.04) samples. Combined effect of In and Ag enhances the *zT* significantly. The highest *zT* value of ~1.0 at 856 K is achieved for $SnAg_{0.025}In_{0.025}Te_{1.05}$, which is significantly higher compared to pristine SnTe sample, controlled In doped SnTe and Ag doped SnTe. Average *zT* of $SnAg_{0.025}In_{0.025}Te_{1.05}$ is ~0.6 by considering the hot and cold end to be 860 and 300 K, respectively, which is comparable to the other high performance SnTe based materials.

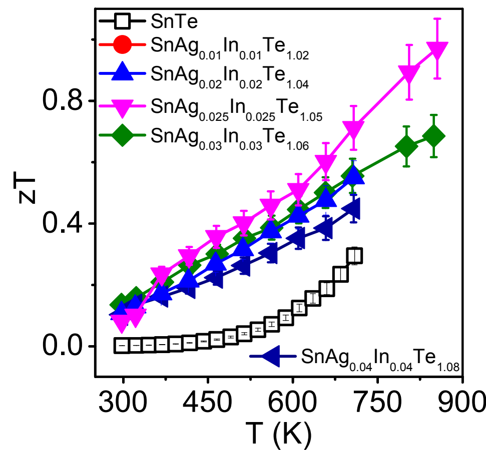

Figure 4A.7 Temperature dependence of thermoelectric figure of merit (zT) of $SnAg_xIn_xTe_{1+2x}$ samples (x = 0-0.04) with 10% error bar.

4A.4 Conclusions

SnTe-$AgInTe_2$ ($SnAg_xIn_xTe_{1+2x}$) shows an enhanced thermoelectric performance over a broad temperature region due to synergistic effect of resonance level formation and

valence band convergence. Indium doping creates a resonance level inside the valence band of SnTe. Ag doping increases the principal band gap of SnTe, resulting in decrease of the energy separation between two valence bands (light and heavy holes) of SnTe, and consequent suppression of the bipolar conduction at high temperature. Effective convergence of the valence bands and the presence of resonance level near the Fermi energy give rise to synergistic enhancement in the Seebeck coefficient in Ag & In co-doped SnTe, resulting in remarkable increase in power factor to 31.4 $\mu W/cmK^2$, which is the highest power factor of SnTe based compounds reported till 2016. As a consequence, the highest zT of ~1 at ~856 K has been achieved. Hence, $SnAg_xIn_xTe_{1+2x}$ has a collective advantage of Ag and In doping on the overall thermoelectric performance of SnTe. The improved zT values over the broad range 300−856 K found in the In & Ag co-doped SnTe makes it a useful thermoelectric material that deserves further investigation and performance optimization through minimization of its lattice thermal conductivity.

4A.5 References

1. Y. Pei, X. Shi, A. LaLonde, H. Wang, L. Chen and G. J. Snyder, *Nature*, 2011, **473**, 66.
2. L. Zhao, H. Wu, S. Hao, C.-I. Wu, X. Zhou, K. Biswas, J. He, T. P. Hogan, C. Uher and C. Wolverton, *Energy Environ. Sci.*, 2013, ***6***, 3346.
3. J. P. Heremans, V. Jovovic, E. S. Toberer, A. Saramat, K. Kurosaki, A. Charoenphakdee, S. Yamanaka and G. J. Snyder, *Science*, 2008, **321**, 554.
4. Q. Zhang, B. Liao, Y. Lan, K. Lukas, W. Liu, K. Esfarjani, C. Opeil, D. Broido, G. Chen and Z. Ren, *Proc. Natl. Acad. Sci. USA,* 2013, **110**, 13261.
5. S. N. Guin, V. Srihari and K. Biswas, *J. Mater. Chem. A*, 2015, **3**, 648.
6. S. N. Guin, A. Chatterjee, D. S. Negi, R. Datta and K. Biswas, *Energy Environ. Sci.*, 2013, **6**, 2603.
7. G. Tan, L.-D. Zhao, F. Shi, J. W. Doak, S.-H. Lo, H. Sun, C. Wolverton, V. P. Dravid, C. Uher and M. G. Kanatzidis, *J. Am. Chem. Soc.*, 2014, **136**, 7006.
8. A. Banik, U. S. Shenoy, S. Anand, U. V. Waghmare and K. Biswas, *Chem. Mater.*, 2015, **27**, 581.
9. G. Tan, F. Shi, J. W. Doak, H. Sun, L.-D. Zhao, P. Wang, C. Uher, C. Wolverton, V. P. Dravid and M. G. Kanatzidis, *Energy Environ. Sci.*, 2015, **8**, 267.
10. G. Tan, F. Shi, S. Hao, H. Chi, T. P. Bailey, L.-D. Zhao, C. Uher, C. Wolverton, V. P. Dravid and M. G. Kanatzidis, *J. Am. Chem. Soc.*, 2015, **137**, 11507.
11. R. Al Rahal Al Orabi, N. A. Mecholsky, J. Hwang, W. Kim, J.-S. Rhyee, D. Wee and M. Fornari, *Chem. Mater.*, 2016, **28**, 376.
12. A. Banik and K. Biswas, *J. Mater. Chem. A*, 2014, **2**, 9620.
13. G. Tan, W. G. Zeier, F. Shi, P. Wang, G. J. Snyder, V. P. Dravid and M. G. Kanatzidis, *Chem. Mater.*, 2015, **27**, 7801.
14. A. Banik and K. Biswas, *J. Solid State Chem.*, 2016, **242**, 43.
15. G. Tan, F. Shi, S. Hao, H. Chi, L.-D. Zhao, C. Uher, C. Wolverton, V. P. Dravid and M. G. Kanatzidis, *J. Am. Chem. Soc.*, 2015, **137**, 5100.
16. G. Paolo, B. Stefano, B. Nicola, C. Matteo, C. Roberto, C. Carlo, C. Davide, L. C. Guido, C. Matteo, D. Ismaila, C. Andrea Dal, G. Stefano de, F. Stefano, F. Guido, G. Ralph, G. Uwe, G. Christos, K. Anton, L. Michele, M.-S. Layla, M. Nicola, M. Francesco, M. Riccardo, P. Stefano, P. Alfredo, P. Lorenzo, S. Carlo, S. Sandro, S. Gabriele, P. S. Ari, S. Alexander, U. Paolo and M. W. Renata, *J. Phys.: Condens. Matter*, 2009, **21**, 395502.
17. J. P. Perdew, K. Burke and M. Ernzerhof, *Phys. Rev. Lett.*, 1996, **77**, 3865.
18. L. Zhang, J. Wang, Z. Cheng, Q. Sun, Z. Li and S. Dou, *J. Mater. Chem. A*, 2016, **4**, 7936.
19. R. Brebrick, *J. Phys. Chem. Solids*, 1963, **24**, 27.
20. R. Brebrick and A. Strauss, *Phys. Rev.*, 1963, **131**, 104.
21. H. Wu, C. Chang, D. Feng, Y. Xiao, X. Zhang, Y. Pei, L. Zheng, D. Wu, S. Gong, Y. Chen, J. He, M. G. Kanatzidis and L.-D. Zhao, *Energy Environ. Sci.*, 2015, **8**, 3298.
22. L.-D. Zhao, X. Zhang, H. Wu, G. Tan, Y. Pei, Y. Xiao, C. Chang, D. Wu, H. Chi, L. Zheng, S. Gong, C. Uher, J. He and M. G. Kanatzidis, *J. Am. Chem. Soc.*, 2016, **138**, 2366.
23. K. Biswas, J. He, I. D. Blum, C.-I. Wu, T. P. Hogan, D. N. Seidman, V. P. Dravid and M. G. Kanatzidis, *Nature*, 2012, **489**, 414.

24. L.-D. Zhao, S.-H. Lo, J. He, H. Li, K. Biswas, J. Androulakis, C.-I. Wu, T. P. Hogan, D.-Y. Chung, V. P. Dravid and M. G. Kanatzidis, *J. Am. Chem. Soc.*, 2011, **133**, 20476.
25. N. V. Kolomoets, *Sov. Phys. Solid State*, 1966, **8**, 799.
26. J. Androulakis, I. Todorov, D.-Y. Chung, S. Ballikaya, G. Wang, C. Uher and M. Kanatzidis, *Phys. Rev. B*, 2010, **82**, 115209.

Chapter 4B

Synergistic Effect of Nanostructuring, Valence Band Convergence and Resonance Level Formation Boost The Thermoelectric Performance of SnTe-SnS

Summary

Integration of large power factor (σS^2) and ultralow lattice thermal conductivity (κ_{lat}) is crucial for the improved thermoelectric performance of the present inorganic solids. SnTe, a Pb-free IV-VI narrow band gap semiconductor, can be a potential thermoelectric material due to its favorable crystal structure and valence band characteristics. In this chapter, we have optimized the thermoelectric performance of self-compensated SnTe by utilizing synergistic effect of valence bands convergence, resonance states formation and all-scale hierarchical nano/meso-architecturing. First, we demonstrate that substitution of Sulfur in the position of Te introduces hierarchically architectured SnS as a second phase in SnTe matrix. Thus, $Sn_{1.03}Te_{0.93}S_{0.07}$ shows room temperature κ_{lat} of ~1.73 W/mK, which is significantly lower than that of pristine $Sn_{1.03}Te$. In the next step, we have optimized the electrical transport properties of $Sn_{1.03}Te_{0.93}S_{0.07}$ via Ag & In co-doping where Ag acts as a valence band convergent and indium creates resonance state in the valence band. Successful modulation of electronic structure through resonance level formation and valence band convergence results in a remarkably enhanced Seebeck coefficient over a wide range of temperatures leading to a maximized power factor of ~32 μW/cmK^2 in $Sn_{1.03}Ag_{0.0275}In_{0.0275}Te_{0.985}S_{0.07}$. Thus, we have achieved a maximum zT of ~1.3 at 871 K for $Sn_{1.03}Ag_{0.0275}In_{0.0275}Te_{0.985}S_{0.07}$.

4B.1 Introduction

The hunt for good thermoelectric materials has concentrated on researching semiconductors that have suitable electronic and phonon band structures so that we could be able to achieve high power factor (σS^2) and low lattice thermal conductivity (κ_{lat}). Coexistences of the resonance level and valence band convergence have been proved to be a powerful strategy to improve the average thermoelectric efficiency (zT_{avg}) of SnTe.[1] Previous sub-chapter prensents ultrahigh power factor in Ag & In codoped SnTe system originating from the synergistic effect of valence band convergence by Ag-doping and resonance level formation via In-doping, which indicates possibility of getting high output thermoelectric power density in $SnAg_xIn_xTe_{1+2x}$ samples.[2] The next remaining challenge was optimization of lattice thermal conductivity of $SnAg_xIn_xTe_{1+2x}$.

Various strategies have been adopted mainly focusing on the reduction of κ_{lat} to enhance zT of SnTe through phonon scattering at hierarchical length scale.[3-10] Extensive studies have been done on the thermoelectric properties of SnTe-SnSe,[3] SnTe-PbTe[9] solid solutions. Use of phase immiscibility is another successful strategy to prepare high performance thermoelectric solids by means of top-down synthesis of nanostructured materials. Thus, κ_{lat} of SnTe has been moderately reduced via introduction of second phase nanoprecipitates like CdS and HgTe.[4,11] Pseudo binary SnTe-SnS system will be another good choice to study the effect of nanostructuring due to large miscibility difference between the SnTe and SnS phases.[12,13] Furthermore, sulfur doping is known to reduce the energy gap of two valence bands at high temperature.[10] This stimulated the study of Ag & In codoped SnTe-SnS system.

This chapter present optimized thermoelectric properties of self-compensated SnTe ($Sn_{1.03}Te$) via reduction of κ_{lat} through nanostructuring followed by desirable electronic structure modification by Ag & In codoping. $Sn_{1.03}Te_{0.93}S_{0.07}$ has shown κ_{lat} of ~1.73 W/mK at room temperature, which can be attributed mainly to the formation of nanostructured SnS-rich phases in SnTe rich matrix, as confirmed from Backscattered electron imaging (BSE) mode field emission scanning electron microscopy (FESEM) and transmission electron microscopy (TEM). Thermoelectric transport properties of $Sn_{1.03}Te_{0.93}S_{0.07}$ have been further optimized through Ag & In co-doping. Ag & In co-doped $Sn_{1.03}Te_{0.93}S_{0.07}$ shows enhanced band gap, indicating the convergence of valence

bands. Thus, by introduction of resonance level (In doping) & valence band convergence (Ag & In codoping), we achieve zT of ~1.33 (at 871 K) and a zT_{avg} of ~0.8 (between 300 and 871 K) in $Sn_{1.03}Ag_{0.0275}In_{0.0275}Te_{0.985}S_{0.07}$.

4B.2 Methods

4B.2.1 Synthesis

Tin (Sn, Alfa Aesar 99.99+ %), tellurium (Te, Alfa Aesar 99.999+ %), sulfur (S, Alfa Aesar 99.999%), silver (Ag, Alfa Aesar 99.999%, metal basis) and indium (In, Alfa Aesar 99.99+ %) were used for synthesis with no additional purification.

High quality crystalline ingots (~7 g) of $Sn_{1.03}Ag_yIn_yTe_{1-x+2y}S_x$ (x = 0-0.1) were synthesized by mixing appropriate ratios of high-purity starting materials of Sn, Ag, In, Te and S in quartz tube. The tubes were sealed under vacuum (10^{-5} Torr) and slowly heated to 900 ^{o} C in 10 hrs, annealed for 10 hrs, and cooled slowly to room temperature (Chapter 2). The as synthesized samples were powdered using mortar and pestle to reduce the grains size in an inert glove box. Spark plasma sintering (SPS) is a well known strategy to enhance thermoelectric performance of materials via creation of mesoscale grain boundary, which efficiently scatter heat carrying phonons with longer mean free path.[14] In order to achieve high thermoelectric performance, we have studied thermoelectric transport properties of SPS processed $Sn_{1.03}Ag_yIn_yTe_{1-x+2y}S_x$ samples. This powder was then pressed into cylindrical shape by SPS method (SPS-211LX, Fuji Electronic Industrial Co., Ltd.) at 773 K for 5 min in a 10 mm diameter graphite die under an axial pressure of 40 MPa in vacuum. Highly dense (~ 98% of theoretical density) disk-shaped pellets with ~10 mm diameter and ~10 mm thickness were obtained. The density of SPS-processed sample is ≥95 % of theoretical density of $SnTe_{1-x}S_x$.

4B.2.2 Characterizations

Powder X-ray diffraction (PXRD) for all of the samples were recorded using a Cu K_α (λ = 1.5406 Å) radiation on a Bruker D8 diffractometer. To estimate the energy difference between principle valence band (VB_L) and conduction band (CB), optical diffuse reflectance measurement has been done with finely ground powder at room temperature

using FT-IR Bruker IFS 66V/S spectrometer in a frequency range of 4000-400 cm^{-1} with 2 cm^{-1} resolution and 50 scans. Absorption (α/Λ) was calculated from acquired reflectance data using Kubelka−Munk equations: $\alpha/\Lambda=(1-R)^2/(2R)$, where R is the reflectance, α and Λ are the absorption and scattering coefficients, respectively. The energy band gaps were derived from α/Λ vs E (eV) plots. BSE mode FESEM experiments were performed using NOVA NANO SEM 600 (FEI, Germany) operated at 15 kV. TEM imaging was performed using an aberration corrected FEI TITAN cubed 80–300 KV transmission electron microscope operating at 300 kV. TEM samples were prepared by conventional mechanical thinning.

4B.2.3 Transport properties

Electrical conductivity and Seebeck coefficients were measured simultaneously under He atmosphere from room temperature to 873 K on a ULVAC-RIKO ZEM-3 instrument system (Details are given in chapter 1). Carrier concentrations were determined using Hall coefficient measurements at room temperature with the setup made by Excel instrument. Four-contact Hall-bar geometry was used for the measurement and a varying magnetic field up to 0.57 Tesla was applied during the measurements. At 300 K, we have estimated the carrier concentration, n_H, from the formula: $n_H=1/eR_H$, where e is the electronic charge, R_H is hall coefficient. Thermal diffusivity, D, was directly measured in the range of 300−873 K by using laser flash diffusivity method in a Netzsch LFA-457. The total thermal conductivity, κ_{total}, was calculated using the formula, $\kappa_{total} = DC_p\rho$ (Details are given in chapter 1).

4B.3 Results & Discussion

The thermoelectric performance of SnTe has been improved via introduction of three rational steps. First, we have introduced the self compensation strategy to reduce the excess carrier density of SnTe.[4] Since self compensated $Sn_{1.03}Te$ is having significantly lower hole concentration (~1.2 x 10^{20} cm^{-3}) compared to pristine SnTe (~4.5 x 10^{20} cm^{-3}), we have used $Sn_{1.03}Te$, as pristine sample. Second, we have studied $Sn_{1.03}Te$-SnS alloy to improve the thermoelectric transport. $Sn_{1.03}Te_{1-x}S_x$ shows much lower lattice thermal

conductivity as compared to that of $Sn_{1.03}Te$ owing to enhanced point defect scattering and formation of SnS-rich nanoprecipitates, as observed in FESEM and TEM images. Finally, powerfactor (σS^2) of $Sn_{1.03}Te_{1-x}S_x$ system has been significantly improved through the preparation of Ag & In co-doped $Sn_{1.03}Te_{1-x}S_x$ ($Sn_{1.03}Ag_yIn_yTe_{1-x+2y}S_x$) system.

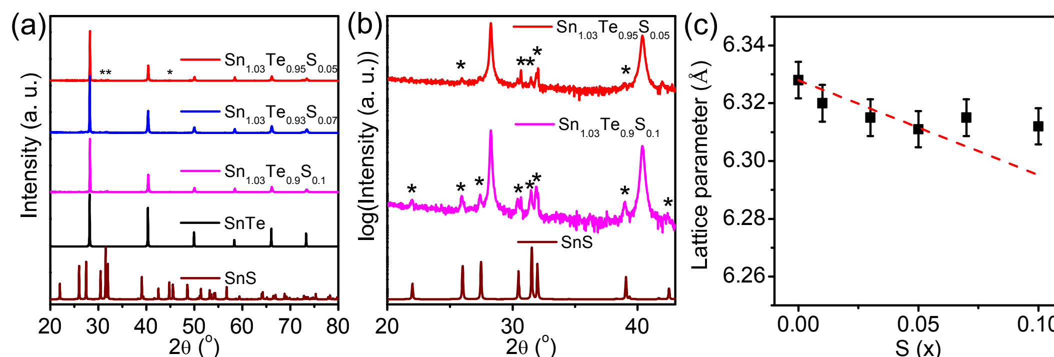

Figure 4B.1. (a) Powder XRD patterns of $Sn_{1.03}Te_{1-x}S_x$ (x = 0-0.1) samples. (b) PXRD patterns of $Sn_{1-x}Ge_xTe$ (x = 0-0.5) in log scale.'*' sign in signifies the presence of SnS- rich second phases. (c) Lattice parameter (*a*) vs. S concentration (*x*) $Sn_{1.03}Te_{1-x}S_x$ (x = 0-0.1) . Dashed line indicates the Vegard's law for solid solution.

Polycrystalline $Sn_{1.03}Te_{1-x}S_x$ samples have been synthesized through solid state melting at 900 °C followed by slow cooling. Figure 4B.1a presents PXRD patterns for $Sn_{1.03}Te_{1-x}S_x$ (x = 0-0.1) samples. Although the main phase could be indexed to cubic Fm-3m, PXRD patterns of $Sn_{1.03}Te_{1-x}S_x$ (for x ≥ 0.05) show additional weak reflections owing to formation of phase separated SnS (Figure 4B.1a and Figure 4B.1b). Figure 4B.1c present lattice parameter of $Sn_{1.03}Te_{1-x}S_x$ samples. Lattice parameter of $Sn_{1.03}Te_{1-x}S_x$ samples reduces as small amounts of S are substituted for Te, which is consistent with the difference in lattice parameters of $Sn_{1.03}Te$ (6.328 Å) and cubic SnS (6.00 Å) (Figure 4B.1c). Lattice parameter reaches the minima for $Sn_{1.03}Te_{0.95}S_{0.05}$, indicating the maximum solubility of SnS in the SnTe matrix at this composition. $Sn_{1.03}Te_{0.95}S_{0.05}$ onwards, lattice parameters of $Sn_{1.03}Te_{1-x}S_x$ start to deviate from Vegard's trend indicating the presence of SnS-rich precipitate, which has been further analyzed with BSE mode FESEM and TEM.

To understand the compositions and surface morphology, backscattered electron (BSE) imaging and energy dispersive X-ray spectroscopy (EDAX) are performed on $Sn_{1.03}Te_{1-x}S_x$ during FESEM. Observed contrast difference indicates phase inhomoginity and formation of phase separated $Sn_{1.03}Te$-SnS. The BSE mode FESEM images of

$Sn_{1.03}Te_{0.95}S_{0.05}$ are presented in Figure 4B.2a and 4B.2b, which show presences of ~5-20 μm size darker contrast precipitates in lighter contrast matrix, indicating formation of SnTe-rich matrix and SnS-rich precipitate. In order to analyze the composition of the matrix and the precipitate, we have performed EDAX both on matrix and precipitate (Figure 4B.2c). The darker contrast precipitates observed in BSE-FESEM are SnS-rich, where as lighter contrast matrix has been identified as SnTe, as seen in Figure 4B.2c. To further confirm the phase composition, we have performed line scanning on a precipitate along with the matrix (highlighted by a black line in Figure 4B.2b), which confirms that the matrix is $Sn_{1.03}Te$ rich, whereas the precipitate is SnS. Large miscibility gap between SnTe and SnS evidenced both in PXRD and back scattered FESEM imaging, can be attributed to large size difference between Te (221 pm) and S (184 pm). Since the sizes of the precipitates are comparatively larger (on the order of μm) than the mean free path of heat-carrying phonons (on the order of nm), such precipitates will not participate significantly in phonon scattering process.

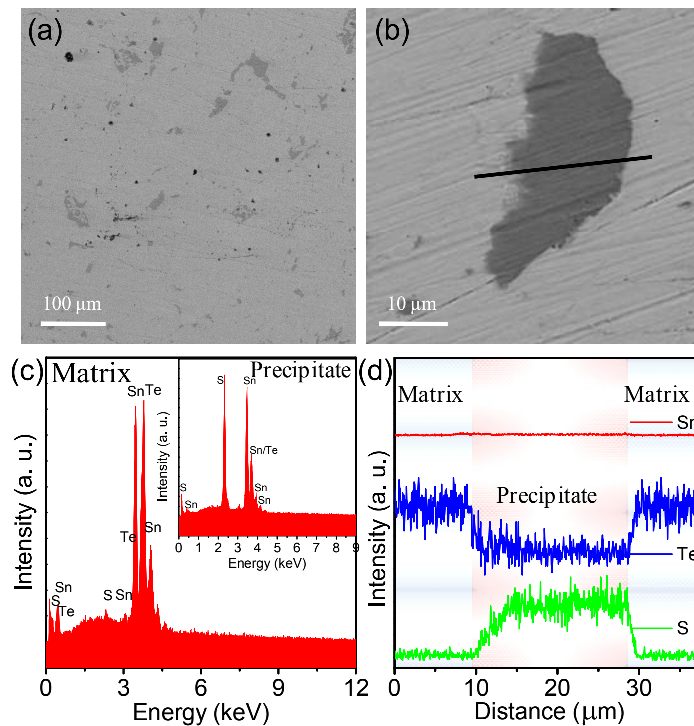

Figure 4B.2 (a and b) Backscattered FESEM images of $Sn_{1.03}Te_{0.93}S_{0.07}$ from the polished surface. (c) EDAX spectra from the matrix. EDAX spectra from the precipitate is given as inset image. (d) EDAX line scan along the precipitate (along the black line in image b).

In addition to larger SnS-rich precipitates, TEM reveals presence of nanodimensional precipitates, as depicted in Figure 4B.3. Low magnification TEM image shows the presence of phase separated nanoprecipitates of irregular shape and size (Figure 4B.3a) in the range of 5–25 nm. The corresponding HRTEM image, shown in Figure 4B.3b further confirms formation of crystalline nanoprecipitate in SnTe-rich matrics (Figure 4B.3b and 4B.3c). We have further characterized nanoprecipitate composition from lattice-spacing calculation and fast furrier transform (FFT) image (inset in Figure 4B.3d) characterization. Presence of (102) lattice plane with d-spacing of 0.324 nm and ED-pattern generated from FFT of HRTEM image of marked region in Figure 4B.3d confirms formation of nanostructured SnS-rich precipitate in SnTe matrix. These nanoprecipitates are known to effectively participate in the scattering of medium wavelengths phonons. Since melt−slow cooling synthesis route was used to prepare $Sn_{1.03}Te_{1-x}S_x$, phase separated SnS slowly grows into multiple-length scale precipitates in the SnTe matrix, resulting in an inhomogeneous multiphase material.

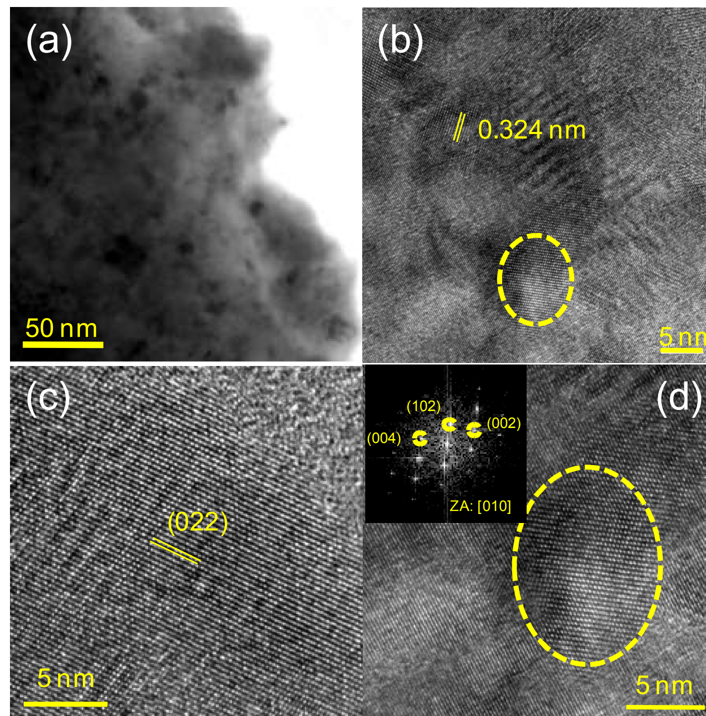

Figure 4B.3 (a) Low magnification TEM image of $Sn_{1.03}Te_{0.93}S_{0.07}$ (b) HRTEM showing presence of SnS nanoprecipitate (marked in yellow) in $Sn_{1.03}Te$ matrix. (c) HRTEM image of $Sn_{1.03}Te$ matrix with corresponding lattice spacing. (d) Zoomed HRTEM image of the nanoprecipitate indicated in (b). Inset is the electron diffraction pattern generated from HRTEM pattern of the precipitate region along the <010> zone axis.

Temperature dependent electrical transport data of $Sn_{1.03}Te_{1-x}S_x$ ingot samples are shown in Figure 4B.4. The room temperature Hall coefficients, R_H, of all $Sn_{1.03}Te_{1-x}S_x$ (x = 0-0.1) samples are positive, which indicate the *p*-type conduction in this system. Electrical conductivity (σ) of the $Sn_{1.03}Te_{1-x}S_x$ (Figure 4B.4a) decreases with temperature representing degenerate semiconducting behavior. Incorporation of sulfur in Te position slightly reduces σ, resulting from reduced carrier mobility (μ) originating from enhanced carrier-impurity scattering, as seen in Table 4B.1. At room temperature, σ of pristine $Sn_{1.03}Te$ is ~ 6725 S/cm, whereas for $Sn_{1.03}Te_{0.93}S_{0.07}$, σ is ~ 5500 S/cm. Figure 4B.4 represents temperature dependence of Seebeck coefficient (S) of $Sn_{1.03}Te_{1-x}S_x$ samples. Positive value of S indicates the *p*-type conduction in the measured temperature range of 300-871 K, which agrees with the Hall measurement. Typically, $Sn_{1.03}Te_{0.93}S_{0.07}$ shows room temperature Seebeck coefficient of ~19 μV/K which increases to ~131 μV/K at 717 K. The faster rise of the Seebeck coefficient at higher temperature (T > 623 K) is reminiscent of the similar but more pronounced behavior of *p*-type PbTe, which is attributed to the increasing contribution of the heavy hole Σ band at rising temperatures due to the thermal excitations (Figure 4B.4c) proposed by Zhang *et al.*[10]

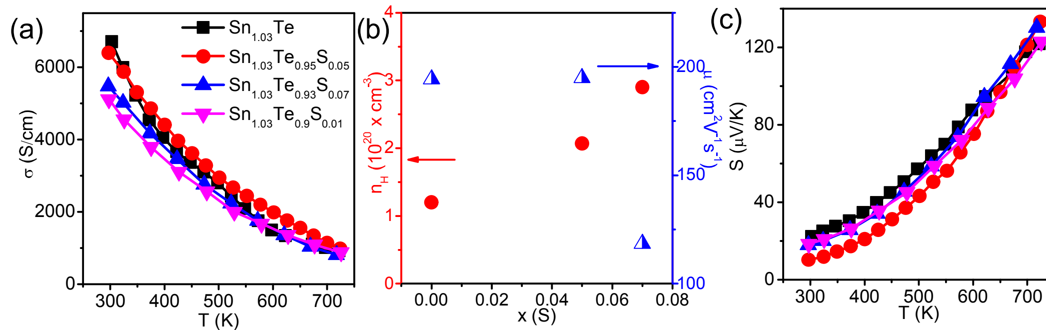

Figure 4B.4 (a) Temperature dependent electrical conductivity (σ) of $Sn_{1.03}Te_{1-x}S_x$ (x = 0-0.1) samples. (b) Room temperature carrier concentrati1on (n_H) and carrier mobility (μ) with respect to sulfur alloying concentration (x) in $Sn_{1.03}Te_{1-x}S_x$. (c) Temperature dependent Seebeck coefficient (S) of $Sn_{1.03}Te_{1-x}S_x$ (x = 0-0.1) samples.

Temperature dependent thermal transport properties of $Sn_{1.03}Te_{1-x}S_x$ samples have been illustrated in Figure 4B.5. κ_{total} of $Sn_{1.03}Te_{1-x}S_x$ decreases with increasing S concentration originating from reduction in both κ_{el} and κ_{lat} (Figure 4B.5c, 4B5d, and 4B.5e). $Sn_{1.03}Te$ is having room temperature κ_{total} of 8.22 W/mK, which reduces to 5.79 W/mK for $Sn_{1.03}Te_{0.93}S_{0.07}$. Decrease in room temperature κ_{el} with increasing sulfur concentration is in well agreement with temperature dependent σ data. We estimated

temperature dependent κ_{lat} by subtracting κ_{el} from κ_{total}. Incorporation of sulfur in $Sn_{1.03}Te$ matrix significantly reduces the κ_{lat} up to x=0.07, as seen in Figure 4B.5e. $Sn_{1.03}Te_{0.93}S_{0.07}$ shows minimized room temperature κ_{lat} of 1.73 W/mK, which reduces to 1.14 W/mK at 717 K. To establish the relation of κ_{lat} with the nanostructural features, we have estimated κ_{lat} of $Sn_{1.03}Te_{1-x}S_x$ based on Klemens's model of disordered alloys (Figure 4B.5f).[15-17] $Sn_{1.03}Te_{1-x}S_x$ shows much lower κ_{lat} compared to theoretically calculated κ_{lat} which confirmed significant contribution of SnS-rich nanostructure in heat carrying phonon scattering process. Optimized κ_{lat} and enhanced temperature dependent Seebeck coefficient of $Sn_{1.03}Te_{0.93}S_{0.07}$ has motivated us to further optimize its thermoelectric transport properties of this composition via electronic structure modification by preparing Ag & In co-doped $Sn_{1.03}Te_{0.93}S_{0.07}$.

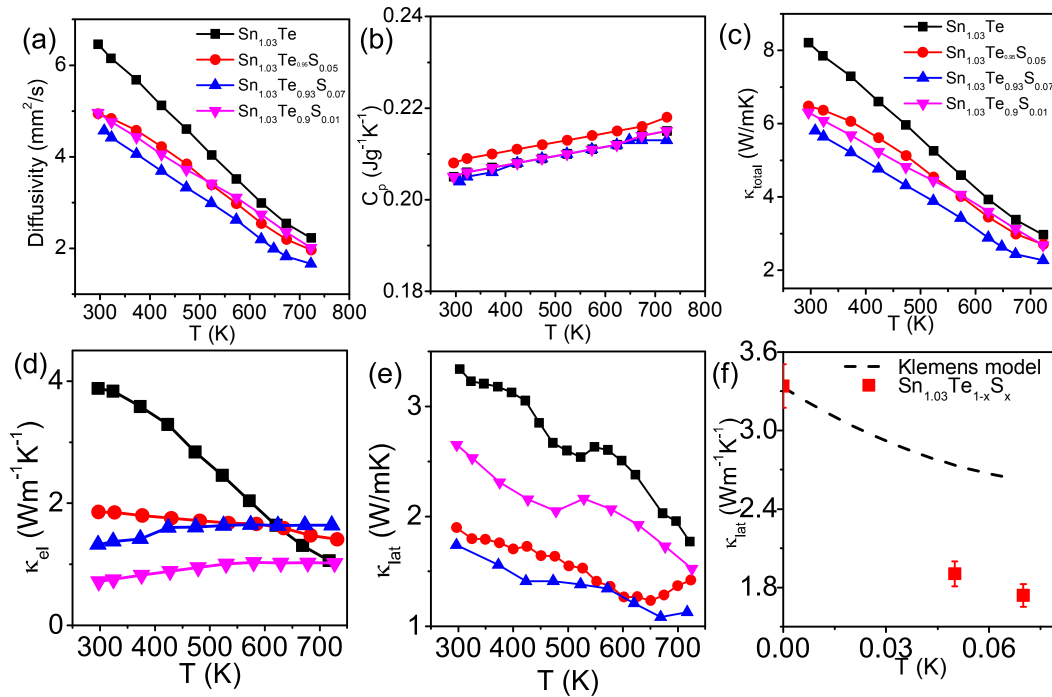

Figure 4B.5 (a) and (b) are temperature dependent thermal diffusivity (D) of heat capacity (C_p) of $Sn_{1.03}Te_{1-x}S_x$ (x = 0-0.1). (c), (d) and (e) are temperature-dependent total thermal conductivity (κ_{total}), electronic thermal conductivity (κ_{el}) and lattice thermal conductivity (κ_{lat}) of $Sn_{1.03}Te_{1-x}S_x$ (x = 0-0.1). (f) Room-temperature κ_{lat} as a function of sulfur alloying concentration. Solid line corresponds to the predicted lattice thermal conductivities considering the mass and strain fluctuation due to Ge incorporation in SnTe lattice based on Klemens model.

Crystalline ingots of $Sn_{1.03}Ag_yIn_yTe_{0.93+2y}S_{0.07}$ (y = 0-0.03) have been prepared via similar melt-cooling reaction at 900° C. All the major peaks in PXRD patterns could be indexed to rocksalt SnTe-structure with Fm-3m space group (Figure 4B.6a). Additional week reflections in PXRD are coming from SnS phase (Pnma crystal structure). We have

measured the optical band gap of $Sn_{1.03}Ag_yIn_yTe_{0.93+2y}S_{0.07}$ (y = 0-0.03) by diffuse reflectance IR spectroscopy (Figure 4B.6b). With increasing dopant concentration, the optical absorption spectra of $Sn_{1.03}Te_{0.93}S_{0.07}$ shows a shift of absorption edge towards higher energy. The derived band gap shows an increase from ~0.09 eV to ~0.133 eV in going from 0 to 3 mole % Ag & In co-doped SnTe. This result is similar to that of MgTe alloyed with SnTe, where MgTe reduces the valence band energy separation by increasing principle band gap of SnTe.[18] Ag & In codoped SnTe samples are known to show significantly large Seebeck coefficient originating from enhanced contribution of second valence band in the electrical transport properties.[2] Previous literature report on the valence band convergence in Ag & In codoped SnTe and presently observed band gap increment indicate successful modulation of electronic structure of $Sn_{1.03}Te_{0.93}S_{0.07}$ via Ag & In co-doping, which has been confirmed from temperature dependent electrical transport data, presented in the following section.

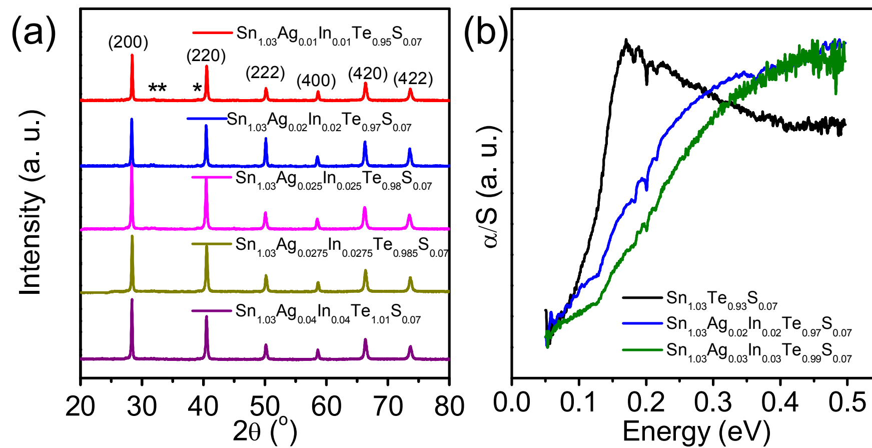

Figure 4B.6 (a) and (b) are Powder XRD patterns and optical absorption spectra of $Sn_{1.03}Ag_yIn_yTe_{0.93+2y}S_{0.07}$ (x = 0-0.04) samples.

Temperature dependent electrical conductivity data are shown in Figure 4B.7a. σ decreases with increasing temperature indicating degenerate semiconducting behavior of $Sn_{1.03}Ag_yIn_yTe_{0.93+2y}S_{0.07}$. In order to understand the electrical transport properties, we have estimated carrier concentration (n_H) from the measurement of Hall coefficient, R_H of $Sn_{1.03}Ag_yIn_yTe_{0.93+2y}S_{0.07}$. The resultant carrier concentration and carrier mobility are given in Table 4B.1. With increasing $AgInTe_2$ concentration room temperature electrical conductivity decreases, which can be attributed to reduced carrier concentration (n_H) of

$Sn_{1.03}Ag_yIn_yTe_{0.93+2y}S_{0.07}$. Typically, for $Sn_{1.03}Ag_{0.0275}In_{0.0275}Te_{0.985}S_{0.07}$ room temperature σ decreases from 2280 S/cm to 1230 S/cm at 870 K. Interestingly, carrier concentration first decreases with increasing $AgInTe_2$ concentration and then decreases, as seen in our previous work,[2,3] where Ag and In first fills the hole generating Sn-vacancy followed by their *p*-type nature. Room temperature hole mobility increases with $AgInTe_2$ alloying, which can be attributed to dominant contribution of Ag & In, as valence band convergent.[2]

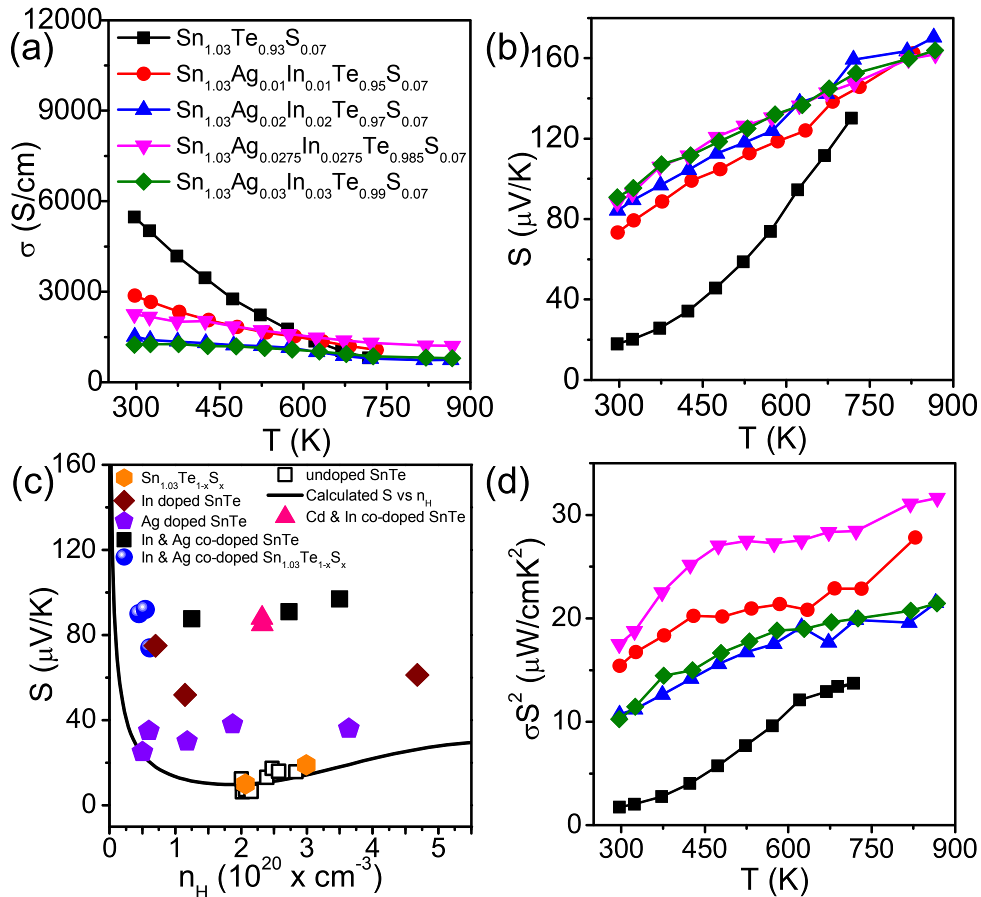

Figure 4B.7 (a) and (b) are temperature dependent electrical conductivity (σ) and Seebeck coefficient (S) of $Sn_{1.03}Ag_yIn_yTe_{0.93+2y}S_{0.07}$ samples. (c) Room temperature S vs. n_H plot of the present $Sn_{1.03}Ag_yIn_yTe_{0.93+2y}S_{0.07}$ samples. The solid line is Pisarenko plot calculated using a two-valence-band model.[19] For comparison, previously reported S vs. n_H experimental data of un-doped SnTe, Ag doped SnTe,[2] In doped SnTe,[2] $SnAg_yIn_yTe_{1+2y}$[2] and In & Cd codoped SnTe[20] are given in (c). (d) Temperature dependent power factor (σS^2) of $Sn_{1.03}Ag_yIn_yTe_{1+2y}S_{0.07}$ samples.

Figure 4B.7b shows temperature dependent Seebeck coefficient of $Sn_{1.03}Ag_yIn_yTe_{0.93+2y}S_{0.07}$. Like $Sn_{1.03}Te_{1-x}S_x$, $Sn_{1.03}Ag_yIn_yTe_{0.93+2y}S_{0.07}$ samples show positive Seebeck coefficient, which support Hall coefficient data. Seebeck coefficient of $Sn_{1.03}Ag_yIn_yTe_{0.93+2y}S_{0.07}$ rises linearly with temperature and $AgInTe_2$ concentration,

which further confirms synergistic effect of resonant level formation and valence band convergence. Typically, for $Sn_{1.03}Ag_{0.0275}In_{0.0275}Te_{0.985}S_{0.07}$, room temperature *S* is ~88 μV/K, which reaches the value of ~161.7 μV/K at 870 K. To understand the synergistic effect of resonance state formation and valence band modification, we have examined carrier concentration dependence of room temperature Seebeck coefficient for $Sn_{1.03}Ag_yIn_yTe_{0.93+2y}S_{0.07}$ and compared it with theoretical *S* vs n_H and previous literature reports (Figure 4B.7c).[2,3,19-22] Like previous case SnTe-AgInTe$_2$, room temperature Seebeck coefficients of $Sn_{1.03}Ag_yIn_yTe_{0.93+2y}S_{0.07}$ are significantly higher as compared to the theoretical Pisarenko plot. Previous report on band structure modification lead by Ag and In co-doping and the room temperature Pisarenko plot confirms synergistic effect of valence band convergence and resonant level formation in $Sn_{1.03}Ag_yIn_yTe_{0.93+2y}S_{0.07}$ samples.[2] Thus, we have achieved room temperature power factor of ~17.44 μW/cmK^2 which further increased to ~32 μW/cmK^2 at 870 K for $Sn_{1.03}Ag_{0.0275}In_{0.0275}Te_{0.985}S_{0.07}$.

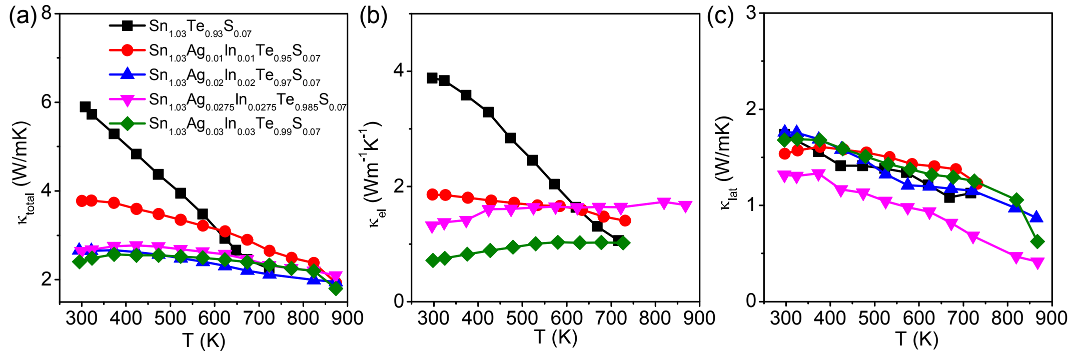

Figure 4B.8 Temperature-dependent (a) total thermal conductivity (κ_{total}), (b) electronic thermal conductivity (κ_{el}) and (c) lattice thermal conductivity (κ_{lat}) of $Sn_{1.03}Ag_yIn_yTe_{0.93+2y}S_{0.07}$ samples.

Temperature dependent thermal transport properties of $Sn_{1.03}Ag_yIn_yTe_{0.93+2y}S_{0.07}$ are presented in Figure 4B.8. Total thermal conductivity, κ_{total} decreases with temperature for all the samples, as seen in Figure 4B.8a. Typically, for $Sn_{1.03}Ag_{0.01}In_{0.01}Te_{0.95}S_{0.07}$, room temperature κ_{total} is ~3.79 W/mK which reaches the value of ~2.65 W/mK. Temperature dependent κ_{el} and κ_{lat} are plotted in Figure 4B.8b and 4B.8c. With increasing dopants' concentration, room temperature κ_{el} decreases, which can be attributed to reduced electrical conductivity originating from low carrier concentration. κ_{lat} was obtained by subtracting κ_{el} from κ_{total}. κ_{lat} decreases with increasing temperature indicating Umpklapp process. However, κ_{lat} does not show significant dependence on dopant's concentration.

Typically, $Sn_{1.03}Ag_{0.0275}In_{0.0275}Te_{0.985}S_{0.07}$ shows room temperature κ_{lat} of 1.32 W/mK, which decreases to 0.5 W/mK at 871 K.

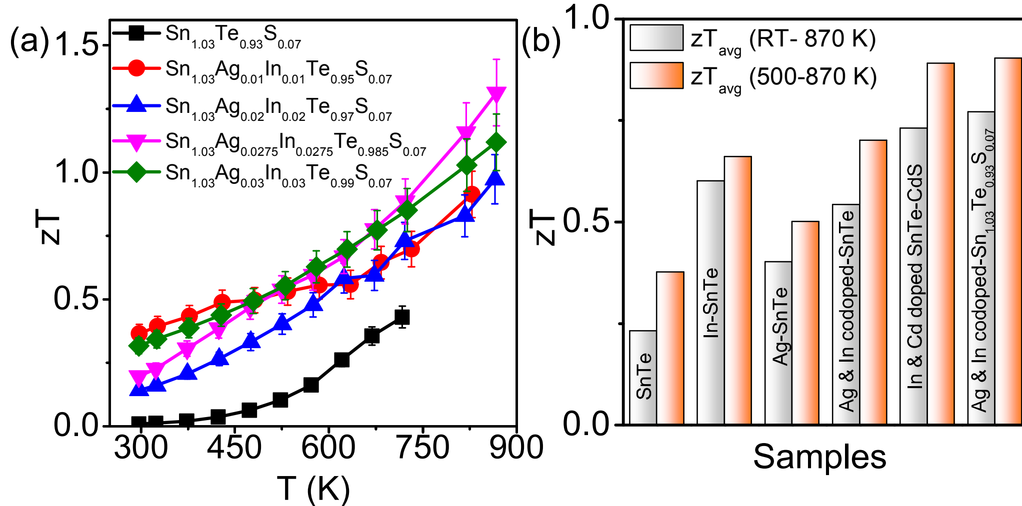

Figure 4B.9 (a) Temperature dependence of thermoelectric figure of merit (*zT*) of $Sn_{1.03}Ag_yIn_yTe_{0.93+2y}S_{0.07}$ samples with 10% error bar. (b) Average *zT* (zT_{avg}) of RT-870 K and 500-870 K for pristine SnTe, In-doped SnTe and Ag-doped SnTe, In and Ag codoped SnTe and In and Ag codoped $Sn_{1.03}Te_{0.93}S_{0.07}$.

High power factor and low κ_{lat} gives rise to significantly enhanced thermoelectric figure of merit in $Sn_{1.03}Ag_yIn_yTe_{0.93+2y}S_{0.07}$ samples (Figure 4B.9). $Sn_{1.03}Ag_{0.0275}In_{0.0275}Te_{0.985}S_{0.07}$ shows highest *zT* of ~1.3 at 871 K temperature, which is significantly higher than that of previously reported $SnAg_yIn_yTe_{1+2y}$. We could able to achieve zT_{avg} of 0.77 and 0.935, when hot and cold end temperatures were 300, 871 K and 500, 871 K, respectively.

4B.4 Conclusions

In conclusion, we have enhanced the thermoelectric performance of SnTe via synergestic modification of electronic structure and significant phonon scattering. Detailed transmission electron microscopic imaging studies reveal that $Sn_{1.03}Te_{0.93}S_{0.07}$ exhibit nanoscale precipitates, resulting in significant scattering of heat carrying phonons. Hence, $Sn_{1.03}Te_{0.93}S_{0.07}$ shows minimum κ_{lat} of 1.14 W/mK at 707 K. Ag & In co-doped $Sn_{1.03}Te_{0.93}S_{0.07}$ system shows significantly high power factor and enhanced *zT* as compared to previous work of Ag & In co-doped SnTe, which made SnTe promising for the mid-temperature thermoelectric application.

4B.5 References

1. A. Banik, S. Roychowdhury and K. Biswas, *Chem. Commun.*, 2018, **54**, 6573.
2. A. Banik, U. S. Shenoy, S. Saha, U. V. Waghmare and K. Biswas, *J. Am. Chem. Soc.*, 2016, **138**, 13068.
3. A. Banik and K. Biswas, *J. Mater. Chem. A*, 2014, **2**, 9620.
4. G. Tan, L.-D. Zhao, F. Shi, J. W. Doak, S.-H. Lo, H. Sun, C. Wolverton, V. P. Dravid, C. Uher and M. G. Kanatzidis, *J. Am. Chem. Soc.*, 2014, **136**, 7006.
5. G. Tan, F. Shi, H. Sun, L.-D. Zhao, C. Uher, V. P. Dravid and M. G. Kanatzidis, *J. Mater. Chem. A*, 2014, ***2***, 20849.
6. L.-D. Zhao, X. Zhang, H. Wu, G. Tan, Y. Pei, Y. Xiao, C. Chang, D. Wu, H. Chi, L. Zheng, S. Gong, C. Uher, J. He and M. G. Kanatzidis, *J. Am. Chem. Soc.*, 2016, **138**, 2366.
7. H. Wu, C. Chang, D. Feng, Y. Xiao, X. Zhang, Y. Pei, L. Zheng, D. Wu, S. Gong, Y. Chen, J. He, M. G. Kanatzidis and L.-D. Zhao, *Energy Environ. Sci.*, 2015, **8**, 3298.
8. A. Banik, B. Vishal, S. Perumal, R. Datta and K. Biswas, *Energy Environ. Sci.*, 2016, **9**, 2011.
9. S. Roychowdhury, U. S. Shenoy, U. V. Waghmare and K. Biswas, *J. Mater. Chem. C*, 2017, **5**, 5737.
10. X. Zhang, D. Wang, H. Wu, M. Yin, Y. Pei, S. Gong, L. Huang, S. J. Pennycook, J. He and L.-D. Zhao, *Energy Environ. Sci.*, 2017, **10**, 2420.
11. G. Tan, F. Shi, J. W. Doak, H. Sun, L.-D. Zhao, P. Wang, C. Uher, C. Wolverton, V. P. Dravid and M. G. Kanatzidis, *Energy Environ. Sci.*, 2015, **8**, 267.
12. H. Liu and L. L. Y. Chang, *J. Alloys Compd.*, 1992, **185**, 183.
13. A. A. Volykhov, V. I. Shtanov and L. V. Yashina, *Inorg. Mater.*, 2008, **44**, 345.
14. K. Biswas, J. He, I. D. Blum, C.-I. Wu, T. P. Hogan, D. N. Seidman, V. P. Dravid and M. G. Kanatzidis, *Nature*, 2012, **489**, 414.
15. P. G. Klemens, *Phys. Rev.*, 1960, **119**, 507.
16. J. Callaway, *Phys. Rev.*, 1959, **113**, 1046.
17. J. He, M. G. Kanatzidis and V. P. Dravid, *Mater. Today*, 2013, **16**, 166.
18. A. Banik, U. S. Shenoy, S. Anand, U. V. Waghmare and K. Biswas, *Chem. Mater.*, 2015, **27**, 581.
19. Q. Zhang, B. Liao, Y. Lan, K. Lukas, W. Liu, K. Esfarjani, C. Opeil, D. Broido, G. Chen and Z. Ren, *Proc. Natl. Acad. Sci. USA,* 2013, **110**, 13261.
20. G. Tan, F. Shi, S. Hao, H. Chi, L.-D. Zhao, C. Uher, C. Wolverton, V. P. Dravid and M. G. Kanatzidis, *J. Am. Chem. Soc.*, 2015, **137**, 5100.
21. G. Tan, W. G. Zeier, F. Shi, P. Wang, G. J. Snyder, V. P. Dravid and M. G. Kanatzidis, *Chem. Mater.*, 2015, **27**, 7801.
22. A. Banik and K. Biswas, *J. Solid State Chem.*, 2016, **242**, 43.

CHAPTER 5

The Origin of Low Thermal Conductivity in $Sn_{1-x}Sb_xTe$: Phonon Scattering via Layered Intergrowth Nanostructures

Chapter 5

The Origin of Low Thermal Conductivity in $Sn_{1-x}Sb_xTe$: Phonon Scattering via Layered Intergrowth Nanostructures[†]

Summary

Inorganic solids with low thermal conductivity are of great interest for thermoelectric applications. Formation of synthetic nanostructures by matrix encapsulation is one of the important strategies for thermal conductivity reduction through phonon scattering. Here, we report reduction of lattice thermal conductivity near to the theoretical minimum limit, κ_{min}, *in SnTe via spontaneous formation of nanodomains of the Sb-rich layered intergrowth* $Sn_mSb_{2n}Te_{3n+m}$ *compounds, which are natural heterostructures. High-resolution transmission electron microscopic images of* $Sn_{1-x}Sb_xTe$ *samples reveals the formation of endotaxial Sb rich nanoprecipitates (2-10 nm) along with super-structured intergrowth nanodomains (10-30 nm), which are the key features responsible for the significant reduction of lattice thermal conductivity in SnTe. This mechanism suggests a new avenue for the nanoscale engineering in SnTe to achieve the low lattice thermal conductivities. Moreover, presence of Sb improves electronic transport properties by alliovalent cation doping which optimizes hole concentration in SnTe. As a result, the enhanced thermoelectric figure of merit, zT, of ~1 has been achieved for the composition of* $Sn_{0.85}Sb_{0.15}Te$ *at 800 K. The high zT sample exhibits the Vickers microhardness value of ~136* H_V *which is double of pristine SnTe and significantly higher than the present state of art thermoelectric materials.*

[†]*Paper based on this study has been published in* ***Energy Environ. Sci***. 2016, *9,* 2011.

5.1 Introduction

The interdependence of electrical conductivity (σ), Seebeck coefficient (S) and electronic thermal conductivity (κ_{el}) complicates the attempt for the development of high performance thermoelectric materials.[1] Only independently tunable parameter is lattice thermal conductivity, κ_{lat}. Combination of low κ_{lat}, large S and optimum σ made PbTe, the leading thermoelectric material for power generation application in the intermediate temperature range of 600-900 K.[2-7] Recently, these strategies have been employed to SnTe with the goal of improvement in zT relative to that of PbTe.[8-10] Recent studies explicitly show that SnTe has a strong potential of being a promising thermoelectric material through valence band engineering,[8,11-14] carrier concentration optimization,[15e,15] and/or all-scale hierarchical architecturing.[9,16-18] Significant enhancement of the Seebeck coefficient has been achieved via the formation of the resonance level in the valence band of SnTe through In doping,[10,19,20] and convergence of valence band valleys by alloying of Cd, Hg, Mg or Mn in SnTe.[8,9,11,13,17] Coexistence of resonance level induced by In doping and band convergence enabled by the Cd doping in SnTe maximized zT up to 1.4 at 900 K.[21]

Pristine SnTe exhibits κ_{lat} of ~2.88 W/mK at room temperature, while the theoretical limit for the minimum lattice thermal conductivity (κ_{min}) of SnTe is ~0.5 W/mK.[9,16] Various efforts focus on the reduction of κ_{lat} to enhance zT of SnTe through phonon scattering at hierarchical length scale. κ_{lat} of SnTe has been reduced through solid solution alloying in SnTe-SnSe, where room temperature κ_{lat} of 1.27 W/mK has been achieved via creation of mass and size contrasts between the host and guest atoms (Chapter 2).[10] Formation of nanostructured SnS has significantly reduced κ_{lat} of self compensated SnTe-SnS system (Chapter 4B). κ_{lat} has been moderately reduced via introduction of CdS and HgTe, as second phase nanoprecipitates[9,17] or alloy formation.[11,16,22] However, only few reports exist which could successfully reduce the κ_{lat} of SnTe near to its theoretical minimum value.[23] These approaches resulted in κ_{lat} value near to ~1 W/mK at room temperature, which is still higher as compared to the theoretical minimum limit κ_{min} of ~0.5 W/mK for SnTe. This hints the presence of enormous room to improve the zT through κ_{lat} reduction in SnTe.

Sb plays an important role in the optimization of κ_{lat} in the PbTe based materials. Sb in PbTe forms nanostructures via matrix encapsulation, which exhibits an ultralow κ_{lat} of

~0.8 W/mK at 300 K.[24] The addition of Sb in $Pb_{9.6}Sb_yTe_{10-x}Se_x$ (y<0.2) is reported to form the spontaneous nano-inclusions of Sb rich phases, which resulted in low κ_{lat} and high *zT*.[25] Interestingly, in *n*-type $AgPb_mSbTe_{2+m}$ systems, compositional fluctuations at the nanoscopic level resulted in a distinct type of nanostructures, which play a key role in achieving the low κ_{lat} and high *zT*.[26] Moreover, the substitution of Sb in PbTe has shown a significant increase in the thermoelectric performance at higher temperatures due to the formation of Sb donor states below the conduction band of PbTe.[27,28] Hence, it would be interesting to study the effect of Sb on the thermoelectric properties of SnTe.

This chapter reports the realization of ultralow κ_{lat} in high quality crystalline ingots of $Sn_{1-x}Sb_xTe$. A detailed microscopic understanding of the origin of the low κ_{lat} in $Sn_{1-x}Sb_xTe$ has been discussed. Transmission electron microscopy reveals the presence of endotaxial nanoprecipitates (2–10 nm) in lower Sb-containing SnTe (e.g. $Sn_{0.96}Sb_{0.04}Te$), whereas with higher Sb concentration (e.g. $Sn_{0.85}Sb_{0.15}Te$), nanodomains (10–30 nm) of layered intergrowth Sb-rich $Sn_mSb_{2n}Te_{3n+m}$ compounds spontaneously form in the SnTe matrix, which are natural heterostructures. These distinct nanostructure–matrix interfaces significantly enhance phonon scattering, which gives rise to κ_{lat} of ~0.67 W/mK in $Sn_{0.85}Sb_{0.15}Te$ near room temperature, which is indeed approaching the theoretical κ_{min} of SnTe. Additionally, aliovalent substitution of Sb^{3+} in SnTe reduces the excess hole concentration, resulting in an enhanced Seebeck coefficient. Consequently, an optimized *zT* of ~1 has been achieved at ~800 K for the $Sn_{0.85}Sb_{0.15}Te$ sample, which makes the $Sn_{1-x}Sb_xTe$ system more attractive for mid-temperature thermoelectric power generation. The high *zT* sample exhibits the Vickers microhardness (mechanical stability) value of ~136 H_V which is double that of pristine SnTe and significantly higher than those of the present state-of-the-art thermoelectric materials.

5.2 Methods

5.2.1 Synthesis

Tin (Alfa Aesar, 99.99+ %), tellurium (Alfa Aesar, 99.999+ %) and antimony (Alfa Aesar, 99.999+ %) were used for synthesis without further purification.

High quality crystalline ingots (~7 g) of $Sn_{1-x}Sb_xTe$ (x = 0-0.2) were synthesized by the melting reaction of appropriate ratios of high-purity starting materials of Sn, Sb and Te in a quartz tube. The tubes were sealed under vacuum (10^{-5} Torr) and slowly heated to 900 ^{o}C over 12 hrs, then soaked for 10 hrs, and cooled slowly to room temperature. The density of as synthesized sample was ≥97 % of its theoretical density.

5.2.2 Characterizations

Powder X-ray diffraction for all of the samples were recorded using a Cu K_α (λ = 1.5406 Å) radiation on a Bruker D8 diffractometer. TEM imaging was performed using an aberration corrected FEI TITAN cubed 80-300 kV transmission electron microscope operating at 300 kV. TEM samples were prepared by conventional mechanical thinning followed by Ar ion milling to perforation in order to generate large electron transparent thin area.

5.2.3 Transport properties

Thermal diffusivity, D, was directly measured in the range 300−873 K by using laser flash diffusivity method in a Netzsch LFA-457. The total thermal conductivity, κ_{total}, was calculated using the formula, $\kappa_{total} = DC_p\rho$ (Details are given in chapter 1). Electrical conductivity and Seebeck coefficients were measured simultaneously under He atmosphere from room temperature to 873 K on a ULVAC-RIKO ZEM-3 instrument system (Details are given in chapter 1). Carrier concentrations were determined using Hall coefficient measurements at room temperature with a PPMS system (Details are given in chapter 1).

5.2.4 Mechanical properties

Microhardness of the samples were measured in the commercial Zwick Roell ZHU 2.5 machine using the diamond indenter on the Vickers hardness scale, where the force was used to be 2N and the indent was kept for 10s. Vickers hardness values (kg.f/mm^2) were determined from the equation of $H_v = 1.854 \mathrm{x} L/(2d)^2$, where L is the indentation load and $2d$ is the diagonal length of the indentation. The impressions of the indenter are show in Figure 5.9. The uncertainty of microhardenss measurement is about 5%.

5.3 Results & Discussion

$Sn_{1-x}Sb_xTe$ (x = 0.0-0.2) samples were synthesized via the vacuum sealed-tube melting reaction at 900 ^oC. Powder X-ray diffraction (PXRD) patterns of pristine and 4–8 mol% Sb containing samples could be indexed to the rocksalt SnTe structure, which shows the absence of any second phase within the detection limit of PXRD (Figure 5.1a). However, for a higher Sb content (x≥0.12) in SnTe, small intensity secondary phase peaks were observed in the PXRD pattern (* mark in Figure 5.1a and 5.1b).

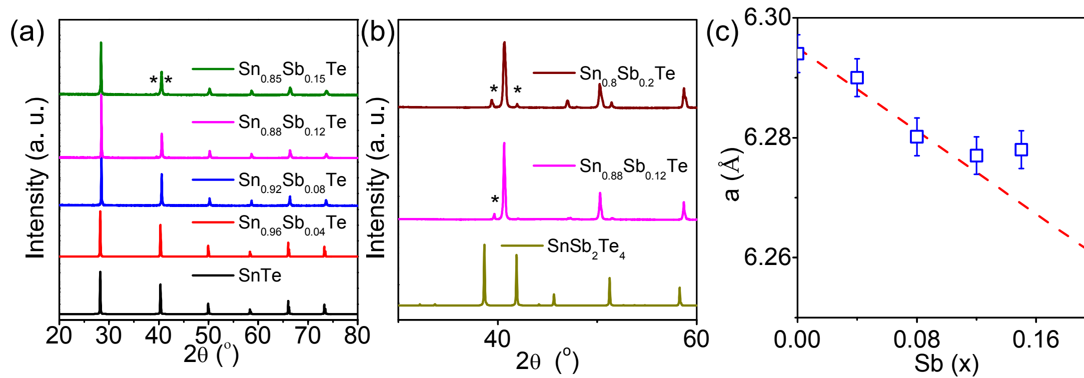

Figure 5.1 (a) Powder XRD patterns of $Sn_{1-x}Sb_xTe$ (x = 0-0.15) samples. (b) Comparison of zoomed powder XRD patterns of $Sn_{1-x}Sb_xTe$ with Sn- based layered intergrowth compound. (c) Lattice parameter (*a*) vs. Sb concentration (*x*) in $Sn_{1-x}Sb_xTe$ (x = 0-0.2).

Second phase peaks in PXRD closely match with the PXRD pattern of the layered intergrowth Sb rich compounds belonging to the homologous series of quasibinary $(SnTe)_m(Sb_2Te_3)_n$ systems, i.e. $Sn_mSb_{2n}Te_{3n+m}$,[29-31] which are natural modulated heterostructures (Figure 5.1b). These compounds usually crystallize in anisotropic layered tetradymite Bi_2Te_2S-type structures with a large unit cell. They can also be viewed as intergrowths of SnTe-type (rocksalt) and Sb_2Te_3-type (hexagonal) phases. The lattice parameter (*a*) extracted from PXRD initially decreases linearly from 6.294 Å to 6.277 Å with the increasing Sb concentration in SnTe following the Vegard's law, which indicates the solid solution nature of $Sn_{1-x}Sb_xTe$ (up to x = 0.12) samples. However, the lattice parameters of $Sn_{1-x}Sb_xTe$ compositions with x≥0.12 do not follow the Vegard's law and deviate from linearity (Figure 5.1c). The presence of small intensity extra peaks in the PXRD pattern and the non-linear relationship between the lattice parameter and Sb concentration indicate the formation of $Sn_mSb_{2n}Te_{3n+m}$ intergrowth nanostructures in the SnTe matrix, which has been further confirmed via transmission electron microscopy analysis, which will be discussed in the following part. The presence of small intensity

extra peaks in the PXRD pattern and the non-linear relationship between the lattice parameter and Sb concentration indicate the formation of $Sn_mSb_{2n}Te_{3n+m}$ intergrowth nanostructures in the SnTe matrix, which has been further confirmed via transmission electron microscopy analysis, as discussed in the following part of this chapter.

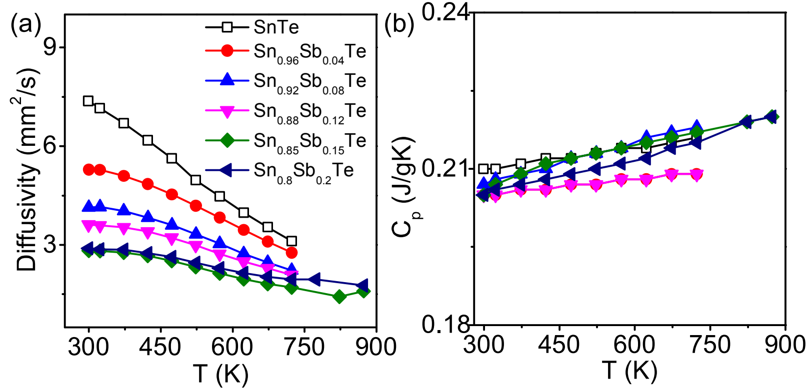

Figure 5.2 (a) and (b) are temperature dependent thermal diffusivity (D) and heat capacity (C_p) of $Sn_{1-x}Sb_xTe$ (x = 0-0.2).

The temperature dependent total thermal conductivity (κ_{total}) of $Sn_{1-x}Sb_xTe$ (x = 0.00–0.20) was estimated from thermal diffusivity (D) data (Figure 5.2a) using the formula, $\kappa_{total} = DC_p\rho$, where C_P is specific heat capacity (Figure 5.2b) and ρ is the density. The substitution of Sb in SnTe substantially reduces the κ_{total} value from ~8.62 W/mK to ~3.4 W/mK for $Sn_{0.8}Sb_{0.2}Te$ at 300 K (Figure 5.3a), which is ~61% reduction compared to pristine SnTe. Contribution of charge carrier in κ_{total} (κ_{el}) has been calculated through Widdemann Franz law, $\kappa_{el} = L.\sigma.T$. We have calculated Lorenz number, L, from fitting of temperature dependent Seebeck data based on SPB model, as discussed in chapter 1 (Figure 5.3b).[32] Large reduction in κ_{total} is attributed to both the significant reduction of κ_{el} (Figure 5.3c) caused by the donor nature of Sb^{3+} in SnTe and the reduction of κ_{lat} (Figure 5.3d). With the increasing Sb content, room temperature κ_{lat} decreases gradually and reaches the minimum value of ~0.67 W/mK for the $Sn_{0.85}Sb_{0.15}Te$ sample. The Klemens model of disordered alloys was applied to predict the variation of lattice thermal conductivity of the $Sn_{1-x}Sb_xTe$ system.[33] According to Klemens theory of disordered alloys, the lattice thermal conductivity of a disordered alloy, κ_{lat}^{d} is determined by:

$$\kappa_{lat}^{d} = \frac{\tan^{-1}(u)}{u}\,\kappa_{lat}^{p} \qquad (5.1)$$

Where κ_{lat}^{p} is the lattice thermal conductivity of a pure alloy and u can be expressed by

$$u^2 = \frac{\pi^2 \Theta_D \Omega}{h v^2} \kappa_{lat}^{p} \Gamma \tag{5.2}$$

Here u is the disorder scaling parameter, Θ_D is the Debye temperature (Θ_D = 140 K for SnTe[16]), h is the Plank constant, υ is the sound velocity (υ = 1800 m s^{-1}, for SnTe[16]), and Ω is the volume per atom and Γ is the scattering parameter that combines the influences from mass, bonding force, and strain contrasts, described as

$$\Gamma = x(1-x)[\left(\frac{\Delta M}{M}\right)^2 + \varepsilon\,(\frac{\Delta a}{xa})^2] \tag{5.3}$$

Where ε is a phenomenological parameter (163) related to the Grüneisen parameter γ (~2.1 for SnTe[16]), M and a are the molar mass and lattice constant of the alloy, ΔM and Δa are the differences in mass and lattice constant between the two constituents.

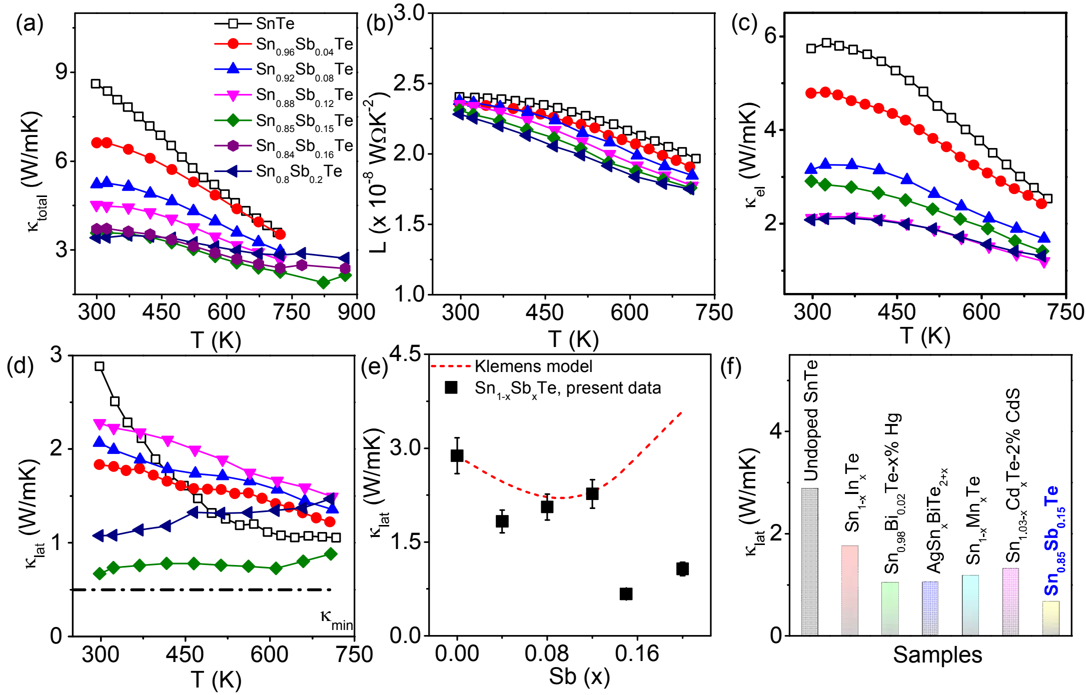

Figure 5.3 Temperature-dependent (a) total thermal conductivity (κ_{total}), (b) Lorenz number (L), (c) electronic thermal conductivity (κ_{el}) and (d) lattice thermal conductivity (κ_{lat}) of $Sn_{1-x}Sb_xTe$ samples (x = 0-0.2). (e) Room-temperature lattice thermal conductivity as a function of Sb alloying fraction x for $Sn_{1-x}Sb_xTe$, 10% error bars are indicated. The dashed line is a solid solution line predicted by the Klemens model.[33] (f) Comparison of the room temperature κ_{lat} of the present $Sn_{0.85}Sb_{0.15}Te$ sample with the previously reported high performance $Sn_{1-x}In_xTe$,[19] Hg/Mn/Cd[9,17,23] alloyed SnTe and SnTe-$AgBiTe_2$[16].

For $Sn_{0.96}Sb_{0.04}Te$, $Sn_{0.92}Sb_{0.08}Te$ and $Sn_{0.88}Sb_{0.12}Te$, experimental κ_{lat} values agree well with the alloy scattering model, indicating the point defect scattering caused by Sb alloying as the dominant factor for phonon scattering with low Sb content in SnTe (Figure 5.3e). However,when x is > 0.12 in $Sn_{1-x}Sb_xTe$, the experimental κ_{lat} lies far below the

Klemens theory line, indicating that additional phonon scattering mechanisms are operative in addition to point defect scattering. The minimum κ_{lat} values obtained in the present $Sn_{1-x}Sb_xTe$ ingot samples are indeed lower than those previously reported for the $Sn_{1-x}In_xTe$,[10,19] Hg/Mn/Cd alloyed SnTe[9,17,23] and SnTe–$AgBiTe_2$ system[16] (Figure 5.3f). Temperature dependent κ_{lat} of $Sn_{0.85}Sb_{0.15}Te$ is found to be close to the theoretical minimum of the lattice thermal conductivity of SnTe (Figure 5.3d and 5.3f), which is calculated by the use of the model proposed by Cahill *et al*.[34]

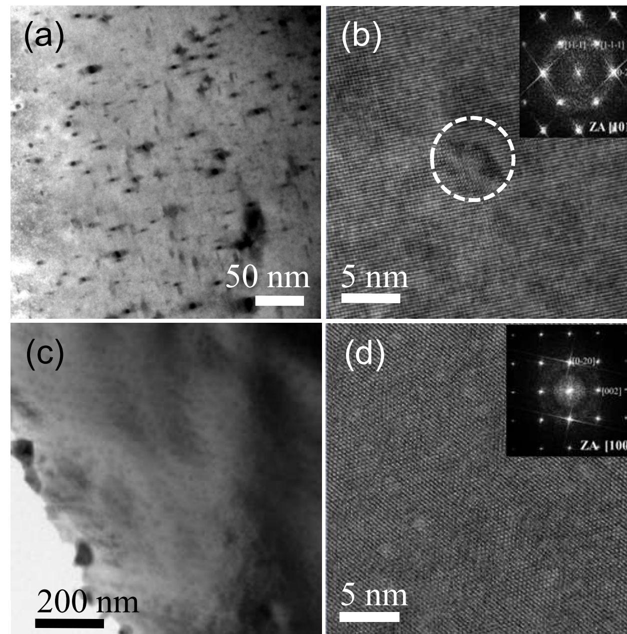

Figure 5.4 Transmission electron microscopy of samples $Sn_{0.96}Sb_{0.04}Te$ and $Sn_{0.92}Sb_{0.08}Te$. (a) Low-magnification TEM image of sample $Sn_{0.96}Sb_{0.04}Te$ showing nanoscale precipitates. (b) HRTEM image of one of the precipitates of $Sn_{0.96}Sb_{0.04}Te$ sample , showing coherent interfaces, highlighted by the circle. The corresponding inset FFT pattern indexed to the cubic rocksalt parent structure. (c) Low-magnification TEM images of the sample shows nanoscale precipitates of $Sn_{0.92}Sb_{0.08}Te$. (d) HRTEM image of $Sn_{0.92}Sb_{0.08}Te$ showing presence of criss-cross lines with 60^0 angle between them. The corresponding inset FFT pattern indexed to the cubic rocksalt parent structure.

In order to investigate the underlying mechanisms of the observed low lattice thermal conductivities of $Sn_{1-x}Sb_xTe$, we have performed a detailed nanostructural examination using transmission electron microscopy (TEM) (see Figure 5.4 and Figure 5.5). Although the PXRD patterns of $Sn_{1-x}Sb_xTe$, x<0.12 indicate ''single phase'' nature, TEM images of $Sn_{1-x}Sb_xTe$ revealed the presence of numerous nanoscale precipitates thought to be favorable for phonon scattering. The TEM images of all ingots showed similar features, and therefore we only show images from the samples of the composition $Sn_{0.96}Sb_{0.04}Te$, $Sn_{0.92}Sb_{0.08}Te$ and $Sn_{0.85}Sb_{0.15}Te$. In Figure 5.4a, 5.4c and 5.5a, low magnification TEM images of $Sn_{0.96}Sb_{0.04}Te$, $Sn_{0.92}Sb_{0.08}Te$ and $Sn_{0.85}Sb_{0.15}Te$ confirm the presence of various

nanoscale precipitates (2–10 nm) with a dark contrast. The endotaxial nature of the nanoprecipitates was confirmed from the electron diffraction pattern, shown in the inset of figure 5.4b and 5.4d, which can be indexed based only on the cubic rocksalt SnTe structure. The size of these small endotaxial nanoprecipitates is similar to that of the mean free path of the heat carrying phonon in SnTe, thus they effectively scatter phonons and reduce κ_{lat} in SnTe. Though it is difficult to quantitatively determine the exact compositions of individual precipitates owing to their overlap with the matrix, energy dispersive X-ray spectroscopy (EDAX) indicates an increase in the Sb signal from the precipitates compared with the matrix regions (Spot m and n in Figure 5.5a; in spot m, atomic percentages of Sn, Sb and Te are 38.7, 2.3 and 58.82, respectively; in spot n, atomic percentages of Sn, Sb and Te are 49.8, 13 and 38.42, respectively).

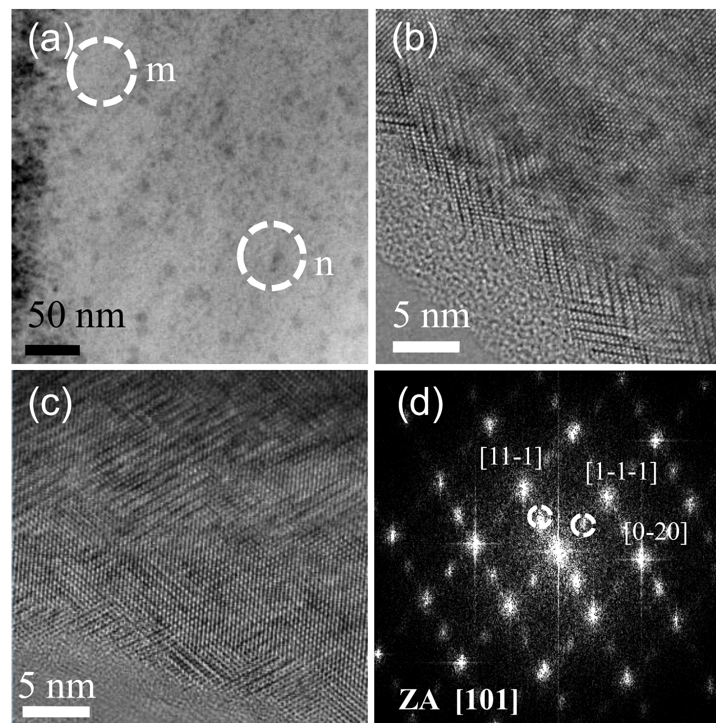

Figure 5.5 (a) Low-magnification TEM image of sample $Sn_{0.85}Sb_{0.15}Te$ showing nanoscale domains highlighted by circles m and n. (b) and (c) are HRTEM images of $Sn_{0.85}Sb_{0.15}Te$ showing the nanodomains of layered intergrowth nanostructures. (d) Electron diffraction pattern indexed to the cubic rocksalt parent structure with white circles indicating superstructure ordering along [111] plane.

For further analysis, we have performed high-resolution TEM (HRTEM) investigations on $Sn_{1-x}Sb_xTe$ samples. Figure 5.4b shows typical phase contrast HRTEM image containing several nanoprecipitates for $Sn_{0.96}Sb_{0.04}Te$. High-resolution imaging shows that the nano inclusions are coherent with the matrix. Such a coherent interface can

contribute to the scattering of phonon with medium and long wavelengths, meanwhile maintaining good carrier transport without excessive scattering.[35] Therefore, under appropriate carrier doping one can expect relatively high mobility. Hence, these nanoscale features are unique in terms of enhancing the performance of thermoelectric properties of SnTe. The HRTEM image of $Sn_{0.92}Sb_{0.08}Te$ shows the existence of characteristics layered criss-cross lines oriented along [111] planes with 60° angle between them (see Figure 5.4d). Such layered nanostructures (10–30 nm) become prominent in the $Sn_{0.85}Sb_{0.15}Te$ sample (see Figure 5.5b & 5.5c). These HRTEM images indicate the presence of layered superstructure nanodomains with features similar to those exhibited in $Na_{1-x}Pb_mSb_yTe_{m+2}$ samples.[36] The superlattice spots along the <111> direction are observed in the fast Fourier transform (FFT) image of the $Sn_{0.85}Sb_{0.15}Te$ sample (see Fig. 5.5d). This indicates a doubling of the lattice period along the <111> directions in real space. At higher Sb concentrations, local Sb segregation along the <111> directions of cubic SnTe forms the nanodomains of layered intergrowth $Sn_mSb_{2n}Te_{3n+m}$, which are embedded in SnTe matrix.

Hence, the presence of superlattice spots along the <111> direction and an extra peak in the PXRD pattern of $Sn_{0.85}Sb_{0.15}Te$ indicate the formation of layered intergrowth nanostructures of Sb rich $Sn_mSb_{2n}Te_{3n+m}$ compounds. These compounds are known to show superstructure ordering spots in electron diffraction due to the modulated intergrowth structure and large unit cell.[37] Superlattice structures generally affect the κ_{lat} via various ways, including modification of the phonon spectrum and phonon localization, and diffuse or specular scattering of phonons at interfaces due to acoustic mismatch.[38,39] Here, the presence of nanodomains of Sb rich layered $Sn_mSb_{2n}Te_{3n+m}$ in SnTe scatters the phonons efficiently through both (a) the interface between matrix (SnTe) and nanodomain and (b) the interfaces between the heterostructured layers within $Sn_mSb_{2n}Te_{3n+m}$. The melting points of most of the layered intergrowth compounds in the homologous series, $M_m(Sb/Bi)_{2n}Te_{3n+m}$, where M: Ge/Sn/Pb, are incongruent; thus, the synthesis of pure bulk phases through traditional high-temperature solid-state melting techniques is really challenging.[29,30,40] Here, we show the stabilization of these layered intergrowth phases in the form of nanodomains through matrix encapsulation, which is intriguing in terms of fundamental solid state inorganic chemistry. Earlier, kinetic low

temperature syntheses have been demonstrated the stabilization of the pure-phase compounds in the $Pb_mBi_{2n}Te_{3n+m}$ family in the form of layered nanosheets.[30]

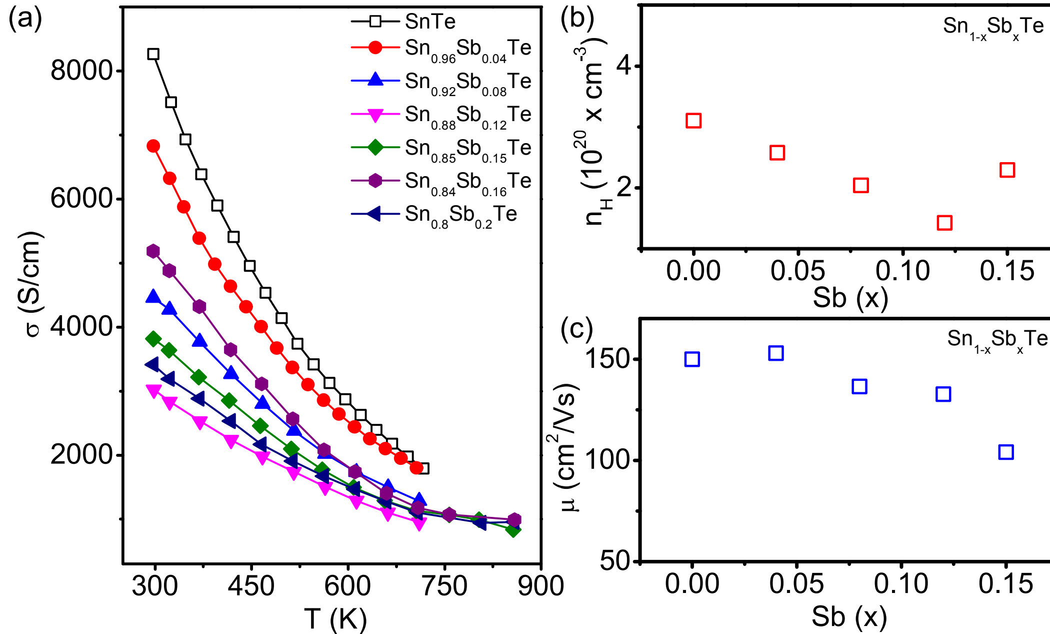

Figure 5.6 (a) Temperature dependent electrical conductivity (σ) of $Sn_{1-x}Sb_xTe$ samples (x = 0-0.2). (b) Carrier concentration (n_H) and (c) carrier mobility (μ) at room temperature with respect to Sb alloying concentration (x) in $Sn_{1-x}Sb_xTe$ (x = 0–0.20).

Figure 5.6 shows the temperature dependent electrical transport properties of $Sn_{1-x}Sb_xTe$ samples. The room temperature Hall coefficients, R_H, of all $Sn_{1-x}Sb_xTe$ (x = 0–0.20) samples are positive, which indicate the *p*-type conduction in this system. For all samples, the electrical conductivity (σ) decreases with the increase in temperature, which is typically observed for a degenerate semiconductor (Figure 5.6a). At room temperature, σ decreases gradually with the increase in donor Sb content in SnTe due to the systematic reduction in *p*-type carrier concentration, n_H (Figure 5.6b). The reduction of hole concentration is attributed to the substitution of aliovalent Sb^{3+} at the Sn^{2+} site in SnTe that contributes the excess electrons to the system from the chemical valence count. Near room temperature, pristine SnTe exhibits a σ value of ~8269 S/cm, which drastically reduces to ~3032 S/cm for the composition of $Sn_{0.88}Sb_{0.12}Te$. Further increase in Sb concentration above x = 0.12 leads to an increase in the σ value from ~3032 S/cm to ~3816 S/cm for the $Sn_{0.85}Sb_{0.15}Te$ sample. The increase in the σ value of Sb concentration above 12 mol% in SnTe is attributed to the increase in hole concentration (Figure 5.6), which results due to the phase separation of Sb-rich $Sn_mSb_{2n}Te_{3n+m}$ nanodomains. This

phase segregation is correlated with the formation of nanostructures, which actually alters the chemical composition of the matrix, and thereby the hole density.[16] A mention must be made that the carrier mobility (μ) remains nearly same (Figure 5.6c) in the case of lower Sb content in SnTe due to endotaxial nature of the nanoprecipitates, which is indeed beneficial for electronic transport.

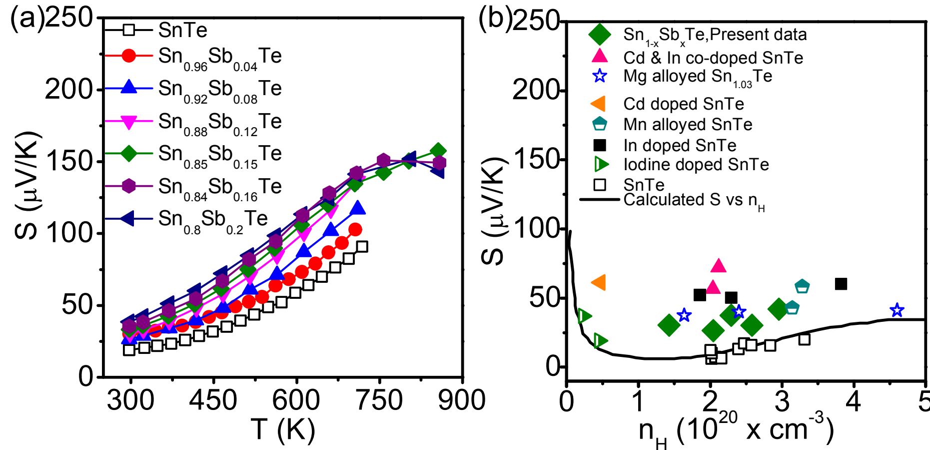

Figure 5.7 (a) Temperature dependent Seebeck coefficient (S) of $Sn_{1-x}Sb_xTe$ samples (x = 0–0.2). (b) Room temperature S vs. n_H plot of the present $Sn_{1-x}Sb_xTe$ samples. For comparison, previously reported S vs. n_H experimental data of un-doped SnTe,[41] Cd and In doped SnTe,[21] Mg alloyed SnTe,[8] Cd doped SnTe,[9] Mn doped SnTe,[11] In doped SnTe,[19] iodine doped SnTe[15] and theoretical Pisarenko curve based on VBM model[19] are given in (b).

Figure 5.7a represents the temperature dependence of Seebeck coefficient (S) of $Sn_{1-x}Sb_xTe$ samples (x = 0–0.20). A positive value of S indicates the p-type conduction in the measured temperature range of 300–860 K, which agrees with the Hall measurement. Pristine SnTe exhibits an S value of ~20 μV/K at 300 K and reaches the maximum value of ~90 μV/K at 700 K. The substitution of Sb in SnTe significantly increases the S value from ~20 μV/K to ~40 μV/K at 300 K. Typically, the room temperature S value of $Sn_{0.85}Sb_{0.15}Te$ is ~34 μV/K, which increases with temperature and reaches the maximum value of ~158 μV/K at 856 K. Above 800 K, S starts decreasing with further increase in temperature for $Sn_{1-x}Sb_xTe$, x>0.15, which corresponds to the onset of bipolar conduction. A room temperature Pisarenko plot, Seebeck coefficient (S) as a function of carrier density (n_H), of $Sn_{1-x}Sb_xTe$ is shown in Figure 5.7b. Theoretical Pisarenko curves have been calculated by considering the contribution of both the light hole (L point) and heavy hole valence band (Σ point) of un-doped SnTe. Here, we have compared the present S vs. n_H data of the present $Sn_{1-x}Sb_xTe$ with the previously reported data of In doped SnTe,[19] Mg doped SnTe,[8] Cd doped SnTe,[9] Mn alloyed SnTe,[11] iodine doped

SnTe,[14,15] and Cd and In co-doped SnTe,[21] and also with the earlier reported theoretical S vs. n_H curve by Zhang *et al*[19]. Particularly, *S* values of $Sn_{1-x}In_xTe$ and Cd/Mg/Hg/Mn alloyed SnTe samples lie far above the theoretical Pisarenko line due to the effect of resonance level formation and valence band convergence, respectively. Here, room temperature *S* values of $Sn_{1-x}Sb_xTe$ samples also reside slightly above the Pisarenko curve. The widely dispersed nanostructures in SnTe are responsible for this unusual behavior. This originates probably due to energy dependent scattering of carriers, leading to an energy filtering effect that enhances the Seebeck coefficient.[42] Similar trend was earlier observed for $AgSbTe_2$–SnTe based alloys.[43]

Figure 5.8a presents temperature dependence of the power factor (σS^2) of $Sn_{1-x}Sb_xTe$ (x = 0–0.20) samples. Benefiting from optimized electrical conductivity and enhancement in Seebeck coefficients, the $Sn_{1-x}Sb_xTe$ samples exhibit significantly higher power factors than those of pristine SnTe samples, with maximum values touching ~25 μW/cmK^2 for $Sn_{0.84}Sb_{0.16}Te$ at 750 K. In Figure 5.8b, we have presented temperature dependent thermoelectric figure of merits, *zT*, of $Sn_{1-x}Sb_xTe$ (x = 0–0.20). The samples show a systematic increase of *zT* with the increasing Sb content in SnTe at around room temperature; however, the occurrence of bipolar conduction seen in the samples with high Sb content (x = 0.15) leads to the deterioration of *zT* at high temperatures. The highest *zT* value of ~1 was achieved for $Sn_{0.85}Sb_{0.15}Te$ at 800 K, which is significantly higher compared to the undoped SnTe sample.

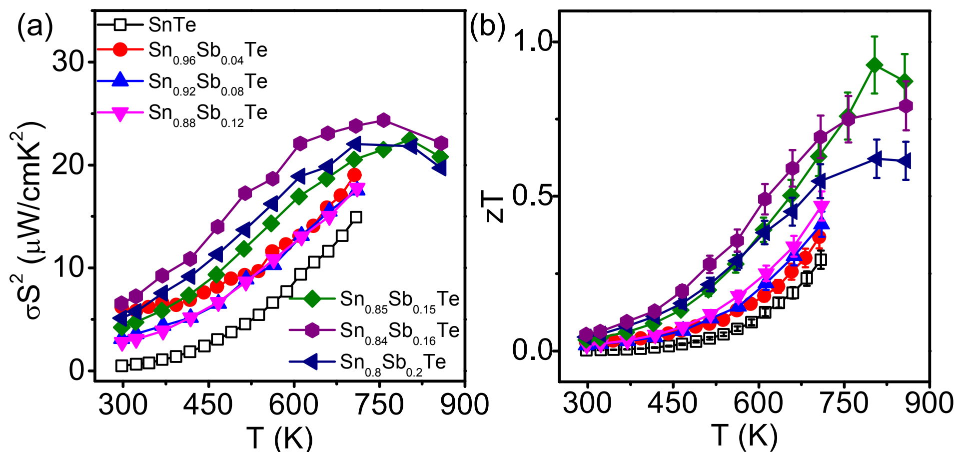

Figure 5.8 Temperature dependence of (a) power factor (σS^2) and (b) *zT* of $Sn_{1-x}Sb_xTe$ samples (x = 0–0.2).

Besides the promising *zT*, one has to look for the good mechanical properties of thermoelectric materials for massmarket applications. The micro-hardness values of SnTe

and $Sn_{0.85}Sb_{0.15}Te$ samples were measured on the Vickers scale using the micro-hardness indentation method (Figure 5.9). Undoped SnTe has a hardness value of ~65 H_V. The substitution of Sb in SnTe increases the micro-hardness value to ~136 H_V (~109% increment in H_V value) for the composition of $Sn_{0.85}Sb_{0.15}Te$. The increase in Vickers micro-hardness (H_V) in $Sn_{1-x}Sb_xTe$ is mainly due to the significant reduction of defects and Sn vacancies caused by Sb substitution. Additionally, nanoscale precipitates block the movement of dislocations in SnTe, which further improves the micro-hardness in $Sn_{1-x}Sb_xTe$. The obtained micro-hardness value of ~136 H_V for $Sn_{0.85}Sb_{0.15}Te$ is significantly higher than that of the state of-the-art thermoelectric materials such as Bi_2Te_3,[44] PbTe,[45] $Pb_{1-x}Sn_xTe$,[46] PbSe,[47] Cu_2S,[48] and Cu_2Se[48].

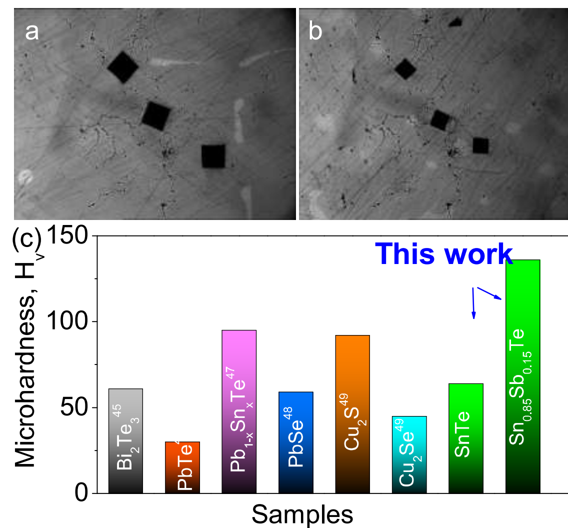

Figure 5.9 (a) and (b) are Vickers micro indentation of SnTe and $Sn_{0.85}Sb_{0.15}Te$, respectively. (c) Vickers microhardness value (H_v) of $Sn_{1-x}Sb_xTe$ (x=0, 0.15) samples are compared with other thermoelectric materials.

5.4 Conclusions

In conclusion, $Sn_{1-x}Sb_xTe$ exhibits an ultralow lattice thermal conductivity approaching the theoretical minimum limit, which is attributed to the formation of spontaneous nanodomains of Sb rich layered intergrowth $Sn_mSb_{2n}Te_{3n+m}$ in SnTe through matrix encapsulation. The segregation of Sb along the <111> direction of SnTe leads to the formation of superlattice structure which resulted in significant phonon scattering to effectively lower κ_{lat}. Additionally, Sb doping in SnTe decreases *p*-type carrier density

due to aliovalent donor dopant nature of Sb^{3+} at the Sn^{2+} site in SnTe. A significant enhancement in the Seebeck coefficient has been achieved due to simultaneous reduction of carrier density and carrier filtering through superstructure nanodomain formation. Hence, the enhanced thermoelectric figure of merit, zT, of ~1 at 800 K has been obtained for the composition of $Sn_{0.85}Sb_{0.15}Te$. For the high zT sample, the measured Vickers microhardness value was ~136 H_V, which is about ~109% higher compared to that of pristine SnTe (~65 H_V).

5.5 References

1. G. J. Snyder and E. S. Toberer, *Nat. Mater.*, 2008, **7**, 105.
2. K. Biswas, J. He, I. D. Blum, C.-I. Wu, T. P. Hogan, D. N. Seidman, V. P. Dravid and M. G. Kanatzidis, *Nature*, 2012, **489**, 414.
3. Y. Pei, X. Shi, A. LaLonde, H. Wang, L. Chen and G. J. Snyder, *Nature*, 2011, **473**, 66.
4. K. Biswas, J. He, Q. Zhang, G. Wang, C. Uher, V. P. Dravid and M. G. Kanatzidis, *Nat. Chem.*, 2011, **3**, 160.
5. K. Biswas, J. He, G. Wang, S.-H. Lo, C. Uher, V. P. Dravid and M. G. Kanatzidis, *Energy Environ. Sci.*, 2011, **4**, 4675.
6. S. N. Girard, J. He, X. Zhou, D. Shoemaker, C. M. Jaworski, C. Uher, V. P. Dravid, J. P. Heremans and M. G. Kanatzidis, *J. Am. Chem. Soc.*, 2011, **133**, 16588.
7. J. P. Heremans, V. Jovovic, E. S. Toberer, A. Saramat, K. Kurosaki, A. Charoenphakdee, S. Yamanaka and G. J. Snyder, *Science*, 2008, **321**, 554.
8. A. Banik, U. S. Shenoy, S. Anand, U. V. Waghmare and K. Biswas, *Chem. Mater.*, 2015, **27**, 581.
9. G. Tan, L.-D. Zhao, F. Shi, J. W. Doak, S.-H. Lo, H. Sun, C. Wolverton, V. P. Dravid, C. Uher and M. G. Kanatzidis, *J. Am. Chem. Soc.*, 2014, **136**, 7006.
10. A. Banik and K. Biswas, *J. Mater. Chem. A*, 2014, **2**, 9620.
11. G. Tan, F. Shi, S. Hao, H. Chi, T. P. Bailey, L.-D. Zhao, C. Uher, C. Wolverton, V. P. Dravid and M. G. Kanatzidis, *J. Am. Chem. Soc.*, 2015, **137**, 11507.
12. R. Al Rahal Al Orabi, N. A. Mecholsky, J. Hwang, W. Kim, J.-S. Rhyee, D. Wee and M. Fornari, *Chem. Mater.*, 2016, **28**, 376.
13. J. He, X. Tan, J. Xu, G. Liu, H. Shao, Y. Fu, X. Wang, Z. Liu, J. Xu, H. Jiang and J. Jiang, *J. Mater. Chem. A*, 2015, **3**, 19974.
14. A. Banik and K. Biswas, *J. Solid State Chem.*, 2016, **242**, 43.
15. M. Zhou, Z. M. Gibbs, H. Wang, Y. Han, C. Xin, L. Li and G. J. Snyder, *Phys. Chem. Chem. Phys.*, 2014, **16**, 20741.
16. G. Tan, F. Shi, H. Sun, L.-D. Zhao, C. Uher, V. P. Dravid and M. G. Kanatzidis, *J. Mater. Chem. A*, 2014, **2**, 20849.
17. G. Tan, F. Shi, J. W. Doak, H. Sun, L.-D. Zhao, P. Wang, C. Uher, C. Wolverton, V. P. Dravid and M. G. Kanatzidis, *Energy Environ. Sci.*, 2015, **8**, 267.
18. L.-D. Zhao, X. Zhang, H. Wu, G. Tan, Y. Pei, Y. Xiao, C. Chang, D. Wu, H. Chi, L. Zheng, S. Gong, C. Uher, J. He and M. G. Kanatzidis, *Journal of the American Chemical Society*, 2016, **138**, 2366.
19. Q. Zhang, B. Liao, Y. Lan, K. Lukas, W. Liu, K. Esfarjani, C. Opeil, D. Broido, G. Chen and Z. Ren, *Proc. Natl. Acad. Sci. USA* 2013, **110**, 13261.
20. G. Tan, W. G. Zeier, F. Shi, P. Wang, G. J. Snyder, V. P. Dravid and M. G. Kanatzidis, *Chem. Mater.*, 2015, **27**, 7801.
21. G. Tan, F. Shi, S. Hao, H. Chi, L.-D. Zhao, C. Uher, C. Wolverton, V. P. Dravid and M. G. Kanatzidis, *J. Am. Chem. Soc.*, 2015, **137**, 5100.
22. O. Falkenbach, A. Schmitz, T. Dankwort, G. Koch, L. Kienle, E. Mueller and S. Schlecht, *Chem. Mater.*, 2015, **27**, 7296.
23. H. Wu, C. Chang, D. Feng, Y. Xiao, X. Zhang, Y. Pei, L. Zheng, D. Wu, S. Gong, Y. Chen, J. He, M. G. Kanatzidis and L.-D. Zhao, *Energy Environ. Sci.*, 2015, **8**, 3298.
24. J. R. Sootsman, R. J. Pcionek, H. Kong, C. Uher and M. G. Kanatzidis, *Chem. Mater.*, 2006, **18**, 4993.

25. P. F. P. Poudeu, J. D'Angelo, H. Kong, A. Downey, J. L. Short, R. Pcionek, T. P. Hogan, C. Uher and M. G. Kanatzidis, *J. Am. Chem. Soc.*, 2006, ***128***, 14347.
26. K. F. Hsu, S. Loo, F. Guo, W. Chen, J. S. Dyck, C. Uher, T. Hogan, E. K. Polychroniadis and M. G. Kanatzidis, *Science*, 2004, **303**, 818.
27. J. R. Sootsman, H. Kong, C. Uher, J. J. D'Angelo, C. I. Wu, T. P. Hogan, T. Caillat and M. G. Kanatzidis, *Angew. Chem.* , 2008, **120**, 8746.
28. K. Hoang, S. D. Mahanti and M. G. Kanatzidis, *Phys. Rev. B*, 2010, **81**, 115106.
29. L. E. Shelimova, O. G. Karpinskii, P. P. Konstantinov, E. S. Avilov, M. A. Kretova and V. S. Zemskov, *Inorg. Mater.*, 2004, **40**, 451.
30. A. Chatterjee and K. Biswas, *Angew. Chem., Int. Ed.*, 2015, **54**, 5623.
31. B. A. Kuropatwa and H. Kleinke, *Z. Anorg. Allg. Chem.*, 2012, **638**, 2640.
32. L.-D. Zhao, S.-H. Lo, J. He, H. Li, K. Biswas, J. Androulakis, C.-I. Wu, T. P. Hogan, D.-Y. Chung, V. P. Dravid and M. G. Kanatzidis, *J. Am. Chem. Soc.*, 2011, **133**, 20476.
33. P. G. Klemens, *Phys. Rev.*, 1960, **119**, 507.
34. D. G. Cahill, S. K. Watson and R. O. Pohl, *Phys. Rev. B*, 1992, **46**, 6131.
35. G. Tan, L.-D. Zhao and M. G. Kanatzidis, *Chem. Rev.*, 2016, **116**, 12123.
36. P. F. P. Poudeu, J. D'Angelo, A. D. Downey, J. L. Short, T. P. Hogan and M. G. Kanatzidis, *Angew. Chem., Int. Ed.*, 2006, **118**, 3919.
37. S. Kuypers, G. van Tendeloo, J. van Landuyt and S. Amelinckx, *J. Solid State Chem.*, 1988, **76**, 102.
38. P. Hyldgaard and G. D. Mahan, *Phys. Rev. B*, 1997, **56**, 10754.
39. G. Chen, *Phys. Rev. B*, 1998, **57**, 14958.
40. Z. S. Aliev, G. I. Ibadova, J.-C. Tedenac and M. B. Babanly, *J. Alloys Compd.*, 2014, **602**, 248.
41. R. Brebrick and A. Strauss, *Phys. Rev.*, 1963, **131**, 104.
42. S. V. Faleev and F. Léonard, *Phys. Rev. B*, 2008, **77**, 214304.
43. Z.-B. Xing, Z.-Y. Li, Q. Tan, T.-R. Wei, C.-F. Wu and J.-F. Li, *J. Alloys Compd.*, 2014, ***615***, 451.
44. L.-D. Zhao, B.-P. Zhang, J.-F. Li, M. Zhou, W.-S. Liu and J. Liu, *J. Alloys Compd.*, 2008, **455**, 259.
45. A. Crocker and M. Wilson, *J. Mater. Sci.*, 1978, **13**, 833.
46. J. Cui, X. Qian and X. Zhao, *J. Alloys Compd.*, 2003, **358**, 228.
47. M. Darrow, W. White and R. Roy, *J. Mater. Sci.*, 1969, **4**, 313.
48. L. Zhao, X. Wang, F. Y. Fei, J. Wang, Z. Cheng, S. Dou, J. Wang and G. J. Snyder, *J. Mater Chem. A*, 2015, **3**, 9432.

CHAPTER 6

Synthesis and Thermoelectric Transport Properties of Nanosheets of Layered 2D Sn-Chalcogenides

Chapter 6A

Synthetic Nanosheets of Natural van der Waals Heterostructures†

Summary

Creation of new van der Waals heterostructures by stacking different two dimensional (2D) crystals on top of each other in a chosen sequence is the next challenge after discovery of graphene, mono/few layer of h-BN and transition metal dichalcogenides. However, chemical syntheses of van der Waals heterostructures are rather rare than the physical preparation techniques. Layered intergrowth compounds in the homologous series of $Sn_mBi_{2n}Te_{3n+m}$ [i.e. $(SnTe)_m(Bi_2Te_3)_n$] are an attractive class of compounds as they resemble to natural van der Waals heterostructures. Further, the heterostructure stacking may give rise to low lattice thermal conductivity (κ_{lat}) due to significant scattering of phonons at the interfaces. Herein, we demonstrate the kinetic stabilization of 2D ultrathin heterostructure (~1.13-2.35 nm thick) nanosheets of layered intergrowth $SnBi_2Te_4$, $SnBi_4Te_7$ and $SnBi_6Te_{10}$, which belong to $Sn_mBi_{2n}Te_{3n+m}$ homologous series, by a simple solution based synthesis. Few-layer nanosheets indeed exhibit ultralow κ_{lat} of 0.3-0.5 W/mK and semiconducting electronic-transport properties with high carrier mobility. Our finding reveals a unique solution towards the synthesis of 2D natural van der Waals heterostructure nanosheets that allows their scalable production along with controlled manipulation of physical properties.

†*Paper based on this study has been published in* ***Angew. Chem., Int. Ed.***, 2017, *56,* 14561.

6A.1 Introduction

Ultralow thermal conductivity originating from nanoscale stabilization of incongruently melting layered intergrowth $Sn_mSb_{2n}Te_{3n+m}$ compounds in SnTe matrix (Chapter 5) has motivated us to study the design, synthesis and properties of new layered ternary tin chalcogenides.[1-3] Phase homology, representing a collection of structures constructed on the same structural rule with certain unit expanding in different dimensions in standard increments, is a powerful approach for the discovery of new compounds with predictable composition and crystal structure.[1-8] Hence, an attractive way to progress the design and prediction of new layered ternary tin chalcogenides with structural diversity is to identify homology which allows arrangement of phases under a widespread parasol. Several of tetradymite-like layered intergrowth ternary compounds exist in the homologous family with formula $A_m^{IV}B_{2n}^{V}Te_{m+3n}$ (A^{IV} = Ge/Sn/Pb; B^{V} = Sb/Bi), where *m* and *n* represent stoichiometry of ATe and B_2Te_3 respectively.[9-12] These layered compounds contain a broad diversity of mixed-layered structures, resembling the van der Waals heterostructures proposed by A. K. Geim,[13] rather than their parent simple Bi_2Te_3 type structure.

Synthesis and investigation of physical properties of two dimensional (2D) nanosheets of layered compounds are interesting due to intrinsic structural directionality owing to dissimilar interlayer and intralayer interactions.[14-23] Recently, presence of emergent number of new 2D materials in the form of stable nanosheets has motivated worldwide efforts to assimilate distinct 2D materials into van der Waals heterostructures,[13,24-28] which opens a pathway to design and predict new materials with novel properties. Weak interlayer interactions in van der Waals solids assist mechanical exfoliation, intercalation and electrochemical exfoliation followed by van der Waals epitaxy to yield few-layer 2D van der Waals heterostructures solids.[29-32] The major challenge in all these physical preparation techniques relies on temperature and chemical stability of parent material.[13] However, the solution based bottom up chemical syntheses, which offers potential advantages over the existing physical deposition techniques, are rare for 2D nanosheets of van der Waals heterostructure solids.

The wide range of important properties of single/few-layer Bi_2Te_3 in the field of topological materials and thermoelectrics have grown interest to study the layered complex structured compounds in the pseudo-binary homologous intergrowth

$A_m^{IV}B_{2n}^{V}Te_{m+3n}$ (A^{IV} = Ge/Sn/Pb; B^{V} = Sb/Bi) family.[7,11,12,33] The majority of the layered compounds in the above homologous series resembles to natural van der Waals heterostructure and is predicted to be 3D-topological insulators.[34-37] Large unit cell with layered heterostructures are expected to exhibit strong phonon scattering and thereby low thermal conductivity, which is important for thermoelectrics. However, most of the layered compounds from the above series exhibit incongruent melting point (Figure 6A.1a),[4] which creates the synthesis of the phase pure compounds challenging through high-temperature traditional solid-state route.

This chapter presents the chemical synthesis of ultrathin 2D nanosheets of layered intergrowth heterostructures, $SnBi_2Te_4$ (m = 1, n = 1), $SnBi_4Te_7$ (m = 1, n = 2) and $SnBi_6Te_{10}$ (m = 1, n = 3) in the $Sn_mBi_{2n}Te_{3n+m}$ homologous family by a simple low temperature solution based method. Efforts to synthesize these compounds in the pure bulk phase by conventional solid state melting at high temperatures followed by cooling are failed due to incongruent melting points (Figure 6A.1a). Only low temperature kinetic bottom up synthesis enables us to stabilize the pure compounds in the form of 2D van der Waals heterostructured nanosheets. High-angle annular dark-field scanning transmission electron microscopy (HAADF-STEM) and high resolution transmission electron microscopy (HRTEM) reveal the stacking sequence and van der Waals heterostructure nature of the $Sn_mBi_{2n}Te_{3n+m}$ nanosheets. Thickness of the nanosheets ranges from 1.13 nm to 2.35 nm and lateral dimension ranges from 1 μm to 2 μm, respectively, which are confirmed by atomic force microscopy (AFM). Temperature dependent electrical transport data reveals the semiconducting electronic transport with high carrier mobility in $Sn_mBi_{2n}Te_{3n+m}$ nanosheets. Importantly, nanosheets of homologous $Sn_mBi_{2n}Te_{3n+m}$ compounds exhibit ultra low lattice thermal conductivity, κ_{lat} (~0.3-0.5 W/mK) due to significant phonon scattering by heterostructure surfaces/interfaces with long unit cell and stacking faults.

6A.2 Methods

6A.2.1 Synthesis

Tin (II) acetate ($Sn(OAc)_2$, Sigma Aldrich), bismuth neodecanoate (90%, Alfa Aesar), tellurium (99.999%, Alfa Aesar), oleylamine (tech. 90%, Sigma Aldrich), tri-*n*-

octylphosphine (tech. 90%, Sigma Aldrich) and 1-dodecanethiol (98%, Alfa Aesar) were used for syntheses without further purification.

Synthesis of $SnBi_2Te_4$ nanosheets. In a typical synthesis, 30 mg (0.126 mmol) of $Sn(OAc)_2$ and 10 mL oleylamine were taken in a 50 mL three neck round bottom flask and heated at 120 °C for 2 hrs under vacuum. The temperature of the resulting solution was raised to 180 °C and kept for 1hr under N_2 atmosphere. The solution was cooled down to room temperature and 183.16 mg (0.253 mmol) of bismuth neodecanoate was added into the clear solution. Then, the reaction mixture was heated to 70 °C under N_2 atmosphere and 1-dodecanthiol was added dropwise. The color of the solution changed to pale yellow. For the complete formation of tin bismuth dodecanethiolate complex, the solution temperature was maintained at 70 ^oC for 10 min. Finally, the solution temperature was increased to 90 ^oC, and a solution of tri-*n*-octylphosphine telluride (TOP-Te) was immediately injected into it (64.66 mg or 0.507 mmol Te). Black colored suspension was observed, which was aged for 2 hrs at 200 ^oC under N_2 atmosphere. Black colored nanosheets of $SnBi_2Te_4$ were precipitated out by adding a 1:1 mixture of hexane and ethanol.

Synthesis of $SnBi_4Te_7$ nanosheets. $SnBi_4Te_7$ nanosheets were synthesized via the similar procedure using stoichiometric ratios of $Sn(OAc)_2$, bismuth neodecanoate and TOP-Te. In a typical synthesis, 30 mg (0.126 mmol) of $Sn(OAc)_2$ and 10 ml oleylamine were taken in a 50 mL three neck round bottom flask and heated at 120 °C for 2 hrs under vacuum. The temperature of the resulting solution was raised to 180 °C and kept for 1hr under N_2 atmosphere. The solution was cooled down to room temperature and 366.32 mg (0.506 mmol) of bismuth neodecanoate was added into the clear solution. Then, the reaction mixture was heated to 70 °C and 1-dodecanthiol was added drop wise. The color of the solution changed to pale yellow. For the complete formation of tin bismuth dodecanethiolate complex, the solution temperature was maintained at 70 ^oC for 10 min. Finally, the solution temperature was increased to 90 ^oC, and a solution of TOP-Te was immediately injected into it (113.14 mg or 0.886 mmol Te). Black colored suspension was observed, which was aged for 2 hrs at 200 ^oC under N_2 atmosphere. Black colored

nanosheets of $SnBi_4Te_7$ were precipitated out by adding a 1:1 mixture of hexane and ethanol.

Synthesis of $SnBi_6Te_{10}$ nanosheets. $SnBi_6Te_{10}$ nanosheets were synthesized via the similar procedure using stoichiometric ratios of $Sn(OAc)_2$, bismuth neodecanoate and TOP-Te. In a typical synthesis, 30 mg (0.126 mmol) of $Sn(OAc)_2$ and 10 mL oleylamine were taken in a 50 mL three neck round bottom flask and heated at 120 °C for 2 hrs under vacuum. The temperature of the resulting solution was raised to 180 °C and kept for 1hrs under N_2 atmosphere. The solution was cooled down to room temperature and 548.56 mg (0.759 mmol) of bismuth neodecanoate was added into the clear solution. Then, the reaction mixture was heated to 70 °C under N_2 atmosphere and 1-dodecanthiol was added dropwise. The color of the solution changed to pale yellow. For the complete formation of tin bismuth dodecanethiolate complex, the solution temperature was maintained at 70 ^{o}C for 10 min. Finally, the solution temperature was increased to 90 ^{o}C, and a solution of TOP-Te was immediately injected into it (161.73 mg or 1.267 mmol Te). Black colored suspension was observed, which was aged for 2 hrs at 200 ^{o}C under N_2 atmosphere. Black colored nanosheets of $SnBi_6Te_{10}$ were precipitated out by adding a 1:1 mixture of hexane and ethanol.

Synthesis of bulk $SnBi_2Te_4$. Bulk polycrystalline ingot of $SnBi_2Te_4$ were synthesized by mixing stoichiometric ratios of high-purity starting materials of Sn, Bi and Te in a quartz tube. The tubes were sealed under vacuum (10^{-5} Torr) and slowly heated to 800 ^{o}C over 12 hrs, soaked at 800 ^{o}C for 10 hrs followed by water quenching.

Removal of capping ligands. In order to measure the electrical and thermal transport properties, the organic capping ligands was removed from the surface of nanosheets by treating nanosheets with hydrazine in chloroform-methanol mixture. Typically, 400 mg as prepared nanosheets were treated with chloroform (~4 ml), methanol (~1.5 ml) and hydrazine (~6 ml) under vigorous stirring. The surfactant free nanosheets were washed several times with ethanol and dried at 60 °C under vacuum.

6A.2.2 Characterizations

Powder X-ray diffraction (PXRD) were recorded using a Cu Kα (λ = 1.5406 Å) radiation on a Bruker D8 diffractometer. X-ray photoelectron spectroscopy (XPS) measurements have been performed with Mg–Kα (1253.6 eV) X-ray source with a relative composition detection better than 0.1% on an Omicron Nano-technology spectrometer. Compositions of the as synthesized $Sn_mBi_{2n}Te_{3n+m}$ nanosheets were determined based on ICP-AES data. ICP-AES measurements were done in Perkin-Elmer Optima 7000DV instrument. Samples were prepared by dissolved powdered nanosheets in aqua regia (HNO_3:HCl = 1:3) followed by dilution with Millipore water. Sn standard (1000 mg/L, Sigma-Aldrich), Bi standard (1000 mg/L, Sigma-Aldrich) and Te standard (1000 mg/L, Sigma-Aldrich) were used for these quantitative detection. The experimental error lies within 1.5 % of the measured value. Atomic force microscopy (AFM) was performed on a Bruker Innova Microscope in tapping mode with 10 nm diameter containing antimony doped Silicon tip. Transmission electron microscope (TEM) experiments were performed using FEI TECNAI $G^2$20 STWIN TEM operating at 200 kV and also using an aberration corrected FEI TITAN3 80-300 kV transmission electron microscope operating at 300 kV. Very dilute solution of nanosheets dispersed in ethanol solution was taken in a holey carbon coated Cu grid for TEM imaging. EDAX compositional analysis, elemental line scan and mapping were carried out during STEM imaging in FEI TECNAI $G^2$20 STWIN TEM. Background was subtracted (using multi-polynomial model) during the data processing for EDAX elemental line scan and mapping (with 500 eV minimum region of interest width). High-resolution TEM (HRTEM) and HAADF-STEM images were taken in aberration corrected FEI TITAN3 80-300 kV transmission electron microscope. Field emission scanning electron microscopy (FESEM) experimentations were performed using NOVA NANO SEM 600 (FEI, Germany) operated at 15 kV.

6A.2.3 Transport properties

To measure the thermoelectric properties, surface cleaned nanosheets were induction hot pressed in vacuum in a graphite die by applying pressure of 70 MPa at 473 K for 10 min (far below the phase separation temperature). Hot pressed sample density was about ~97 % of the theoretical density. Electrical conductivity (σ) and Seebeck coefficients (S) were measured simultaneously under He atmosphere from room temperature to 873 K on a

ULVAC-RIKO ZEM-3 instrument system (Details is given in chapter 1). Carrier concentrations were determined Hall coefficient measurements at room temperature with equipment developed by Excel Instrument, India. (Details is given in chapter 1).Thermal diffusivity, *D*, was directly measured in the range 300−873 K by using laser flash diffusivity method in a Netzsch LFA-457. The total thermal conductivity, κ_{total}, was calculated using the formula, $\kappa_{total} = DC_p\rho$ (Details is given in chapter 1).

6A.3 Results & Discussion

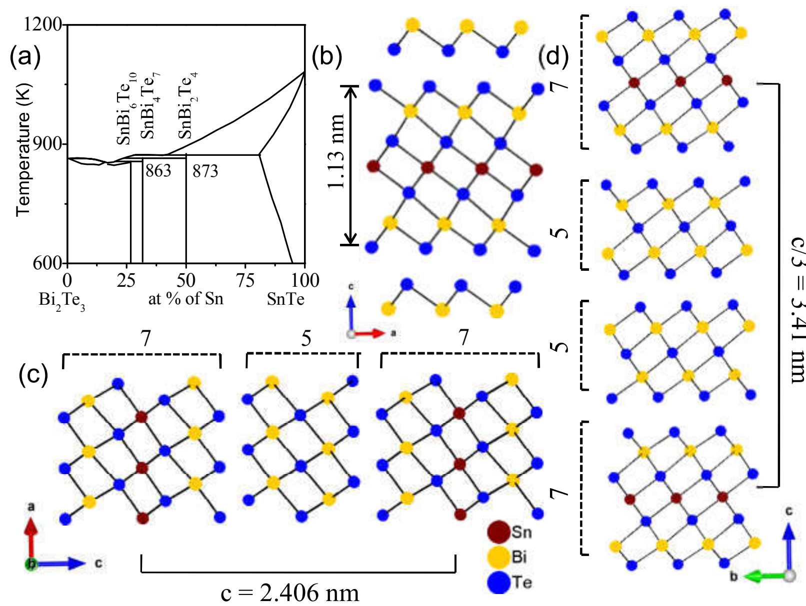

Figure 6A.1 (a) Pseudobinary phase diagram of the SnTe–Bi_2Te_3 homologous family showing the presence of incongruently melting compounds. (b) Crystal structure of $SnBi_2Te_4$ showing the 1.13 nm thick seven layers of $SnBi_2Te_4$. (c) Crystal structure of natural van der Waals heterostructure $SnBi_4Te_7$ showing the stacking of quintuple layers of Bi_2Te_3 and septuple layers of $SnBi_2Te_4$. (d) Crystal structure of $SnBi_6Te_{10}$ showing the stacking of $SnBi_2Te_4$ and Bi_2Te_3 along the c-axis in 7557 sequence.

$SnBi_2Te_4$ [i.e. (SnTe)(Bi_2Te_3)] is a member of $Sn_mBi_{2n}Te_{3n+m}$ homologous series with anisotropic layered tetradymite-type structure (*R*-3*m* space group)(Figure 6A.1b).[4] The unit cell of $SnBi_2Te_4$ consists of septuple layers, which are stacked along the *c*-axis by van der Waals interactions. Each septuple layer is composed of seven covalently bonded atomic planes [Te2–Bi–Te1–Sn–Te1–Bi–Te2] with 1.13 nm thickness.[10,38] The structure of $SnBi_2Te_4$ could be depicted as the intergrowth of rock-salt SnTe and hexagonal Bi_2Te_3 type phases (Figure 6A.1b). The second layered compound, $SnBi_4Te_7$ [i.e.

$(SnTe)_1(Bi_2Te_3)_2$], crystallizes in trigonal structure (*P*-3*m*1 space group) with a long unit cell (c = 2.406 nm). The structure of $SnBi_4Te_7$ is created by two types of subunits, a quintuple layered (QL) Bi_2Te_3 and a septuple layered (SL) $SnBi_2Te_4$, which are stacked along the *c*-axis with maintaining the 5757 sequence by van der Waals interactions (Figure 6A.1c).[4] $SnBi_6Te_{10}$ [i.e. $(SnTe)_1(Bi_2Te_3)_3$] is another example of van der Waals heterostructure solid from this homologous family, where $SnBi_2Te_4$ and Bi_2Te_3 subunits are stacked along the *c*-axis in 7557 sequence (Figure 6A.1d).

We have developed a general procedure to synthesize different heterostructured nanosheets ($SnBi_2Te_4$, $SnBi_4Te_7$ and $SnBi_6Te_{10}$) by only changing nominal composition of the precursors (anhydrous tin acetate, $Sn(OAc)_2$; bismuth neodecanoate and tri-n-octyl phosphine telluride (TOP-Te)). In a typical synthesis, first we have prepared a clear solution of Sn precursor by dissolving anhydrous tin acetate, $Sn(OAc)_2$, in oleylamine at 180 °C under N_2 atmosphere. Then, bismuth neodecanoate (bismuth precursor) was added to the reaction mixture. The resulting solution was then heated to 70 ^oC. Then, 1-dodecanethiol was added at 70 ^oC and maintained at the temperature for 10 min. Formation of tin bismuth dodecanethiolate complex is indicated by the pale yellow color of reaction mixture (Figure 6A.2).[22] Finally, the temperature of the reaction was increased to 90 ^oC, and TOP-Te solution was injected. A black color suspension was identified (Figure 6A.2), which was heated at 200 ^oC for 2 hrs. Black powders of $Sn_mBi_{2n}Te_{3n+m}$ nanosheets were precipitated out by the addition hexane and ethanol (1:1 mixture).

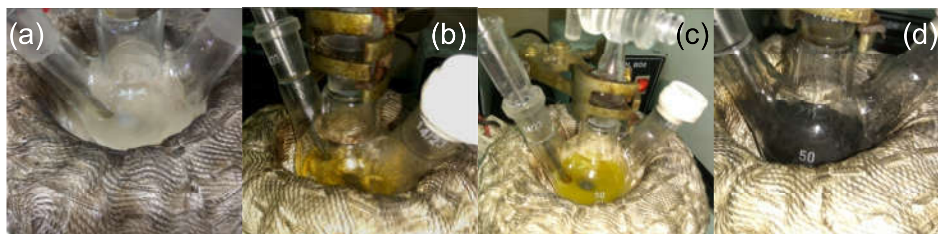

Figure 6A.2 Different steps of the reaction:(a) Milky white solution of $Sn(OAc)_2$ in oleylamine, (b) clear solution, after evacuation at 100 °C for 2 hrs followed by heating at 180 ^oC for 1 hr in N_2 atmosphere, (c) pale yellow color solution of tin bismuth dodecanthiolate complex and (d) black dispersion of $SnBi_2Te_4$ nanosheets after injection of Te-TOP in (c) at 90 °C.

Conventional solid state melting of the constituent elements in vacuum sealed quartz tube (10^{-5} Torr) at 800 ^oC for 10 hrs and subsequent water quenching do not produce phase pure polycrystalline bulk $SnBi_2Te_4$ and $SnBi_4Te_7$. SnTe was identified as an impurity phase with the bulk $SnBi_2Te_4$ (Figure 6A.3a). This is resulting from the incongruent melting of these intergrowth compounds (Figure 6A.1a). Polycrystalline

$SnBi_2Te_4$ and $SnBi_4Te_7$ samples have been synthesized earlier by subsequent heating of required elements above melting point followed by prolonged annealing via peritectic reaction (ca. at 770 K for 1000 hrs).[9] Nanoparticles/nanopowders of $SnBi_2Te_4$ have also been synthesized earlier via solvothermal reaction for long duration (30 hrs), but the solution based synthesis of 2D nanosheets of this compound was not reported so far.[39] The present solution phase kinetic controlled synthesis allows the stabilization of pure compounds, $SnBi_2Te_4$, $SnBi_4Te_7$ and $SnBi_6Te_{10}$, as 2D nanosheets, which is otherwise difficult to achieve via traditional high temperature melting reaction. The problem of phase separation was eliminated in the present low temperature synthesis, where the precursor decomposition and bottom up chemical reactions in solution are the key steps. In addition, the present low temperature soft chemical synthesis is necessary to arrest the pure layered compounds in the form of exotic nanosheets of van der Waals heterostructures.

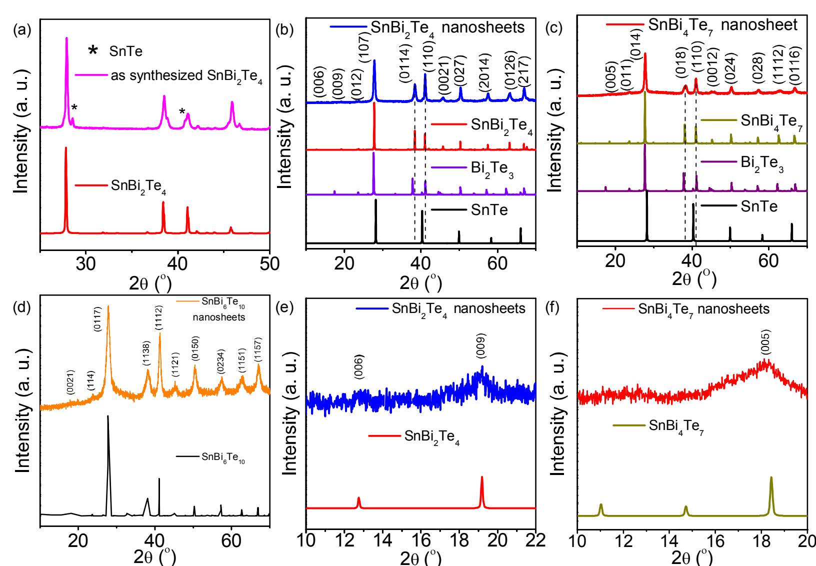

Figure 6A.3 (a) Powder XRD pattern of bulk $SnBi_2Te_4$ synthesized by high temperature melting reaction. SnTe was observed as impurity due to incongruent melting nature of $SnBi_2Te_4$, which has been marked by *. (b), (c) and (d) are PXRD patterns of $SnBi_2Te_4$, $SnBi_4Te_7$ and $SnBi_6Te_{10}$ nanosheets, respectively. Dotted lines confirm the deviation of the PXRD pattern of the $Sn_mBi_{2n}Te_{3n+m}$ nanosheets from that of Bi_2Te_3. (e) and (f) are zoomed PXRD patterns of as synthesized $Sn_mBi_{2n}Te_{3n+m}$ nanosheets. The low intensity of (00*l*) reflections relative to those of bulk counterpart indicate reduced periodicity along the crystallographic *c*-axis, which indirectly suggests formation of 2D nanosheets. Further, different low angle peaks for (00*l*) reflections [eg. $SnBi_2Te_4$, (009) at 19.1° and $SnBi_4Te_7$, (005) at 18.41 °] distinguish the phases from each other and also from Bi_2Te_3.

PXRD patterns of the as prepared samples could be indexed based on pure $SnBi_2Te_4$ (space group *R-3m*; Figure 6A.3b), $SnBi_4Te_7$ (space group *P-3m1*; Figure 6A.3c) and $SnBi_6Te_{10}$ (space group *R-3 m*; Figure 6A.3d). Low intensity of low angle (*00l*)

reflections suggests reduced periodicity along the crystallographic *c*-axis (Figure 6A.3e and 6.3Af). In spite of certain noticeable deviations (eg. the dashed lines in Figure 6A.3b and 6.3Ac; and low angle peaks in Figure 6A.3e and 6.3Af), generally the PXRD patterns of the nanosheets appeared similar to that of Bi_2Te_3, which confirm that layered compounds in the homologues $Sn_mBi_{2n}Te_{3n+m}$ are derived from the parent layered Bi_2Te_3 structure.

The actual elemental compositions of different nanosheet samples were obtained from different techniques like ICP-AES and EDAX. The actual compositions determined by these two independent techniques are indeed near to the nominal compositions (Table 6A.1), which indicate successful control over the composition in the current synthetic technique.

Table 6A.1 Nominal compositions and measured compositions of the as-synthesized $Sn_mBi_{2n}Te_{3n+m}$ nanosheets determined by ICP-AES and EDAX.

Nominal composition	ICP-AES composition	EDAX composition
$SnBi_2Te_4$	$SnBi_{2.4}Te_{3.5}$	$SnBi_{1.68}Te_{3.47}$
$SnBi_4Te_7$	$SnBi_{3.75}Te_{6.28}$	$SnBi_{3.36}Te_{6.33}$
$SnBi_6Te_{10}$	$SnBi_{6.11}Te_{9.34}$	$SnBi_{5.8}Te_{10}$

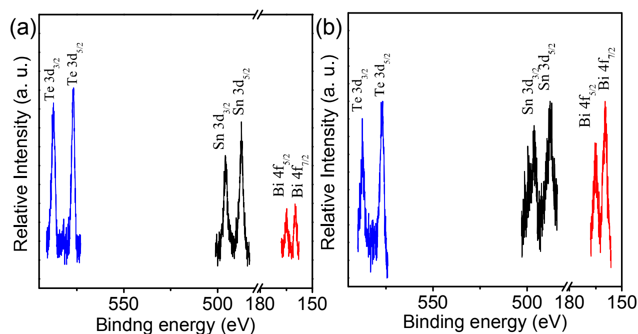

Figure 6A.4 (a) and (b) are XPS spectrum of $SnBi_2Te_4$ and $SnBi_4Te_7$ nanosheets, respectively.

We have also performed XPS on $SnBi_2Te_4$ and $SnBi_4Te_7$ nanosheets (Figure 6A.4a and 6A.4b respectively). The Sn 3d spin-orbit doublet peaks have appeared at 486.14 and 494.54 eV with separation of 8.4 eV, which can be assigned to Sn $3d_{5/2}$ and Sn $3d_{3/2}$, respectively. This is in agreement with binding energy values of Sn (II).[40] Peaks due to Bi $4f_{7/2}$ and Bi $4f_{5/2}$ have appeared at 158.36 and 163.62 eV resulting from Bi (III) states.[41]

Photoelectron spectrum of the Te 3d core level shows two peaks at energies of 572.62 and 582.82 eV which are in good agreement with the binding energies seen in the Te 3d spectra.[11]

Ultrathin nature of different $Sn_mBi_{2n}Te_{3n+m}$ nanosheets has been confirmed from various microscopic technique (Figure 6A.5). AFM demonstrates the freestanding $SnBi_2Te_4$ nanosheets with the thickness of one SL (ca. 1.13 nm) in Figure 6A.5a. The lateral dimension of the $SnBi_2Te_4$ nanosheets ranges from 0.5 to 1 μm. The inset in Figure 6A.5a shows the Tyndall light scattering effect of dispersed $SnBi_2Te_4$ nanosheet in toluene, which confirms colloidal nature of the nanosheets. 2D sheet morphology was further evidenced from TEM (Figure 6A.5b) and FESEM images (inset of Figure 6A.5b). A high-resolution TEM (HRTEM) image of a $SnBi_2Te_4$ nanosheet clearly shows lattice spacing of 0.321 nm, which corresponds to the (107) plane of $SnBi_2Te_4$ (Figure 6A.5c). The selected-area electron diffraction (SAED) pattern measured from a single-sheet of $SnBi_2Te_4$ showed a single-crystalline pattern (inset of Figure 6A.5c). We have also observed polycrystalline SAED pattern from other region due to overlap of several nanosheets, which could be further indexed to pure $SnBi_2Te_4$ (inset of Figure 6A.5c).

The single phase homogeneity was confirmed by EDAX elemental mapping on $SnBi_2Te_4$ nanosheet (Figure 6A.5d) during scanning transmission electron microscopy (STEM). Presence of Sn, Bi and Te in $SnBi_2Te_4$ nanosheet is further confirmed by EDAX elemental line scan during STEM (Figure 6A.5e). In Figure 6A.5f, we show the AFM image of a $SnBi_4Te_7$ nanosheet with a thickness (~ 2.35 nm) of one twelve-layer stack which is formed by successive stacking of a QL of Bi_2Te_3 and a SL of $SnBi_2Te_4$ (see Figure 6A.1c). 2D thin-sheet morphology of the $SnBi_4Te_7$ sample was further confirmed by TEM (Figure 6A.5g). The SAED pattern of the $SnBi_4Te_7$ nanosheet indicates the single-crystalline nature with sixfold symmetry (inset, Figure 6A.5g). HRTEM image of the $SnBi_4Te_7$ nanosheet clearly shows lattice spacing of 0.322 nm, which corresponds to the (014) plane of $SnBi_4Te_7$ (Figure 6A.5h). Lattice parameters calculated from SAED patterns and PXRD data are in close agreement (Table 6A.2). 2D Nanosheet morphology and heterostructure nature of $SnBi_6Te_{10}$ was confirmed using TEM and HRTEM analysis (Figure 6A.5i).

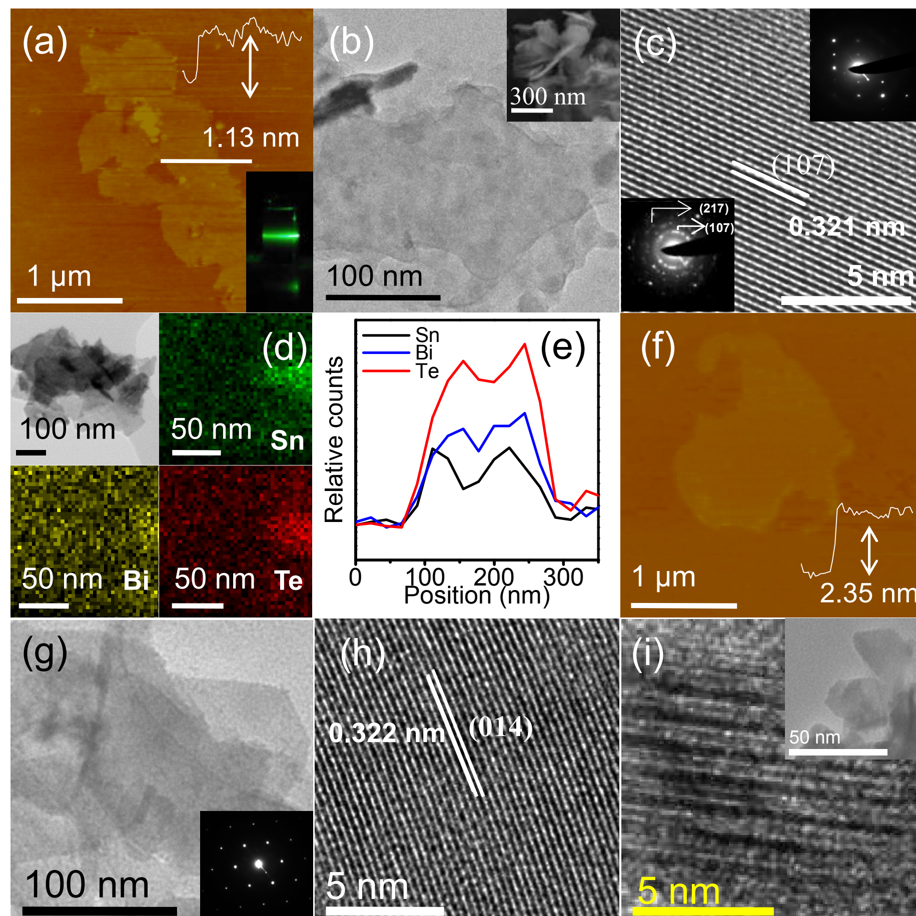

Figure 6A.5 (a) AFM image of a $SnBi_2Te_4$ nanosheet. The inset in (a) shows the Tyndall light scattering effect of $SnBi_2Te_4$ nanosheet dispersed in toluene. (b) TEM image of a $SnBi_2Te_4$ nanosheet. The inset in (b) shows the FESEM image of $SnBi_2Te_4$ nanosheets. (c) HRTEM image showing the crystalline nature of as synthesized of $SnBi_2Te_4$ nanosheet. The inset images are SAED patterns from single and polycrystalline (ring patthern) $SnBi_2Te_4$ nanosheet. (d) EDAX color mapping for Sn, Bi, and Te of a $SnBi_2Te_4$ nanosheet during STEM imaging. (e) EDAX line scan for $SnBi_2Te_4$ nanosheet. (f) AFM image of a $SnBi_4Te_7$ nanosheet. (g) TEM image of $SnBi_4Te_7$ nanosheet. The inset in (g) shows the SAED pattern of a single $SnBi_4Te_7$ nanosheet (h) HRTEM image of a $SnBi_4Te_7$ nanosheet. (i) TEM (inset image) and HRTEM image of $SnBi_6Te_{10}$.

Table 6A.2 Calculated lattice parameters from PXRD data and SAED patterns.

Composition of nanosheets	Space group	Lattice parameters from PXRD	Lattice parameter from SAED
$SnBi_2Te_4$	R-3m	a = 4.40 Å, c = 41.60 Å α = β = 90°, γ = 120°	a = 4.40 Å c = 41.49 Å α = β = 90°, γ = 120°
$SnBi_4Te_7$	P-3m1	a = 4.40 Å, c = 23.95 Å α = β = 90°, γ = 120°	a = 4.46 Å c = 24.2 Å α = β = 90°, γ = 120°

In order to understand the van der Waals heterostructure nature and stacking sequence of the layers, $Sn_mBi_{2n}Te_{3n+m}$ nanosheets were studied in details by HRTEM and high-angle annular dark-field scanning transmission electron microscopy (HAADF-STEM) investigations on relatively thick (4-8 nm) area of the few-layer nanosheets. The bright field HRTEM images of $SnBi_2Te_4$ validate presence of ordered layered structure which is periodically arranged along the crystallographic *c*-axis (Figure 6A.6a). Few layer nanosheets of $SnBi_2Te_4$ are built up from stacking of few single modules (septuple layers, SL), each of which is 1.13 nm thick and is separated by van der Waals gap (Figure 6A.6a). HAADF-STEM image of $SnBi_2Te_4$ nanosheet, shown in Figure 6A.6b, reveals the long-range ordered sequence of each $SnBi_2Te_4$ septuple layers [Te2–Bi–Te1–Sn–Te1–Bi–Te2] along *c*-axis. Since HAADF-STEM is an incoherent dark-field imaging technique, the intensity is directly associated with the scattering and the images demonstrate *Z*-contrast. The equally spaced darkest lines represent the van der Waals gap with an extent of ~0.36 nm. The separation of two subsequent darkest lines in the HAADF image is 1.13 nm, which is the thickness of each septuple layer $SnBi_2Te_4$ (dotted blue line in Figure 6A.6b). HAADF-STEM intensity profile in Figure 6A.6c measured along the blue dotted line in Figure 6A.6b indicates atomic positions in $SnBi_2Te_4$. First, the intensity increases, then it reaches the maximum value for the brightest layer (Bi atoms); while, from brightest layer to center of stack (Te-Sn-Te), the intensity decreases. This intensity profile yields each stack thickness of 1.13 nm, which further confirms formation of $SnBi_2Te_4$ (Figure 6A.6c). HAADF- (HR) STEM in Figure 6A.6d shows typical atomic resolution of $SnBi_2Te_4$ structure with the stack length of 1.13 nm along crystallographic c-axis.

HRTEM and HAADF-STEM images in Figure 6A.7a, 6.7Ab and 6.7Ac, confirm the van der Waals heterostructure nature of as synthesized $SnBi_4Te_7$ nanosheets. In Figure 6A.7a, we show the bright field HRTEM image of $SnBi_4Te_7$ nanosheet. $SnBi_4Te_7$ nanosheet has been observed to be built up from stacking of two types of modules with the thickness of 1.13 nm ($SnBi_2Te_4$) and 0.84 nm (Bi_2Te_3), respectively, which are separated via van der Waals gap (Figure 6A.7a). Figure 6A.7b shows typical HRTEM image of few-layer $SnBi_4Te_7$ nanosheets which clearly demonstrates structural arrangement and stacking of Bi_2Te_3 and $SnBi_2Te_4$ along the crystallographic *c*-axis. The HAADF-STEM image in Figure 6A.7c further shows the presence of periodically

arranged twelve layer stack of $SnBi_4Te_7$ consisting QL of Bi_2Te_3 (Te−Bi−Te−Bi−Te) and a SL of $SnBi_2Te_4$ (Te−Bi−Te−Sn−Te−Bi−Te), representing the synthetic van der Waals heterostructure compound. The stacking thickness of 2.203 nm is evidenced from HAADF-STEM image of $SnBi_4Te_7$ (Figure 6A.7c). Analysis of the intensity profile extracted from HAADF-STEM image along the dotted line in Figure 6A.7c reveals $SnBi_4Te_7$ as a synthetic van der Waals heterostructure consisting two subunits of Bi_2Te_3 and $SnBi_2Te_4$ (Figure 6A.7d). Furthermore, layer Stacking faults and missing layers (Figure 6A.8) were observed in HRTEM and HAADF- STEM images of $Sn_mBi_{2n}Te_{3n+m}$ nanosheets.

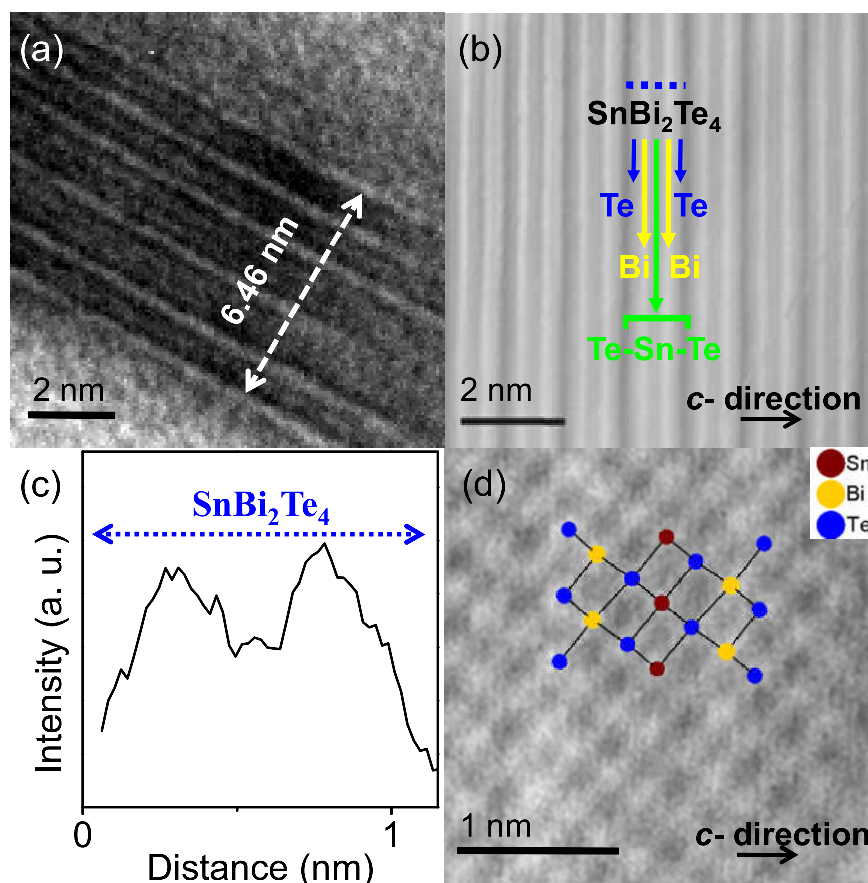

Figure 6A.6 (a) Bright field HRTEM image shows layered structures of $SnBi_2Te_4$ with periodical fringes corresponding to layer number. The white bar of length 6.46 nm confirms presence of 5 equally spaced $SnBi_2Te_4$ stacks connected via van der Waals interaction. (b) HAADF-STEM image shows` long-range ordered sequence of $SnBi_2Te_4$ blocks with a schematic of the atomic layer sequence in structures built from $SnBi_2Te_4$. (c) HAADF-STEM line scan of the intensity along the dashed lines. (d) HAADF-STEM image showing, that $SnBi_2Te_4$ consists of septuple atomic layers of Sn, Bi and Te atoms and separated from each other via van der Waals interactions along the *c*-axis.

The natural van der Waals heterostructure nature and long unit cell of $Sn_mBi_{2n}Te_{3n+m}$ motivated us to investigate thermal conductivity and other relevant thermoelectric properties. To measure the thermoelectric properties, first, the capping ligands were removed by the treatment of hydrazine, methanol and chloroform mixture to the as-synthesized samples, as mentioned in the method section. FT- IR spectra in Figure 6A.9a confirmes removal of capping agent via disappearance of N-H and C-H frequency modes after hydrazine treatment.

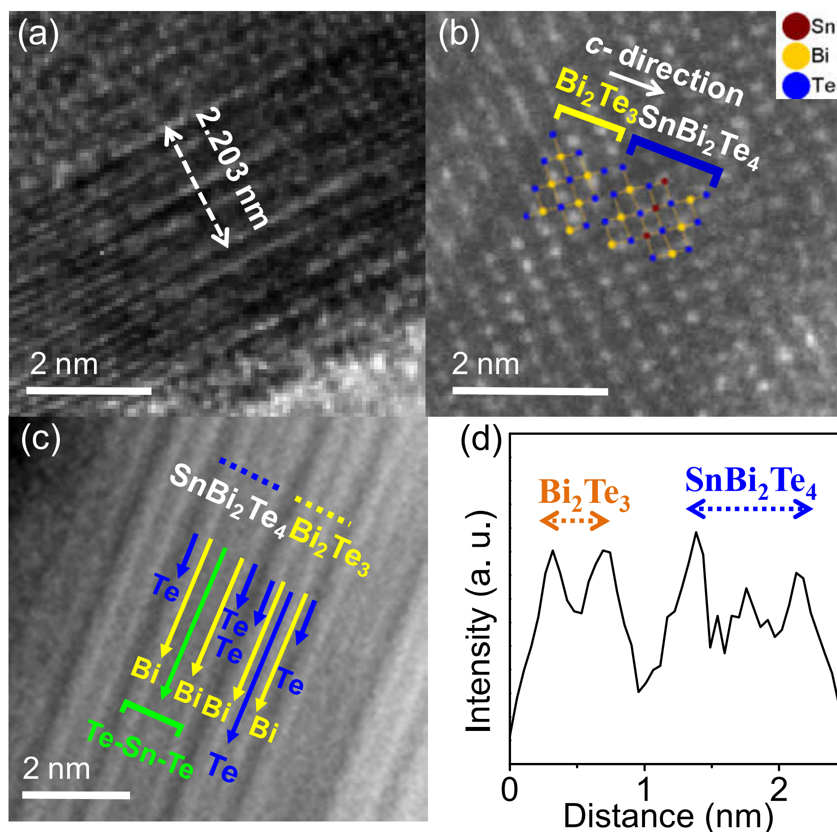

Figure 6A.7 (a) and (b) HRTEM images of $SnBi_4Te_7$ showing stacking sequences in structures built by a quintuple layers of Bi_2Te_3 and septuple layers of $SnBi_2Te_4$. (c) HAADF image of $SnBi_4Te_7$ showing presence of 57 stacking of Bi_2Te_3 and $SnBi_2Te_4$. (d) HAADF- STEM line scan of the intensity along the dashed lines.

In order to decide the temperature range of the measurement, we have annealed the surface-cleaned nanosheets at various temperatures. The heterostructure nanosheets are stable up to 523 K and annealing at further higher temperatures (573 K) leads to phase separation of thermodynamically stable binary phases (Figure 6A.9b). This further confirms the kinetic stabilization of pure $Sn_mBi_{2n}Te_{3n+m}$ compounds as nanosheets by the bottom up synthesis at low temperature.

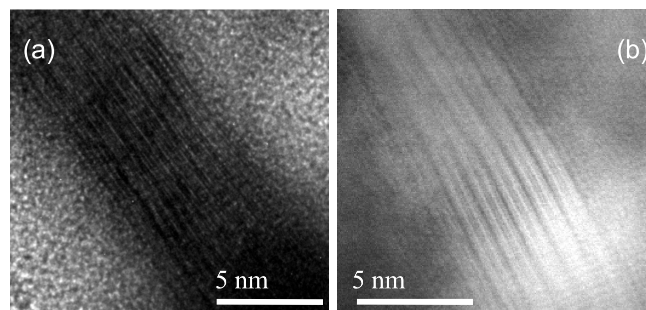

Figure 6A.8 (a) HRTEM and (b) HAADF-STEM images show presence layer staking fault in as synthesized $Sn_mBi_{2n}Te_{3n+m}$ nanosheets.

The surface-cleaned nanosheets were induction hot-pressed (70 MPa at 473 K) under Argon atmosphere. The electrical conductivity (σ) and Seebeck coefficient (S) were measured from 300 to 473 K along the same hot pressing direction (Figure 6A.10). The σ values for $SnBi_2Te_4$ and $SnBi_4Te_7$ samples were 1365 and 20 S/m, respectively, at room temperature (Figure 6A.10a). The sign of hall coefficient is positive for both, $SnBi_2Te_4$ and $SnBi_4Te_7$, which confirms *p*- type conduction. The room temperature carrier concentration (n_H) values of $SnBi_2Te_4$ and $SnBi_4Te_7$ are measured to be 1.6 x 10^{17} cm^{-3} and 6 x 10^{16} cm^{-3}, respectively. The carrier mobility values are estimated to be ~538 cm^2/Vs and ~17.6 cm^2/Vs for $SnBi_2Te_4$ and $SnBi_4Te_7$ nanosheets, respectively. Layered intergrowth compounds, $SnBi_2Te_4$ and $SnBi_4Te_7$, are predicted to be topological insulators with metallic surface states.[34-37] Dominant surface states in the present in 2D ultrathin topological phases may offer scattering resistant carrier with high carrier mobility.

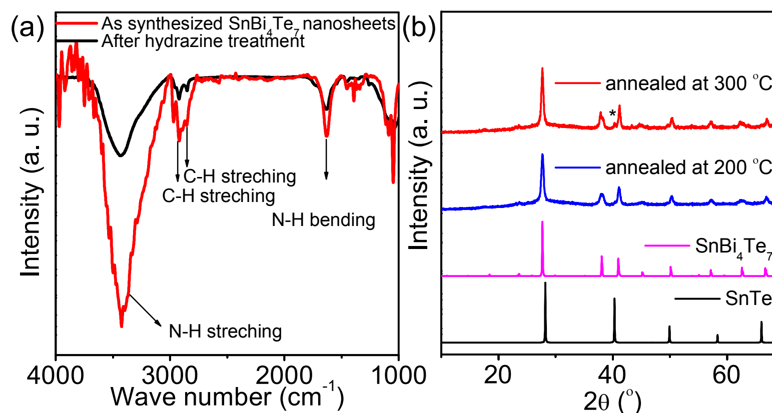

Figure 6A.9 (a) FT- IR spectra of synthesized $SnBi_4Te_7$ nanosheet, before and after the hydrazine treatment. Spectra shows disappearance of N-H and C-H frequency mode after hydrazine treatment. (b) PXRD patterns of $SnBi_4Te_7$ nanosheets at different annealing temperature.

The room-temperature S values for the $SnBi_2Te_4$ and $SnBi_4Te_7$ samples were 118 and 103 μV/K, respectively (Figure 6A.10b). Temperature dependent Seebeck data passes through maxima at ~420 K for both the samples, which is due to bipolar conduction, typical for narrow band gap semiconductors. Nanosheets samples generally exhibit higher Seebeck coefficient and lower electrical conductivity compared to the pristine bulk counterpart due to lower *p*-type carrier concentration of nanosheets (Table 6A.3).[38]

Table 6A.3 Comparison of the electronic tranport properties of present $Sn_mBi_{2n}Te_{3n+m}$ nanosheets with their bulk counterparts, previously reported[38] at room temperature.

Composition	2D Nanosheets		Bulk	
	σ (S/m)	S (μV/K)	σ (S/m)	S (μV/K)
$SnBi_2Te_4$	1365	118	175000	30 (Ref. 38)
$SnBi_4Te_7$	20	103	30000	120 (Ref. 38)

The thermal conductivity (κ_{total}) of the hot-pressed $Sn_mBi_{2n}Te_{3n+m}$ nanosheets was measured along the same direction of the electronic transport in 300 to 473 K ranges. Near room temperature, nanosheets of $Sn_mBi_{2n}Te_{3n+m}$ exhibit low thermal-conductivity (κ_{total}) values of 0.5 and 0.31 W/mK, for $SnBi_2Te_4$ and $SnBi_4Te_7$, respectively (Figure 6A.10c). Thermal conductivity remains almost flat over the temperature range of 300 to 473 K. At room temperature, $Sn_mBi_{2n}Te_{3n+m}$ nanosheets exhibit ultralow lattice thermal conductivity (κ_{lat}) of 0.49 W/mK and 0.3 W/mK for $SnBi_2Te_4$ and $SnBi_4Te_7$, respectively (Figure 6A.10d), which were estimated by subtracting electronic thermal conductivity (κ_{el}) from κ_{total}. This low κ_{lat} values were observed owing to phonon scattering mainly by the surfaces/interfaces between the layers of long periodic heterostructure. Further, layer Stacking faults and missing layers (Figure 6A.8) added up in the significant phonon scattering. 2D heterostructure nanosheets of $SnBi_4Te_7$ exhibit lower κ_{lat} values (~0.3 W/mK) compared to that of the bulk counterpart[38] and nanosheets of Bi_2Te_3[42] and $SnBi_2Te_4$ (Figure 6A.10d).

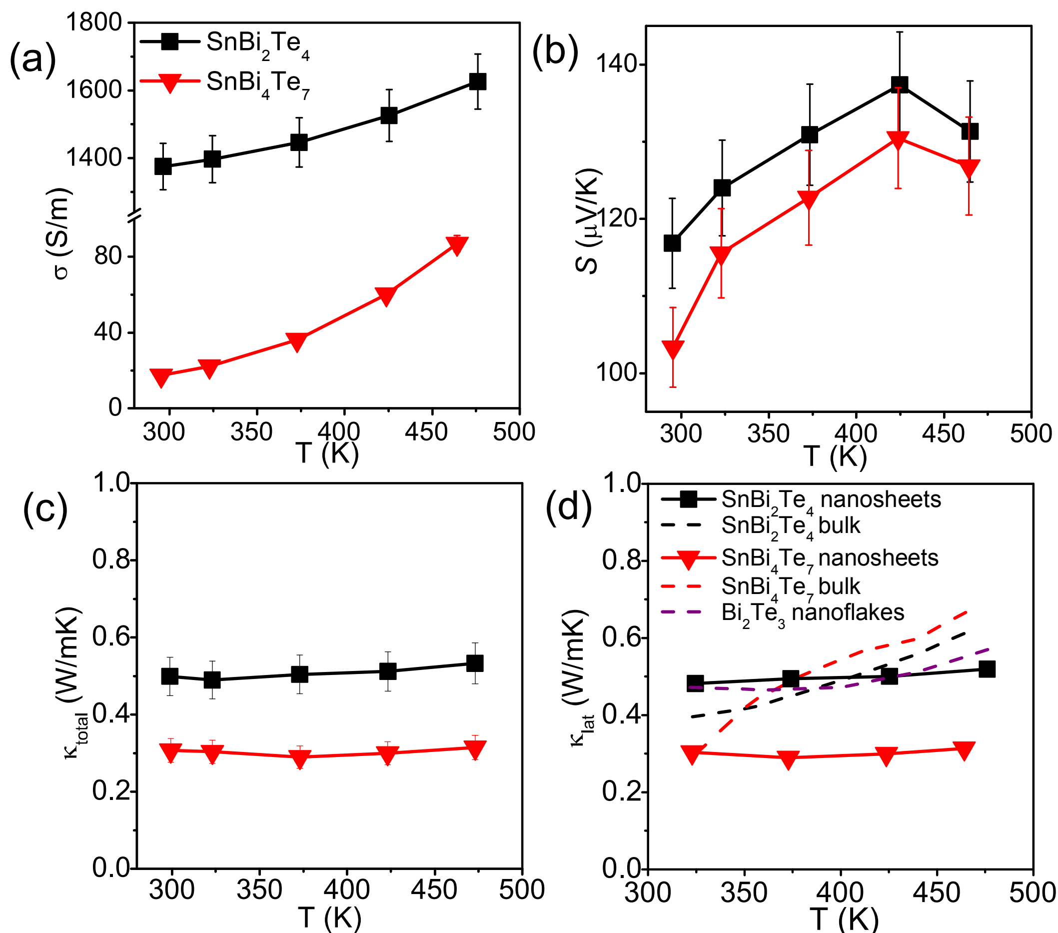

Figure 6A.10 Temperature-dependent (a) electrical conductivity (σ), (b) Seebeck coefficient (S), and (c) thermal conductivity (κ_{total}) and (d) lattice thermal conductivity (κ_{lat}) of $SnBi_2Te_4$ and $SnBi_4Te_7$ nanosheets. For comparison, temperature dependent lattice thermal conductivity (κ_{lat}) of bulk samples $Sn_mBi_{2n}Te_{3n+m}$ and Bi_2Te_3 nanoflakes are plotted in (d).

6A.4 Conclusions

We have presented a generalized facile low temperature synthetic route for the preparation of van der Waals heterostructure nanosheets in the homologous $Sn_mBi_{2n}Te_{3n+m}$ series. The stabilization of pure $Sn_mBi_{2n}Te_{3n+m}$ intergrowth compounds is ascribed to the low temperature kinetic synthesis and effect of nano dimensionality, which is fairly difficult by conventional solid state synthesis at high temperature. HRTEM and HAADF-STEM analysis indicate the detailed structural stacking sequence and atomic arrangements, which indeed confirms that the few layer nanosheets of $Sn_mBi_{2n}Te_{3n+m}$ are natural van der Waals heterostructure. Large unit cell with

heterostructured surface/interface and stacking faults are responsible for significant phonon scattering, which make these layered material attractive for low thermal conductivity application. Undoubtedly, identification of phase homology and a general synthetic strategy to synthesize pure homologous intergrowth compounds demonstrate great promise for the chemical synthesis of van der Waals heterostructure nanosheets. Thus, the synthetic skill to prepare layered intergrowths with controlled and well-defined nanostructures, offers guide to judge the probable longevity of research on synthetic van der Waals heterostructure solids, beyond conventional physical techniques.

6A.5 References

1. M. G. Kanatzidis, *Acc. Chem. Res.*, 2005, **38**, 361.
2. M. G. Kanatzidis, *Inorg. Chem.*, 2017, **56**, 3158.
3. C. N. R. Rao and K. Biswas, *Essentials of Inorganic Materials Synthesis* John Wiley & Sons, Inc, 2015.
4. J. Rouxel, A. Meerschaut and G. A. Wiegers, *J. Alloys Compd.*, 1995, **229**, 144.
5. M. Ruck and P. F. Poudeu Poudeu, *Z. Anorg. Allg. Chem.*, 2008, **634**, 482.
6. P. F. Poudeu and M. G. Kanatzidis, *Chem. Commun.*, 2005, 2672.
7. M. Ohta, D. Y. Chung, M. Kunii and M. G. Kanatzidis, *J. Mater. Chem. A*, 2014, **2**, 20048.
8. G. Radovsky, R. Popovitz-Biro, D. G. Stroppa, L. Houben and R. Tenne, *Acc. Chem. Res.*, 2014, **47**, 406.
9. L. E. Shelimova, O. G. Karpinskii, P. P. Konstantinov, E. S. Avilov, M. A. Kretova and V. S. Zemskov, *Inorg. Mater.*, 2004, **40**, 451.
10. O. G. Karpinskii, L. E. Shelimova, M. A. Kretova, E. S. Avilov and V. S. Zemskov, *Inorg. Mater.*, 2003, **39**, 240.
11. A. Chatterjee and K. Biswas, *Angew. Chem., Int. Ed.*, 2015, **54**, 5623.
12. A. Banik, B. Vishal, S. Perumal, R. Datta and K. Biswas, *Energy Environ. Sci.*, 2016, **9**, 2011.
13. A. K. Geim and I. V. Grigorieva, *Nature*, 2013, **499**, 419.
14. A. K. Geim and K. S. Novoselov, *Nat. Mater.*, 2007, **6**, 183.
15. C. Tan, X. Cao, X.-J. Wu, Q. He, J. Yang, X. Zhang, J. Chen, W. Zhao, S. Han, G.-H. Nam, M. Sindoro and H. Zhang, *Chem. Rev.*, 2017, **117**, 6625.
16. C. N. R. Rao, A. K. Sood, K. S. Subrahmanyam and A. Govindaraj, *Angew. Chem., Int. Ed.*, 2009, **48**, 7752.
17. V. Nicolosi, M. Chhowalla, M. G. Kanatzidis, M. S. Strano and J. N. Coleman, *Science*, 2013, **340**, 1226419.
18. M. Chhowalla, H. S. Shin, G. Eda, L.-J. Li, K. P. Loh and H. Zhang, *Nat. Chem.*, 2013, **5**, 263.
19. L.-D. Zhao, S.-H. Lo, Y. Zhang, H. Sun, G. Tan, C. Uher, C. Wolverton, V. P. Dravid and M. G. Kanatzidis, *Nature*, 2014, **508**, 373.
20. K. Park, K. Ahn, J. Cha, S. Lee, S. I. Chae, S. P. Cho, S. Ryee, J. Im, J. Lee, S. D. Park, M. J. Han, I. Chung and T. Hyeon, *J. Am. Chem. Soc.*, 2016, **138**, 14458.
21. Y. Sun, H. Cheng, S. Gao, Q. Liu, Z. Sun, C. Xiao, C. Wu, S. Wei and Y. Xie, *J. Am. Chem. Soc.*, 2012, **134**, 20294.
22. J. S. Son, M. K. Choi, M.-K. Han, K. Park, J.-Y. Kim, S. J. Lim, M. Oh, Y. Kuk, C. Park, S.-J. Kim and T. Hyeon, *Nano Lett.*, 2012, **12**, 640.
23. S. Saha, A. Banik and K. Biswas, *Chem. - Eur. J.*, 2016, **22**, 15634.
24. M. B. Alemayehu, M. Falmbigl, K. Ta, J. Ditto, D. L. Medlin and D. C. Johnson, *Angew. Chem., Int. Ed.*, 2015, **54**, 15468.
25. C. Tan and H. Zhang, *J. Am. Chem. Soc.*, 2015, **137**, 12162.
26. Q. Ke, C. Guan, X. Zhang, M. Zheng, Y.-W. Zhang, Y. Cai, H. Zhang and J. Wang, *Adv. Mater.*, 2017, **29**, 1604164.
27. Z. Zheng, X. Zhang, C. Neumann, D. Emmrich, A. Winter, H. Vieker, W. Liu, M. Lensen, A. Golzhauser and A. Turchanin, *Nanoscale*, 2015, **7**, 13393.
28. D. Jariwala, T. J. Marks and M. C. Hersam, *Nat. Mater.*, 2017, **16**, 170.

29. M. Velický, P. S. Toth, A. M. Rakowski, A. P. Rooney, A. Kozikov, C. R. Woods, A. Mishchenko, L. Fumagalli, J. Yin, V. Zólyomi, T. Georgiou, S. J. Haigh, K. S. Novoselov and R. A. W. Dryfe, *Nat. Com.*, 2017, **8**, 14410.
30. C. Tan, Z. Zeng, X. Huang, X. Rui, X.-J. Wu, B. Li, Z. Luo, J. Chen, B. Chen, Q. Yan and H. Zhang, *Angew. Chem., Int. Ed.*, 2015, **54**, 1841.
31. D. Sun and R. E. Schaak, *Chem. Mater.*, 2017, **29**, 817.
32. Y.-C. Lin, N. Lu, N. Perea-Lopez, J. Li, Z. Lin, X. Peng, C. H. Lee, C. Sun, L. Calderin, P. N. Browning, M. S. Bresnehan, M. J. Kim, T. S. Mayer, M. Terrones and J. A. Robinson, *ACS Nano*, 2014, **8**, 3715.
33. L. Pan, J. Li, D. Berardan and N. Dragoe, *J. Solid State Chem.*, 2015, **225**, 168.
34. K. Nakayama, K. Eto, Y. Tanaka, T. Sato, S. Souma, T. Takahashi, K. Segawa and Y. Ando, *Phys. Rev. Lett.*, 2012, **109**, 236804.
35. K. Yang, W. Setyawan, S. Wang, M. B. Nardelli and S. Curtarolo, *Nat. Mater.*, 2012, **11**, 614.
36. M. G. Vergniory, T. V. Menshchikova, I. V. Silkin, Y. M. Koroteev, S. V. Eremeev and E. V. Chulkov, *Phys. Rev. B*, 2015, **92**, 045134.
37. R. Vilaplana, J. A. Sans, F. J. Manjón, A. Andrada-Chacón, J. Sánchez-Benítez, C. Popescu, O. Gomis, A. L. J. Pereira, B. García-Domene, P. Rodríguez-Hernández, A. Muñoz, D. Daisenberger and O. Oeckler, *J. Alloys Compd.*, 2016, **685**, 962.
38. B. A. Kuropatwa and H. Kleinke, *Z. Anorg. Allg. Chem.*, 2012, **638**, 2640.
39. Y. Deng, X.-s. Zhou and C.-W. Nan, *Phys. Status Solidi A*, 2003, **199**, 265.
40. R. B. Shalvoy, G. B. Fisher and P. J. Stiles, *Phys. Rev. B*, 1977, **15**, 1680.
41. A. Ambrosi, Z. Sofer, J. Luxa and M. Pumera, *ACS Nano*, 2016, **10**, 11442.
42. Y. Min, J. W. Roh, H. Yang, M. Park, S. I. Kim, S. Hwang, S. M. Lee, K. H. Lee and U. Jeong, *Adv. Mater.*, 2013, **25**, 1425.

Chapter 6B

Ultrathin Few Layer Nanosheets of *n*-type $SnSe_2$†

Summary

Layered p-block metal chalcogenides are renowned for thermoelectric energy conversion due to their low thermal conductivity caused by bonding asymmetry and anharmonicity. Recently, single crystalline layered SnSe has created sensation in thermoelectrics due to its ultralow thermal conductivity and high thermoelectric figure of merit. Tin diselenide ($SnSe_2$) is an additional layered compound belonging to Sn-Se phase diagram, which possesses CdI_2 type structure. However, synthesis of pure phase bulk $SnSe_2$ by conventional solid state route still remains challenging. Herein, we present a simple solution-based low-temperature synthesis of ultrathin (3-5 nm) few layers (4-6 layers) nanosheets of Cl doped $SnSe_2$, which possess n-type carrier concentration of 2×10^{18} cm^{-3} with carrier mobility of ~30 cm^2/Vs at room temperature. $SnSe_2$ exhibits band gap of ~1.6 eV and semiconducting electronic transport in the 300-630 K range. An ultralow thermal conductivity of ~0.67 W/mK has been achieved at room temperature in hot-pressed dense pellet of Cl-doped $SnSe_2$ nanosheets due to anisotropic layered structure, which gives rise to effective phonon scattering.

†*Paper based on this study has been published in* ***Chem. Eur. J.***, 2016, *22,* 15634.

6B.1 Introduction

Inorganic layered solids, a versatile source of two-dimensional (2D) nanosystems, have emerged as a hot spot of extensive research due to their exotic physical properties.[1-5] Two dimensional layered metal chalcogenides (LMCs) are important contender of this family with their unique electronic structures and important properties arising from special crystal structure, weak interlayer van der Waals interaction, variable compositions and rich phase stability. Hence LMCs provide a large library of solids for both the understanding of fundamental solid state chemistry and the potential applications.[6-9] Few layer nanosheets of layered Bi_2X_3 (X= Te, Se, S) have shown promising thermoelectric properties resulting from enhanced metallic surface states, high carrier mobility and low thermal conductivity.[10-12] Additionally, recent reports show the kinetic stabilization of low thermal conductive layered intergrowth compounds in the family of $(MX)_m(E_2X_3)_n$, [M= Pb, Sn; E = Bi, Sb; X= Te, Se] either via solution based synthesis (Chapter 6A)[13,14] or via matrix encapsulation (Chapter 5).[15]

Tin selenide (SnSe), a narrow band gap semiconductor, belongs to the sub-group of typical LMCs. Single crystal of SnSe has been discovered to be a superior thermoelectric material resulting from ultralow thermal conductivity.[16-18] An outstanding thermoelectric figure of merit (zT) of ~2.6 has been measured in single crystalline SnSe because of anharmonic and anisotropic bonding.[16] Recently, nanoplates of *p*-type SnSe was synthesized by colloidal synthesis, which shows excellent thermoelectric power factor.

Other than SnSe, tin diselenide ($SnSe_2$) is an additional layered compound belonging to Sn-Se phase diagram (Figure 6B.1).[19] $SnSe_2$ is a semiconductor with layered CdI_2-type structure, where the Se^{2-} anions form a hexagonal close packing (hcp) arrangement with the Sn^{4+} cations occupying alternating layers of octahedral sites (Figure 6B.1a).[20,21] Sn planes are sandwiched between the two Se planes with the Sn in the center of an octahedral cage formed by the Se ions, which are covalently bonded to form 2D Se–Sn–Se unit layers, and the layers stack along the crystallographic *c*-axis interacting via van der Waals interaction (Figure 6B.1b). This layered structure along *c*-axis gives rise to the anisotropic electro-optical properties in bulk $SnSe_2$,[20] which renders it as a versatile material for wide variety of applications. However, synthesis of pure phase bulk $SnSe_2$ by conventional solid state route still remains challenging (Figure 6B.1c). Synthesis of polycrystalline bulk $SnSe_2$ required annealing at 600 °C for several days (ca. 100 hrs),

which was also characterized to be impure due to the presence of additional SnSe phase.[22] $SnSe_2$ flower like nanostructures with nanoplate petals were synthesized by the solvothermal reaction of organo-tin and organo-selenium precursors with prolonged reaction time (24 hrs).[23,24] Solution processed thick nanodisc or nanoplates of $SnSe_2$ recently showed promising performance as supercapacitor and anode materials for Li-ion batteries.[25,26] Other $SnSe_2$ nanostructures such as nanoflakes, nanoplates quantum dots were synthesized by chemical vapor deposition,[27,28] ball milling,[29] thermal decomposition,[30] and solvothermal reaction[31].

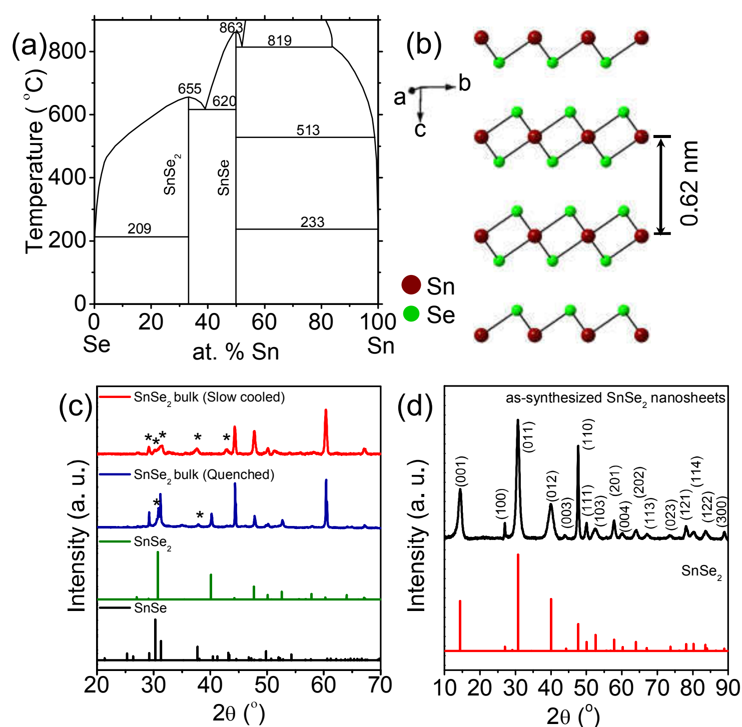

Figure 6B.1 (a) Phase diagram of the Sn–Se system showing the presence of SnSe and $SnSe_2$ compounds.[19] (b) Crystal structure of $SnSe_2$ showing layered structure. (c) Powder XRD pattern of as-synthesized bulk $SnSe_2$. Presence of SnSe impurity was observed (marked with *). (d) Powder XRD patterns of as-prepared $SnSe_2$ nanosheets.

This chapter demonstrates the first facile low temperature colloidal synthesis of *n*-type ultrathin (3-5 nm) few layer nanosheets (4-6 layers) of Cl-doped $SnSe_2$. Nanosheets of $SnSe_2$ exhibits band gap of ~1.6 eV at room temperature and semiconducting electronic transport in the 300-630 K. Few layer Cl-doped $SnSe_2$ possess *n*-type carrier concentration of 2×10^{18} cm^{-3}, which is actually higher than that of the undoped $SnSe_2$ nanosheets indicating successful Cl doping through $SnCl_2$ precursor in solution synthesis. *n*-type carrier mobility was measured to be ~30 cm^2/Vs at room temperature for Cl-doped

$SnSe_2$. Cl-doping optimizes the *n*-type carrier concentration in $SnSe_2$ nanosheets, which enhances the thermoelectric power factor. Ultralow thermal conductivity of ~0.67 W/mK is evidenced at room temperature in the hot pressed dense pellet of Cl-doped $SnSe_2$ nanosheets due to effective phonon scattering caused by anisotropic layered structure.

6B.2 Methods

6B.2.1 Synthesis

Tin (II) chloride anhydrous ($SnCl_2$, 99.99%, Sigma Aldrich), tin (II) acetate ($Sn(OAc)_2$, Sigma Aldrich), oleylamine (OAm, tech. 90%, Sigma Aldrich) and selenium powder (Se, 99.99%, Sigma Aldrich) were used for synthesis without further purification.

Synthesis of bulk $SnSe_2$. Bulk polycrystalline ingots of $SnSe_2$ were synthesized by high temperature melting of the constituent elements (Sn and Se) at 850 °C for 8 hrs followed by slow cooling and water-quenching process.

Synthesis of $SnSe_2$ nanosheets. In a typical synthesis of colloidal $SnSe_2$ nanosheets, 28.5 mg (0.15 mmol) $SnCl_2$ and 10 ml OAm were taken in a 50 mL three neck round bottom flask and heated at 120 °C in vacuum for 1 hour to get a homogeneous clear solution. The solution was cooled to room temperature and 23.7 mg (0.3 mmol) of Se powder was added to it. Then the reaction mixture was heated to 150 °C in nitrogen atmosphere. Black colored suspension was observed (Figure 6B.2), which was heated for 1 hour. Black colored suspension of $SnSe_2$ nanosheets were washed several times with hexane and ethanol mixture to remove surface adsorbed OAm. Finally the product was air dried and collected as powder. The same procedure was repeated with 35.5 mg (0.15 mmol) $Sn(OAc)_2$ instead of $SnCl_2$ for synthesis of $SnSe_2$ nanosheets from tin acetate.

Removal of capping ligands. In order to remove the organic capping ligands, the material (as prepared nanosheets) collected from few syntheses (~1.2 g) were taken in a quartz tube and was vacuum (10^{-5} torr) sealed. The tube was slowly heated to 250 °C over 8 hrs, then soaked for 3 hrs, and cooled slowly to room temperature. Due to this heat treatment, the surface capping ligand OAm get detached from the $SnSe_2$ nanosheets

surface and after cooling get condensed and remain as liquid droplets at the top part of the inner wall of the tube. The surfactant free nanosheets were collected from the tube.

6B.2.2 Characterizations

Powder X-ray diffraction (PXRD) for all the samples were recorded using a Cu Kα (λ = 1.5406 Å) radiation on a Bruker D8 diffractometer. To estimate optical band gap, optical diffuse reflectance measurement has been performed at the range of 200 nm to 3000 nm using a Perkin Elmer Lambda 900, UV/Vis/NIR spectrometer. The energy band gaps were derived from α/Λ vs. E (eV) plots (Details is given in chapter 1). Field emission scanning electron microscopy (FESEM) experiments were performed using NOVA NANO SEM 600 (FEI, Germany) operated at 15 kV. Transmission electron microscopy (TEM) experiments were performed using JEOL JEM3010 TEM fitted with a Gatan CCD camera operating at a 300 kV accelerating voltage and also using FEI TECNAI G^2 20 STWIN TEM operating at 200 kV. One drop of nanosheets dispersed in ethanol solution was taken in a holey carbon coated Cu grid for TEM imaging. EDAX compositional analysis and mapping were performed during scanning transmission electron microscope (STEM) imaging. Background was subtracted (using multi-polynomial model) during the data processing for EDAX elemental mapping (with 500 eV minimum region of interest width). Errors in the determination in compositions of nanosheets in EDAX measurements is nearly 5%. Raman spectroscopy measurements were carried out with a HORIBA LABRAM HR800 spectrometer. The excitation wavelength of the laser was 514 nm. X-ray photoelectron spectroscopy (XPS) measurement has been performed with Mg−Kα (1253.6 eV) X-ray source with a relative composition detection better than 0.1% on an Omicron Nano-technology spectrometer. Atomic force microscopy (AFM) was done on a Bruker Innova Microscope in tapping mode with an antimony doped Silicon tip with 10 nm resolution. Thermogravimetric analysis (TGA) was performed using a TGA/DSC 2 STAR instrument in the temperature range of 300–878 K under nitrogen atmosphere with a ramp rate of 5 K/min. FTIR spectra was recorded using a Bruker IFS 66v/S spectrometer.

6B.2.3 Transport properties

In order to measure their thermoelectric properties, the surface cleaned $SnSe_2$ nanosheets were hot pressed in vacuum (10^{-3} Torr) in a graphite die by applying pressure of 40 MPa at 673 K for 30 min. Hot pressed sample density was about ~95% of theoretical density. Electrical conductivity (σ) and Seebeck coefficients (S) were measured in same directions for a particular sample. σ and S were measured simultaneously on a sample of the dimension, 2 mm ×3 mm ×8 mm, under a He atmosphere from room temperature to 623 K by ULVAC RIKO ZEM3 system (Measurement details are given in chapter 1). Thermal diffusivity, D, was directly measured on a sample of 10 mm diameter and 2 mm thickness, in the range of 300–623 K by using laser flash diffusivity method in a Netzsch LFA-457 instrument (Measurement details are given in chapter 1). Temperature dependent heat capacity, C_p, was derived using standard sample (pyroceram) in LFA-457, which is in good agreement with the Dulong–Petit C_p value. The total thermal conductivity, κ_{total}, was calculated using the formula, $\kappa_{total} = DC_p\rho$, where ρ is the density of the sample, measured using the sample dimension and mass.

6B.3 Results & Discussion

In order to prepare pure phase Cl doped $SnSe_2$ nanosheets, a clear precursor solution of Sn was prepared first by dissolving tin chloride ($SnCl_2$) in oleylamine at 120 ^oC under vacuum (10^{-3} Torr) for 1 hr. The pale-yellow color of the resulting solution indicates the formation of $SnCl_2$-oleylamine complex (Figure 6B.2). Then the solution was cooled to room temperature and two equivalents amount of Se powder were added under N_2 atmosphere in Schelenk line. The reaction mixture was heated to 150 °C in N_2 atmosphere and black colored suspension was observed immediately (Figure 6B.2), which was aged for 1 hour at 150 ^oC. The product was washed and precipitated using hexane and ethanol as the solvent and anti-solvent respectively, as mentioned in the experimental section. Finally, the product was air dried and collected as powder. We can scale up the synthesis of Cl-doped $SnSe_2$ nanosheets up to 2 g. We have also prepared the undoped $SnSe_2$ nanosheets by using tin acetate instead of tin chloride as Sn precursor.

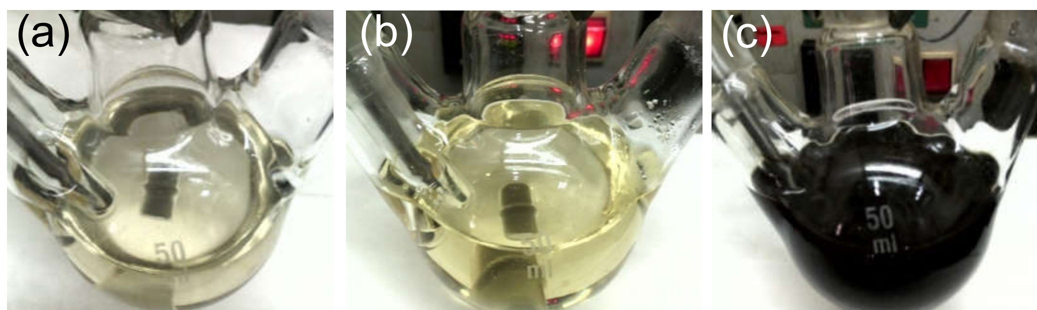

Figure 6B.2 Different steps of the reaction: (a) Milky white solution of $SnCl_2$ in OAm, (b) pale yellow color solution of $SnCl_2$-OAm complex after heating at 120 °C under vacuum (10^{-3} Torr) for 1 hr and (c) black dispersion of $SnSe_2$ nanosheets at end of reaction.

Our approach to synthesize pure-phase polycrystalline bulk counterpart of $SnSe_2$ by melting the nominal constituent elements at 850 °C for 8 hrs followed by slow cooling or water-quenching was proven to be unsuccessful. SnSe was identified as a second phase along with the $SnSe_2$ phase in bulk synthesis (Figure 6B.1c). The present simple and quick solution based bottom-up approach at low temperature (kinetic conditions) enables the stabilization of pure $SnSe_2$ in the form of nanosheets, which is rather difficult by conventional high-temperature solid-state synthesis. The present low-temperature kinetic synthesis helps to avoid the formation of phase-separated impurities, where decomposition of the precursor and bottom-up soft chemical reaction are the key steps. Low-temperature synthesis is also important to arrest the pure phases in the form of exotic nanostructures.

PXRD patterns of the as-synthesized $SnSe_2$ nanosheets could be indexed to the pure hexagonal $SnSe_2$ (*P-3m1* space group, JCPDS #01-089-2939, see Figure 6B.1d). The optical band gap of the $SnSe_2$ sample prepared by $SnCl_2$ precursor is measured to be ~ 1.6 eV (Figure 6B.3). The $SnSe_2$ sample prepared from $SnCl_2$ shows slightly higher band gap compared to that of the $SnSe_2$ sample prepared from tin acetate precursor (Figure 6B.3), which is due to the in-situ Cl-doping in $SnSe_2$ nanosheets by $SnCl_2$ during synthesis. Cl doping in Se sublattice of $SnSe_2$ increases the band gap due to the higher electronegativity of Cl compared to that of Se.[32,33] Tyndall light scattering of as-synthesized $SnSe_2$ nanosheets dispersed in hexane confirms the colloidal nature of the sample (inset in Figure 6B.3).

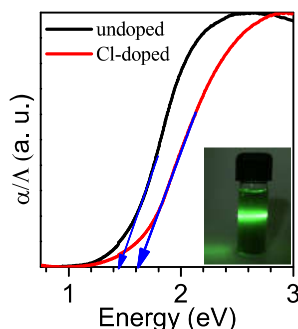

Figure 6B.3 Room temperature optical absorption spectra of as-synthesized undoped and Cl-doped $SnSe_2$ nanosheets. The inset image shows the Tyndall light scattering of $SnSe_2$ nanosheets dispersed in hexane.

The Raman spectrum of the as-synthesized samples indicates the presence of pure $SnSe_2$ phase (Figure 6B.4a). The peak at 117/cm corresponds to the E_g mode (in plane vibration) and the intense peak observed at 187 cm^{-1} was attributed to the A_{1g} mode (out of plane vibration) of $SnSe_2$.[34]

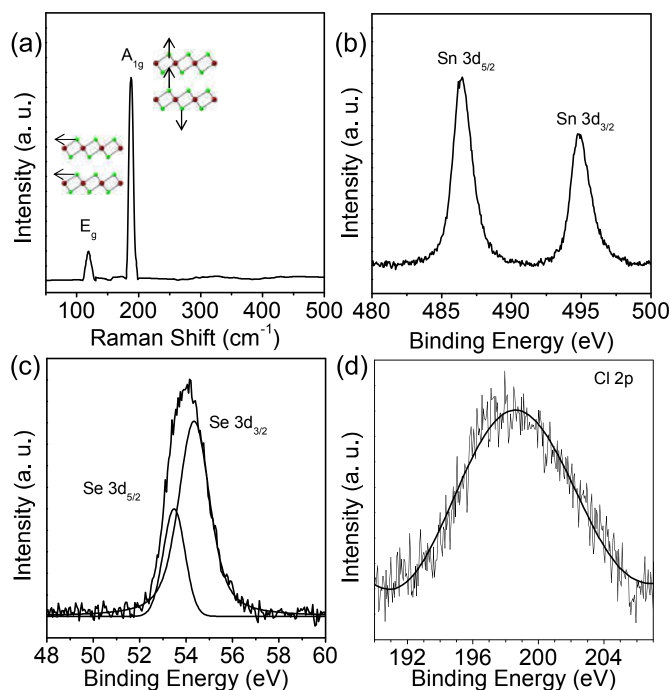

Figure 6B.4 (a) Raman spectra of Cl-doped $SnSe_2$ nanosheets. High-resolution XPS of b) Sn 3d, c) Se 3d, and d) Cl 2p in Cl-doped $SnSe_2$ nanosheets.

To further confirm the presence of Sn, Se and Cl, we have performed XPS of as synthesized $SnSe_2$ nanosheets samples (Figure 6B.4b). The Sn 3d spin–orbit doublet peaks were appeared at 486.5 eV and 494.9 eV with splitting of 8.4 eV (Figure 6B.4b), which can be assigned to Sn $3d_{5/2}$ and Sn $3d_{3/2}$, respectively. This is in good agreement with the value of Sn (IV). Peaks due to Se $3d_{5/2}$ and Se $3d_{3/2}$ have appeared as a broad

peak at 53.91 eV (Figure 6B.4c). The XPS peak at 198.7 eV suggests presence of Cl- ion in $SnSe_2$ nanosheet sample (Figure 6B.4d). Energy dispersive X-ray analysis (EDAX) of the nanosheets confirms the 1-1.5 mol% Cl doping in $SnSe_2$.

Surface morphology of the as-synthesized $SnSe_2$ was investigated using FESEM, TEM and AFM. A morphology resembling 2D thin sheets was evident from the FESEM (Figure 6B.5a) and TEM images (Figure 6B.5b-c). The Cl-doped $SnSe_2$ shows ultrathin folded nanosheets like morphology with thickness of few nanometers (Figure 6B.5b-c), whereas the undoped $SnSe_2$ shows 2D hexagonal nanoplates like morphology with lateral dimensions ranging from 200 to 600 nm (Figure 6B.6).

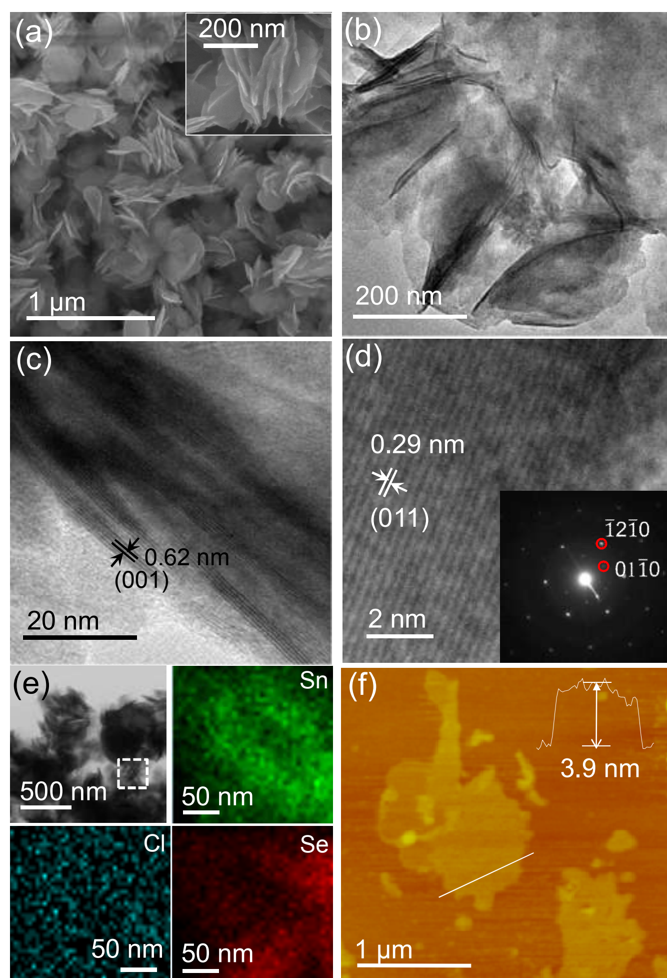

Figure 6B.5 (a) FESEM image of Cl doped $SnSe_2$ nanosheets. The inset in (a) shows a magnified FESEM image. (b) TEM image of Cl doped $SnSe_2$ nanosheets. HRTEM image of Cl doped $SnSe_2$ nanosheets showing (c) interlayer separation with bent edges and (d) distance between (011) planes. Inset of (d) shows SAED pattern of a single nanosheet. (e) STEM image of the nanosheets and EDAX color mapping for Sn, Se and Cl in the nanosheets during STEM imaging (from the highlighted portion of the STEM image). (f) AFM image of Cl doped $SnSe_2$ nanosheets and the height profile showing a thickness of ~3.9 nm.

The high-resolution TEM (HRTEM) image of the bent edges in Cl-doped $SnSe_2$ nanosheets showed a interlayer spacing of 0.62 nm which is the lattice spacing of (001) planes (interlayer distance) of hexagonal $SnSe_2$ (Figure 6B.5). This result further indicates that each nanosheets forms by accumulation of few layers (4-6) of $SnSe_2$ via van der Waals interaction along crystallographic *c*-axis as shown in Figure 6B.1b. The HRTEM image in Figure 6B.5d shows (011) planes of Cl-doped $SnSe_2$ nanosheets with lattice spacing of 0.29 nm. The selected-area electron diffraction (SAED) pattern recorded for a single-sheet region of Cl-doped $SnSe_2$ showed a single-crystalline pattern with typical six-fold symmetry (inset in Figure 6B.5d). EDAX elemental color mapping measured during STEM imaging shows the presence of Sn, Se and Cl in $SnSe_2$ nanosheets synthesized by $SnCl_2$ route (Figure 6B.5e). AFM further confirms the ultrathin nature of the $SnSe_2$ nanosheets. Typical AFM images of freestanding Cl-doped $SnSe_2$ nanosheets indicate a thickness corresponding to six layers (~3.9 nm) with lateral dimension of ~1 μm (see Figure 6B.5f).

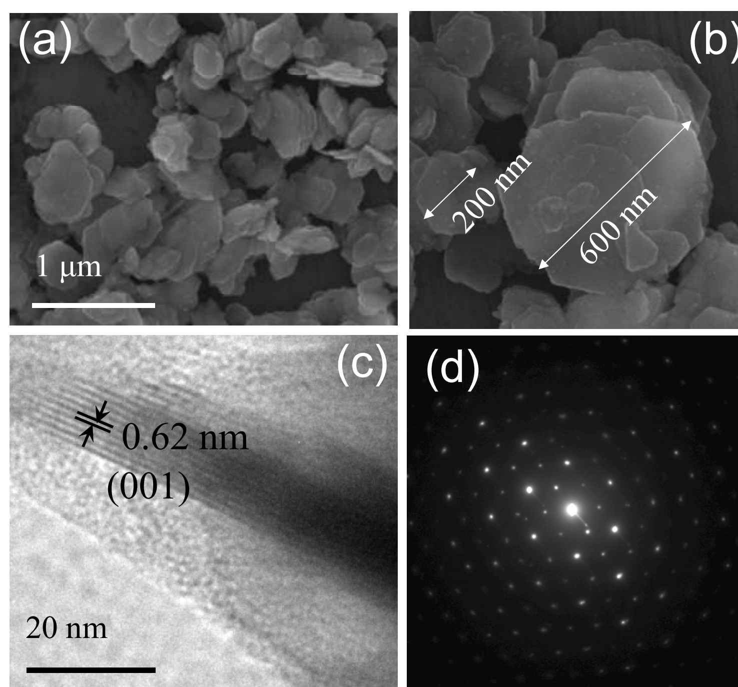

Figure 6B.6 (a) FESEM images of undoped $SnSe_2$ nanosheets synthesized by Sn-acetate route. (b) Zoomed FESEM image of the same, (c) HRTEM images of undoped $SnSe_2$ nanosheets showing few layers, (d) SAED pattern of a single $SnSe_2$ nanosheet.

In order to measure the thermoelectric properties, the organic ligands on $SnSe_2$ were first removed by heat-treatment of well-dried as synthesized $SnSe_2$ powders in a vacuum-

sealed quartz tube at 250 ^{0}C for 3 hrs. We have chosen heat treatment rather than conventional hydrazine treatment route for removal of capping agent because $SnSe_2$ reacts with hydrazine hydrate.[35] During this thermal treatment, no change in structure and composition was observed, as indicated by the PXRD taken before and after the heat treatment (Figure 6B.7). In this process all the organics were removed from the $SnSe_2$, which was further confirmed from the TGA (Figure 6B.7b) and infra-red (FT-IR) spectra (Figure 6B.7c).

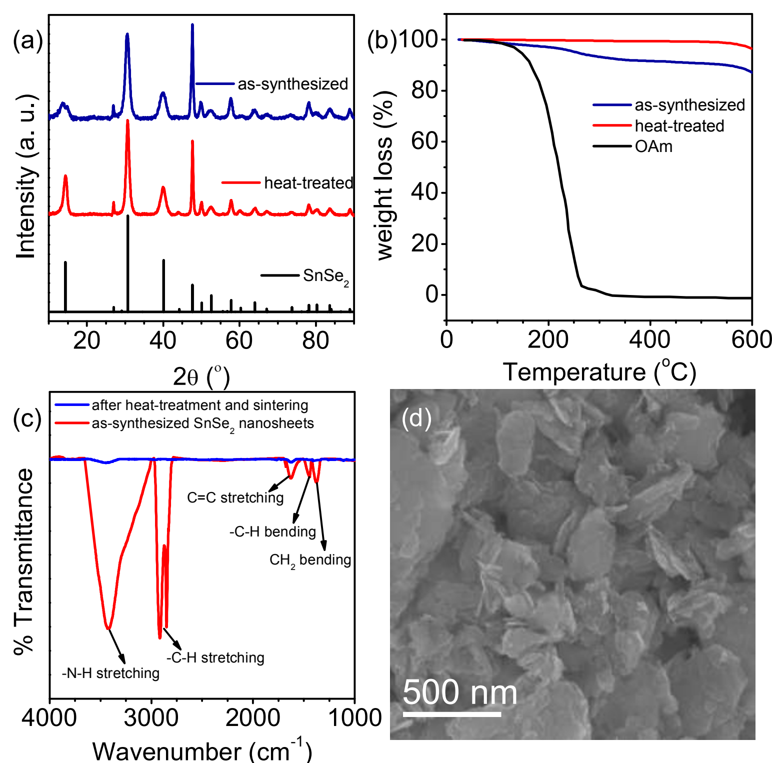

Figure 6B.7 (a) Powder XRD pattern of as-synthesized $SnSe_2$ nanosheets and $SnSe_2$ nanosheets after heat-treatment. (b) TGA curves of $SnSe_2$ nanosheets before and after the heat-treatment. (c) FT-IR spectra of $SnSe_2$ nanosheets, before and after the heat treatment. Spectra shows disappearance of C-H and N-H vibrations after the heat treatment. (d) FESEM image of hot pressed $SnSe_2$ nanosheets.

To measure the thermoelectric properties, the surface-cleaned nanosheets were hot-pressed into pallets under vacuum (10^{-3} Torr) in a graphite die by applying a pressure of 40 MPa at 673 K for 30 mins. The sample became more compact and the adjacent nanosheets were closely attached to each other, retaining the few-layer nature of the sample, as can be seen from FESEM image of the sample after hot-pressing (Figure 6B.7d). The measured density of the pellet was ~95% of the theoretical density. Mention must be made that both electronic and thermal transport properties were measured along

the pressing direction of the hot pressed pellet of $SnSe_2$ nanosheets. The temperature-dependent thermoelectric properties of nanostructured $SnSe_2$ synthesized by $SnCl_2$ and $Sn(OAc_2)$ route in the range of 300−650 K are presented in Figure 6B.8. Electrical conductivity (σ) and Seebeck coefficient (S) were measured simultaneously under He atmosphere by a ULVAC-RIKO ZEM-3 instrument. At room temperature, σ value of the Cl-doped $SnSe_2$ sample is 9.6 S/cm, which linearly increases with increasing temperature to 17 S/cm at 610 K (Figure 6B.8a), indicating the semiconducting nature of $SnSe_2$ nanosheets. The Cl-doped $SnSe_2$ exhibits relatively higher σ than that of undoped $SnSe_2$ synthesized by tin acetate route (Figure 6B.8a), which indicates successful Cl doping in $SnSe_2$ through $SnCl_2$ route. Negative value of S indicates the n-type conduction in Cl-doped $SnSe_2$. Typically, Cl-doped $SnSe_2$ has a S value of ~ −235.7 μV/K at 300 K, which increases to ~ −292.4 μV/K at ~610 K (Figure 6B.8b). Notably, both σ and S increases simultaneously with temperature. Similar properties have been observed earlier in nanoplates of SnSe and Bi_2Se_3 samples.[11,36] Although the reasons of such transport properties require further investigation, increasing nature of σ and S with temperature raises power factor to a respectable value at high temperature. The room temperature value of the power factor (σS^2) is ~0.53 μW/cmK^2, which increases up to 1.46 μW/cmK^2 at 610 K (Figure 4b). Cl-doped $SnSe_2$ possess (1.46 μW/cmK^2) which is significantly higher σS^2 than that of the undoped $SnSe_2$ (0.75 μW/cmK^2) at 610 K (Figure 6B.8c).

The room temperature hall coefficient of Cl-doped $SnSe_2$ nanosheets is negative, which confirms n-type conduction. Typically, for Cl-doped $SnSe_2$ sample, the room temperature n-type carrier concentration was measured to be 2 × 10^{18} cm^{-3}, which is higher compared to that of undoped $SnSe_2$ nanosheets (7 × 10^{17} cm^{-3}) synthesized by tin acetate route. Cl^- alliovalently dopes in Se^{2-} sublattice and contribute one extra electron. We have estimated carrier mobility in Cl-doped $SnSe_2$ nanosheets using the formula $\sigma = ne\mu$, where e is the electronic charge. The estimated carrier mobility value is ~30 cm^2/Vs.

The total thermal conductivity, κ_{total}, of the samples was estimated in the temperature range of 300−630 K using the formula, $\kappa = DC_p\rho$, where D is the thermal diffusivity, C_p is specific heat, and ρ is density of the sample. Nanosheets of Cl-doped $SnSe_2$ exhibited low thermal conductivity (κ_{total}) values ranging from 0.67 to 0.4 W/mK in the temperature range of 300–630 K (Figure 6B.8c). Similarly, undoped $SnSe_2$ possess low thermal conductivity (Figure 6B.8c). The κ_{lat} was obtained after subtraction of the electronic part,

κ_{el}, from the total κ_{total}. Although the morphology of undoped and Cl-doped $SnSe_2$ nanosheet is apparent from TEM and FESEM, we have compared the κ_{lat} of undoped and Cl-doped $SnSe_2$ nanosheets. Low κ_{lat} value was observed due to efficient phonon scattering by both the interfaces between the layers of $SnSe_2$ and the nanoscale grains in the nanosheets samples. $1/T$ dependence of κ_{lat} indicates that the Umklapp phonon scattering process is dominant in the temperature range. Theoretical minimum of the thermal conductivity (κ_{min}) of $SnSe_2$ along crystallographic *c*-axis was earlier calculated to be 0.4 W/mK,[37] which is in good agreement with our experimental κ_{lat} value for hot pressed Cl-doped $SnSe_2$ nanosheets. Thermoelectric figure of merit, *zT*, of 0.22 has been observed for Cl- doped $SnSe_2$ at 610 K.

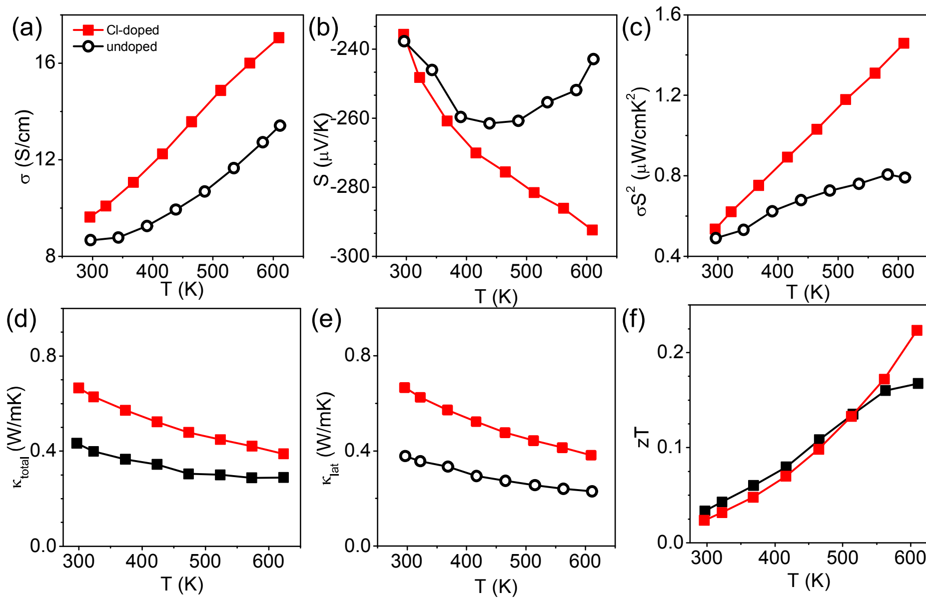

Figure 6B.8 Temperature dependent (a) electrical conductivity (σ), (b) Seebeck coefficient (S), (c) power factor (σS^2), (d) total thermal conductivity (κ_{total}), (e) lattice thermal conductivity (κ_{lat}) and (f) *zT* of undoped and Cl-doped $SnSe_2$ nanosheets.

6B.4 Conclusions

In summary, few layer nanosheets (3-5 nm thickness) of Cl-doped $SnSe_2$ have been successfully synthesized by a facile and novel low-temperature solution-based method. The stabilization of the pure-phase of $SnSe_2$ in the form of nanosheets is attributed to the kinetic low-temperature synthesis and the influence of the nanoscale regime, and is

otherwise difficult to achieve by high-temperature solid-state bulk-phase synthesis. Cl-doped $SnSe_2$ nanosheets exhibit optical band gap of 1.6 eV at room temperature and n-type semiconducting electronic transport properties over the 300-630 K temperature range. Cl-doping in $SnSe_2$ nanosheets increases the *n*-type carrier concentration, which actually enhances the thermoelectric power factor. Moreover, nanoscale grain boundaries and layered anisotropic structure scatter the heat carrying phonons, thereby decreasing κ_{lat} to as low as ~0.67 W/mK at room temperature.

6B.5 References

1. V. Nicolosi, M. Chhowalla, M. G. Kanatzidis, M. S. Strano and J. N. Coleman, *Science*, 2013, **340**, 1226419.
2. J. N. Coleman, M. Lotya, A. O'Neill, S. D. Bergin, P. J. King, U. Khan, K. Young, A. Gaucher, S. De, R. J. Smith, I. V. Shvets, S. K. Arora, G. Stanton, H.-Y. Kim, K. Lee, G. T. Kim, G. S. Duesberg, T. Hallam, J. J. Boland, J. J. Wang, J. F. Donegan, J. C. Grunlan, G. Moriarty, A. Shmeliov, R. J. Nicholls, J. M. Perkins, E. M. Grieveson, K. Theuwissen, D. W. McComb, P. D. Nellist and V. Nicolosi, *Science*, 2011, **331**, 568.
3. M. Chhowalla, H. S. Shin, G. Eda, L.-J. Li, K. P. Loh and H. Zhang, *Nat. Chem.*, 2013, **5**, 263.
4. X. Cao, C. Tan, X. Zhang, W. Zhao and H. Zhang, *Adv. Mater.*, 2016, **28**, 6167.
5. K. Xu, P. Chen, X. Li, C. Wu, Y. Guo, J. Zhao, X. Wu and Y. Xie, *Angew. Chem., Int. Ed.*, 2013, **52**, 10477.
6. C. Tan, Z. Zeng, X. Huang, X. Rui, X.-J. Wu, B. Li, Z. Luo, J. Chen, B. Chen, Q. Yan and H. Zhang, *Angew. Chem., Int. Ed.*, 2015, **54**, 1841.
7. C. N. R. Rao, H. S. S. Ramakrishna Matte and U. Maitra, *Angew. Chem., Int. Ed.*, 2013, **52**, 13162.
8. H. Li, J. Wu, Z. Yin and H. Zhang, *Acc. Chem. Res.*, 2014, **47**, 1067.
9. C. Tan and H. Zhang, *Chem. Soc. Rev.*, 2015, **44**, 2713.
10. Y. Zhao, R. W. Hughes, Z. Su, W. Zhou and D. H. Gregory, *Angew. Chem., Int. Ed.*, 2011, **50**, 10397.
11. Y. Sun, H. Cheng, S. Gao, Q. Liu, Z. Sun, C. Xiao, C. Wu, S. Wei and Y. Xie, *J. Am. Chem. Soc.*, 2012, **134**, 20294.
12. M. K. Jana, K. Biswas and C. N. R. Rao, *Chem. - Eur. J.*, 2013, **19**, 9110.
13. A. Chatterjee and K. Biswas, *Angew. Chem., Int. Ed.*, 2015, **54**, 5623.
14. A. Chatterjee, S. N. Guin and K. Biswas, *Phys. Chem. Chem. Phys.*, 2014, **16**, 14635.
15. A. Banik, B. Vishal, S. Perumal, R. Datta and K. Biswas, *Energy Environ. Sci.*, 2016, **9**, 2011.
16. L.-D. Zhao, S.-H. Lo, Y. Zhang, H. Sun, G. Tan, C. Uher, C. Wolverton, V. P. Dravid and M. G. Kanatzidis, *Nature*, 2014, **508**, 373.
17. L.-D. Zhao, G. Tan, S. Hao, J. He, Y. Pei, H. Chi, H. Wang, S. Gong, H. Xu, V. P. Dravid, C. Uher, G. J. Snyder, C. Wolverton and M. G. Kanatzidis, *Science*, 2016, **351**, 141.
18. K. Peng, X. Lu, H. Zhan, S. Hui, X. Tang, G. Wang, J. Dai, C. Uher, G. Wang and X. Zhou, *Energy Environ. Sci.*, 2016, **9**, 454.
19. F. A. S. Al-Alamy, A. A. Balchin and M. White, *J. Mater. Sci.*, 1977, **12**, 2037.
20. J. Y. Harbec, B. M. Powell and S. Jandl, *Phys. Rev. B*, 1983, **28**, 7009.
21. I. Chung, K. Biswas, J.-H. Song, J. Androulakis, K. Chondroudis, K. M. Paraskevopoulos, A. J. Freeman and M. G. Kanatzidis, *Angew. Chem., Int. Ed.* , 2011, **50**, 8834.
22. S. I. Kim, S. Hwang, S. Y. Kim, W.-J. Lee, D. W. Jung, K.-S. Moon, H. J. Park, Y.-J. Cho, Y.-H. Cho, J.-H. Kim, D.-J. Yun, K. H. Lee, I.-t. Han, K. Lee and Y. Sohn, *Sci. Rep.*, 2016, **6**, 19733.
23. P. Ramasamy, P. Manivasakan and J. Kim, *CrystEngComm*, 2015, **17**, 807.
24. Z. Fang, S. Hao, L. Long, H. Fang, T. Qiang and Y. Song, *CrystEngComm*, 2014, **16**, 2404.

25. C. Zhang, H. Yin, M. Han, Z. Dai, H. Pang, Y. Zheng, Y.-Q. Lan, J. Bao and J. Zhu, *ACS Nano*, 2014, **8**, 3761.
26. J. Choi, J. Jin, I. G. Jung, J. M. Kim, H. J. Kim and S. U. Son, *Chem. Commun.*, 2011, **47**, 5241.
27. X. Zhou, L. Gan, W. Tian, Q. Zhang, S. Jin, H. Li, Y. Bando, D. Golberg and T. Zhai, *Adv. Mater.*, 2015, **27**, 8035.
28. Y. Huang, K. Xu, Z. Wang, T. A. Shifa, Q. Wang, F. Wang, C. Jiang and J. He, *Nanoscale*, 2015, **7**, 17375.
29. M. Achimovicova, K. Lucenildo da Silva, N. Daneu, A. Recnik, S. Indris, H. Hain, M. Scheuermann, H. Hahn and V. Sepelak, *J. Mater. Chem.*, 2011, **21**, 5873.
30. X. Yu, J. Zhu, Y. Zhang, J. Weng, L. Hu and S. Dai, *Chem. Comm.*, 2012, **48**, 3324.
31. J. Yu, C.-Y. Xu, Y. Li, F. Zhou, X.-S. Chen, P.-A. Hu and L. Zhen, *Sci. Rep.*, 2015, **5**, 17109.
32. S. N. Guin, V. Srihari and K. Biswas, *J. Mater. Chem. A*, 2015, **3**, 648.
33. W. G. Zeier, A. Zevalkink, Z. M. Gibbs, G. Hautier, M. G. Kanatzidis and G. J. Snyder, *Angew. Chem., Int. Ed.*, 2016, **55**, 6826.
34. A. J. Smith, P. E. Meek and W. Y. Liang, *J. Phys. C: Solid State Phys.*, 1977, **10**, 1321.
35. D. B. Mitzi, *Inorg. Chem.*, 2005, **44**, 3755.
36. G. Han, S. R. Popuri, H. F. Greer, J.-W. G. Bos, W. Zhou, A. R. Knox, A. Montecucco, J. Siviter, E. A. Man, M. Macauley, D. J. Paul, W.-g. Li, M. C. Paul, M. Gao, T. Sweet, R. Freer, F. Azough, H. Baig, N. Sellami, T. K. Mallick and D. H. Gregory, *Angew. Chem., Int. Ed.*, 2016, **55**, 6433.
37. B.-Z. Sun, Z. Ma, C. He and K. Wu, *Phys. Chem. Chem. Phys.*, 2015, **17**, 29844.

CHAPTER 7

Engineering Ferroelectric Instability to Achieve Ultralow Thermal Conductivity and High Thermoelectric Performance in $Sn_{1-x}Ge_xTe$

Chapter 7

Engineering Ferroelectric Instability to Achieve Ultralow Thermal Conductivity and High Thermoelectric Performance in $Sn_{1-x}Ge_xTe$

Summary

High thermoelectric performance of a crystalline solid requires it to have low thermal conductivity while exhibiting high carrier mobility, which is one of the utmost materials challenges. Ferroelectric lattice instability in a solid results in softening of polar optical phonons and the associated increase in dielectric constant screens the charge carriers from scattering at various defects. This chapter demonstrate how these localized ferroelectric instability induced soft polar phonons effectively scatter the heat carrying acoustic phonons and help achieve ultralow lattice thermal conductivity of SnTe by engineering the instability near room temperatures via Ge (x = 0-30 mol%) alloying. Short-range chain-like structures with correlated local Ge off-centering distortions in the cubic $Sn_{1-x}Ge_xTe$ *scatter acoustic phonons, resulting in an ultralow lattice thermal conductivity of ~ 0.67 W/mK. The mobility of charge carriers, however, remains high due to dielectric screening of the charge carriers associated with ferroelectric instability. Additionally, Sb doping in* $Sn_{1-x}Ge_xTe$ *enhances the Seebeck coefficient due to p-type carrier optimization and valence band convergence, which leads to synergistic boost in the thermoelectric figure of merit, zT, to ~ 1.6 at 721 K. The concept of engineering ferroelectric instability to achieve ultralow thermal conductivity while retaining high carrier mobility is applicable to other crystalline solids, which opens up a general opportunity to enhance the thermoelectric performance.*

7.1 Introduction

Innovative design of solid state structures and compositions with low thermal conductivity while maintaining the high electrical transport is the way forward to high performance thermoelectric (TE) materials, which offer an environment friendly solution for recovery of waste heat in the form of electricity.[1,2] The crux of improving a material's thermoelectric performance involves essentially the optimization of three interdependent material properties: electrical conductivity (σ), Seebeck coefficient (S) and thermal conductivity (κ_{total} = electronic (κ_{el}) + lattice (κ_{lat}) thermal conductivity) which govern the dimensionless thermoelectric figure of merit, $zT = \sigma S^2 T / (\kappa_{lat} + \kappa_{el})$.[3] The reduction in κ_{lat} by devising an efficient mechanism of scattering heat carrying acoustic phonons is one of the most effective and widely used avenues for high performance thermoelectrics.[4-6] Innovative material design like broadband phonon scatterings based on extrinsic all-scale hierarchical nano/meso-architectures[5,7] or intrinsic material properties,[8] e.g., complex crystal structures,[9] part-crystalline part-liquid state,[10] bonding asymmetry,[11,12] superionic substructure with liquid-like cation disordering,[13-15] lone-pair induced bond anharmonicity[16] and anisotropic layered crystal structure[17,18] have been employed in the past to achieve low κ_{lat}. However, in many of these approaches like the introduction of nano/meso-architectures, the reduction in κ_{lat} comes with a cost of reduced charge carrier mobility (μ) and electrical conductivity.

This chapter present a new strategy to significantly reduce the κ_{lat} without degrading carrier mobility by engineering the local ferroelectricity instability in a crystalline solid. A ferroelectric phase transitions is typically marked by temperature dependent softening of polar transverse optical (TO) phonons at the center of the Brillouin zone with its energy becoming comparable to that of heat transporting acoustic phonons.[19] This results in a strong acoustic-optical phonon coupling,[20,21] and consequently cause significant scattering of acoustic phonons,[22] and low κ_{lat} in solids. The same soft polar optical phonons cause divergently large dielectric response near the ferroelectric instability, and hence the screening of the mobile charge carriers from scattering at impurities/defects, enhancing the charge carrier mobility.[23-26] Therefore, successful deployment of the ferroelectric instability in thermoelectric solid will be an effective approach to achieve low κ_{lat} while retaining the high carrier mobility.

We demonstrate that engineering of local ferroelectric instability can be used to achieve high thermoelectric performance in inorganic solids like tin telluride (SnTe). SnTe has recently emerged as an environment friendly alternative to PbTe for mid-temperature thermoelectric power generation.[27-34] The global centrosymmetric room temperature rocksalt structure of SnTe, however, has a lattice instability originating from resonant bonding[35-40] and undergoes a temperature dependent paraelectric to ferroelectric transition with rhombohedral (*R-3m*) structure below 100 K.[41] Ferroelectricity in its rhombohedral phase originates from relative displacements of the Sn and Te sublattice along [111] direction.[41-45] In the close proximity of the ferroelectric transition, SnTe exhibits softening of the zone centre (Γ-point) TO phonon modes[36,46] and the frequencies of these TO phonons are in fact lower in the cubic phase compared to that of the rhombohedral phase.[45] This local ferroelectric instability associated with soft TO phonons in cubic SnTe, can be employed to further improve its thermoelectric performance by reducing the κ_{lat} without degrading the electrical transport properties. However, ferroelectric phase transition and softening of TO phonons in SnTe occur in a temperature regime of ≤ 100 K, making it impractical to use this instability for thermoelectric power generation at high temperatures.

Here, we have utilized the substitution of Ge (0–30 mol%) in SnTe to strengthen its local ferroelectric instability near room temperatures and achieve soft phonon modes in a wide range of momenta around ferroelectric instability. $Sn_{1-x}Ge_xTe$ exhibits unstable phonon branches not only at the Brillouin zone center (characteristic of displacive phase transition), but also wave-vectors in a large domain in Brillouin zone. In real space, this results in chain like local off-centering of Ge in the cubic SnTe lattice. We have experimentally established the presence of low frequency phonon modes (soft mode) *via* Raman spectroscopy. Soft TO phonons associated with ferroelectric instability couple strongly with strain and scatter heat carrying acoustic phonons, and thereby reduce the κ_{lat} to ~ 0.67 W/mK at 300 K in $Sn_{0.7}Ge_{0.3}Te$. Further, $Sn_{1-x}Ge_xTe$ samples exhibit high carrier mobility which can be ascribed to effective dielectric screening of charge carriers from the charged impurities/defects and suppressed scattering. With synergy among ultra-low κ_{lat}, high carrier mobility and enhanced Seebeck coefficient, we achieve highest thermoelectric figure of merit, zT, of ~ 1.6 at 721 K in carrier optimized Sb-doped $Sn_{0.7}Ge_{0.3}Te$ ($Sn_{0.57}Sb_{0.13}Ge_{0.3}Te$). This report opens up a new avenue to inhibit thermal

conduction while retaining high carrier mobility in crystalline solids by employing local distortion associated with ferroelectric instability.

7.2 Methods

7.2.1 Synthesis

Tin (Alfa Aesar 99.99+ %), germanium (Aldrich 99.999%), tellurium (Alfa Aesar 99.999+ %) and antimony (Alfa Aesar 99.999+ %) were used for synthesis without further purification.

High quality polycrystalline ingots of $Sn_{1-x}Ge_xTe$ (x = 0–0.5) have been synthesized by melting the stoichiometric amount of Sn, Ge and Te in vacuum sealed (10^{-5} Torr) quartz tube. The tubes were kept vertically in a box furnace and slowly heated to 900 ^{o}C over 12 hrs, then kept for 10 hrs, and cooled slowly to room temperature. Sb alloyed $Sn_{1-x}Ge_xTe$ samples have been prepared via similar method. For the measurement of the electrical and thermal transport properties, ingots were cut and polished in the shape of bar and coin respectively.

To improve the thermoelectric properties, we have done spark plasma sintering (SPS) of the highest zT composition, $Sn_{0.57}Sb_{0.13}Ge_{0.3}Te$. The melt grown ingots were ground into fine powders using a mortar and pestle to reduce the grains size in an inert glove box. This powder was then pressed into cylindrical shape by SPS method (SPS-211LX, Fuji Electronic Industrial Co., Ltd.) at 773 K for 5 min in a 10 mm diameter graphite die under an axial pressure of 40 MPa in vacuum. Highly dense (~ 98% of theoretical density) disk-shaped pellets with ~10 mm diameter and ~10 mm thickness were obtained.

7.2.2 Characterizations

Powder X-ray diffraction (PXRD) for all the samples were recorded using a Cu Kα (λ = 1.5406 Å) radiation on a Bruker D8 diffractometer. DSC data were collected by METTLER-TOLEDO Differential Scanning Calorimeter (DSC 822 e) with a heating/cooling rate of 1 K/min between 253 and 300 K in N_2 atmosphere. To estimate optical band gap, IR diffuse reflectance measurements was performed with finely ground powder at room temperature using FT-IR Bruker IFS 66 V/S spectrometer in a frequency

range of 4000-400 cm^{-1} with 2 cm^{-1} resolution and 50 scans. The energy band gaps were derived from α/Λ vs. E (eV) plots. Backscattered electron imaging (BSE) mode field emission scanning electron microscopy (FESEM) experiments were performed using NOVA NANO SEM 600 (FEI, Germany) operated at 15 kV. EDAX compositional analysis was performed during FESEM imaging. Background was subtracted (using multi-polynomial model) during the data processing for EDAX elemental mapping (with 500 eV minimum region of interest width). Errors in the determination in compositions of nanosheets in EDAX measurements is nearly 5%. Transmission electron microscopy (TEM) imaging was performed using an aberration corrected FEI TITAN cubed 80–300 kV transmission electron microscope operating at 300 kV. TEM samples were prepared by conventional mechanical thinning. Raman measurements were carried out using Horiba HR-Evolution spectrometer with 532 nm excitation laser. Ultra-low frequency filters were used to record the spectrum in the range of 18–200 cm^{-1}. Frequency of local modes around Ge atoms can be represented as

$$\omega_0 = \omega_{TO}(SnTe)\left[1 + \frac{(M_{Ge} - M_{Sn})}{M_{Sn}}\right]^{-1/2} \tag{7.1}$$

Where M_{Ge} and M_{Sn} are the atomic masses of Ge and Sn, respectively, and ω_0 is the frequency of the local modes around Ge. Frequency of local modes due to Ge atom doping is estimated to be ~ 24 to 27 cm^{-1} which are in well agreement with the calculated and observed soft modes at ~ 19, 27 and 36 cm^{-1}.

7.2.3 Transport properties

Electrical conductivity and Seebeck coefficients were measured simultaneously under He atmosphere from room temperature to 873 K on a ULVAC-RIKO ZEM-3 instrument system (measurement details is given in chapter 1). Carrier concentrations were determined using Hall coefficient measurements at room temperature with equipment made by Excel instrument. Four-contact Hall-bar geometry was used for the measurement and a varying magnetic field up to 0.57 Tesla was applied during the measurements. At 300 K, we have estimated the carrier concentration, n_{H}, from the formula: $n_{\mathrm{H}}=1/eR_{\mathrm{H}}$, where e is the electronic charge, R_{H} is hall coefficient. Thermal diffusivity, D, was directly measured in the range of 300−873 K by using laser flash diffusivity method in a

Netzsch LFA-457. The total thermal conductivity, κ_{total}, was calculated using the formula, $\kappa_{total} = DC_p\rho$ (measurement details is given in chapter 1).

7.2.4 Computational details

We used density functional theoretical (DFT) methods as implemented in QUANTUM ESPRESSO (QE) code,[47] taking into account only the valence electrons and replacing the potential of the ionic core with a pseudopotential. We used a generalized gradient approximation (GGA)[48] to the exchange-correlation energy functional as parameterized by Perdew, Burke, and Ernzerhof (PBE).[49] To describe the interactions between valence electrons and ions, we used Projected Augmented–Wave (PAW) potentials. Valence and semi-core electronic states of Sn, Te and Ge were considered through the use of pseudopotentials (in $4d^{10}$ $5s^2$ $5p^2$, $4d^{10}$ $5s^2$ $5p^4$, and $3d^{10}$ $4s^2$ $4p^2$configurations respectively). SnTe crystallizes in the rocksalt structure belonging to *F*m-3m space group, with two atoms in the primitive unit cell and eight atoms in the conventional cubic unit cell. Pristine and Ge substituted SnTe were simulated using conventional cubic unit cell containing four SnTe. Electronic wave functions and charge density were represented in plane wave basis sets truncated with cut-off energies of 45 Ry and 400 Ry respectively. The Brillouin Zone (BZ) integrations were sampled on a uniform 20 x 20 x 20 mesh of k-points. The discontinuity in occupation numbers of electronic states was smeared using a Fermi-Dirac distribution function with broadening of $k_BT = 0.003$ Ry. We determined lattice dynamical properties of SnTe and $Sn_{0.75}Ge_{0.25}Te$ in their optimized structures obtained after vc-relaxation at the experimental lattice parameter. The PBE optimized lattice parameters of SnTe (a = b = c = 6.37 Å) and $Sn_{0.75}Ge_{0.25}Te$ (a = b = c = 6.28 Å) were considered for further calculations. Dynamical matrices were calculated within the Density Functional Perturbation Theory (DFPT) on a 2 x 2 x 2 q-points grid in the Brillouin Zone.[50] We Fourier interpolated these dynamical matrices to obtain the phonon dispersion along high symmetry lines (Γ - X - M - Γ - R - X - M - R) in the Brillouin zone. We estimated the measure of strain phonon coupling (couplings between acoustic and optical phonons) using a finite difference formula of $\partial\omega_0^2(\epsilon)/\partial\epsilon$ having calculated squared phonon frequencies at strained structures. We used scalar relativistic pseudopotentials (SOC = 0) in DFT-LR calculations of phonons.

7.3 Results & Discussion

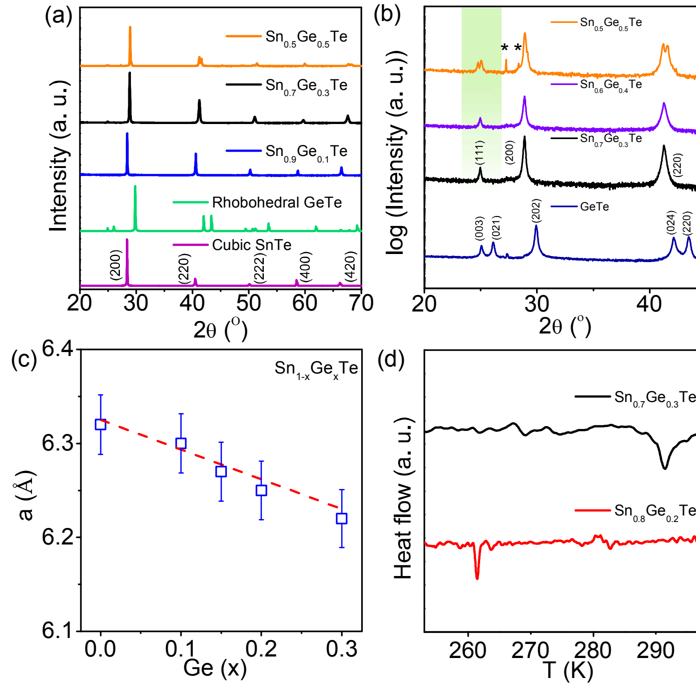

Figure 7.1 (a) Powder XRD patterns of $Sn_{1-x}Ge_xTe$ (x = 0-0.5) samples showing Ge-concentration dependent structural phase transition, represented by splitting of (220) peak. (b) PXRD patterns of $Sn_{1-x}Ge_xTe$ (x = 0-0.5) in log scale. Colored region indicates enhanced intensity of (111) reflection. '*' sign in $Sn_{0.5}Ge_{0.5}Te$ indicates the presence of Ge- rich second phases. (c) Lattice parameter (*a*) vs. Ge concentration (*x*) in $Sn_{1-x}Ge_xTe$ (x = 0-0.3). Dashed line indicates the Vegard's law for solid solution. (d) DSC signal of $Sn_{1-x}Ge_xTe$ samples as a function of temperature.

The room temperature powder X-ray diffraction (PXRD) patterns of $Sn_{1-x}Ge_xTe$ (x = 0–0.5) (Figure 7.1a) confirms the face centered cubic (Fm-3m) structure for x < 0.5. The gradual increase in the intensity of odd reflections (e.g., (111) peak in the marked region of Figure 7.1b) and linear decrease in the lattice parameter from 6.32 Å in SnTe to 6.22 Å in $Sn_{0.7}Ge_{0.3}Te$ (Figure 7.1c) in accordance with Vegards law indicate the progressive substitution of Sn by Ge in cubic SnTe structure. The increasing concentration of Ge in SnTe, however, amplifies the local distortion of the cubic structure along (111) direction when the Ge concentration is below 40 mol% in SnTe. Further increasing the Ge concentration to 50 mol%, the splitting of (111) and (220) peaks is evidenced in $Sn_{0.5}Ge_{0.5}Te$ (Figure 7.1a and Figure 7.1b). The local rhombohedral distortion in the cubic structure in $Sn_{1-x}Ge_xTe$ arises from the smaller atomic radii of Ge (Ge^{2+}: 87 pm) compared to that of Sn (Sn^{2+}: 93 pm)[51] and is the primary cause of the ferroelectric instability.[52] This behavior is further confirmed by the increase in cubic to rhombohedral phase transition temperature with increasing Ge concentration in SnTe which is evident in

differential scanning calorimetry (DSC) study (Figure 7.1d).[53] While this cubic to rhombohedral phase transition occurs below 100 K in pristine SnTe, the 30 mol% of Ge alloying enhances the transition to near room temperature (T_c ~ 291 K in x = 0.3).

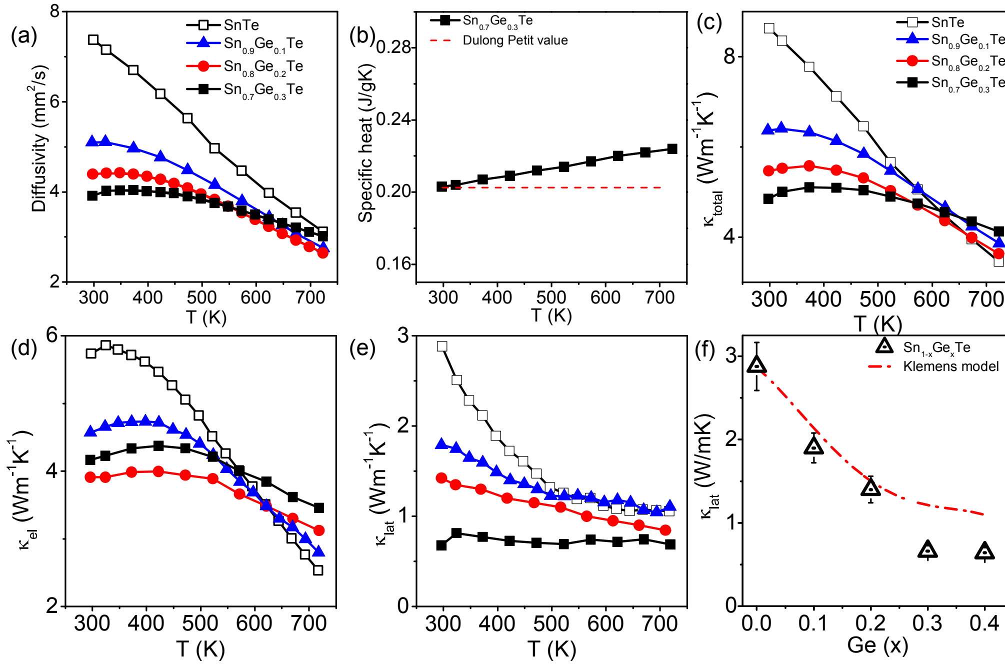

Figure 7.2 (a) Temperature dependent diffusivity (D) of $Sn_{1-x}Ge_xTe$ (x =0-0.3). (b) Typical temperature dependent heat capacity (C_p) of $Sn_{0.7}Ge_{0.3}Te$, which is in well agreement with Dulong Petit C_p value (Red line). (c), (d) and (e) are temperature-dependent total thermal conductivity (κ_{total}), electronic thermal conductivity (κ_{el}) and lattice thermal conductivity (κ_{lat}) of $Sn_{1-x}Ge_xTe$. (f) Room-temperature κ_{lat} as a function of Ge alloying concentration. Solid line corresponds to the predicted lattice thermal conductivities considering the mass and strain fluctuation due to Ge incorporation in SnTe lattice based on Klemens model.

In Figure 7.2, we present temperature dependent thermal transport properties of $Sn_{1-x}Ge_xTe$ (x = 0–0.3) samples. GeTe alloying in SnTe substantially reduces the κ_{total} from ~ 8.66 W/mK for SnTe to ~ 4.84 W/mK for $Sn_{0.7}Ge_{0.3}Te$ at 300 K (Figure 7.2c). The strong scattering of the heat carrying acoustic phonons by soft TO phonons associated with the local ferroelectric instability in the proximity of room temperature in $Sn_{0.7}Ge_{0.3}Te$ is a possible cause for huge reduction in κ_{lat} value from ~ 2.89 W/mK in SnTe to ~ 0.67 W/mK in $Sn_{0.7}Ge_{0.3}Te$ at 300 K (Figure 7.2e). This κ_{lat} value of ~ 0.67 W/mK nearly reaches the minimum theoretical value of lattice thermal conductivity, κ_{min} (~ 0.44 W/mK) of SnTe estimated with Cahill's model.[54] While κ_{lat} values are in good agreement with the Klemens model of disordered alloys (Figure 7.2f)[55] for the $Sn_{1-x}Ge_xTe$ samples for $x \leq 0.2$, indicating a predominant role of solid solution point defects in phonon scattering caused by Ge alloying in SnTe up 20 mol% of Ge; the Klemens model largely

overestimates the κ_{lat} value of $Sn_{0.7}Ge_{0.3}Te$ ($x \geq 0.3$). Backscattered electron imaging (BSE) mode FESEM and TEM images further confirm the absence of any secondary nano/micro-precipitates (Figure 7.3), and therefore negate the effect of nano-structuring on κ_{lat} of $Sn_{0.7}Ge_{0.3}Te$. These observations strongly imply that low frequency (soft) phonon modes associated with strong localized ferroelectric instability play a predominant role in the reduction of κ_{lat} in $Sn_{0.7}Ge_{0.3}Te$.

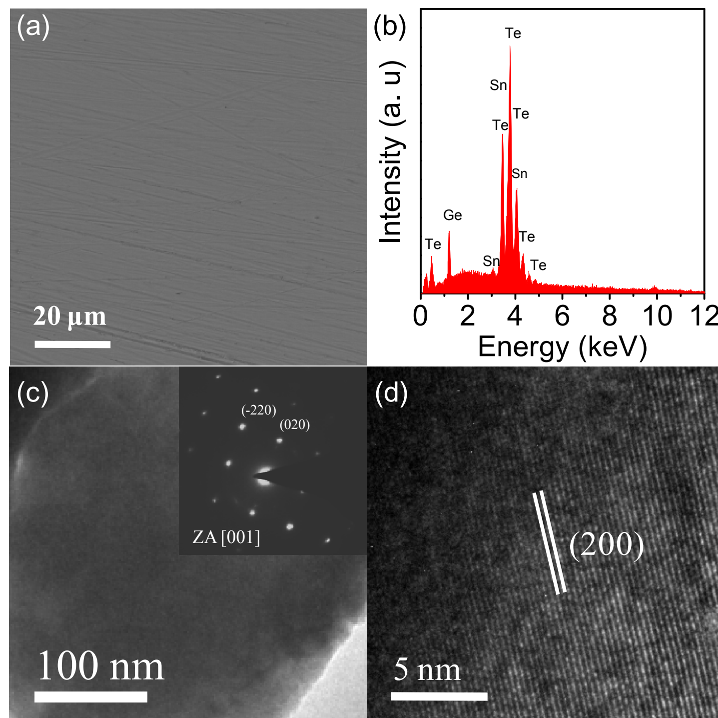

Figure 7.3 (a) & (b) Back scattered FESEM image and EDAX performed on matrix of $Sn_{0.7}Ge_{0.3}Te$. (c) Bright field TEM image of $Sn_{0.7}Ge_{0.3}Te$. Inset electron diffraction pattern is indexed to the rocksalt cubic SnTe structure (d) HRTEM image of $Sn_{0.7}Ge_{0.3}Te$ showing (200) planes of $Sn_{0.7}Ge_{0.3}Te$.

In order to understand the origin of ultralow κ_{lat} and effects of Ge atom in the lattice dynamics of $Sn_{1-x}Ge_xTe$, the phonon dispersion of SnTe and $Sn_{0.75}Ge_{0.25}Te$ were calculated within first-principles based Density Functional Perturbation Theory (DFPT) (Figure 7.4a and 7.4b, respectively). The optical phonons of cubic SnTe (at T = 0 K) exhibit a triply degenerate instability with frequency (ω) of 23i cm^{-1} at Γ-point (Figure 7.4a and Figure 7.5a). Ferroelectricity in SnTe originates from condensation of these three unstable modes, giving a rhombohedral distortion in the cubic phase, through off-centering of Sn atoms as seen in the earlier pair distribution function (PDF)[37] and Extended X-Ray Absorption Fine Structure (EXAFS)[38] analysis. Phonon dispersion of

cubic $Sn_{0.75}Ge_{0.25}Te$ exhibits a much stronger instability at $\omega \sim 91i\ cm^{-1}$ (Figure 7.4b and Figure 7.5b) at Γ-point. An interesting feature evident in it (Figure 7.4b) is the presence of unstable modes at all wave vectors in the Brillouin zone except near R-point $\left(= \frac{\pi}{a}(1,1,1)\right)$. Fourier analysis of such instabilities gives a real space picture of local distortions with chain-like regions of short-range order,[56] and the size of such distorted polar region ~ $1/q_c$ (q_c is the wave vector at which the branches of unstable phonon cross zero). This signifies the local displacements of Ge atoms along the chains of Ge–Te–Sn–Te-Ge–Te in cubic $Sn_{1-x}Ge_xTe$. The character of phase transition in SnTe (unstable modes only at wave vectors close to the zone centre) thus changes from displacive to order-disorder type transition in $Sn_{0.75}Ge_{0.25}Te$.[57] Atomic displacements of the unstable phonon modes at *Γ*-point of SnTe and Ge-alloyed SnTe (inset in Figure 7.4c and Figure 7.5) show that Ge-displacements dominate the local instability in $Sn_{0.75}Ge_{0.25}Te$, while the structural instability in SnTe involves displacements of both Sn and Te sublattices. The off-centred site is favored energetically due to the large ionic size difference between Sn^{+2} and Ge^{2+} (Ge^{2+}: 87 pm; Sn^{2+}: 93 pm), higher polarization power of Ge^{2+} as compared to Sn^{2+} arising from stronger stereochemical activity of ns^2 lone pair in $Sn_{0.75}Ge_{0.25}Te$.[58,59] We calculated the Born effective charges (Z^*) which reveals higher polarization power (significant deviations of Z^* from their nominal valence charges) of Ge^{2+} as compared to Sn^{2+} in $Sn_{0.75}Ge_{0.25}Te$ (Sn: $Z^*_{xx/yy/zz} = 6.63$; Ge: $Z^*_{xx/yy/zz} = 10.11$; Te: $Z^*_{xx/yy/zz} = -7.71$). Significantly stronger ferroelectric instability in $Sn_{1-x}Ge_xTe$ results in higher transition temperatures than that in SnTe.

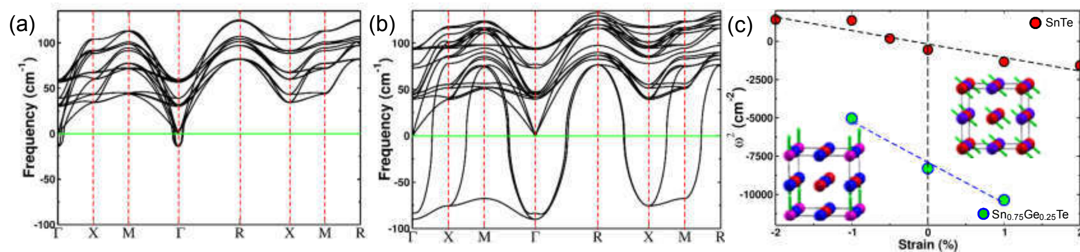

Figure 7.4 Phonon dispersion of (a) SnTe and (b) $Sn_{0.75}Ge_{0.25}Te$ in the centrosymmetric cubic rock salt structure at the theoretical lattice parameter without the inclusion of spin-orbit coupling (SOC), exhibiting unstable *Γ*-point TO modes frequencies at 23i cm^{-1} and 93i cm^{-1} respectively. (c) Dependence of the ω^2 (ϵ) of unstable phonon at zone centre on hydrostatic strain where strain is $(a-a_0)/a_0$ with a_0=6.37Å for SnTe and a_0=6.28Å for $Sn_{0.75}Ge_{0.25}Te$. Visualisation of the atomic displacements of unstable phonons at the zone centre (Red in colour), Te (Blue in colour), and Ge (Pink in colour) are shown.

We determined the nature and extent of cationic off-centering in SnTe and $Sn_{0.75}Ge_{0.25}Te$ by introducing small cationic displacements along <111> direction, and

relaxing the structure to a minimum of energy. In SnTe, relaxation of the distorted structure results in off-centering of all Sn atoms by ~ 0.06 Å and a negligible off-centering of Te atoms (~ 0.003 Å). In $Sn_{0.75}Ge_{0.25}Te$, however, Ge atoms are off-centered by ~ 0.17 Å, significantly higher than that of Sn atoms (~ 0.03-0.04 Å), accompanied by off-centering of Te atoms by ~ 0.08 Å. Thus, larger negative frequencies, along with prominent off-centering of Ge and the presence of higher polarization in the $Sn_{0.75}Ge_{0.25}Te$, corroborate higher transition temperature of Ge alloyed SnTe than of SnTe.[57] Phonons at Γ-point of Ge off-centered structure of $Sn_{0.75}Ge_{0.25}Te$ do not exhibit any unstable modes, with the lowest three optical modes at frequencies of 29 cm^{-1}, 32 cm^{-1} and 32 cm^{-1} (related to the unstable modes of the cubic structure with ω = 91i cm^{-1}), confirming its stability at low temperature.

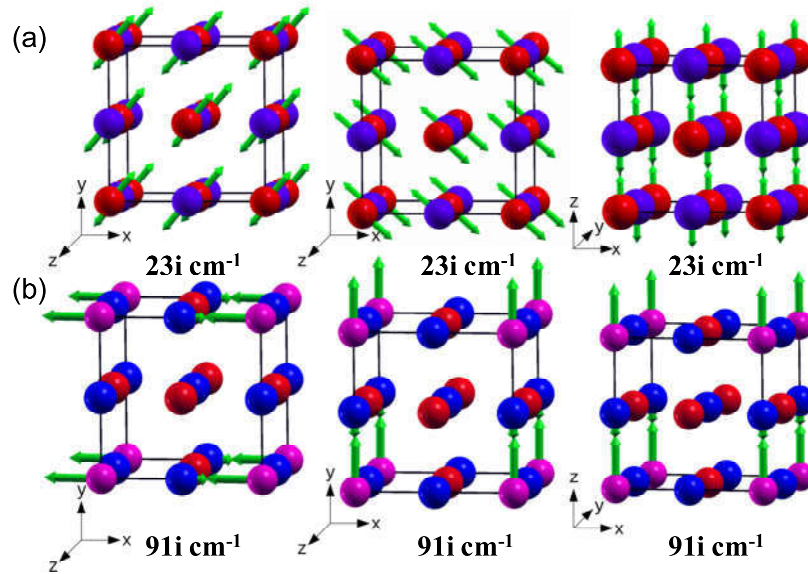

Figure 7.5 Visualisation of the atomic displacements of unstable phonons at the zone centre of (a) SnTe and (b) $Sn_{0.75}Ge_{0.25}Te$, respectively. Sn (Red in colour), Te (Blue in colour), and Ge (Pink in colour).

Thermal conductivity of a solid is controlled by anharmonic interactions between phonons. In SnTe, the interactions between the low energy optical phonons and acoustic phonons are most relevant. We estimated the strength of lattice anharmonicity quantified by strain-phonon coupling $\partial \omega^2(\epsilon)/\partial \epsilon$, where ω is the frequency of unstable optical mode and $\epsilon = (a-a_0)/a_0$ is the strain applied in the system, a_0 being the theoretical lattice constant. The magnitude of $\partial \omega_0^2(\epsilon)/\partial \epsilon$ gives the third order anharmonic coupling

between optical and acoustic phonons, and our estimated values are 785 cm^{-2} and 2664 cm^{-2} for SnTe and $Sn_{0.75}Ge_{0.25}Te$ (Figure 7.4c), respectively. Thus, stronger anharmonic interactions between the unstable optical phonons (local polar distortions) and acoustic phonons (strain) in $Sn_{1-x}Ge_xTe$ than in SnTe result in stronger scattering of its heat carrying acoustic phonons. With increasing Ge concentration in SnTe, the sharp decrease in κ_{lat} with increasing temperature changes to a nearly temperature independent behavior of κ_{lat} of $Sn_{0.7}Ge_{0.3}Te$. This is consistent with our picture of the chain-like regions of a random local off-centering of Ge atoms, which are present well above T_c, and the associated structural disorder scatter the acoustic phonons strongly.

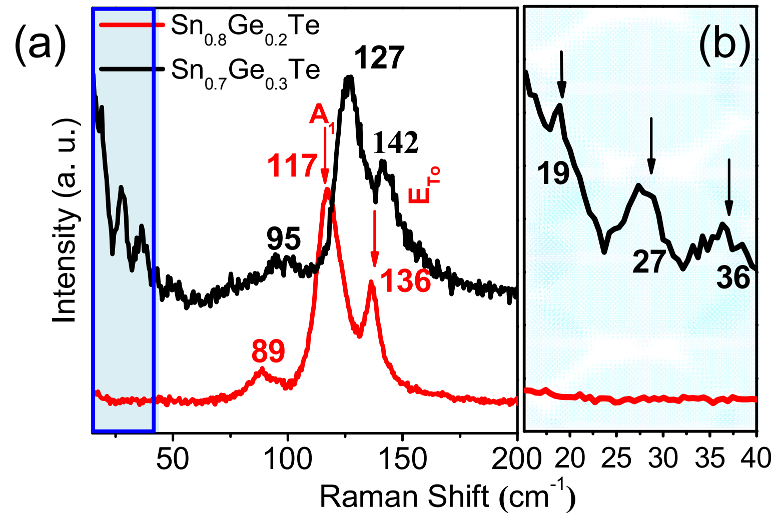

Figure 7.6 (a) Raman spectra of $Sn_{0.8}Ge_{0.2}Te$ and and $Sn_{0.7}Ge_{0.3}Te$ at room temperature. Magnified image of peaks enclosed in blue dashed box is shown in (b).

We used Raman spectroscopy to validate the presence of soft phonon modes near room temperature in $Sn_{0.7}Ge_{0.3}Te$ (Figure 7.6). While no modes of the rocksalt structure of SnTe are Raman active,[60] local distortions of the cubic phase progressively increase with increasing Ge concentration and the off-centering of the Ge in the cubic structure of SnTe is sufficient to break the symmetry and yield Raman active modes. Thus, we find optical phonon modes of $Sn_{1-x}Ge_xTe$ via Raman spectroscopy (Figure 7.6a) at ~ 90 cm^{-1}, ~ 117 cm^{-1} and ~ 136 cm^{-1}, which are commonly observed due to Te atom vibrations.[61] Among these, the mode at 117 cm^{-1} is assigned to A_1 symmetry, which is related to the longitudinal optical phonon mode (LO phonon modes). The modes at 90 cm^{-1} and 136 cm^{-1} are assigned to E_{TO} (TO phonon modes). Shifts in A_1 and E_{TO} mode frequencies to higher frequencies with increasing Ge concentration are consistent with our calculated

phonon dispersions (Figure 7.4a and 7.4b). However, the low energy soft modes and localized modes at 19 cm^{-1}, 27 cm^{-1} and 36 cm^{-1} belong exclusively to $Sn_{0.7}Ge_{0.3}Te$, which constitute the signatures of local displacements of Ge associated with ferroelectric insatiability near room temperature (Figure 7.6b). As shown by our calculations, these modes are responsible for scattering of acoustic modes and low lattice thermal conductivity.

To optimize the excess *p*-type carrier concentration of $Sn_{1-x}Ge_xTe$, we have doped trivalent Sb^{3+} in $Sn_{0.7}Ge_{0.3}Te$, which not only optimizes electronic transport properties but also decreases κ_{el}, and thus the κ_{total}. The PXRD patterns (Figure 7.7a) of Sb doped $Sn_{1-x}Ge_xTe$ ($Sn_{0.7-y}Sb_yGe_{0.3}Te$, y = 0–0.13) confirms the solid solution nature with linearly decreasing lattice parameter from 6.22 Å for $Sn_{0.7}Ge_{0.3}Te$ to 6.19 Å for $Sn_{0.57}Sb_{0.13}Ge_{0.3}Te$ (Figure 7.7b).

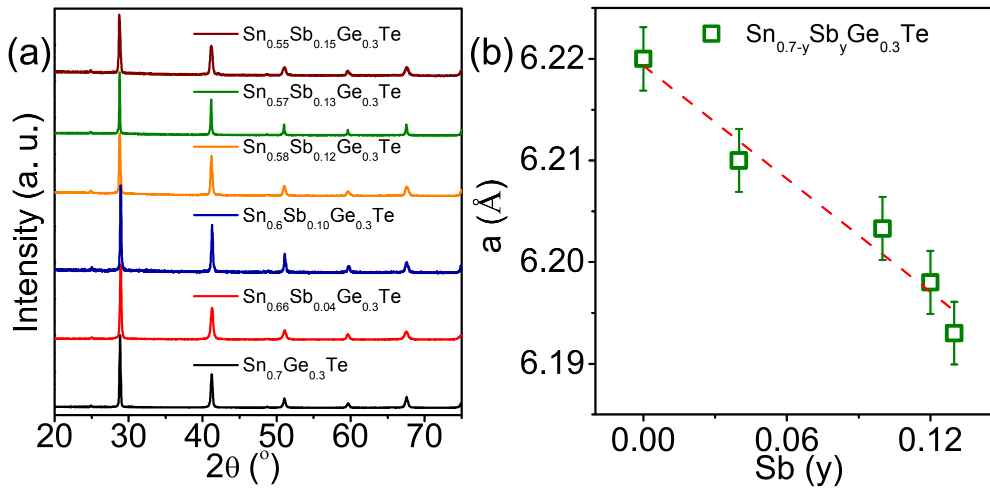

Figure 7.7 (a) Powder XRD patterns of $Sn_{0.7-y}Sb_yGe_{0.3}Te$ (y = 0-0.15). (b) Lattice parameter (*a*) vs. Sb concentration (y) plot for $Sn_{0.7-y}Sb_yGe_{0.3}Te$ (y = 0-0.13).

The reduction in *p*-type carrier concentration (n_H) due to Sb doping is evident in Table 7.1. Room temperature κ_{el} drastically reduces from ~ 4.16 W/mK for $Sn_{0.7}Ge_{0.3}Te$ to ~ 1.44 W/mK for $Sn_{0.57}Sb_{0.13}Ge_{0.3}Te$ (Figure 7.8b). As a result, the room temperature κ_{total} reduces from 4.84 W/mK in $Sn_{0.7}Ge_{0.3}Te$ to 2.01 W/mK in $Sn_{0.57}Sb_{0.13}Ge_{0.3}Te$ (Figure 7.8a). To further reduce thermal conductivity, we have performed mechanical grinding and spark plasma sintering (SPS) of $Sn_{0.57}Sb_{0.13}Ge_{0.3}Te$ and obtained an ultralow value of κ_{lat} of ~ 0.44 W/mK at 728 K in $Sn_{0.57}Sb_{0.13}Ge_{0.3}Te$ (Figure 7.8c).

Table 7.1 Room temperature carrier concentration (n_H) and carrier mobility (μ) of $Sn_{1-x}Ge_xTe$ (x = 0–0.3) and $Sn_{0.7-y}Sb_yGe_{0.3}Te$. We have also compared our data with previously reported carrier concentration and mobility of SnTe based samples.

Sample	n_H (10^{19} cm^{-3})	μ (cm^2/Vs)
SnTe	33	170
$Sn_{0.9}Ge_{0.1}Te$	11	370
$Sn_{0.8}Ge_{0.2}Te$	8.3	418
$Sn_{0.7}Ge_{0.3}Te$	8.9	421
$Sn_{0.66}Sb_{0.04}Ge_{0.3}Te$	5.44	300
$Sn_{0.57}Sb_{0.13}Ge_{0.3}Te$	4.5	310
$Sn_{0.88}Sb_{0.12}Te$ (For comparison)[33]	15	130
SnTe-CdTe-CdS (For comparison)[29]	5.63	237
$Sn_{0.97}Bi_{0.03}Te$–3% SnSe (For comparison)[62]	8.5	355
$Sn_{0.97}Bi_{0.03}Te$–3% SnSe (For comparison)[62]	8.7	344
$Sn_{0.98}Bi_{0.03}Te$-HgTe (For comparison)[63]	9.3	257

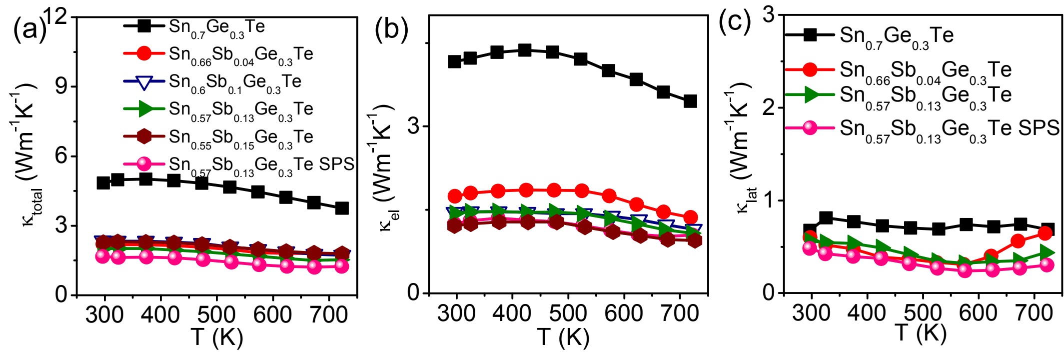

Figure 7.8 Temperature-dependent (a) total thermal conductivity (κ_{total}), (b) electronic thermal conductivity (κ_{el}) and (c) lattice thermal conductivity (κ_{lat}) of $Sn_{0.7-y}Sb_yGe_{0.3}Te$ (y = 0-0.15) samples.

The temperature variation of electrical conductivity (σ) of $Sn_{1-x}Ge_xTe$ exhibits degenerate semiconducting behavior (Figure 7.9a) which primarily originates from intrinsic Sn vacancies.[64] Typically, the room temperature σ value is 5989 S/cm for $Sn_{0.7}Ge_{0.3}Te$ which reduces to 2507 S/cm at 710 K. Room temperature σ decreases with increasing Ge concentration and reaches a minimum value in the $Sn_{0.8}Ge_{0.2}Te$ due to the decrease in *p*-type carrier concentration (n_H) (Table 7.1). The progressive substitution of Sn by Ge fills the Sn vacancies and thereby reduces the hole concentration (n_H). The room temperature carrier mobility, μ, however, remains high with Ge alloying (Table 7.1) and testifies to the increased dielectric screening of the mobile charge carriers from impurity/defect scattering in the proximity of paraelectric to ferroelectric phase transition.[26] Similar increase in carrier mobility due dielectric screening has earlier been observed in complex oxides[23] and $Pb_{1-x}Sn_xSe$[25]. We have compared the carrier mobility of

$Sn_{1-x}Ge_xTe$ with other SnTe based materials that posses similar carrier concentrations (Table 7.1), which shows comparatively higher values of μ in Ge alloyed samples. Further reduction in carrier concentration (Table 7.1) due to Sb doping reduces σ over the entire measured temperature range in the $Sn_{0.7-y}Sb_yGe_{0.3}Te$ (y = 0–0.15) samples (Figure 7.10a). The room temperature σ ~ 5989 S/cm for $Sn_{0.7}Ge_{0.3}Te$ decreases to 2291 S/cm in $Sn_{0.57}Sb_{0.13}Ge_{0.3}Te$. Although the room temperature carrier mobility of the $Sn_{0.7-y}Sb_yGe_{0.3}Te$ samples decreases compared to $Sn_{0.7}Ge_{0.3}Te$ sample (Table 7.1) due to enhanced disorder scattering, it is still higher than that of the pristine SnTe and $Sn_{1-y}Sb_yTe$, which further testify to the Ge alloying induced strengthening of ferroelectric instability and the consequent dielectric screening scenario discussed above. The SPS processed $Sn_{0.57}Sb_{0.13}Ge_{0.3}Te$ sample exhibits a further reduction in electrical conductivity due to increased grain boundary scattering of mobile charge carriers (Figure 7.10a).

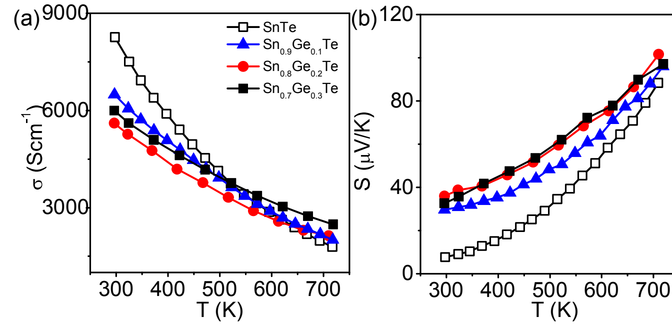

Figure 7.9 (a) and (b) are temperature dependent electrical conductivity (σ) and Seebeck coefficient (S) of $Sn_{1-x}Ge_xTe$, respectively.

The positive value of Seebeck coefficient (S) across the measured temperature range of 300–723 K (Figure 7.10b) indicates the dominant *p*-type charge transport in $Sn_{1-x}Ge_xTe$. Typically, the room temperature S value is ~ 32 μV/K in $Sn_{0.7}Ge_{0.3}Te$ which increases to ~ 100 μV/K at 721 K. The measured S value of SnTe is consistent with the previous reports and the theoretically calculated Pisarenko line (Figure 7.10d) using two valance band model (VBM) considering the contribution from both the non-parabolic light hole (L point) and parabolic heavy hole (Σ point) valence band with energy separation (ΔE) of 0.3 eV. $Sn_{1-x}Ge_xTe$, however, shows deviation with significantly higher S values from the theoretically estimated Pisarenko line similar to the previous cases of valence band convergence.[29,51] Experimentally measured larger principal band gap (Figure 7.10c) additionally suggests that Ge alloying results in electronic structure

modification via valance band convergence. To further validate this point, we calculated the Pisarenko line considering two valance band model by varying the energy gap (ΔE) between the light and heavy hole valance bands. *S* value of $Sn_{0.7}Ge_{0.3}Te$ falls on Pisarenko curve with ΔE = 0.25 eV (Figure 7.10d & 7.10e) which indeed suggests the valance band convergence.

The reduction in energy gap between the two valence bands (ΔE = 0.25 eV of $Sn_{0.7}Ge_{0.3}Te$ as compared to ΔE = 0.35 eV of SnTe) results in enhanced Seebeck coefficient in $Sn_{0.7}Ge_{0.3}Te$. The Sb doping in $Sn_{0.7}Ge_{0.3}Te$ ($Sn_{0.7-y}Sb_yGe_{0.3}Te$) further enhances the Seebeck coefficient (Figure 7.10b, 7.10d, 7.10e) because of the decrease in energy separation between the two valence bands (ΔE = 0.15 eV for $Sn_{0.57}Sb_{0.13}Ge_{0.3}Te$ in Figure 7.10e). Typically, the room temperature *S* value of the SPS processed $Sn_{0.57}Sb_{0.13}Ge_{0.3}Te$ is ~ 68 μV K^{-1} which reaches the maximum of ~ 174 μV/K at 721 K. The SPS processed $Sn_{0.57}Sb_{0.13}Ge_{0.3}Te$ sample exhibits highest power factor σS^2 with room temperature value of ~ 9.7 μW/cmK^2 which increases to ~ 27μW/cmK^2 at 721 K (Figure 7.10f).

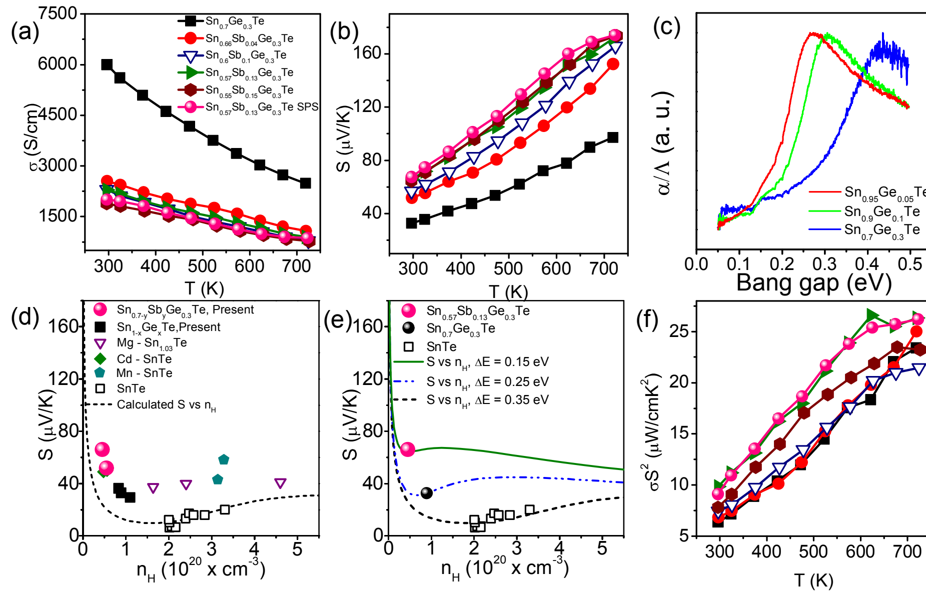

Figure 7.10 Temperature-dependent (a) electrical conductivity (σ), (b) Seebeck coefficient (*S*) of $Sn_{1-x}Ge_xTe$ (x = 0-0.3). (c) Room temperature optical absorption spectra of $Sn_{1-x}Ge_xTe$ (x = 0-0.3). (d) Room temperature *S* vs. n_H plot of the present $Sn_{1-x}Ge_xTe$ and $Sn_{0.7-y}Sb_yGe_{0.3}Te$ samples. For comparison, previously reported S vs. n_H experimental data of un-doped SnTe,[27] Mg alloyed SnTe,[30] Cd doped SnTe,[29] Mn doped SnTe,[51] and theoretical Pisarenko curve based on VBM model are given in (d). (e) Pisarenko lines for $Sn_{0.7}Ge_{0.3}Te$ and $Sn_{0.7-y}Sb_yGe_{0.3}Te$ are calculated based on a two-valence-band model, considering reduced energy separation of valence bands via Ge alloying and Sb alloying. The experimental *S* vs. n_H values for $Sn_{0.7}Ge_{0.3}Te$ and $Sn_{0.7-y}Sb_yGe_{0.3}Te$ are in well agreement with theoretical Pisarenko confirming modification of electronic structure. (f) Temperature dependent power factor (σS^2) of $Sn_{0.7-y}Sb_yGe_{0.3}Te$ (y = 0-0.15).

Benefitting from the drastic reduction in κ_{lat} due to soft TO phonon modes generated by local ferroelectric instability and consequent high carrier mobility due to dielectric screening, along with a enhanced Seebeck coefficient due to valance band convergence, a maximum zT of ~ 1.6 has been achieved in the SPS processed $Sn_{0.57}Sb_{0.13}Ge_{0.3}Te$ at 721 K (Figure 7.11). A much higher zT is achieved in $Sn_{0.7-y}Sb_yGe_{0.3}Te$, notably in comparison with $Sn_{1-y}Sb_yTe$ and SnTe, which conclusively demonstrates the role of Ge substitution in engineering the ferroelectric-instability. Considering the hot and cold end temperature to be 720 K and 300 K, respectively, an average zT ~ 0.9 is found in SPS processed $Sn_{0.57}Sb_{0.13}Ge_{0.3}Te$ which is higher than any of the previously reported SnTe based materials in this temperature window.[31]

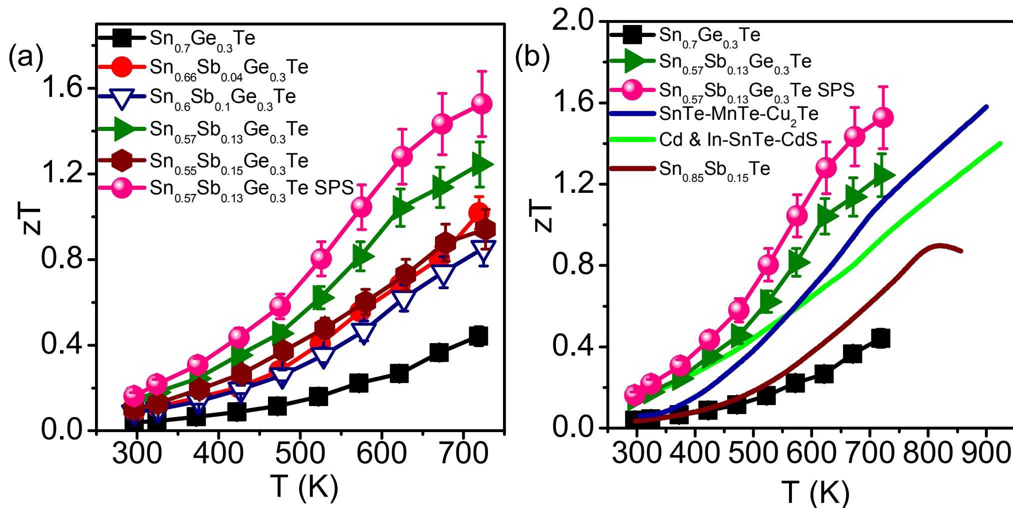

Figure 7.11 (a)Temperature-dependent zT of $Sn_{0.7-y}Sb_yGe_{0.3}Te$ (y = 0-0.15) samples. (b) Temperature dependent zT of $Sn_{0.7}Ge_{0.3}Te$ and $Sn_{0.57}Sb_{0.13}Ge_{0.3}Te$, comparing with those of the reported high performance SnTe-based materials.

7.4 Conclusions

In conclusion, we have demonstrated how engineering of ferroelectric instability induced local structural distortions and softening of the TO phonon modes yield ultralow thermal conductivity in Ge alloyed SnTe. Near ferroelectric instability in $Sn_{1-x}Ge_xTe$, the carrier mobility is shown to remain high due to strong dielectric screening of charge carriers from scattering centers like the impurities/defects. Further, Sb substitution enhances the Seebeck coefficient significantly by optimizing the p-type carrier concentration and

reducing the energy offset between two valence bands of SnTe. As a result of synergy between these mechanisms, *zT* of 1.6 is achieved in $Sn_{0.57}Sb_{0.13}Ge_{0.3}Te$ at 721 K. The strategy of improving thermoelectric performance by tuning localized ferroelectric instability and associated local structural distortion as demonstrated here opens up a new avenue to development of high performance thermoelectrics. This new strategy is engaging, particularly, because it can be readily applied to further boost the thermoelectric performance of materials like SnSe and GeTe, which are close to ferroelectric instabilities.

7.5 References

1. G. Tan, L.-D. Zhao and M. G. Kanatzidis, *Chem. Rev.*, 2016, **116**, 12123.
2. Z.-H. Ge, L.-D. Zhao, D. Wu, X. Liu, B.-P. Zhang, J.-F. Li and J. He, *Mater. Today*, 2016, **19**, 227.
3. L.-D. Zhao, V. P. Dravid and M. G. Kanatzidis, *Energy Environ. Sci.*, 2014, **7**, 251.
4. Y. Xiao, H. Wu, W. Li, M. Yin, Y. Pei, Y. Zhang, L. Fu, Y. Chen, S. J. Pennycook, L. Huang, J. He and L.-D. Zhao, *J. Am. Chem. Soc.*, 2017, **139**, 18732.
5. K. Biswas, J. He, I. D. Blum, C.-I. Wu, T. P. Hogan, D. N. Seidman, V. P. Dravid and M. G. Kanatzidis, *Nature*, 2012, **489**, 414.
6. M. Samanta and K. Biswas, *J. Am. Chem. Soc.*, 2017, **139**, 9382.
7. G. Tan, F. Shi, S. Hao, L.-D. Zhao, H. Chi, X. Zhang, C. Uher, C. Wolverton, V. P. Dravid and M. G. Kanatzidis, *Nat. Commun.*, 2016, **7**, 12167.
8. M. K. Jana and K. Biswas, *ACS Energy Lett.*, 2018, **3**, 1315.
9. G. J. Snyder and E. S. Toberer, *Nat. Mater.*, 2008, **7**, 105.
10. B. Li, H. Wang, Y. Kawakita, Q. Zhang, M. Feygenson, H. L. Yu, D. Wu, K. Ohara, T. Kikuchi, K. Shibata, T. Yamada, X. K. Ning, Y. Chen, J. Q. He, D. Vaknin, R. Q. Wu, K. Nakajima and M. G. Kanatzidis, *Nat. Mater.*, 2018, **17**, 226.
11. M. K. Jana, K. Pal, A. Warankar, P. Mandal, U. V. Waghmare and K. Biswas, *J. Am. Chem. Soc.*, 2017, **139**, 4350.
12. M. K. Jana, K. Pal, U. V. Waghmare and K. Biswas, *Angew. Chem., Int. Ed.*, 2016, **55**, 7792.
13. H. Liu, X. Shi, F. Xu, L. Zhang, W. Zhang, L. Chen, Q. Li, C. Uher, T. Day and G. J. Snyder, *Nat. Mater.*, 2012, **11**, 422.
14. S. Roychowdhury, M. K. Jana, J. Pan, S. N. Guin, D. Sanyal, U. V. Waghmare and K. Biswas, *Angew. Chem., Int. Ed.*, 2018, **57**, 4043.
15. A. A. Olvera, N. A. Moroz, P. Sahoo, P. Ren, T. P. Bailey, A. A. Page, C. Uher and P. F. P. Poudeu, *Energy Environ. Sci.*, 2017, **10**, 1668.
16. D. Morelli, V. Jovovic and J. Heremans, *Phys. Rev. Lett.*, 2008, **101**, 035901.
17. L.-D. Zhao, S.-H. Lo, Y. Zhang, H. Sun, G. Tan, C. Uher, C. Wolverton, V. P. Dravid and M. G. Kanatzidis, *Nature*, 2014, **508**, 373.
18. M. Samanta, K. Pal, P. Pal, U. V. Waghmare and K. Biswas, *J. Am. Chem. Soc.*, 2018, **140**, 5866.
19. W. Cochran, *Adv. Phys.*, 1960, **9**, 387.
20. R. M. Murphy, É. D. Murray, S. Fahy and I. Savić, *Phys. Rev. B*, 2017, **95**, 144302.
21. T. Seddon, J. M. Farley and G. A. Saunders, *Solid State Commun.*, 1975, **17**, 55.
22. O. Delaire, J. Ma, K. Marty, A. F. May, M. A. McGuire, M. H. Du, D. J. Singh, A. Podlesnyak, G. Ehlers, M. D. Lumsden and B. C. Sales, *Nat. Mater.*, 2011, **10**, 614.
23. W. Siemons, M. A. McGuire, V. R. Cooper, M. D. Biegalski, I. N. Ivanov, G. E. Jellison, L. A. Boatner, B. C. Sales and H. M. Christen, *Adv. Mater.*, 2012, **24**, 3965.
24. D. Jena and A. Konar, *Phys. Rev. Lett.*, 2007, **98**, 136805.
25. P. Dziawa, B. J. Kowalski, K. Dybko, R. Buczko, A. Szczerbakow, M. Szot, E. Łusakowska, T. Balasubramanian, B. M. Wojek, M. H. Berntsen, O. Tjernberg and T. Story, *Nat. Mater.*, 2012, **11**, 1023.
26. X. Zhang and Y. Pei, *npj Quantum Mater.*, 2017, **2**, 68.
27. A. Banik, S. Roychowdhury and K. Biswas, *Chem. Commun.*, 2018, **54**, 6573.
28. Q. Zhang, B. Liao, Y. Lan, K. Lukas, W. Liu, K. Esfarjani, C. Opeil, D. Broido, G. Chen and Z. Ren, *Proc. Natl. Acad. Sci. USA* 2013, **110**, 13261.

29. G. Tan, L.-D. Zhao, F. Shi, J. W. Doak, S.-H. Lo, H. Sun, C. Wolverton, V. P. Dravid, C. Uher and M. G. Kanatzidis, *J. Am. Chem. Soc.*, 2014, **136**, 7006.
30. A. Banik, U. S. Shenoy, S. Anand, U. V. Waghmare and K. Biswas, *Chem. Mater.*, 2015, **27**, 581.
31. G. Tan, F. Shi, S. Hao, H. Chi, L.-D. Zhao, C. Uher, C. Wolverton, V. P. Dravid and M. G. Kanatzidis, *J. Am. Chem. Soc.*, 2015, **137**, 5100.
32. A. Banik, U. S. Shenoy, S. Saha, U. V. Waghmare and K. Biswas, *J. Am. Chem. Soc.*, 2016, **138**, 13068.
33. A. Banik, B. Vishal, S. Perumal, R. Datta and K. Biswas, *Energy Environ. Sci.*, 2016, **9**, 2011.
34. W. Li, L. Zheng, B. Ge, S. Lin, X. Zhang, Z. Chen, Y. Chang and Y. Pei, *Adv. Mater.*, 2017, **29**, 1605887.
35. U. V. Waghmare, N. A. Spaldin, H. C. Kandpal and R. Seshadri, *Phys. Rev. B*, 2003, **67**, 125111.
36. S. Katayama and H. Kawamura, *Solid State Commun.*, 1977, **21**, 521.
37. K. R. Knox, E. S. Bozin, C. D. Malliakas, M. G. Kanatzidis and S. J. L. Billinge, *Phys. Rev. B*, 2014, **89**, 014102.
38. K. V. Mitrofanov, A. V. Kolobov, P. Fons, M. Krbal, T. Shintani, J. Tominaga and T. Uruga, *Phys. Rev. B*, 2014, **90**, 134101.
39. L. Aggarwal, A. Banik, S. Anand, U. V. Waghmare, K. Biswas and G. Sheet, *J. Materiomics*, 2016, **2**, 196.
40. S. Lee, K. Esfarjani, T. Luo, J. Zhou, Z. Tian and G. Chen, *Nat. Commun.*, 2014, **5**, 3525.
41. M. Sist, E. M. Jensen Hedegaard, S. Christensen, N. Bindzus, K. F. F. Fischer, H. Kasai, K. Sugimoto and B. Brummerstedt Iversen, *IUCrJ*, 2016, **3**, 377.
42. G. S. Pawley, W. Cochran, R. A. Cowley and G. Dolling, *Phys. Rev. Letters*, 1966, **17**, 753.
43. M. Iizumi, Y. Hamaguchi, K. F. Komatsubara and Y. Kato, *J. Phys. Soc. Jpn.*, 1975, **38**, 443.
44. K. Murase and S. Sugai, *Solid State Comm.*, 1979, **32**, 89.
45. C. D. O'Neill, D. A. Sokolov, A. Hermann, A. Bossak, C. Stock and A. D. Huxley, *Phys. Rev. B*, 2017, **95**, 144101.
46. S. Sugai, K. Murase and H. Kawamura, *Solid State Commun.*, 1977, **23**, 127.
47. G. Paolo, B. Stefano, B. Nicola, C. Matteo, C. Roberto, C. Carlo, C. Davide, L. C. Guido, C. Matteo, D. Ismaila, C. Andrea Dal, G. Stefano de, F. Stefano, F. Guido, G. Ralph, G. Uwe, G. Christos, K. Anton, L. Michele, M.-S. Layla, M. Nicola, M. Francesco, M. Riccardo, P. Stefano, P. Alfredo, P. Lorenzo, S. Carlo, S. Sandro, S. Gabriele, P. S. Ari, S. Alexander, U. Paolo and M. W. Renata, *J. Phys.: Condens. Matter*, 2009, **21**, 395502.
48. X. Hua, X. Chen and W. A. Goddard, *Phys. Rev. B*, 1997, **55**, 16103.
49. J. P. Perdew, K. Burke and M. Ernzerhof, *Phys. Rev. Lett.*, 1996, **77**, 3865.
50. S. Baroni, S. de Gironcoli, A. Dal Corso and P. Giannozzi, *Rev. Mod. Phys.*, 2001, **73**, 515.
51. G. Tan, F. Shi, S. Hao, H. Chi, T. P. Bailey, L.-D. Zhao, C. Uher, C. Wolverton, V. P. Dravid and M. G. Kanatzidis, *J. Am. Chem. Soc.*, 2015, **137**, 11507.
52. J. N. Bierly, L. Muldawer and O. Beckman, *Acta Metall.*, 1963, **11**, 447.
53. I. Hatta and W. Rehwald, *J. Phys. C: Solid State Phys.*, 1977, **10**, 2075.
54. D. G. Cahill, S. K. Watson and R. O. Pohl, *Phys. Rev. B*, 1992, **46**, 6131.

55. P. G. Klemens, *Phys. Rev.*, 1960, **119**, 507.
56. H. Krakauer, R. Yu, C.-Z. Wang, K. M. Rabe and U. V. Waghmare, *J. Phys.: Condens. Matter*, 1999, **11**, 3779.
57. A. I. Lebedev and I. A. Sluchinskaya, *Phys. Solid State*, 2007, **49**, 1132.
58. J. Trajic, A. Golubovic, M. Romcevic, N. Romcevic, S. Nikolic and N. N. Vladimir, *J. Serb. Chem. Soc.*, 2007, **72**, 55.
59. W. G. Zeier, A. Zevalkink, Z. M. Gibbs, G. Hautier, M. G. Kanatzidis and G. J. Snyder, *Angew. Chem., Int. Ed.*, 2016, **55**, 6826.
60. L. Brillson and E. Burstein, *Phys. Rev. Lett.*, 1971, **27**, 808.
61. S. Acharya, J. Pandey and A. Soni, *Appl. Phys. Lett.*, 2016, **109**, 133904.
62. G. Mahan and J. Sofo, *Proc. Natl. Acad. Sci. U. S. A.*, 1996, **93**, 7436.
63. G. Tan, F. Shi, J. W. Doak, H. Sun, L.-D. Zhao, P. Wang, C. Uher, C. Wolverton, V. P. Dravid and M. G. Kanatzidis, *Energy Environ. Sci.*, 2015, **8**, 267.
64. U. Jun-ichi, J. Manu and O. Toshihiro, *Jpn. J. Appl. Phys.*, 1962, **1**, 277.

List of Publications

- Included in thesis

1. **A. Banik**, S. Roychowdhury and K. Biswas, “Journey of tin chalcogenides towards high performance thermoelectrics and topological material”, ***Chem. Commun.***, 2018, **54**, 6573-6590 (Perspective article).
2. **A. Banik** and K. Biswas, “Synthetic nanosheets of natural van der Waals heterostructures”, ***Angew. Chem. Int. Ed.***, 2017, **56**, 14561-14566.
3. **A. Banik**, U. S. Shenoy, S. Saha, U. V. Waghmare and K. Biswas, “High power factor and enhanced thermoelectric performance of SnTe-AgInTe_2: Synergistic effect of resonance level and valence band convergence”, ***J. Am. Chem. Soc***., 2016, **138**, 13068-13075.
4. S. Saha, **A. Banik** and K. Biswas, “Few layer nanosheets of *n*-type $SnSe_2$”, ***Chem. Eur. J***., 2016, **22**, 15634–15638.
5. **A. Banik**, B. Vishal, S. Perumal, R. Datta and K. Biswas, “The origin of low thermal conductivity in $Sn_{1-x}Sb_xTe$: Phonon scattering via layered intergrowth nanostructures”, ***Energy Environ. Sci.***, 2016, **9**, 2011-2019.
6. **A. Banik**, L. Aggarwal, S. Anand, U. V. Waghmare, K. Biswas and G. Sheet, “Local ferroelectricity in thermoelectric SnTe above room temperature driven by competing phonon instabilities and soft resonant bonding”, ***J. Materiomics***, 2016, **2**, 196-202.
7. **A. Banik** and K. Biswas, “AgI alloying in SnTe boosts the thermoelectric performance via simultaneous valence band convergence and carrier concentration optimization”, ***J. Solid State Chem.,*** 2016, **242**, 43-49.
8. **A. Banik**, U. S. Shenoy, S. Anand, U. V. Waghmare and K. Biswas, “Mg Alloying in SnTe facilitates valence band convergence and optimizes thermoelectric properties”, ***Chem. Mater.,*** 2015, **27**, 581- 587.
9. **A. Banik** and K. Biswas, “Lead free thermoelectrics: promising performance in *p*-type $SnTe_{1-x}Se_x$ system”, ***J. Mater. Chem. A,*** 2014, **2**, 9620-9625.

- Not included in thesis

10. S. Chandra, **A. Banik** and K. Biswas, “*n*-Type ultrathin few-layer nanosheets of Bi doped SnSe: Synthesis and thermoelectric properties”, ***ACS Energy Lett.***, 2018, **3**, 1153-1158.
11. P. Pal, S. Saha, **A. Banik**, A. Sarkar and K. Biswas, “All-solid-state mechanochemical synthesis and post-synthetic transformation of inorganic perovskite-type halides”, ***Chem. Eur. J***., 2018, **24**, 1811–1815.
12. **A. Banik** and K. Biswas, “Low-temperature soft-chemical synthesis and thermoelectric properties of barium-filled *p*-type skutterudite nanocrystals”, ***Mater. Sci. Semicond. Process,*** 2014, **27**, 593-598.

Book Chapter

1. S. N. Guin, **A. Banik** and K. Biswas, Thermoelectric energy conversion in layered metal chalcogenides, in the book “2-D Inorganic Materials beyond Graphene", Eds. C. N. R. Rao and U. V. Waghmare, World Scientific (Singapore), **2017**, 239-274.

Biography

Ananya Banik obtained her B.Sc. degree from Presidency University, Kolkata in 2012 and her MS degree in Chemical Science in 2015 from the Jawaharlal Nehru Centre for Advanced Scientific Research (JNCASR). Currently she is pursuing her Ph. D. under the supervision of Prof. Kanishka Biswas at New Chemistry Unit, Jawaharlal Nehru Centre for Advanced Scientific Research (JNCASR), Bangalore, India. Her research work focuses on the solid state inorganic chemistry of metal chalcogenides with special emphasis on thermoelectric energy conversion based on bulk and nanostructured Sn-chalcogenides and their structure-property relationship. She has been selected for the award of INSPIRE Fellowship (2015), Department of Science & Technology, Government of India. She has also been the recipient the Best Poster Award at "An International Symposium on Solid State Chemistry", December 2016, Bangalore, India. She has been selected for oral presentation in "256th ACS National Meeting" Boston, MA, USA, August, 2018 and an International Travel Support (2018), from Science and Research Board, Department of Science and Technology (DST), Government of India, to attend the meeting.